

The
University
Of
Sheffield.

Department
Of
Mechanical
Engineering

Measuring Friction at an Interface Using Nonlinear Ultrasonic Response

Xiangwei LI

June 2018

Supervisors: Prof. R. Dwyer-Joyce and Prof. M. Marshall

A thesis submitted in partial fulfilment of the requirements for the degree
of Doctor of Philosophy

ABSTRACT

Contacts of rough surfaces are present in almost all machines and mechanical components. Friction at the rough interface cause energy dissipation, wear and damage of surfaces. Engineers are interested in knowing the frictional conditions at contact interfaces. Despite friction being such a fundamental phenomenon, it is surprisingly difficult to measure reliably as results depend on the test method measurement environment. Methods have been developed to measure the friction and sliding contact tribometers are devised mostly in a laboratory environment. Their applications in measuring friction in-situ in a real contact is a challenge. Therefore, the aim of this research is to develop an ultrasonic method to measure friction and friction coefficient in-situ in a contact interface.

Ultrasonic methods developed for non-destructive testing have been used to measure tribological parameters, such as oil film thickness, viscosity and pressure, in-situ bearings and machines. In conventional ultrasonic techniques, pulses are low power and when they strike an interface they do not result in a change in the contact state. The process is linear and elastic. However, high power sound waves can cause opening or closing of an interface, or interfacial slip; this is non-linear. Recently Contact Acoustic Nonlinearity (CAN) has drawn interest due to its potential in the non-destructive evaluation. When high power bulk shear ultrasound propagates through a compressed rough contact interface, higher order frequency components, higher odd order harmonics ($3f$, $5f$, etc.) are generated in both transmitted and reflected waves. The nonlinear nature of the stick-slip phenomenon in friction may be the source of nonlinearity.

In this study, nonlinearity due to the interaction of a shear ultrasonic wave with a frictional interface has been initially investigated numerically. A one-dimensional numerical model has been employed to understand contact nonlinearity generation and its dependence on incident ultrasonic amplitude, contact pressure and friction coefficient. The third harmonic increases and then decreases when contact stress rises, which suggests that nonlinearity generation due to the 'stick-slip' motion occurs at low contact stress and is restricted at high contact pressure. Harmonic generation at the contact was secondly investigated experimentally using a high frequency nonlinear ultrasonic technique. Methods were developed to separate the

contact nonlinearity from the measured ultrasonic nonlinearity. Contact nonlinearity originating from a rough interface are assessed under various test conditions. Experimental measurement shows good agreement with the numerically computed nonlinearity.

Two strategies were developed to estimate the friction coefficient using experimentally measured contact nonlinearity in conjunction with the numerical computation. The ultrasonically measured friction coefficient agrees reasonably with the sliding test results and published data. Using the contact nonlinearity, the ultrasonic method shows the usefulness in measuring the friction coefficient in-situ in a contact interface.

NOMENCLATURE

Roman symbols

A_0	Amplitude of incident wave
A_1	Fundamental frequency amplitude
A_3	Third order harmonic amplitude
$A_{contact}$	Ultrasound displacement at interface (m)
A_i	Data A
B_i	Data B
c	Speed of sound (m/s)
c_l	Speed of sound of longitudinal wave (m/s)
c_s	Speed of sound of shear wave (m/s)
C_a	Coefficient a
C_b	Coefficient b
d	Wave travelling distance (m)
D	Effective dimension of piezo element (m)
E	Elastic modulus (Pa)
E_u	Energy of ultrasound (J)
f	Frequency (Hz)
F	Coulomb friction (N)
G	Shear modulus (Pa)
h	Separation of contacting surfaces (m)
H	Hardness of material (Pa)
k	Wavenumber (rad/m)
K	Interfacial stiffness (Pa/m)
l	Specimen length (m)
L	Surface profile sampling length (m)

M	Coefficient M
N	Nonlinearity coefficient
N_d	Near field distance (m)
N_f	Frequency constant of piezo element (Hz)
P_{nom}	Nominal contact pressure (Pa)
r	Courant-Friedrichs-Lewy condition
R	Reflection coefficient
R_a	Arithmetic average roughness (m)
R_q	Root mean square roughness (m)
R_E	Power reflection coefficient
T	Transmission coefficient
T_E	Power transmission coefficient
u	Displacement of wave propagation (m)
V_{p-p}	Peak to peak voltage (V)
V_{rms}	Root mean square voltage (V)
W	Weight of mass (N)
z	Asperity height relative to mean line (m)
Z	Acoustic impedance (Pas/m)

Greek symbols

α	Attenuation coefficient (1/m)
θ	Oblique angle of an incident wave
λ	Wavelength (m)
μ	Friction coefficient
μ_k	Dynamic (kinetic) friction coefficient
μ_A	Mean of Data A
μ_B	Mean of Data B
ξ	Dimensionless stress
ρ	Density (kg/m ³)
σ	Normal stress at interface (Pa)
σ_n	Normal stress component (Pa)

σ_u	Stress of ultrasound (Pa)
σ_A	Standard deviation
σ_B	Standard deviation
$\sigma_{cut-off}$	Normal stress where slip stops (Pa)
σ_{peak}	Normal stress at peak of nonlinearity (Pa)
τ	Shear stress induced by ultrasound (Pa)
ν	Poisson's ratio
ω	Angular frequency (rad/s)

Subscript

I	Material <i>I</i>
II	Material <i>II</i>
i	Numerical space index
j	Numerical time index

ACKNOWLEDGEMENT

The author would like to acknowledge the excellent encourage, inspiration and guidance given by Prof. Rob Dwyer-Joyce throughout this project. Without his help, it would not be possible to complete this work. The attitude towards the scientific research, the optimism and patience that the author has learned from him will benefit the author for a lifetime.

The author would also like to thank the University of Sheffield for the financial support.

Thanks to all staffs, postdocs and PhDs in the Tribology group for their kindness and support. Thanks to Mr Dave Butcher and Mr Luke Callaghan for their great technical support. Thanks to Dr Juanjuan Zhu, Dr Robin Mills, Dr Henry Brunskill, Dr Andy Hunter and Dr Michele Schirru for their assistance and advice, especially on experimental skills. Thanks to Mr Geogios Tyreas, Miss Olivia Manfredi, Mr Gary Nicholas, Mr Joseph Kanja, Mr Marcello Cadeddu, Mr Sushil Simkhada, Mr Tomos Brenchley, Mr Mattia Lai and Mr David Fort for the great discussions and help.

Thanks to all my friends for their encouragement throughout this project.

Finally, the author would like to dedicate this work to his parents, Mr Guoqiang Li and Mrs Li Li, who have always been supporting and encouraging the author. A special thanks to his wife, Mrs Lijie Zhang, for her love, encouragement and patience.

CONTENTS

Abstract.....	i
Nomenclature.....	iii
Acknowledgement.....	vi
Contents	vii
List of Figures	xii
List of Tables	xxi
1 Introduction.....	1
1.1 Statement of the Problem.....	1
1.2 Aims and Objectives	2
1.3 Layout of the Thesis	3
2 Background on Contact.....	5
2.1 Rough Contact Interface	5
2.2 Friction Model	6
2.3 Friction Measurement.....	8
2.4 Friction Coefficient of a Metal-Metal Contact.....	9
2.5 Stick-Slip Phenomenon and Tangential Contact.....	10
2.6 Conclusion	11
3 Theory of Ultrasound	12
3.1 Fundamentals of Ultrasound.....	12
3.1.1 The Basic Principles of Ultrasound	12
3.1.1.1 Longitudinal Wave	13
3.1.1.2 Transverse Wave	14
3.1.2 Ultrasound Propagation in Materials	15
3.1.2.1 Speed of Sound.....	15
3.1.2.2 Acoustic Impedance	17
3.1.2.3 Attenuation.....	17
3.1.3 Ultrasound Propagation at Boundaries.....	18
3.1.3.1 Reflection and Transmission	18

3.1.3.2	Snell's Law and Mode Conversion	19
3.2	Using Ultrasound to Measure Contact Interface	20
3.2.1	Interfacial Stiffness	20
3.2.2	Tribological Parameters.....	22
3.3	Nonlinear Ultrasound.....	22
3.4	Conclusion	25
4	Ultrasonic Technique Apparatus.....	26
4.1	Ultrasonic Generation Using Ultrasonic Transducers.....	26
4.1.1	The Piezoelectric Effect.....	27
4.1.2	Piezoelectric Element.....	27
4.1.3	Ultrasonic Transducers.....	29
4.1.4	Near Field Effect.....	32
4.1.5	Ultrasonic Signal Characteristics	33
4.2	Ultrasonic Function Generator.....	35
4.2.1	Excitation Waveforms	36
4.2.2	Excitation Mode and Repetition Rate.....	36
4.3	Power Amplifier.....	37
4.3.1	Excitation Amplitude.....	37
4.3.2	Signal Amplification.....	38
4.4	Ultrasonic Digitiser	40
4.4.1	Sampling Rate	42
4.4.2	Amplitude Resolution and Range	42
4.4.3	Bandwidth	42
4.4.4	Number of Channels.....	43
4.4.5	Filters.....	43
4.5	Ultrasonic Measurement Configurations	43
4.6	Conclusion	44
5	Modelling of Ultrasonic Nonlinearity at a Frictional Interface	45
5.1	Analytical Model.....	45
5.1.1	Mathematical Model of Ultrasound at Interface.....	45
5.1.2	Time Harmonic Waveform.....	48
5.1.3	Analytical solution	50
5.2	Numerical Study.....	54
5.2.1	Numerical Model.....	54

5.2.2	Numerical Implementation.....	56
5.2.3	Numerical Simulation Results	59
5.2.3.1	Time Evolution	59
5.2.3.2	Dimensionless Stress.....	62
5.2.3.3	Comparison with Analytical Solutions	63
5.2.3.4	Energy Conservation Energy Dissipation.....	64
5.2.3.5	Effect of Amplitude of Incident Ultrasound and Contact Stress	66
5.2.3.6	Effect of Friction Coefficient.....	70
5.3	Conclusions.....	76
6	Experimental Configuration for Measuring Ultrasonic Nonlinearity at Rough Contacts.....	78
6.1	Introduction	78
6.2	Experimental Configurations.....	79
6.2.1	High Frequency Nonlinear Ultrasonic Technique.....	79
6.2.2	Ultrasonic Apparatus.....	80
6.2.3	Loading Equipment	81
6.2.4	Test Specimens.....	82
6.3	Extra Experimental Considerations.....	84
6.3.1	Piezoelectric Element or Ultrasonic Probe.....	84
6.3.2	Amplifier and Amplification Level	87
6.3.3	Shear Wave Couplant.....	88
6.3.4	Transducer Alignment	90
6.3.5	Data Acquisition.....	93
6.3.5.1	Number of Captures (Repetition)	93
6.3.5.2	Digitising Voltage Scale and Sensitivity.....	95
6.4	Signal Processing Method.....	99
6.4.1	Method of Extracting Frequency Amplitude.....	99
6.4.2	Effect of Signal Truncation and Windowing.....	103
6.5	Laser Vibrometer Measurement	106
6.5.1	Laser Measurement Equipment.....	107
6.5.2	Laser Measurement Configurations.....	107
6.5.3	Laser Measurement Results.....	111
6.6	Conclusion	116
7	Measurement of Ultrasonic Nonlinearity at Rough Contacts	117

7.1	Normally Incident Shear Wave Experiment Configuration.....	117
7.1.1	Pitch-Catch Transmission Configuration.....	118
7.1.2	Pitch-Catch Reflection Configuration.....	124
7.1.3	Comparison of Pitch-Catch Transmission and Reflection Configurations	129
7.2	Method of Removing Nonlinearity from Other Sources.....	135
7.2.1	Solid-Air Contact Interface.....	136
7.2.2	Solid-Solid Contact Interface with Low Power Input.....	139
7.2.3	Input Power Evolution.....	142
7.2.4	Reference Consideration and Contact Harmonic Estimation	144
7.2.4.1	Estimation Using Low Power Solid-Solid Contact.....	144
7.2.4.2	Estimation Using Solid-Air Contact.....	146
7.2.4.3	Estimation Using Solid-Air Contact with Low Power Solid-Solid Contact	147
7.3	Normally Incident Shear Wave Results.....	149
7.3.1	Varying Incident Amplitude	150
7.3.2	Varying Contact Stress.....	152
7.3.3	Experimental Results.....	155
7.4	Measurement of Ultrasonic Nonlinearity at Rough Interface - Subsequent Echoes.....	157
7.4.1	Experimental Configuration.....	157
7.4.2	Ultrasonic Nonlinearity in Subsequent Echoes.....	160
7.5	Conclusion	165
8	Estimation Coefficient of Friction Using Ultrasonic Nonlinearity.....	166
8.1	Comparison Experimental Work with Numerical Study.....	166
8.1.1	Dimensionless Stress.....	167
8.1.1.1	Coefficient of Friction Measurement Using Sliding Test.....	167
8.1.1.2	Shear Stress Introduced by Ultrasound at Contact Interface.....	169
8.1.1.3	Computation of Dimensionless Stress	170
8.1.2	Comparison Experimental Work with Numerical Study.....	171
8.1.3	Ultrasonic Nonlinearity at Rough Contact Interface: From Numerical Model to Experimental Work.....	177
8.2	Estimation of the Coefficient of Friction.....	179
8.2.1	Contact Nonlinearity Coefficient.....	179
8.2.2	Friction Coefficient Estimation Using 'Cut-Off' Stress.....	181

8.2.2.1	Normal Stress at The Peak of Ultrasonic Nonlinearity	182
8.2.2.2	From Normal Stress at The Peak to The Cut-Off Stress	182
8.2.2.3	Estimation of Friction Coefficient Using Cut-Off Stress Strategy	184
8.2.3	Correlation Experiment with Numerical Model.....	187
8.2.4	Coefficient of Friction Estimation Using Ultrasound	192
8.2.4.1	Estimation Friction Coefficient	192
8.2.4.2	Friction Coefficient Comparison.....	194
8.3	Conclusion	196
9	General Discussion	197
9.1	Limitation of Experimental Approach.....	197
9.2	Limitation of Numerical Study.....	198
9.2.1	Numerical Implementation.....	198
9.2.2	Contact Mechanics.....	199
9.3	Limitation of Prediction of Friction Coefficient	200
9.4	Pilot Study of an Alternative Method	200
9.4.1	Test Configuration and Preparation.....	201
9.4.1.1	Test Rig.....	201
9.4.1.2	Experimental Parameters.....	203
9.4.2	Experimental Results.....	204
9.4.2.1	Sensor Configuration I.....	204
9.4.2.2	Sensor Configuration II.....	206
9.5	From Lab measurement to Practical Application.....	208
9.5.1	Practical Estimation Friction Coefficient	208
9.5.2	From Lab Measurement to Practical Application	210
10	Conclusions.....	212
10.1	Modelling Nonlinearity Generation from a Frictional Interface.....	212
10.2	Developing an Ultrasonic Method in Measuring Contact Nonlinearity	213
10.3	Developing an Ultrasonic Method to Measure Friction Coefficient at an Interface	214
10.4	Future Works.....	214
	References.....	216
	Appendix A	225

LIST OF FIGURES

Figure 2.1 Profile of a rough surface (Johnson, 1985).	6
Figure 2.2 Examples of static friction models. (a) Coulomb friction. (b) Coulomb friction with viscous friction. (c) Friction discontinuous at zero velocity. (b) Friction with continuous velocity dependence, known as Stribeck effect (Olsson et al., 1998).	8
Figure 2.3 Schematic diagram of FFM. Normal and friction forces are measured by cantilever deflection by optical interference (Ruan and Bhushan, 1994).	9
Figure 3.1 Schematic diagram of particles ‘mass-spring’ analogy.	13
Figure 3.2 Schematic diagram of the longitudinal wave.	14
Figure 3.3 Schematic diagram of transverse wave.	14
Figure 3.4 Schematic diagram of transverse waves: (a). Vertically polarised transverse wave; (b). Horizontally polarised transverse wave.	15
Figure 3.5 Reflection and transmission of a plane sound wave at a boundary.	18
Figure 3.6 Schematic diagram of obliquely incident wave and its reflection and transmission.	20
Figure 3.7 Representation of ultrasound at rough contact interfaces. (a) Incidence, reflection and transmission. (b) Loading and deflection; (c) The spring model representation (Gonzalez-Valadez et al., 2010).	21
Figure 3.8 Concept of contact acoustic nonlinearity at micro crack (Jhang, 2009).	23
Figure 4.1 Example of shear polarised piezoceramic elements.	28
Figure 4.2 Schematic diagram of commercial ultrasonic transducer.	29
Figure 4.3 (a) Schematic diagram of angle beam transducer; (b) Example of angle beam transducer.	30
Figure 4.4 (a) Schematic diagram of normal incidence shear wave transducer; (b) Example of normal incidence shear wave transducer.	31
Figure 4.5 Example of amplitude from a shear wave piezoelectric element (PIC255, PI) and shear wave transducer (V155, Olympus).	32
Figure 4.6 Sound field from a planar transducer or piezoelectric element.	33
Figure 4.7 Signal characteristics of a normal incidence shear wave transducer V153 (a) Time domain signal and waveform duration; (b) Frequency spectrum and bandwidth (Reproduced Olympus transducer test form).	34
Figure 4.8 Examples of ultrasonic function generator. (a) TTi arbitrary function generator. (b) Function generator incorporated in a Picoscope.	35
Figure 4.9 Examples of signal amplifier. (a) AR low power amplifier. (b) RITEC high power amplifier.	38
Figure 4.10 Harmonic distortion of a 5kW output using a RITEC amplifier (Reproduced from Ritec Amplifier Specification).	40
Figure 4.11 Examples of digitiser. (a) GWINSTEK Oscilloscope. (b) Digitiser incorporated in PicoScope.	41
Figure 4.12 ultrasonic measurement process and configurations.	44

Figure 5.1 Simplified contacting interface and shear polarised ultrasound wave.....	46
Figure 5.2 Contacting interface slips under high-power incident shear ultrasound and remains closed under compressive contact pressure.....	47
Figure 5.3 At interface, shear stress of ultrasound, friction force, contact state alternation and critical time as in Table 5.1. The amplitude of incident shear wave is $5nm$ and corresponding shear stress is $0.26MPa$	50
Figure 5.4 At interface, displacement incident, reflected and transmitted waves after interacting with the frictional interface.....	51
Figure 5.5 At interface, stress of incident, reflected and transmitted waves after interacting with the frictional interface.....	52
Figure 5.6 Frequency spectrum of incident, reflected and transmitted waves after interacting with the frictional interface.....	53
Figure 5.7 Simplified one-dimensional model system.....	55
Figure 5.8 Space and time discretisation for one-dimensional system.....	56
Figure 5.9 Numerical computation procedure.....	58
Figure 5.10 Example of numerical solution of ultrasonic wave striking a frictional interface.	60
Figure 5.11 Time evolution of displacement and shear stress at $x = -L$	61
Figure 5.12 Frequency spectrum of displacement at $x = -L$	61
Figure 5.13 Incident wave, computed 'reflected' wave as the true transmitted wave and computed true reflected wave at $x = -L$	62
Figure 5.14 Numerical and analytical solutions comparison of ultrasound wave interaction with frictional interface, subject to varying contact stress.	64
Figure 5.15 Energy transported by incident, transmitted and reflected wave and energy dissipated at the friction interface, subject to various contact stress.....	66
Figure 5.16 Fundamental and third harmonic amplitude of transmitted wave subject to varying amplitude of incident ultrasound and normally applied contact stress.	68
Figure 5.17 Fundamental and third harmonic amplitude of reflected wave subject to varying amplitude of incident ultrasound and normally applied contact stress.....	69
Figure 5.18 Fundamental and third harmonic amplitude of both transmitted and reflected waves vs dimensionless stress ξ	70
Figure 5.19 Fundamental and third harmonic amplitude of both transmitted and reflected waves subject to varying static friction coefficient.	72
Figure 5.20 Fundamental and third harmonic amplitude of both transmitted and reflected waves vs dimensionless stress ξ , subject to varying static friction coefficient.	73
Figure 5.21 Fundamental and third harmonic amplitude of both transmitted and reflected waves subject to varying dynamic friction coefficient.....	75
Figure 5.22 Fundamental and third harmonic amplitude of both transmitted and reflected waves vs dimensionless stress ξ , subject to varying dynamic friction coefficient.....	76
Figure 6.1 Schematic diagram of the high frequency nonlinearity ultrasonic technique applied in this work.	80
Figure 6.2 Schematic diagram of the loading configuration.....	82
Figure 6.3 (a) NOVATECH loadcell and amplifier. (b) Loadcell calibration relationship.	82
Figure 6.4 Aluminium alloy test specimens with various dimensions.....	83
Figure 6.5 Aluminium alloy test specimen with shear polarised piezoelectric element.....	86

Figure 6.6 Frequency response of shear polarised piezoelectric element subject: (a) nominal 1MHz; (b) nominal 2MHz; (c) nominal 3MHz and (d) nominal 5MHz. Elements were excited with short-duration pulse and the first reflected signal were selected for FFT operation.	86
Figure 6.7 (a) Frequency response of a normal incidence shear wave transducer subject to $4Vp - p$, $90Vp - p$ and $280Vp - p$ excitations. (b) 3 rd order harmonic relative to fundamental frequency amplitude subject to various excitation voltages (100 repetitions).	88
Figure 6.8 Comparison of couplant effect in shear wave signal measurement. Shear transducer mounted (a) with improperly couplant and (b) with proper couplant, subject to $20Vp - p$ excitation of a 10-cycle tone burst (100 repetitions).	90
Figure 6.9 Schematic diagram of alignment of normal incidence shear wave ultrasonic sensors.	91
Figure 6.10 (a) Schematic diagram of locations of normal incidence shear wave ultrasonic sensors. (b) Measurement of fundamental A_1 , third order harmonic frequency A_3 and the ratio A_3/A_1 (50 repetitions).	91
Figure 6.11 (a) Schematic diagram of angle alignment of normal incidence shear wave ultrasonic sensors. (b) Measurement of fundamental A_1 , 3 rd order harmonic frequency A_3 and their ratio A_3/A_1 (50 repetitions).	92
Figure 6.12 Schematic diagram of signal acquisition.	93
Figure 6.13 Averaged frequency spectra subject to various number of captures (repetitions). A tone burst of 15-cycle sine wave sent to test specimen S1 and the reflected signal received.	94
Figure 6.14 (a) Mean and standard deviation of fundamental A_1 . (b) Mean and standard deviation of the 3 rd order harmonic frequency A_3 .	95
Figure 6.15 Effect of various digitising voltage scale on harmonics measurement (12-bit digitisation). (a) Time domain using 5V scale. (b) Frequency spectrum of the first reflection signal captured using 5V scale. (c) Time domain using 2V scale. (d) Frequency spectrum of the first reflection signal captured using 2V scale. (e) Time domain using 1V scale. (f) Frequency spectrum of the first reflection signal captured using 1V scale. (g) Time domain using 500mV scale. (h) Frequency spectrum of the first reflection signal captured using 500mV scale. (i) Time domain using 200mV scale. (j) Frequency spectrum of the first reflection signal captured using 200mV scale.	96
Figure 6.16 (a) Mean and standard deviation of fundamental A_1 subject to various digitising voltage scales. (b) Mean and standard deviation of the 3 rd order harmonic frequency A_3 subject to various digitising voltage scales.	97
Figure 6.17 (a) Averaged time domain signal subject to various digitising voltage scales (b) Averaged frequency spectra. A tone burst of 15-cycle sine wave sent to test specimen S1 and reflected signal received and digitised (50 repetitions).	98
Figure 6.18 (a) Mean and standard deviation of fundamental A_1 subject to various digitising voltage scales. (b) Mean and standard deviation of the 3 rd order harmonic frequency A_3 subject to various digitising voltage scales.	98
Figure 6.19 Schematic diagram of the signal processing method to extract high order harmonics.	100
Figure 6.20 (a) Original time domain signal (b) Extracted target signal with and without windowing. A tone burst of 15-cycle sine wave propagating through test specimen H1 (50 repetitions).	101

Figure 6.21 (a) Frequency spectrum using FFT. (b) Time domain signal using bandpass filter. (c) Total harmonic distortion analysis. . A tone burst of 15-cycle sine wave propagating through test specimen H1 (50 repetitions).	101
Figure 6.22 (a) Fundamental frequency amplitude, A_1 (b) The 3 rd harmonic amplitude, A_3 (c) The ratio A_3/A_1 subject to various normal loads and extracted using three methods. A tone burst of 15-cycle sine wave propagating through test specimen H1 (50 repetitions).102	102
Figure 6.23 (a) Original time domain signal and truncated signal with various length. (b) Frequency spectrum of the various truncated length. A tone burst of 15-cycle sine wave propagating through test specimen H1 (50 repetitions).....	103
Figure 6.24 (a) Fundamental frequency amplitude, A_1 (b) The 3 rd harmonic amplitude, A_3 (c) The ratio A_3/A_1 subject to various truncation length. A tone burst of 15-cycle sine wave propagating through test specimen H1 (50 repetitions).....	104
Figure 6.25 (a) Averaged target signal of 15-cycle sinusoidal wave. (b) Frequency spectrum of the target signal in (a) subject to different window functions. A tone burst of 15-cycle sine wave propagating through test specimen H1 (50 repetitions).....	105
Figure 6.26 (a) Fundamental frequency amplitude, A_1 (b) The 3 rd harmonic amplitude, A_3 (c) The ratio A_3/A_1 subject to various truncation length and window functions. A tone burst of 15-cycle sine wave propagating through test specimen H1 (50 repetitions).....	105
Figure 6.27 Polytec laser sensor head and vibrometer controller (Reproduced from Polytec datasheet).	107
Figure 6.28 (a) Schematic diagram of displacement amplitude measurement using laser vibrometer: transducer on the edge of specimen ('Edge' method). (b) Measurement arrangement.....	108
Figure 6.29 (a) Schematic diagram of displacement amplitude measurement using laser vibrometer: reflective prism bonded at the centre of specimen ('Mirror' method). (b) Reflective prism bonded on the specimen.....	109
Figure 6.30 (a) Schematic diagram of displacement amplitude measurement using laser vibrometer: 45° oriented reflective prism. (b) Adjustable reflective prism at the centre of specimen (45-degree angle method). (c) Displacement decomposition in x and y directions.	110
Figure 6.31 (a) Ultrasonic measurement using pulse-echo method for test specimen S with probe V153, subject to varying excitations. (b) Corresponding simultaneous laser vibrometer measurement. Signal encircled received first by laser vibrometer and then by ultrasound digitiser. (75 repetitions).....	111
Figure 6.32 (a) Laser measured velocity and (b) laser measured displacement of test specimen S with probe V153, subject to varying excitations.	112
Figure 6.33 Shear polarised ultrasound displacement measurement using different laser vibrometer configurations subject to amplification levels. (a) Probe V153 on Specimen S. (b) Probe V153 on Specimen L. (c) Probe V152 on Specimen S. (d) Probe V152 on Specimen L. (75 repetitions).	113
Figure 6.34 Shear polarised ultrasound displacement measurement using 45° angle subject to excitations versus the pulse-echo ultrasonic measurement. (a) Probe V153 on Specimen S. (b) Probe V153 on Specimen L. (c) Probe V152 on Specimen S. (d) Probe V152 on Specimen L. (75 repetitions).....	114

Figure 6.35 Shear wave ultrasound displacement and its corresponding ultrasonic pulse-echo amplitude for transducer V153 and V152 and test specimen S and L. (75 repetitions).	114
Figure 6.36 Shear polarised ultrasound introduced shears stress and its corresponding ultrasonic pulse-echo amplitude for transducer V153 and V152 and test specimen S and L. (75 repetitions).	115
Figure 7.1 Schematic diagram of the test configuration: pitch-catch transmission arrangement.	118
Figure 7.2 Pitch-catch transmission arrangement comparison. (a) two separate test specimens with contact interface. (b) a single test specimen without contact interface.	119
Figure 7.3 (a) Time domain signal in the test with contact interface (L1-S4, excitation 90V, normal stress 0.12MPa, 100 repetitions). (b) Schematic diagram of two separate test specimens with contact interface.	121
Figure 7.4 (a) Time domain signal in the test without contact interface (H1, excitation 90V, normal stress 0.12MPa, 100 repetitions). (b) Schematic diagram of a single test specimen without contact interface.	121
Figure 7.5 (a) Fundamental frequency amplitude A_1 , (b) The third order harmonic A_3 , (c) The ratio A_3/A_1 subject to various normal stresses and incident amplitudes of the two separate test specimens with contact interface (L1-S4, 100 repetitions).	122
Figure 7.6 (a) Two separate test specimens with contact interface under low normal load. (b) Two separate test specimens with contact interface under high normal load.	123
Figure 7.7 (a) Fundamental frequency amplitude A_1 , (b) The third order harmonic A_3 , (c) The ratio A_3/A_1 subject to various normal stresses and incident amplitudes of a single test specimen without contact interface (H1, 100 repetitions).	124
Figure 7.8 Schematic diagram of the test configuration: pitch-catch reflection arrangement.	125
Figure 7.9 Pitch-catch reflection arrangement comparison. (a) Two separate test specimens with solid-solid contact interface. (b) A single test specimen with solid-air contact interface.	126
Figure 7.10 (a) Time domain signal in the test using reflection configuration (S1-Air, excitation 90V, 100 repetitions). (b) Schematic diagram of pitch-catch reflection test with solid-solid or solid-air contact interface.	127
Figure 7.11 (a) Fundamental frequency amplitude A_1 , (b) The third order harmonic A_3 , (c) The ratio A_3/A_1 subject to various normal stresses and incident amplitudes of the test with solid-solid contact interface (S1-S4, 100 repetitions).	128
Figure 7.12 (a) Fundamental frequency amplitude A_1 , (b) The third order harmonic A_3 , (c) The ratio A_3/A_1 subject to various normal stresses and incident amplitudes of test with solid-air contact interface (S1-Air, 100 repetitions).	129
Figure 7.13 The third harmonic amplitude A_3 of test with contact interface (L1-S4) and without contact interface (H1) using pitch-catch transmission configurations (100 repetitions).	130
Figure 7.14 The third harmonic amplitude A_3 of test with solid-solid interface (S1-S4) and solid-air interface (S1-Air) using pitch-catch reflection configuration (100 repetitions).	131

Figure 7.15 (a) Two test specimens with contact interface under low normal loads. (b) Two test specimens with contact interface under high normal loads. (c) Contact nonlinearity generation region for (a) and (b).....	132
Figure 7.16 (a) Fundamental frequency amplitude A_1 , (b)The third order harmonic A_3 , (c) The ratio A_3/A_1 subject to various normal stresses and incident amplitudes of the pitch-catch transmission arrangement (L1-S4, 100 repetitions).	133
Figure 7.17 Contact nonlinearity measurable zone. (a) Limited measurable zone for transmission configuration. (b) Measurable zone for reflection configuration.....	134
Figure 7.18 Possible source of system built-in nonlinearity from in the solid-air contact interface test using pitch-catch arrangement.....	136
Figure 7.19 (a) The fundamental frequency amplitude A_1 , (b) The third harmonic amplitude A_3 of solid-air contact interface (S1-Air) subject to various amplification levels and normally applied loads (100 repetitions).	137
Figure 7.20 The third harmonic amplitude A_3 of solid-air contact interface (S1-Air) subject to various excitation voltages (100 repetitions).	138
Figure 7.21 Possible source of system built-in nonlinearity from in the solid-solid contact interface test using pitch-catch arrangement subject to low power input.	139
Figure 7.22 (a) The fundamental frequency amplitude A_1 , (b) The third harmonic amplitude A_3 , (c) The ratio A_3/A_1 of reflected signal from solid-solid contact interface subject to low amplification (2V peak-peak) and normally applied loads (100 repetitions).....	141
Figure 7.23 The normalised fundamental frequency amplitude A_1 of reflected signal from solid-solid contact interface (S1-S4) subject to various amplification and normally applied loads (100 repetitions)	143
Figure 7.24 The third harmonic amplitude A_3 and the ratio A_3/A_1 of reflected signal from solid-solid contact interface (S1-S4) subject to various normally applied loads at excitation voltage (a) and (b); 2V; (c) and (d): 5V; (e) and (f) 9V; (g) and (h): 45V. (100 repetitions).	143
Figure 7.25 The measured third harmonic of a reflected signal, the system harmonic and the contact harmonic subject to various loads at (a) 2V, (b) 140V and (c) 420V. (S1-S4, 100 repetitions).....	145
Figure 7.26 The measured third harmonic of a reflected signal, the system harmonic and the contact harmonic subject to various loads at (a) 2V, (b) 140V and (c) 420V. (S1-S4, 100 repetitions).....	147
Figure 7.27 The measured third harmonic of a reflected signal, the system harmonic and the contact harmonic subject to various loads at (a) 2V, (b) 140V and (c) 420V. (S1-S4, 100 repetitions).....	148
Figure 7.28 Percentage of contact harmonic in the total measured third harmonic amplitude of test specimen S1-S4.	149
Figure 7.29 (a) Contact harmonic amplitude; (b) normalised contact harmonic amplitude subject to lower power inputs.	150
Figure 7.30 (a) Contact harmonic amplitude; (b)Normalised contact harmonic amplitude subject to higher power inputs. (c) Measurable zone for increasing incidence amplitude.	151
Figure 7.31 Normalised contact harmonic amplitude and fitting curve subject to higher power inputs (Test specimen S1-S4, 100 repetitions).	152

Figure 7.32 Two test specimens with contact interface under (a) low normal stress; (b) higher normal stress and (c) high normal stress.....	153
Figure 7.33 (a) Contact stiffness (b) contact harmonic A_3 amplitude subject to higher power inputs and varying normal contact stresses. (c) Contact stiffness and contact harmonic A_3 amplitude subject to higher power inputs.(Test specimen S1-S4, 100 repetitions).....	154
Figure 7.34 Contact nonlinearity amplitude (the third harmonic A_3) subject to varying incident voltage and contact stress: (a) Test specimen S1-S4. (b) Test specimen S1-S2. (c) Test specimen S1-L1. (d) Test specimen S1-L3. (e) Contact nonlinearity measurable zone.	156
Figure 7.35 Pitch-catch reflection arrangement. (a) two test specimens with same length l . (b) two test specimens with length l and $2l$	157
Figure 7.36 Time domain signal in the test specimens (S1-S4, both length l) subject to varied normal force (excitation 420V, 100 repetitions). (b) Schematic diagram of reflected and transmitted signal inside specimens.....	159
Figure 7.37 Time domain signal in the test specimens (S1-L1, length l and $2l$) subject to varied normal force (excitation 420V, 100 repetitions). (b) Schematic diagram of reflected and transmitted signal inside specimens.	159
Figure 7.38 Test specimens (length l and l) subject to varying normal stress (Excitation 420V, 100 repetitions). (a) Fundamental frequency amplitude A_1 and the third order harmonic A_3 in Echo 1. (b) Schematic diagram of Echo 1. (c) Fundamental frequency amplitude A_1 and the third order harmonic A_3 in Echo 2. (d) Schematic diagram of Echo 2. (e) Fundamental frequency amplitude A_1 and the third order harmonic A_3 in Echo 3. (f) Schematic diagram of Echo 3.	161
Figure 7.39 Test specimens (length l and $2l$) subject to varying normal stress (Excitation 420V, 100 repetitions). (a) Fundamental frequency amplitude A_1 and the third order harmonic A_3 in Echo 1. (b) Schematic diagram of Echo 1. (c) Fundamental frequency amplitude A_1 and the third order harmonic A_3 in Echo 2. (d) Schematic diagram of Echo 2. (e) Fundamental frequency amplitude A_1 and the third order harmonic A_3 in Echo 3. (f) Schematic diagram of Echo 3.	162
Figure 7.40 The third harmonic A_3 originated at contact interface in all echoes subject to varying normal stress. (a) Test specimens S1-S4 (length l and l , 100 repetitions). (b) Test specimens S1-L1 (length l and $2l$, 100 repetitions).....	163
Figure 7.41 (a) Schematic diagram of nonlinear interaction of ultrasound at rough contact interface for multiple echoes. (b) Rough contact interface with asperities in the experiment. (c) Flat contact interface in the numerical work.	164
Figure 8.1 (a) Schematic diagram of sliding test for friction coefficient measurement. (b) Measuring friction coefficient using the sliding test.	168
Figure 8.2 (a) Dimensionless stress ξ for all test conditions for test specimen S1-S4. (b) Contact nonlinearity measurable zone for S1-S4.....	171
Figure 8.3 Comparison of the third harmonic A_3 originated at contact interface subject to varying normal stress and excitations (90V, 280V and 560V) vs (a) Dimensionless stress ξ . (b) Normal stress σ . (Test specimen S1-S4, 100 repetitions).....	173
Figure 8.4 Comparison of the fundamental frequency A_1 subject to varying normal stress and excitations (90V, 280V and 560V) vs (a) Dimensionless stress ξ . (b) Normal stress σ . (Test specimen S1-S4, 100 repetitions).....	175

Figure 8.5 Comparison of the third harmonic A_3 vs normal stress. (a) Numerical computation. (b) Experimental result. (Test specimen S1-S4, excitations 90 – 560V).....	176
Figure 8.6 Comparison of the third harmonic A_3 vs dimensionless stress. (a) Numerical computation. (b) Experimental result. (Test specimen S1-S4, excitations 90 – 560V).....	176
Figure 8.7 Contact nonlinearity generation in different cases. (a) Contact made on smooth plate plane. (b) Rough surfaces under low normal stress, contact on load-bearing asperities. (c) Rough surfaces under high normal stress, contact developed on new load-bearing asperities.....	178
Figure 8.8 Estimation friction coefficient using cut-off stress. Normalised contact nonlinearity A_3 vs Dimensionless stress ξ and (b) Normal stress σ . (Test specimen S1-S4, excitation 280V, 100 repetitions).....	181
Figure 8.9 Estimation cut-off point using the peak point in numerical study.....	183
Figure 8.10 Procedure of estimation friction coefficient using cut-off stress strategy.....	184
Figure 8.11 Numerical and analytical solution of harmonic generation (from Chapter 5) fitted with quadratic function.....	185
Figure 8.12 Estimation friction coefficient using cut-off stress for test specimens S1-S4. (a) Shear stress by ultrasound 1.70MPa (excitation 420V) (b) Shear stress by ultrasound 2.30MPa (excitation 560V).....	186
Figure 8.13 Estimation friction coefficient using cut-off stress strategy for test specimens S1-S4. (a) Shear stress by ultrasound vs normal stress at interface (excitations 90 – 560V). (b) Peak points used in friction coefficient estimation.....	187
Figure 8.14 Procedure of estimation friction coefficient using correlation strategy: correlation of experimental data with numerical computation.....	189
Figure 8.15 Estimation friction coefficient using correlation strategy for test specimens S1-S4. (a) Shear stress by ultrasound 1.70MPa (excitation 420V). (b) Shear stress by ultrasound 2.30MPa (excitation 560V).....	190
Figure 8.16 Estimation friction coefficient using correlation strategy for test specimens S1-S4. (a) Numerically computed nonlinearity and (b) experimentally measured nonlinearity subject to various excitations (2 – 560V) and normal stress. (c) Friction coefficient estimation.....	191
Figure 8.17 Estimation friction coefficient using cut-off stress strategy. (a) Test specimen No. vs friction coefficient. (b) Comparison between friction measurement using sliding test and ultrasound. (c) Test specimen No. vs friction coefficient for all the test conditions. (d) Comparison between friction measurement using sliding test and ultrasound for all the test conditions.....	193
Figure 8.18 Estimation friction coefficient using correlation strategy. (a) Test specimen No. vs friction coefficient. (b) Comparison between friction measurement using sliding test and ultrasound. (c) Test specimen No. vs friction coefficient for all the test conditions. (d) Comparison between friction measurement using sliding and ultrasound for all the test conditions.....	194
Figure 8.19 (a) Comparison between friction coefficient measured using ultrasonic strategies with sliding test and other published values for aluminium contacts. (b) Surface roughness of test specimens.....	195
Figure 9.1 Possible signs of fretting on the contacting surface of test specimen S1.....	198

Figure 9.2 Oblique shear incident wave meeting at a contact interface. Normal and tangential stress components at the interface.	201
Figure 9.3 Al alloy wedge with 25° inclination in the experimental work.....	202
Figure 9.4 (a) Sensor configuration I. (b) Sensor configuration II.....	204
Figure 9.5 Harmonic generation at rough contact interface (Wedge-S4) using Configuration I. (a) Second and third harmonic generation subject to varying normal stress and excitation (a) 140V and (b) 280V (100 repetitions). (c) The second harmonic A_2 generation and (d) The third harmonic A_3 generation subject to varying normal stress and excitations (45 – 280V).....	205
Figure 9.6 Harmonic generation at rough contact interface (Wedge-S4) using Configuration II. (a) Second and third harmonic generation subject to varying normal stress and excitation (a) 140V and (b) 280V, (100 repetitions). (c) The second harmonic A_2 generation and (d) The third harmonic A_3 generation subject to varying normal stress and excitations (45 – 280V).....	207

LIST OF TABLES

Table 3.1 Physical properties of some materials (Kinsler et al., 2000).....	17
Table 3.2 Reflection and transmission coefficient for some material pairs.....	19
Table 4.1 Example of longitudinal and shear piezoelectric element.....	28
Table 4.2 Near field length for different shear wave transmitter in Aluminium.....	33
Table 4.3 Characteristics of normal incidence shear wave transducers from Olympus transducer test forms.....	35
Table 4.4 Key features of two difference ultrasonic signal amplifier.....	39
Table 4.5 Key features of two difference ultrasonic digitiser.....	41
Table 5.1 Critical time of contact state alternation.....	49
Table 5.2 Parameters used in time-harmonic signal study.....	51
Table 5.3 Parameters used in numerical study.....	59
Table 5.4 Parameters used in numerical study. Varying amplitude of incident ultrasound and contact stress.....	66
Table 5.5 Parameters used in numerical study. Varying static coefficient of friction.....	71
Table 5.6 Parameters used in numerical study. Varying dynamic friction coefficient.....	74
Table 6.1 Summary of the ultrasonic apparatus applied in this experiment work.....	81
Table 6.2 Aluminium alloy specimens dimension and surface roughness.....	84
Table 6.3 Summary of the displacement measurement arrangement using laser vibrometer.....	110
Table 7.1 Test conditions in pitch-catch transmission arrangement.....	120
Table 7.2 Test conditions in pitch-catch reflection arrangement.....	126
Table 7.3 Possible source of nonlinearity in the solid-air contact interface using pitch-catch reflection arrangement.....	136
Table 7.4 Test conditions in solid-air contact interface.....	137
Table 7.5 Possible source of nonlinearity in the solid-solid contact interface under low power input using pitch-catch reflection arrangement.....	140
Table 7.6 Test conditions in solid-air contact interface.....	140
Table 7.7 Test conditions in solid-solid contact interface: power evolution.....	142
Table 7.8 Test conditions in pitch-catch reflection arrangement.....	158
Table 8.1 Friction coefficient measurement using sliding test.....	169
Table 8.2 Shear stress by ultrasound at contact interface.....	170
Table 8.3 Difference between numerical and experimental work.....	179
Table 8.4 Estimated normal stress at the peak position in numerical and experimental work, from Figure 8.3.....	182
Table 8.5 Various peak point of ultrasonic nonlinearity.....	183
Table 9.1 Laser vibrometer measurement with 25° wedge at varying input levels.....	203

1 INTRODUCTION

1.1 Statement of the Problem

Friction occurs in every machine and mechanical component. Energy waste caused by friction can account for a large fraction of energy consumption. Sometimes friction is desired such as clutches and brakes. But also friction is unwanted because excessive friction not only leads to energy waste but also causes wear, damage and failure of mechanical components and machines. Engineers are interested in knowing the frictional force and friction coefficient to guide their mechanical design and practical machine operation.

Despite friction being such a fundamental phenomenon, it is surprisingly difficult to measure reliably. Results depend on the test method, the test environment and critically on the surface preparation. Methods have been developed to measure the friction force and sliding contact tribometers are devised mostly in laboratory environment. Pin-on-disc is the common friction measurement rigs at the macro scale (Dunkin and Kim, 1996). Atomic force microscope is widely used in measuring frictional force at the microscale (Ruan and Bhushan, 1994). Although both measurement configurations have been widely implemented in laboratories, their application in measuring friction in-situ in a real contact is a challenge. In this work we investigate ultrasound to both cause the sliding motion and measure the resulting signal.

Ultrasonic methods have recently been developed in a large body of work recently as they can be implemented in real industrial environments. Non-destructive testing

where ultrasound is applied in detecting defects and cracks has been extended to measure tribological parameters in-situ in bearings and machines such as contact stiffness (Drinkwater et al., 1996), oil film thickness (Dwyer-Joyce et al., 2004) and lubricant viscosity (Schirru et al., 2015a). In conventional ultrasonic techniques, pulses are low power and when they strike an interface they do not result in a change in the contact state. The process is linear and elastic. However, high power sound waves can cause opening or closing of an interface, or interfacial slip; this is non-linear.

Recently Contact Acoustic Nonlinearity (CAN) has drawn interest due to its potential in non-destructive evaluation. Information undetectable using traditional acoustic techniques can be extracted when ultrasound interacts with a rough interface. When high power bulk shear ultrasound propagates through a compressed rough contact interface, higher order frequency components, higher odd order harmonics ($3f$, $5f$, etc.) are generated in both transmitted and reflected waves (O'Neill et al., 2001). The nonlinear nature of the stick-slip phenomenon in friction may be the source of nonlinearity. Previous studies (Hirose 1994; O'Neill et al., 2001; Pecorari 2003; Meziane et al., 2011) have mainly focused on analytical and numerical study of ultrasonic nonlinearity at contact interface.

In this study, nonlinearity due to the interaction of a shear ultrasonic wave with a frictional interface is investigated in three parts. Firstly, a simple numerical model is employed to investigate the harmonic generation due to the nonlinear stick-slip motion at a frictional contact interface under shear wave oscillations and the effects of incident wave amplitude, contact stress and friction coefficient are studied. In the second part, harmonic generation at the contact is investigated experimentally using a high frequency nonlinear ultrasonic technique. Nonlinearity generation originating from the rough contact interface is assessed under various test conditions. In the third part, the friction coefficient of the contact is estimated using the experimental contact nonlinearity.

1.2 Aims and Objectives

The aim of this research is to develop an ultrasonic method to measure friction and friction coefficient in-situ in a contact interface.

To achieve the aim, several objectives are set.

- Develop a numerical model to study the nonlinearity generation of the interaction of a high-power shear wave with a frictional contact interface. Investigate the effect of incident ultrasound amplitude, contact stress and friction coefficient on the nonlinearity generation.
- Investigate experimental approaches to carry out the measurement of nonlinearity generation.
- Apply the experimental approach to access the activation of stick-slip phenomenon experimentally and measure the nonlinearity generation at a rough contact interface. Investigate the effect of incident ultrasound amplitude and contact stress on the measured nonlinearity.
- Develop a method to measure the friction coefficient using the ultrasonic nonlinearity. Apply the method to estimate the friction coefficient of a rough contact interface.

1.3 Layout of the Thesis

In Chapter 2, the contact of engineering surfaces is briefly presented. Friction models and methods of measuring friction and friction coefficient are reported.

In Chapter 3, the theory of ultrasound is presented. The fundamentals of ultrasound propagating within a host material are introduced. The interaction of ultrasound with a boundary is reported. Conventional linear ultrasonic technique to measure at a contact interface is described. Following the linear ultrasound, nonlinear ultrasound is also introduced. The non-classical nonlinear ultrasound, i.e. contact acoustic nonlinearity, is reported along with its applications of characterising the contact interface.

In Chapter 4, the apparatus used in the ultrasonic technique is presented. The hardware used in the current research work for measuring ultrasonic nonlinearity is introduced, particularly including the means of generating the ultrasound wave, amplifying the wave and acquiring the ultrasonic signal.

In Chapter 5, a numerical method is employed in conjunction with an analytical approach to understand the nonlinear interaction of high-power ultrasound meeting a frictional interface. Nonlinearity generation resulting from the stick-slip phenomenon at the frictional interface is investigated using a simple one-dimensional numerical model. Following investigations focus on the parameters

affecting the nonlinearity generation such as amplitude of incident ultrasound, contact stress and coefficient of friction.

In Chapter 6, the experimental preparations to measure the nonlinearity generation from a rough interface is investigated. The high frequency nonlinear ultrasonic technique is introduced along with the signal processing procedures. Experimental variables influencing the measurement of nonlinearity generation are discussed. Incident stress of a shear polarised ultrasound is measured using laser vibrometer.

In Chapter 7, the experimental measurement of nonlinearity generation at a rough interface is carried out. Practical test configuration is discussed and the method of removing the system inherent nonlinearity is followed. Measurement of nonlinearity generation is carried out on various incident ultrasound amplitudes and contact stresses. Measurement of nonlinearity is also carried out using subsequent echoes.

In Chapter 8, the contact nonlinearity generation detected experimentally is compared with the numerical model. Two strategies for estimating the coefficient of friction at a rough interface is investigated using the contact nonlinearity. The estimated friction coefficient is compared with published data.

In Chapter 9, estimation of friction coefficient using ultrasonic nonlinearity is briefly discussed. The usefulness and limitation of the ultrasonic technique is discussed. This is followed by the evaluation of an alternative method of generating contact nonlinearity using an oblique incidence. Considerations of transferring the ultrasonic technique in practical applications are briefly presented.

Chapter 10 contains general conclusions and recommendations for further work.

2 BACKGROUND ON CONTACT

This chapter briefly presents the contact of engineering surfaces. Friction models, methods of measuring friction and friction coefficient of a metal-metal contact are introduced.

2.1 Rough Contact Interface

In engineering circumstances, topographically smooth surfaces are extremely rare. Plastic deformation can hardly succeed in flattening an initially rough surface resulting in an ideal smooth surface (Johnson, 1985). A rough surface is characterised by several statistical parameters. These parameters can be measured by a surface profilometer where a stylus is drawn over a sample length on a surface and a magnified surface profile is reproduced. Two simplest parameters centre-line-average, R_a and root mean square, R_q are most commonly applied in characterising surface height, defined as follows:

$$R_a = \frac{1}{L} \int_0^L |z| dx, \quad (2.1)$$

$$R_q = \sqrt{\frac{1}{L} \int_0^L z^2 dx}, \quad (2.2)$$

where L is the sampling length, x is surface coordinate and z is the height of the profile relative to the mean line along x direction.

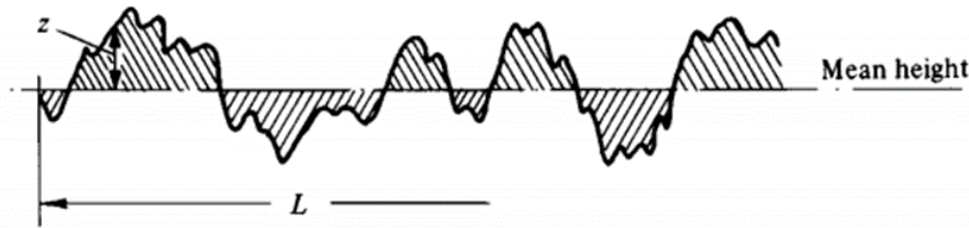


Figure 2.1 Profile of a rough surface (Johnson, 1985).

Understanding the mechanism of contact of rough surfaces is important in better comprehension of friction, wear and other tribological problems. When two rough surfaces are brought together, initial contact occurs on several asperities. Asperity contact can be described by the Hertzian model (Johnson, 1985), where asperities are considered as elastic balls. The real contact area of two rough surfaces thence is the sum of contacting zones of the elastic balls in the Hertzian model. The contact is discontinuous within the apparent contact zone and is much smaller when compared to the nominal contact size (McCool, 1986).

Many statistical models have been established to analyse rough contact and interface. One simple model was derived by Greenwood and Williamson, which uses statistical parameters to characterise surface roughness (Greenwood and Williamson, 1966). This model assumes a spherical summit with a fixed radius, Gaussian distribution of summit heights and elastic deformation of asperities. Another model for elastic contact of rough surface is derived by Bush, Gibson and Thomas (1975). Asperity summits are assumed to be elliptical, which introduces another curvature radius in defining the contacting summits. Random principle orientation, aspect ratio and distribution makes the calculation of contact area and average load complicated (McCool, 1986).

2.2 Friction Model

When two rough surfaces are in contact and there is tangentially relative motion, friction is present as the resistance to prevent the relative motion. Energy dissipation is associated with friction in relative sliding motion. Therefore, extra work is required to overcome the dissipated energy. There have been many efforts to reduce or eliminate friction in machines. Numerous research has expressed great

interest in investigating friction. Amontons stated the laws of friction quantitatively (Williams, 2005):

- The friction force is proportional to the normal load in sliding;
- The friction force is independent of the apparent contact area.

The ratio of the tangential friction force to the normal load is defined as the coefficient of friction, denoted as μ . This dimensionless quantity has been widely used as it characterises the sliding ease of a material over another.

Two types of friction coefficient, static friction coefficient μ_s and kinetic friction coefficient μ_k (also known as dynamic friction coefficient) need to be distinguished. Static friction coefficient is associated with the resistance at the onset of the relative sliding motion. After the motion has started, friction opposing the continuance of relative motion is represented by kinetic friction coefficient. At the onset of relative tangential motion, the frictional force tends to be slightly greater than the frictional resistance in the sliding process, which is known as the third Amontons' law of friction (Williams, 2005).

To understand the frictional behaviour, many models have been established. Two categories have been specified, static and dynamic models. The Coulomb model is the simplest static model where frictional force is independent of velocity (Hutchings and Hutchings, 2017), described as:

$$F = \mu P, \quad (2.3)$$

where F is the Coulomb friction and P the normal load. Coulomb model is ideal and friction at zero velocity is not specifically defined. A complicated nonlinear model can be derived, by taking viscous loss due to lubricants, static friction and Stribeck effect, where friction decreases with increasing velocity, that considers low velocities (Olsson et al., 1998).

Dynamic friction models have also drawn interest for researchers for the purposes of friction simulation and compensation (Olsson et al., 1998). Dahl (1968) proposed a simple model which was derived from the stress-strain relationship. The rate-independent model can depict the pre-sliding behaviour but lacks the ability to capture Stribeck effect and stick-slip phenomenon (Olsson et al., 1998).

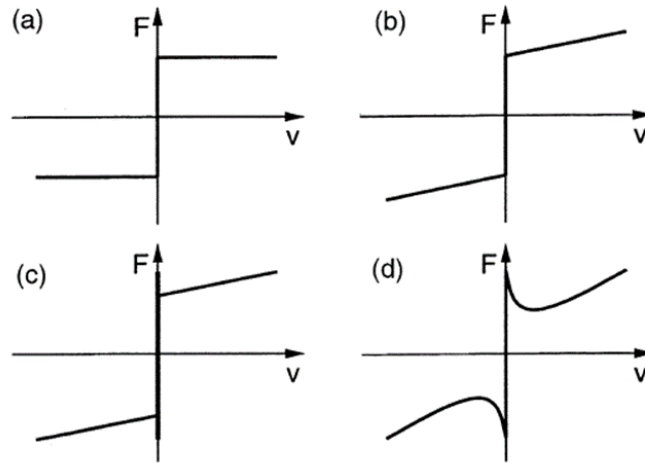


Figure 2.2 Examples of static friction models. (a) Coulomb friction. (b) Coulomb friction with viscous friction. (c) Friction discontinuous at zero velocity. (d) Friction with continuous velocity dependence, known as Stribeck effect (Olsson et al., 1998).

2.3 Friction Measurement

Engineers primarily rely on knowledge of the frictional force and friction coefficient to guide their mechanical design and practical machine operation. Methods have been developed to measure the friction force and devices are developed mostly in laboratory environment. The fundamental feature of many friction measurement devices is to measure the tangential force in the case where a known normal force is applied simultaneously. Pin-on-disc setup and its variations are the most common configuration in tribology laboratories for macroscopic friction measurement (Dunkin and Kim, 1996).

On microscope or atomic scope, frictional force can be measured by Atomic Force Microscope (AFM) or Friction Force Microscope (FFM) (Figure 2.3). AFM was developed from Scanning Tunnelling Microscope to measure small interactions at nanoscale between AFM tip and sample surfaces. Small frictional force is determined by measuring the motion of a cantilever beam with a tiny mass either electrically or optically. Due to its capability of measuring friction force and surface topography simultaneously, AFM and variations were used in the field of micro-tribology which deals with friction at atomic scale (Ruan and Bhushan, 1994). One modified AFM that measures both normal and frictional forces, is known as Friction Force Microscope generally. The friction force is measured by determining the deflection of cantilever either mechanically or electrically.

In both pin-on-disc configurations and AFMs/FFMs, the friction force determined is sliding phase and the friction coefficient is the kinetic one. Those setups can hardly be used in measuring static friction. Centrifugal Friction Apparatus (CFA) was developed to determine static friction forces (Dunkin and Kim, 1996).

In reviewing the available approaches in friction measurement, problems and ambiguities remain unresolved although a large body of work has been focused to better understand the friction and friction coefficient. Measured stylus force may not accurately represent the true friction force with micro-tribological techniques (Blau, 2001). Friction coefficient is vulnerable to changes in system. Many factors can influence frictional behaviour and the friction coefficient. Thence pin-on-disc configurations in microscope and AFM or FFM at micro level, may succeed in measuring friction and friction coefficient in laboratory environment, however can hardly be modified in real operation-oriented tests.

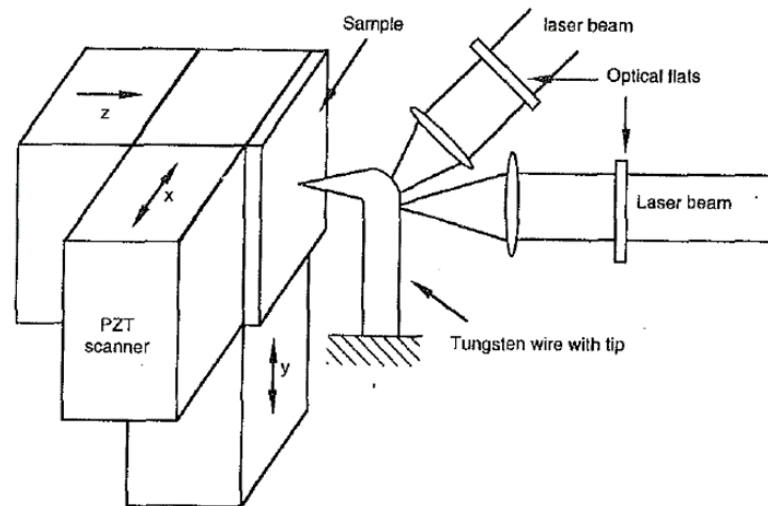


Figure 2.3 Schematic diagram of FFM. Normal and friction forces are measured by cantilever deflection by optical interference (Ruan and Bhushan, 1994).

2.4 Friction Coefficient of a Metal-Metal Contact

The friction at a metal-metal contact has been previously investigated and several mechanisms have been used to explain and estimate the friction. The adhesion force developed at the real contact asperity junctions and the deformation force needed to plough the asperities on a softer surface by the harder one is considered as two

sources of friction. For adhesion force, the friction coefficient is estimated by the ratio of shear strength and hardness of the softer material (Bowden and Tabor, 1964). Generally, the friction coefficient for metal-metal contact is approximately 0.2. When ploughing is considered together with the adhesion, friction coefficient is approximately 0.2 to 0.3. The difference between theory and experimental work is explained using work-hardening and junction growth mechanisms (Hutchings and Hutchings, 2017).

2.5 Stick-Slip Phenomenon and Tangential Contact

The phenomenon of stick-slip motion has interested many researchers (Rabinowicz 1951; Dieterich 1978; Feeny et al., 1998). A simple mechanical system consisting of a mass and a spring models the stick-slip motion. When the mass is carried by an external force the spring is stretched, and spring force and friction force are in equilibrium. The mass and the counterface 'stick'. Further displacement of the mass leads to a larger spring force which draws the mass back towards its origin and this is the 'slip' phase. The elastic force in spring decreases until it equals the kinetic friction. At this point, 'slip' stops and 'stick' continues. Other models have also been developed to describe the 'stick-slip' motion (Bengisu and Akay 1999; Kligerman and Varenberg 2014; Wang et al., 2017). The 'stick-slip' motion is discontinuous and nonlinear, which can result in unwanted oscillations and reduced stability of a system (Rusli and Okuma, 2007).

'Stick-slip' phenomenon occurs at a tangential contact. Research on tangential contact of rough surfaces has also been developed recently. Mindlin developed a model to solve the tangential contact problem using Hertz elastic theory and Coulomb friction model (Etsion, 2010). 'Stick-slip' behaviour at the tangential contact was modelled. Based on Mindlin's work, further research has extended the investigation to consider varying friction coefficient at elastic, elastic-plastic contact conditions (Eriten et al., 2010) and stick-slip behaviour under oscillating tangential force (Chaudhry and Kailas, 2013). GW statistical model has also been applied (Wang et al., 2017) to study the tangential rough contact problem and the 'stick-slip' behaviour.

2.6 Conclusion

In this chapter, the background on engineering contact has briefly been presented. Asperity contact is described by the Hertzian model and statistical models, i.e. Greenwood and Williamson model is to characterise the actual asperity contact of rough surfaces. Various models have been developed to study the friction at a rough contact. Rigs and methods are designed to measure friction at different scales and they are mainly limited to laboratories. 'Stick-slip' phenomenon at a rough tangential contact has been recently investigated. The nonlinear nature of stick-slip motion provides a useful way to measure friction at a rough contact.

3 THEORY OF ULTRASOUND

In this chapter, the background of the ultrasound technique used in this research is presented. This chapter provides the basic definition of the ultrasonic wave and the principles of ultrasound propagation. The principle behind the ultrasonic wave interacting with the contact interface is introduced. Following the conventional ultrasound theory, the nonlinear ultrasound and its application at a contacting interface, which is of the interest in this research work, is introduced.

3.1 Fundamentals of Ultrasound

3.1.1 The Basic Principles of Ultrasound

Sound is essentially the propagation of the mechanical oscillation of particles through a host medium. The host medium is in the form of solid, liquid and gases. When the mechanical oscillations occur at a frequency beyond the audible range of the human ear, generally greater than 20kHz, the sound is referred to as ultrasound.

There are several modes of oscillation that sound wave can propagation in solids. Plane waves are the sound waves with constant frequency and the front of the waves travel as a parallel plane (Achenbach, 1973). Longitudinal and transverse waves are the two types of plane wave and their propagations are within the host medium, normally referred to as bulk wave.

The host medium is comprised of particles which are bonded together elastically. This structure can be analogous to a mass-spring system, as shown in Figure 3.1. When an external displacement or stress is applied to a group of particles, a sound wave is generated in the host material. Particles move forwards and the elastic bonds between the particles tend to resist the movement, make particles move backwards. Under the repeated excitation and resistance, particles oscillate about their initial positions and zones of expansion and compression are created. The expansion and compression transfers to the neighbouring particles. The propagation of particle oscillation through the host medium induces the sound wave.

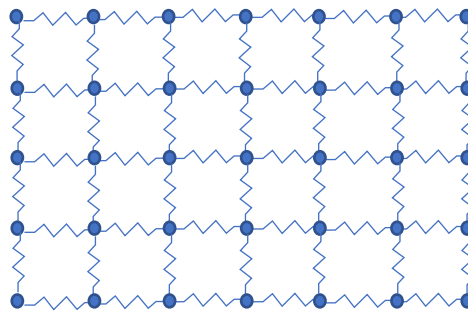


Figure 3.1 Schematic diagram of particles 'mass-spring' analogy.

3.1.1.1 Longitudinal Wave

For the longitudinal wave, particle oscillation is the same direction as the wave propagation direction, as shown in Figure 3.2. When a longitudinal wave is present in the solid, parts of the body in tension and parts in compression alternate. The wavelength, λ is defined as the distance between each cycle, e.g. from tension zone to the adjacent zone. The longitudinal wave is also known as dilatational wave or P-wave (pressure wave or primary wave). The P-wave is supported in the solids, liquids and gases.

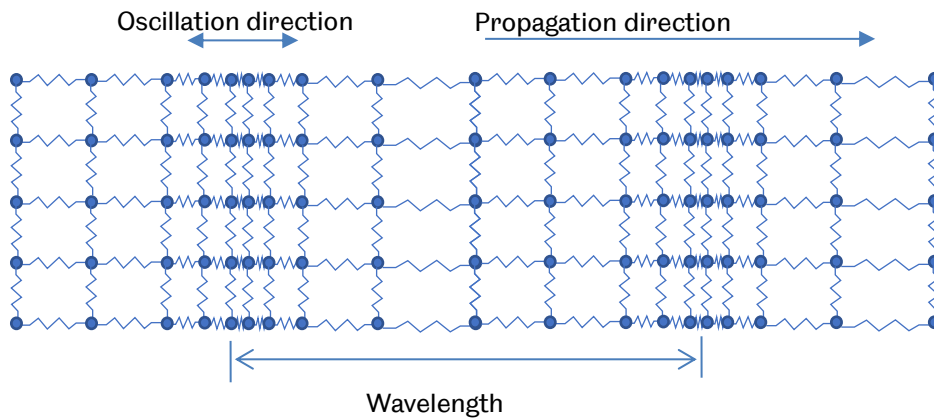


Figure 3.2 Schematic diagram of the longitudinal wave.

3.1.1.2 Transverse Wave

In the transverse wave, the particle oscillation is perpendicular to the wave propagation direction, as illustrated in Figure 3.3. The wavelength, λ is defined as the distance between the adjacent oscillation peaks or valleys. Unlike the longitudinal wave, the transverse wave is mainly supported in solid materials and some very viscous liquids. The shear wave is also known as the rotational wave or S-wave (shear wave or secondary wave).

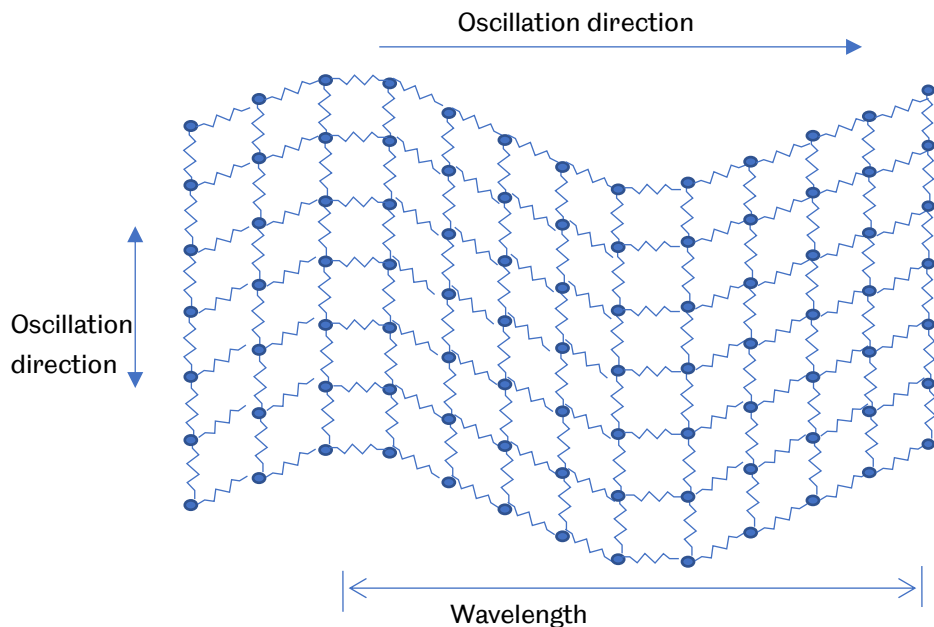


Figure 3.3 Schematic diagram of transverse wave.

The transverse wave is in two forms. Generally, the displacement direction is in the plane normal to the propagation direction, the transverse wave is defined as 'vertically' polarised transverse wave, or SV-wave (Figure 3.4 (a)); the oscillation direction is normal to the plane normal to the travelling direction, the transverse wave is called 'horizontally' polarised transverse wave, or SH-wave (Figure 3.4 (b)) (Achenbach, 1973).

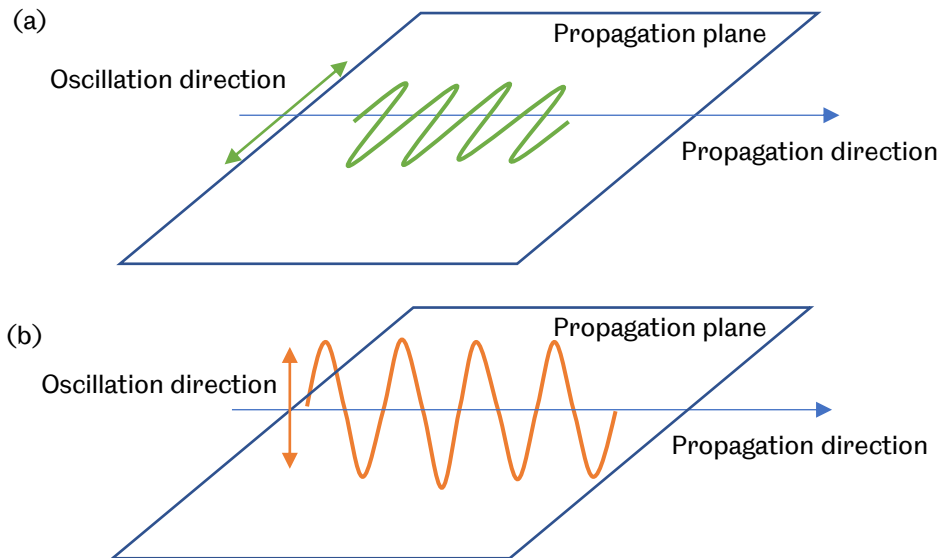


Figure 3.4 Schematic diagram of transverse waves: (a). Vertically polarised transverse wave; (b). Horizontally polarised transverse wave.

3.1.2 Ultrasound Propagation in Materials

In different host materials, ultrasound propagation varies. The travelling rate, the ability to travel from one material to the other and the energy lost during wave propagation are the parameters which depend on the host medium properties.

3.1.2.1 Speed of Sound

In the 'mass-spring' analogy, the elastic strength of the 'spring' determines the rate of ultrasound propagation, commonly known as the speed of sound (sometimes phase velocity). The other velocity, namely the group velocity, is used in characterising the dispersive waves. In this research work, only the non-dispersive wave is considered and the phase velocity is used.

The speed of sound for various host media is calculated using the elastic constants, namely the elastic modulus, E , the Poisson's ratio, ν , and the density ρ . Speed of sound for longitudinal wave, c_l is defined as follows:

$$c_l = \sqrt{\frac{E}{\rho} \frac{(1-\nu)}{(1+\nu)(1-2\nu)}} \quad (3.1)$$

For transverse wave, the speed of sound, c_s is defined as:

$$c_s = \sqrt{\frac{E}{\rho} \frac{1}{2(1+\nu)}} = \sqrt{\frac{G}{\rho}}, \quad (3.2)$$

where G is the shear modulus of the host material.

Speed of sound can also be linked with the particle oscillation frequency in the following relationship:

$$c = \lambda f. \quad (3.3)$$

It should be mentioned that generally the elastic constants are directionally dependent on crystalline materials. The speed of sound in these materials differs in various directions. The speed of sound also depends on the stress that applied to the material and the temperature. It is also noticed that in Equation (3.1) and (3.2), the speed of sound is independent of frequency, which indicates a non-dispersive wave.

Speed of sound can be measured using a 'time-of-flight' technique experimentally. The time, t taken for a sound wave travelling through a known distance, d is measured and the speed of sound is given as:

$$c = \frac{d}{t} = \frac{2x}{t}, \quad (3.4)$$

where x is the material thickness using the commonly applied pulse-echo configuration.

Wavelength at a given frequency is then obtained by rearranging Equation (3.3):

$$\lambda = \frac{c}{f}. \quad (3.5)$$

3.1.2.2 Acoustic Impedance

The ability of sound wave travelling from one material to the other is determined by acoustic impedance, Z is defined as the product of speed of sound and density:

$$Z = \rho c. \quad (3.6)$$

Acoustic properties of some materials are given in Table 3.1.

Table 3.1 Physical properties of some materials (Kinsler et al., 2000).

Material	Density ρ (kg/m³)	Speed of sound c (m/s)	Acoustic Impedance Z (Pas/m)
Steel	7700	6100	47×10^6
Aluminium	2700	6300	17×10^6
Water	998	1481	1.48×10^6
Castor oil	950	1540	1.45×10^6

3.1.2.3 Attenuation

A sound wave travels through a material, reduction of ultrasonic energy is known as attenuation and it occurs in several forms, namely radiation, absorption and scattering. Radiation describes the energy divergence. Absorption is the energy loss to overcome the internal friction and then converted as heat dissipation. Scattering describes a sound wave diverges from its original course when it meets defects, flaws, impurities or grain boundaries. The total attenuation in the material is determined using the following equation:

$$A_d = A_0 e^{-\alpha d}, \quad (3.7)$$

where A_0 is the initial ultrasound amplitude, A_d the amplitude when sound wave travels for a distance d and α is known as the attenuation coefficient. In metallic materials, the attenuation is usually low compared to softer materials.

3.1.3 Ultrasound Propagation at Boundaries

When a sound wave strikes to a boundary or an interface formed by two dissimilar materials, a portion of the incident wave will travel through and the rest will be reflected backwards if the boundary is perfectly bonded. The portion of the ultrasonic wave transmitted through or reflected from the boundary is determined by the two host material properties and the orientation of the incident wave relative to the boundary.

3.1.3.1 Reflection and Transmission

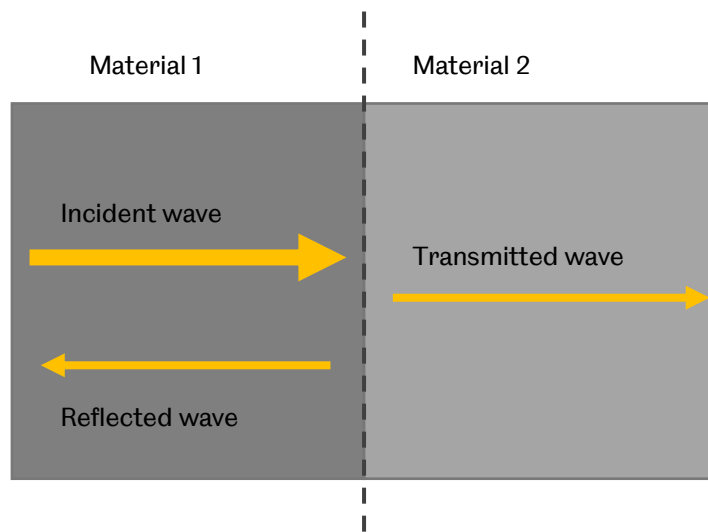


Figure 3.5 Reflection and transmission of a plane sound wave at a boundary.

A simple case is that when a plane sound wave strikes at a boundary normally, as shown in Figure 3.5. At the boundary, the continuity of sound pressure and the continuity of the normal component of particle velocity must be satisfied. After a number of mathematical manipulation (Kinsler et al., 2000), the pressure reflection coefficient, R , which is defined as:

$$R = \frac{Z_{II} - Z_I}{Z_{II} + Z_I}, \quad (3.8)$$

where Z_I and Z_{II} are the acoustic impedance of the Material I and II respectively. The pressure transmission coefficient, T is derived in a similar form:

$$T = \frac{2Z_{II}}{Z_{II} + Z_I}, \quad (3.9)$$

$$T = 1 + R. \quad (3.10)$$

When the power of a sound wave is considered, the power reflection coefficient, R_E are defined by:

$$R_E = R^2 = \left(\frac{Z_{II} - Z_I}{Z_{II} + Z_I} \right)^2. \quad (3.11)$$

As energy is conserved, the total power of reflected and transmitted sound wave must be equal to the power of the incident wave. The power transmission coefficient, T_E are defined as:

$$T_E = 1 - R_E = \frac{4Z_{II}Z_I}{(Z_{II} + Z_I)^2}. \quad (3.12)$$

Based on the material properties given in Table 3.1, the pressure reflection coefficient is calculated, as shown in Table 3.1. A positive pressure reflection coefficient indicates a sound wave travels from an acoustically harder material to an acoustically softer material.

Table 3.2 Reflection and transmission coefficient for some material pairs.

Material I	Material II	R	T	R_E	T_E
Steel	Steel	0	1	0	1
Steel	Water	-0.939	0.061	0.88	0.12
Water	Steel	0.939	1.939	0.88	0.12

3.1.3.2 Snell's Law and Mode Conversion

When a plane sound wave strikes an interface of two dissimilar materials obliquely, the amplitude and the propagation direction of both reflected and transmitted signal is determined by the Snell's law, defined as:

$$\frac{c_I}{c_{II}} = \frac{\sin \theta_I}{\sin \theta_{II}}, \quad (3.13)$$

where c_I and c_{II} is the speed of sound of reflected or transmitted waves and θ_I and θ_{II} is the angle between the propagation direction and the normal line of the boundary, as shown in Figure 3.6.

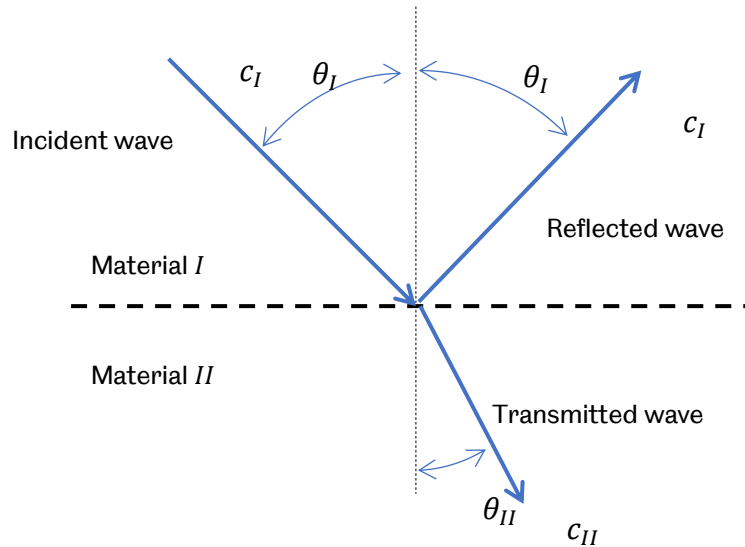


Figure 3.6 Schematic diagram of obliquely incident wave and its reflection and transmission.

In some cases, when an oblique wave strikes a boundary, other mode of sound wave is generated, i.e. transverse wave generated from longitudinal wave or vice versa, which is known as mode conversion. Snell's law still holds true. c_I and c_{II} are the speed of sound of either longitudinal or transverse in the host material. Various cases of mode conversion can be found in references (Achenbach, 1973; Krautkramer and Krautkramer, 1990).

3.2 Using Ultrasound to Measure Contact Interface

3.2.1 Interfacial Stiffness

Contact of rough surfaces has drawn many researchers' attention and various approaches have been implemented in investigation. Contact stiffness was developed in characterising contact interface with ultrasound (Tattersall, 1973). Spring model (Schoenberg, 1980; Baik and Thompson, 1984; Margetan et al., 1988) was proposed to define the boundary conditions when rough surfaces are in contact. The spring is used to represent the interaction at contact interface and its strength, known as interfacial stiffness K is defined by:

$$\begin{aligned}
K &= \frac{\text{increase in contact pressure on the adjacent surfaces}}{\text{increase in separation between adjacent surfaces}} \\
&= -\frac{dP_{nom}}{dh},
\end{aligned} \tag{3.14}$$

where P_{nom} is nominal contact pressure and h is the separation of contacting surfaces. It should be noted that interfacial stiffness is nonlinear. An infinite stiffness ($K = \infty$) represents perfect contact. According to the definition, contact interfacial stiffness in GW model and BGT model have been derived to further assess these rough contact models (McCool, 1986; Królikowski and Szczepek, 1991).

Contact interfacial stiffness has been a key parameter in many investigations where ultrasonic techniques were used because contact interfacial stiffness can be linked to ultrasonic reflection or transmission coefficient theoretically. Understanding of contact interface has been developed with the concept of interfacial stiffness and the aid of ultrasound. Baik and Thompson (1984) investigated the relationship of contact stiffness and interfacial topography for imperfect interface with a proposed quasi-static model. Królikowski and Szczepek attempted to evaluate the real contact area (1991) and phase shift of reflection coefficient (1992). Tangential stiffness was also investigated (Nagy, 1992; Królikowski and Szczepek, 1993) and the ratio of tangential to normal stiffness was found useful in characterising various imperfect interfaces. Many efforts have also been spent on improving the knowledge of contact interface (Drinkwater et al., 1996; Lavrentyev et al., 1998; Dwyer-Joyce et al., 2001; Biwa et al., 2006; Gonzalez-Valadez et al., 2010).

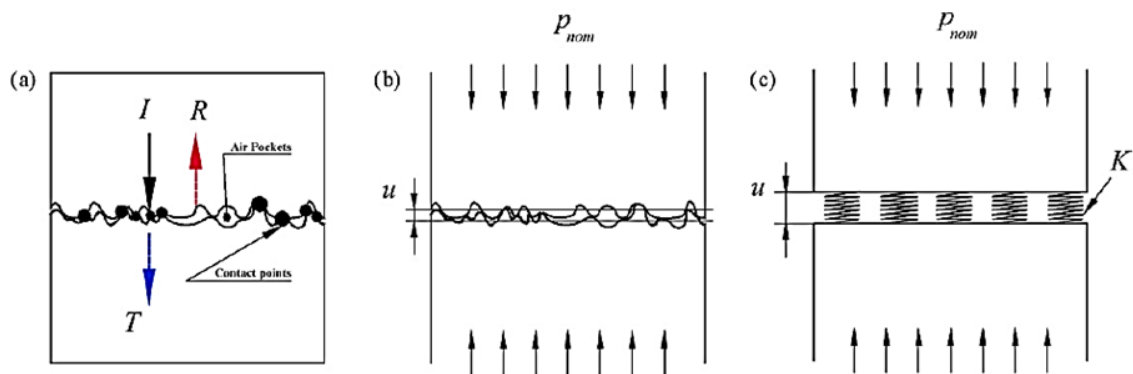


Figure 3.7 Representation of ultrasound at rough contact interfaces. (a) Incidence, reflection and transmission. (b) Loading and deflection; (c) The spring model representation (Gonzalez-Valadez et al., 2010).

3.2.2 Tribological Parameters

As a non-destructive testing tool, ultrasound has been extended to measure tribological parameters in-situ in bearings and machines such as contact oil film thickness (Dwyer-Joyce et al, 2004; Reddyhoff et al., 2005), lubricant viscosity (Schirru et al., 2015a) and contact pressure (Chen et al., 2015). These ultrasonic methods show the effectiveness and usefulness in the in-situ measurement at a contact, which provides more detailed and comprehensive information about tribological systems.

3.3 Nonlinear Ultrasound

Ultrasound has been used as a non-destructive testing tool in various applications for several decades. Traditional ultrasonic NDE methods use phase velocity, group velocity, attenuation and coefficient of reflection and transmission to detect defects and determine material properties. Defects measured by traditional ultrasound technique are generally gross open cracks where ultrasound propagation discontinues. The frequency of the output ultrasonic signal is not affected by the presence of defects. However, the traditional linear ultrasonic methods can hardly detect microcracks and material degradation. The limitation leads to the development of nonlinear ultrasonic techniques.

Nonlinear ultrasound techniques measure the frequency change which occurs when ultrasonic waves interact with defects. Frequency difference includes higher harmonic generation, sub-harmonic generation, shift of resonance and mixed frequency response (Jhang, 2009). The most common nonlinear phenomenon is the higher harmonic generation, which is considered by two mechanisms, the classical nonlinear elasticity and contact acoustic nonlinearity (CAN).

Classical nonlinear ultrasound is related to the elastic behaviour of bulk materials. The normal linear elastic relationship described by Hooke's Law is extended to account for higher-order elastic terms (Van Den Abeele and Breazeale, 1996). The nonlinearity generation due to material and has been applied in characterising fatigue (Cantrell, 2004) and degradation of materials (Jhang and Kim, 1999). In this research work, attention focuses on contact interfaces rather than the bulk materials and therefore the classical nonlinear ultrasound is not at the centre of the following research.

In this work, research focuses on the contact interfaces and the non-classical nonlinear ultrasound is pronounced. When an ultrasonic wave with a large amplitude interacts with an imperfect contact interface, higher order frequency components are generated, which is known as contact acoustic nonlinearity (CAN). The nonlinearity results from the repeated contact of two imperfect surfaces under oscillating tension and compression (Buck et al., 1978). Ultrasound can only propagate across the contact interface when the imperfect contact is closed under compressive load. When tension is applied, imperfect contact is in an open state and cannot allow any waves to penetrate. The nonlinearity is shown in the distorted ultrasound which can be detected by higher harmonic generation (Barnard et al., 1997). The open and close status of the interface is known as the ‘clapping’ mechanism (Solodov, 1998).

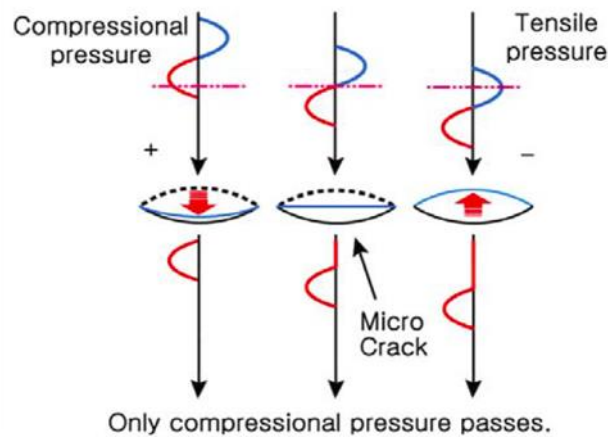


Figure 3.8 Concept of contact acoustic nonlinearity at micro crack (Jhang, 2009).

Many investigations have focused on the contact acoustic nonlinearity. Richardson (1979) proposed a one-dimensional continuum model to represent the unbounded interface. Though the model is somewhat over-idealised, it makes an analytical solution to the nonlinear problem available. The second harmonic generation was found to be most efficient at an intermediate level of the ratio of externally applied stress to stress amplitude of acoustic wave. Experiments have been carried out to evaluate the usefulness of CAN in non-destructive testing of imperfect interfaces and cracks (Zhou and Shui, 1992; Solodov et al., 1993; Solodov, 1998; Donskoy et al., 2001; Chen et al., 2006).

When the gap in contacting rough surfaces is much smaller than the ultrasound wavelength, interfacial stiffness is the dependent parameter. Researchers modified the quasi-static model and derived the expression for second order interfacial

stiffness in solving nonlinear propagation problems (Pecorari, 2003; Kim et al., 2006). A simple power-law relation between interfacial stiffness and contact pressure was proposed (Biwa et al., 2004) based on rough surface contact mechanics to predict the acoustic nonlinearity of interfaces. The nonlinearity parameter of the contact interface was investigated and it has been found that this parameter is an interfacial property, independent of amplitude of incident waves (Biwa et al., 2004; Biwa et al., 2006). The NDE application of the nonlinearity parameter has also drawn great interest, such as in determining the adhesive bonding strength (Yan et al., 2009).

Many researchers have shown great interest in investigating the nonlinearity of ultrasound at contacting interface and they focus on the bulk longitudinal wave (Richardson, 1979; Biwa et al., 2004; Yan et al., 2009). Second order harmonics are generated due to the 'clapping' mechanism of the kissing bonds when ultrasound interacts with the contact interface normally, which has great potential in NDE applications. Contact acoustic nonlinearity of bulk shear wave (Mendelsohn and Doong, 1989; Hirose, 1994; Solodov, 1998; O'Neill et al., 2001; Pecorari, 2003) and surface acoustic wave (Solodov et al., 1993; Kawashima et al., 2002) has also been studied.

Mendelsohn and Doong (1989) implemented the boundary element method to study the shear horizontal slip motion at an interface. Hirose (1994) applied two-dimensional boundary integral equations to in-plane motion in solving the dynamic contact of rough surfaces problems. Later O'Neill (2001) adopted Richardson's model to investigate the shear horizontal wave interaction with the contact interface. Nonlinear interaction of shear ultrasound was also studied using interface contact model derived from the GW model (Pecorari, 2003; Pecorari and Poznić, 2005). The friction at contact interfaces is a possible source for the nonlinearity because of the stick-slip phase alternation under normal compressive load. It is shown that when bulk shear wave interacts with the contact interface, only odd higher order harmonics can be generated numerically. Although the amplitude of odd harmonics of shear incident wave is much smaller than the second harmonic of longitudinal waves, nonlinear interaction of shear ultrasound may be useful in determining friction and friction coefficient (Hirose, 1994; O'Neill et al., 2001). Energy dissipation during nonlinear interaction was also investigated under friction laws (Meziane et al., 2011).

Recently, contact acoustic nonlinearity using an oblique incidence and harmonics generation at contact have been investigated (Blanloeuil et al., 2013; Blanloeuil et al., 2014a; Blanloeuil et al., 2016). Harmonics generation strongly depends on the

incidence angle. When ultrasound interacts with a contact at certain angles, nonlinear 'clapping' and 'slipping' effects occurs even if a shear polarised wave is used. High order even and odd harmonics are coupled and generated. The evolution of harmonics helps to improve the understanding of a contact. Another ultrasound technique (non-collinear mixing technique) using two incidences have also been studied at an interface. The effectiveness of this method has shown its potential in understanding the nonlinear behaviour of a contact and also the non-invasive application in characterising a contact interface (Blanloeuil et al., 2014b; Blanloeuil et al., 2015; Pecorari, 2015; Zhang et al., 2016).

In the previous research work, the contact acoustic nonlinearity has shown the potential in characterising a frictional interface. Previous work on the nonlinearity generation at a frictional interface primarily focused on the analytical and numerical study. Experimental work in this field, particularly on the interaction between a shear polarised ultrasound with a frictional contact is inadequate. The following research work mainly focuses on the experimental investigation on the contact acoustic nonlinearity originating at a frictional contact and its usefulness in measuring friction of a rough contact using a shear ultrasound.

3.4 Conclusion

In this chapter, the basic definition of the ultrasonic wave, the principles of ultrasound propagation and the interaction between an ultrasonic wave and an interface has been introduced. The conventional ultrasound has shown the usefulness in characterising and measuring contact tribological parameters. The contact acoustic nonlinearity from the nonlinear interaction between an ultrasound and a contact has demonstrated its great potential in characterising a frictional interface. Experimental investigation on nonlinearity generation at a rough contact and its usefulness in measuring friction at the interface is needed. In the following research the non-classical nonlinear ultrasound and the contact acoustic nonlinearity is employed to study the nonlinear interaction of an ultrasound at a frictional interface.

4 ULTRASONIC TECHNIQUE APPARATUS

The chapter aims to introduce the apparatus used in the ultrasonic technique, with a particular emphasis on the hardware used in this research work. In this chapter, the means of generating the ultrasound wave, amplifying the wave and acquiring the ultrasonic signal is introduced.

4.1 Ultrasonic Generation Using Ultrasonic Transducers

As described in the previous chapter, propagation of the sound wave only occurs when there is an initial excitation, i.e. particle oscillation applied to the host material. A number of approaches are available for the initiation of the particle displacement, namely the piezoelectric method, mechanical method, thermal method, electrostatic method, electrodynamic method, magnetostrictive method and optical method (Krautkramer and Krautkramer, 1990). The piezoelectric method is used in this research. The ultrasonic transducer in this work refers to the device converting the electrical energy into the mechanical energy and vice-versa using the piezoelectric effect.

4.1.1 The Piezoelectric Effect

The direct piezoelectric effect discovered in 1880 describes the phenomenon that when a material is pressurised mechanically, an electrical potential is generated across the material. When a potential is applied across the material electrically, deformation is generated, which is known as the inverse piezoelectric effect. The inverse piezoelectric effect is now commonly employed for generating ultrasound and the direct effect give premises for receiving ultrasound.

4.1.2 Piezoelectric Element

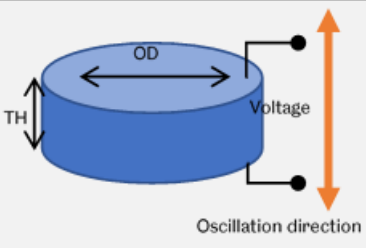
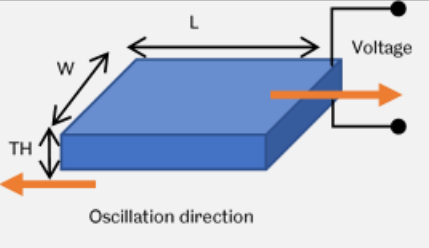
Materials with this property are known as piezoelectric materials. Quartz, lead meta-niobate, barium titanate and lead-zirconate-titanate (PZT) are common piezoelectric materials. The PZT materials are widely selected in ultrasonic examination and evaluations, as the piezo-ceramic materials can be fabricated into various shapes and function in different modes.

When using a bare piezo-ceramic element as an ultrasound transmitter, the wave mode and the frequency of the sound wave is determined by the element size and polarisation direction. The fundamental frequency of a piezoelectric element is determined by the frequency constant, N_f and the effective dimension of the piezo element, D as:

$$f = \frac{N_f}{D}. \quad (4.1)$$

The effective dimension is the thickness of a longitudinal or shear mode plate, the diameter of a radial mode disc or the length of a longitudinal mode rod. Examples of longitudinal mode disc element and shear mode plate are given in Table 4.1. The oscillation mode at the fundamental frequency is dominant only when the dimension of the piezoelectric element meets some requirements.

Table 4.1 Example of longitudinal and shear piezoelectric element.

	Longitudinal disc	Shear plate
Element dimension		
	$OD \gg TH$	$L \approx W \gg TH$

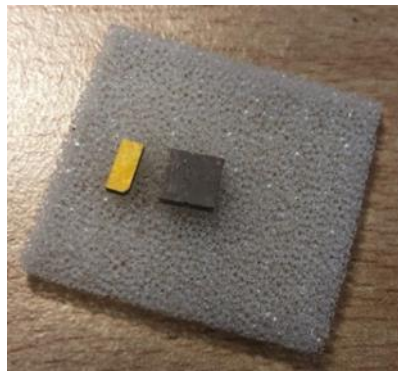


Figure 4.1 Example of shear polarised piezoceramic elements.

Figure 4.1 shows an example of shear polarised piezoceramics elements. The notch on the element either in the centre of one edge or at a corner indicates the direction of polarisation.

When exciting a piezoceramic element at the fundamental resonant frequency, the amplitude of oscillation is at its maximum. The element can also be forced to oscillate when the applied voltage alternates at a frequency different to the fundamental frequency. The amplitude of oscillation is generally less than the maximum at the fundamental resonant frequency. It is also found that when a piezoelectric element is excited, not only the fundamental resonance frequency f_r , but also the odd harmonics $3f_r$, $5f_r$, etc. are excited (Krautkramer and Krautkramer, 1990).

4.1.3 Ultrasonic Transducers

A variety of ultrasonic transducers are designed and widely used in numerous non-destructive testing and evaluating applications utilising the piezoelectric elements. A schematic diagram of a commercial transducer is shown in Figure 4.2. Generally, the ultrasonic transducer consists of piezoelectric elements, damping material, front protective layer, shielding and housing and electrical system.

The piezoceramic element functions at the desired frequency with the aid of an electrical system. The damping material is usually attenuative and dense so that the ultrasound originating from the top face of the piezoelectric element is dissipated. The undesired oscillation, such as reverberation is also suppressed. Additionally, it can mechanically protect the piezoelectric element from shocks. The protective layer provides wear and corrosion protection, which makes the piezoelectric element function in some harsh testing environments and conditions. It also bridges the difference between the acoustic impedance of the piezoelectric element and the test specimen. In such cases, normally a quarter wavelength thickness protective layer is selected.

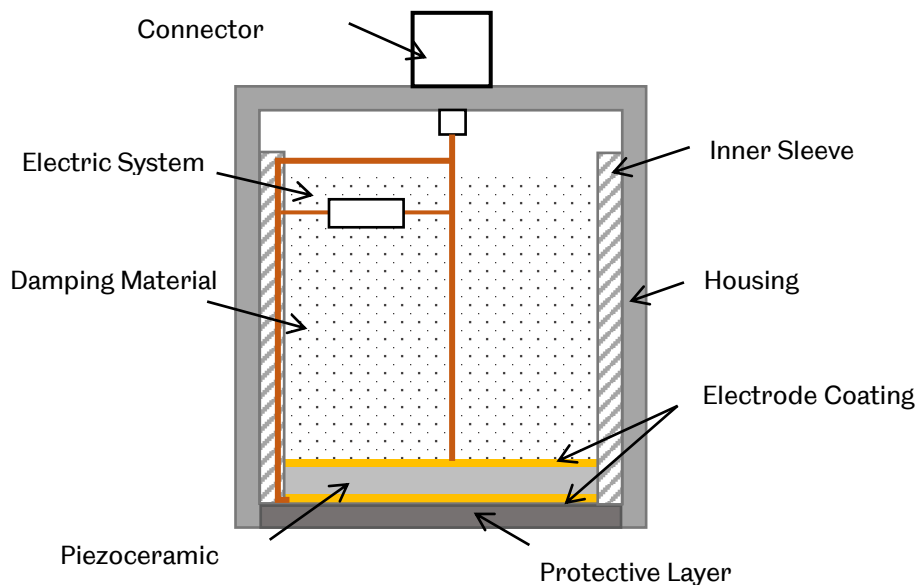


Figure 4.2 Schematic diagram of commercial ultrasonic transducer.

The design of commercial ultrasonic probe in Figure 4.2 is commonly seen in longitudinal wave transducers. To generate shear waves, two configurations of

commercial probes are available. The first configuration is the angle beam transducer, as shown in Figure 4.3, where a longitudinal probe is mounted on a wedge with a fixed angle. This type of transducer uses the Snell's Law and mode conversion to convert the longitudinal wave into a shear wave at a specific angle.

The second configuration is the normal incidence shear wave transducer, as shown in Figure 4.4. The schematic diagram in Figure 4.2 also applies to this type of shear wave transducer. The only difference is that the active element incorporated in the housing is shear polarised piezoelectric element instead of longitudinal. A shear wave emitted from such a probe propagates in the direction normal to the contact plane without other wave modes compared to an angle wedge transducer. When using this type of probe to generate a shear wave, attention must be paid to the following two aspects. As shear wave is not supported in liquid, high viscosity couplant, unlike the low viscous coupling gel used with longitudinal probe, must be applied at the contact interface between the probe and test specimens. As the oscillation direction of shear wave is normal to its propagation direction, the orientation of the shear wave probe needs to be carefully selected, especially in the pitch-catch and through-transmission measurement configuration, where two transducers are employed. Only when the polarisation direction of these two transducers are aligned or parallel can the shear wave signals be captured.

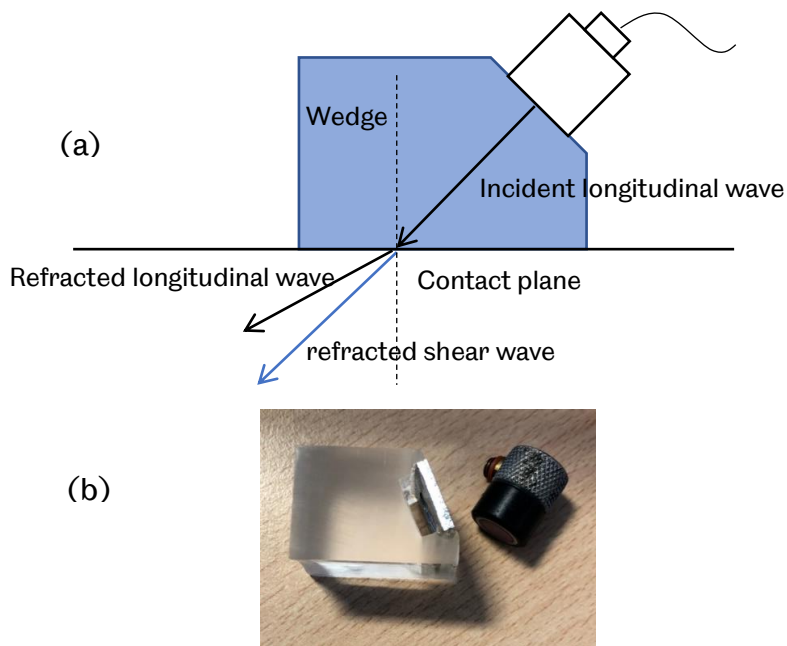


Figure 4.3 (a) Schematic diagram of angle beam transducer; (b) Example of angle beam transducer.

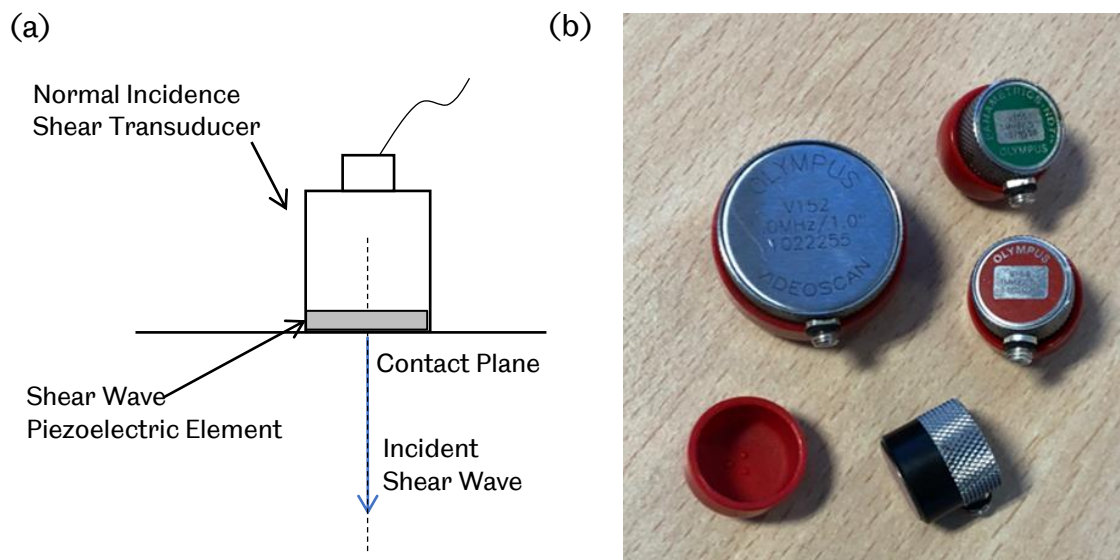


Figure 4.4 (a) Schematic diagram of normal incidence shear wave transducer; (b) Example of normal incidence shear wave transducer.

Examples of amplitudes from a shear wave piezoelectric element (PIC 255, 6mm element size, PI) and a transducer (V155, 6mm element size, Olympus) are shown in Figure 4.5. The piezo element and the transducer were bonded on an aluminium alloy specimens with a thickness of 31.84mm and a range of excitation voltages were used. The returning signals were received using a shear wave transducer (V155, 12.7mm element size, Olympus). Smaller amplitudes were obtained from the transducer compared with the piezoelectric element. Damping material at the back of the piezo-element inside the transducer damped the oscillation of the piezo-element and resulted in a reduced amplitude.

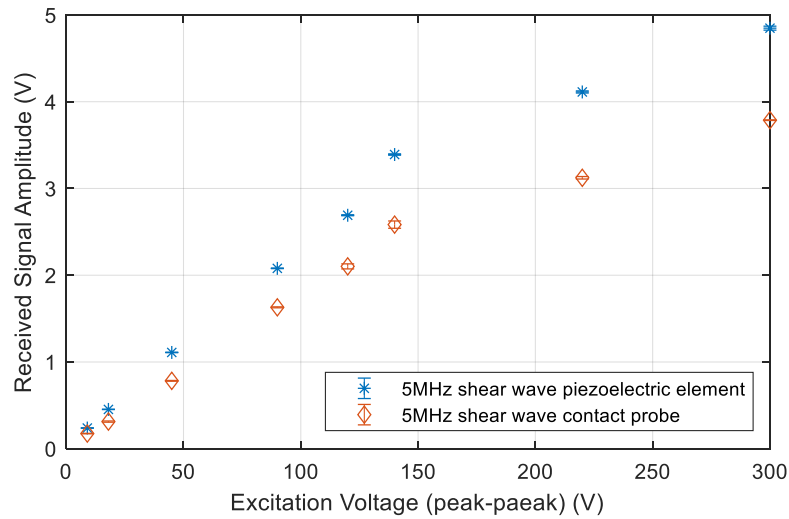


Figure 4.5 Example of amplitude from a shear wave piezoelectric element (PIC255, PI) and shear wave transducer (V155, Olympus).

4.1.4 Near Field Effect

When a sound wave is generated using either piezoelectric elements or commercial ultrasonic transducers, sound pressure is not uniformly distributed along the propagation direction. The interference between different oscillation points on the piezoelectric element is the cause of the sound field variation. As indicated in Figure 4.6, the sound field is divided into the near field and the far field. The near field is the zone from the transducer or piezoelectric element to the last maximum of the sound pressure and in between there are several local maxima and minima. In this region, the fluctuation of sound pressure makes the ultrasonic measurement difficult. From the last maximum of the sound pressure starts the far field, where the sound pressure gradually decreases to zero. In the far field, the ultrasonic measurement is less problematic and more reliable. To utilise the maximum sound energy, measurement signal should be acquired close to the end of the near field.

The length of the near field, N_d of a shear oscillator is estimated using the following relationship (Krautkramer and Krautkramer, 1990):

$$N_d = \frac{D^2 f}{4c}, \quad (4.2)$$

where D is the active element diameter, f the oscillation frequency and c the speed of sound in the test material. The near field of the shear polarised piezoelectric

element in Figure 4.1 and the normal incidence shear wave probe in Figure 4.4 is listed in Table 4.2.

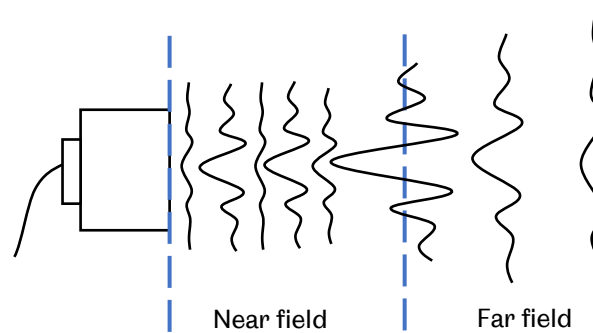


Figure 4.6 Sound field from a planar transducer or piezoelectric element.

Table 4.2 Near field length for different shear wave transmitter in Aluminium.

Probe type	Dimension (mm)	Frequency (MHz)	Speed of sound in Aluminium (m/s)	Near field length (mm)
PIC255	6	1	3130	2.87
V152	25.4	1	3130	51.5
V153	12.7	1	3130	12.8
V155	12.7	5	3130	64.4

4.1.5 Ultrasonic Signal Characteristics

An ultrasonic wave generated from a transducer is characterised by waveform duration, centre frequency and bandwidth. Waveform duration with the unit of microseconds is defined as the time between the lower and upper band of a certain amplitude level. As illustrated in Figure 4.7 (a), the -14dB level waveform duration is the time difference between the lower and upper time at 20% of the peak amplitude. The bandwidth (MHz) is the frequency difference at 50% of the peak frequency amplitude as shown in Figure 4.7 (b). Centre frequency is the mean frequency of lower and upper frequency at 50% of the signal amplitude. The bandwidth (%) therefore is defined in Equation (4.3). In this work of research, the spectrum parameters are more focused on.

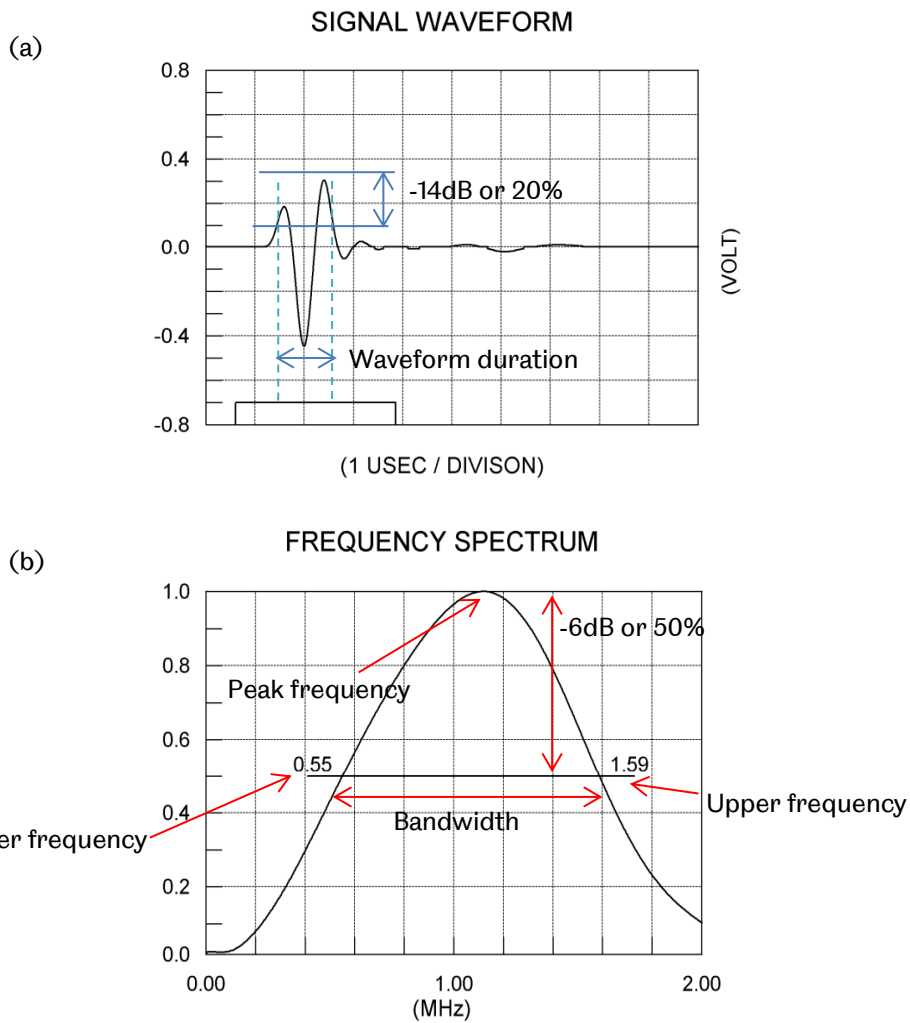


Figure 4.7 Signal characteristics of a normal incidence shear wave transducer V153 (a) Time domain signal and waveform duration; (b) Frequency spectrum and bandwidth (Reproduced Olympus transducer test form).

$$bandwidth(\%) = \frac{bandwidth (MHz)}{centre frequency} \times 100\% \quad (4.3)$$

The characteristics of the normal incidence shear wave transducer is summarised in Table 4.3. It is noted that the peak frequency is different from the nominal and the centre frequency. The bandwidth of these probes is significant in the following research work, particularly for the V155 5MHz transducer as it is used as a wideband receiver.

Table 4.3 Characteristics of normal incidence shear wave transducers from Olympus transducer test forms.

Characteristics	V152 (1022255)	V153 (1098151)	V155
-14dB waveform duration (μ s)	1.327	1.171	0.390
Nominal frequency (MHz)	1	1	5
Centre frequency (MHz)	0.94	1.07	4.89
Peak frequency (MHz)	1.02	1.12	4.19
Bandwidth (MHz)	0.82	1.04	3.79
Bandwidth (%)	86.79	97.05	77.44

4.2 Ultrasonic Function Generator

A working piezoelectric element or transducer generates ultrasonic signals only when they are connected to an ultrasonic function generator or waveform generator. The ultrasonic function generator functions to trigger a transducer and force it to excite and generate a specific waveform. There are various types of ultrasonic function generator available for different applications. Figure 4.8 shows some examples of ultrasonic function generator. Some of the main features of an ultrasonic generator are briefly discussed.

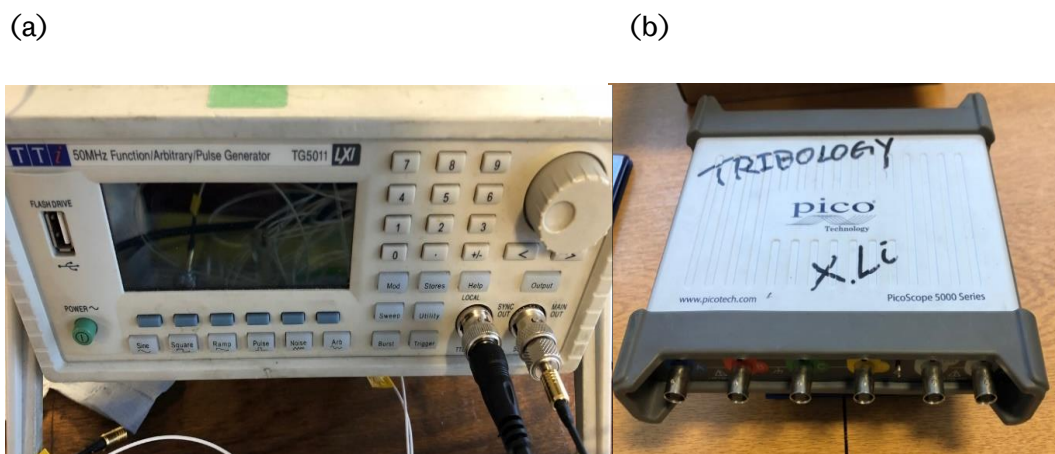


Figure 4.8 Examples of ultrasonic function generator. (a) TTI arbitrary function generator. (b) Function generator incorporated in a Picoscope.

4.2.1 Excitation Waveforms

Numerous waveforms are available from an ultrasonic function generator to excite an ultrasonic transducer, including standard spike-shape pulse, square waveform, sine waveform and even arbitrary waveforms. A spike-shaped pulse is a commonly used excitation waveform and it is widely employed in non-destructive testing where a wide bandwidth is needed. The other widely applied excitation is a sinusoidal waveform. Using such excitation, not only efficiency is achieved but also the ultrasonic frequency precision is improved when the sine waveform frequency is aligned with the characteristic frequency. If the piezoelectric element in the transducer is broadband and well damped, a range of frequencies can be generated with a single transducer, by altering the sinusoidal waveform frequency. The shape of excitations from an ultrasonic function generator is less important than the received signal shape, as an excitation waveform transmits through the piezoelectric element, amplifier, host material and its features, such as material properties and reflecting features (Krautkramer and Krautkramer, 1990). Carefully selected excitation waveforms still facilitate the ultrasonic testing. In the following research work, sinusoidal waveform is used.

4.2.2 Excitation Mode and Repetition Rate

Various excitation modes are available to excite an ultrasonic probe. In the Burst mode, one burst of excitation waveform, consisting of a finite number of cycle, is produced at each trigger signal. In this mode, the waveform is only settable at a single frequency. In Sweep mode, a waveform with a range of continuous frequencies is produced. Using this mode, multi-frequency features can be used. Gated mode only allows waveform excitation excited when the gate signal is true. Continuous mode is also available where the waveform is continuously produced without pause. In the following experimental work, a burst of a number of cycles sinusoidal waveform is used as the excitation mode.

The repetition rate determines the speed of the excitation triggering, i.e. the number of excitations per second. The repetition rate is generally selected depending on the test configuration. If the repetition rate is too high in a pulse-echo configuration, the reflection signal from the first trigger will interfere with the second or third excitations. In the following experimental work, the time for subsequent reflections to attenuate until no longer visible is less than a millisecond, which is the minimum delay between excitation pulses. The maximum pulse rate is therefore

approximately 1000Hz. Considering the safe operation of a gated amplifier, a repetition rate of 25Hz is selected.

4.3 Power Amplifier

4.3.1 Excitation Amplitude

The voltage output of the ultrasonic function generator shown in Figure 4.9 is maximum $10V_{p-p}$ for the arbitrary function generator and $4V_{p-p}$ for the Picoscope, which are generally low for some non-destructive testing applications. High voltage excitations can be achieved using power amplifier. Some amplifiers are incorporated with an ultrasonic function generator so the excitation waveform is directly amplified and then passed to excite an ultrasonic transducer.

Attention must be paid to the voltage driving the transducer or piezoelectric element. The voltage applied across the piezoelectric element is limited to approximately 50V per millimetre of the piezo element thickness when the element is subject to a negative spike excitation. For a low-frequency transducer where the piezoelectric element is thick, the voltage applied across the element can be higher. A 600V short duration negative spike can be applied to transducers with 5MHz or lower frequencies (Olympus NDT Inc, 2006).

In some cases where the burst mode of sinusoidal excitation is used, apart from the voltage, the average power dissipation to the transducer is also limited and it should be below 125mW. Exciting transducer beyond such limit tends to overheat the piezoelectric element and in a more severe case depolarise the element. The averaged power can be determined from the applied voltage, duty cycle and transducer impedance as follows:

$$V_{rms} = \frac{0.707 \times V_{p-p}}{2}, \quad (4.4)$$

$$P_{average} = \frac{Duty\ Cycle \times V_{rms}^2 \times \cos(\text{phase angle})}{transducer\ impedance}, \quad (4.5)$$

$$No.\ of\ cycles\ in\ a\ burst = \frac{frequency \times Duty\ Cycle}{Repetition\ Rate}. \quad (4.6)$$

4.3.2 Signal Amplification

Numerous types of signal amplifier are available for various non-destructive testing applications. Signal amplification can be applied to the excitation waveforms before driving the ultrasonic transducer or to the returned signal from a test specimen. Most amplifiers can be used in both configurations. With an amplified ultrasonic signal, the measurement reproducibility is improved in testing of a non-ultrasonic-favoured material, such as materials with high attenuation like composites or cast iron. An amplified ultrasonic signal increases the accuracy of measurement when great time resolution is required. Amplified excitation also facilitates and improves the efficiency of driven transducers. When the amplifier is applied on received ultrasonic signals, the amplified signal will make the most use of the vertical range of an ultrasonic receiver to increase the measurement accuracy.

Features such as frequency bandwidth, gain level and power output are generally considered when selecting a signal amplifier. These features of two different ultrasonic amplifiers (shown in Figure 4.9) used in this research work are summarised in Table 4.4.



Figure 4.9 Examples of signal amplifier. (a) AR low power amplifier. (b) RITEC high power amplifier.

Table 4.4 Key features of two difference ultrasonic signal amplifier.

Key features	AR low power amplifier	RITEC high power amplifier
Working mode	Continuous-wave amplifier	Gated amplifier
Power output	100W	5kW
Frequency range	10kHz – 250MHz	200kHz – 20MHz
Gain level	49dB	n/a
Output pulse voltage	n/a	~140V – ~1500V (peak-peak)
Maximum duty cycle	n/a	0.3%

It is noticed that the RITEC high power amplifier sets a limit on the duty cycle, as the working mode of a gated amplifier is very different from a conventional continuous-wave (CW) amplifier. A CW amplifier operates continuously when the switch is on while a gated amplifier only works for a limited duration of time when a gate signal is passed to the amplifier. If it receives no gate signal, then the gated amplifier is not operating. This feature of the gated amplifier is advantageous compared to a CW amplifier. The limited duty cycle enables a high burst power while keeping the averaged power very low. The duty cycle, peak burst power and averaged power can be determined using Equation (4.7)-(4.9). For example, when a burst of 10 cycles at 1 MHz, repeated 50 times per second, is amplified to 500V signal into a 50Ω impedance, the RMS burst power is approximately 625W, the duty cycle is 0.05% and the averaged power is 0.31W.

$$Duty\ cycle = Burst\ width\ (s) \times Repetition\ Rate\ (Hz) \times 100\% \quad (4.7)$$

$$P_{rms} = \frac{(0.707 \times V_{peak})^2}{Nominal\ output\ impedance} \quad (4.8)$$

$$P_{average} = Duty\ cycle \times P_{rms} \quad (4.9)$$

The other advantage of a gated amplifier over a CW amplifier is that the noise level is low. When the gate signal is off, the amplifier is not operating and thus the noise is not amplified, which ensures a good signal-to-noise ratio.

The harmonic distortion is considered when using the amplifier. When a single frequency excitation signal is passed to an amplifier, higher order frequencies signals sometimes appear, especially when a carelessly designed amplifier or a faulty

amplifier is used, or if the amplifier is improperly operated. Example of harmonic distortion with a 5kW output burst is illustrated in Figure 4.10. Harmonics distortions are at least 20dB less than the main driving frequency content. Attention must be paid when the higher frequency content is considered using an amplifier.

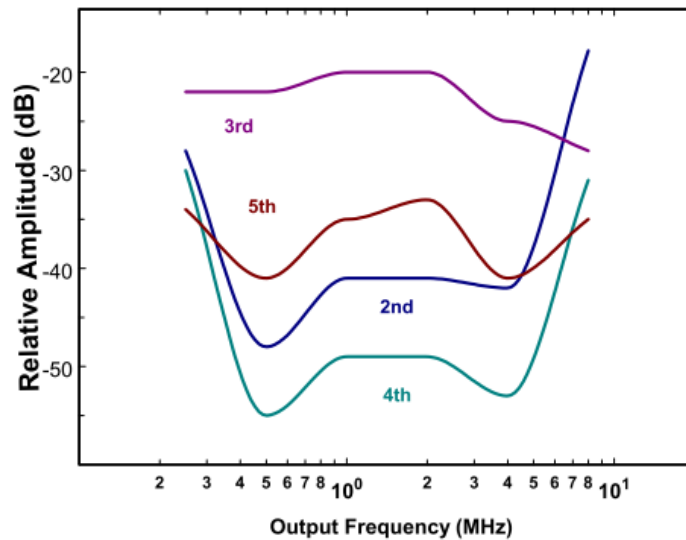


Figure 4.10 Harmonic distortion of a 5kW output using a RITEC amplifier (Reproduced from Ritec Amplifier Specification).

In the following research work, excitation signals need amplification to drive ultrasonic transducers and the higher order harmonic components are of particular interest. Therefore, the gated amplifier is selected due to its merits of efficiency of driving piezo-elements with high burst power, low noise level and low harmonic distortions.

4.4 Ultrasonic Digitiser

When a returned ultrasonic signal is received by a transducer, it is converted to a digital form using a device called digitiser, which is also known as analogue-to-digital converter (ADC). Once the received waveform is digitised, it will be stored in memory or passed onto a processor for signal processing. The digitised signal is well maintained compared to an analogue signal which is subject to noise commonly in ultrasonic equipment. Examples of frequency used digitisers are shown in Figure 4.11. Figure 4.11 (a) shows a digital storage oscilloscope, which primarily digitises

received waveforms and displays them on the screen in real-time. The device in Figure 4.11 (b) is another type of modern designed compact digitiser. It digitises returned signals with a PC connected, which enables customised real-time processing via a control software.

The main features of digitiser are the sampling rate, amplitude resolution, bandwidth and number of channels when selecting an appropriate digitiser. These characteristics of both digitisers shown in Figure 4.11 are listed in Table 4.5.

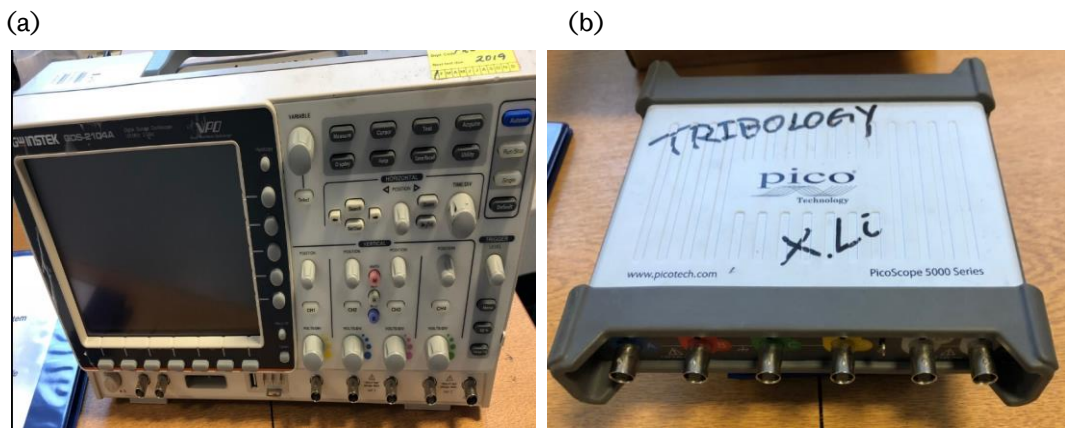


Figure 4.11 Examples of digitiser. (a) GWINSTEK Oscilloscope. (b) Digitiser incorporated in PicoScope.

Table 4.5 Key features of two difference ultrasonic digitiser.

Key features	GWinstek Oscilloscope GDS2104A	PicoScope 5444B
Number of channels	4	4
Bandwidth ($-3dB$)	200MHz	200MHz for 8 to 15 bits
Vertical resolution	8 bits	8, 12, 14, 15 and 16 bits
Maximum input range	$300V_{rms}$	$\pm 20V$
Maximum sampling rate	2GS/s for 1 channel	500MS/s for 1 channel at 12 bits
Buffer memory	n/a	256MS at 12 bits

4.4.1 Sampling Rate

Sampling rate determines the number of samples in one second that the digitiser converts from analogue to digital signals and its unit is Hz or S/s (samples per second). In some applications, the waveform shape requires to be well maintained and, in such applications, and as a rule of thumb, the sampling rate generally is 10 times higher than the target frequency used in tests (Brunskill, 2013). For example, a transducer operating at 1MHz requires a sampling rate at least 10MHz to preserve the waveform shape. An insufficiently high sampling rate will cause aliasing. In the following research work, the sampling frequency is 500MS/s, which is sufficiently higher than the high-order harmonic frequency 3MH to prevent aliasing.

4.4.2 Amplitude Resolution and Range

Amplitude resolution, sometimes known as vertical resolution, is the minimum voltage division size of a digitised signal. In applications where amplitude measurement is of importance, such as measuring tiny amplitude changes of a signal or a small flaw reflection signal next to a relatively large reflection, a sufficient fine voltage division enables these features to be detected accurately. Amplitude range is the maximum voltage of a digitised signal. The amplitude range should be just large enough to capture the target digitised signal.

If a voltage range of 10V is digitised using an 8-bit digitiser, $2^8 = 256$ divisions are obtained, and the minimum voltage resolution is 0.039V. However, for a 12-bit digitiser, the voltage range is divided into 4096 steps, with a minimum voltage of 0.0024V, which improve the voltage measurement accuracy.

Both digitisers in Figure 4.10 enables selectable amplitude range and voltage resolution. Various combinations of voltage range and resolution make the digitiser applicable in many ultrasonic testing applications.

4.4.3 Bandwidth

The bandwidth of a digitiser is the range of frequencies that the digitiser operates appropriately. Generally, the bandwidth is defined as the frequency range with a -3dB amplitude. If the frequency of a waveform is out of the bandwidth of a digitiser, such waveform can still be digitised but the waveform is heavily distorted. In

practice, a digitiser with a bandwidth at least twice the highest frequency component should be utilised to preserve the waveform shape.

4.4.4 Number of Channels

The number of channels determines the number of different signals that can be captured simultaneously. A multi-channel digitiser enables the recording of multiple signals during testing. Once more channels are activated, the sampling rate of a digitiser is compromised.

4.4.5 Filters

A filter is a device that only allows a selected range of frequency contents to pass through. The filter can be incorporated in a signal amplifier, such as the RITEC amplifier in Figure 4.9 (b), integrated with a digitiser or a stand-alone hardware. Using a filter can effectively reduce the bandwidth of a returned signal. Low pass filter which allows low-frequency components and rejects high frequencies such as high frequency travelling electric signal, is applied to improve the signal to noise ratio. High pass filter rejects the low-frequency signals such as vibration signal and can be used to eliminate the large recovery trend due to a high-power excitation.

4.5 Ultrasonic Measurement Configurations

Having discussed the apparatus commonly employed in measurement, a flow diagram illustrates the configuration of these pieces of hardware in ultrasonic tests in Figure 4.12. This work of research follows this process.

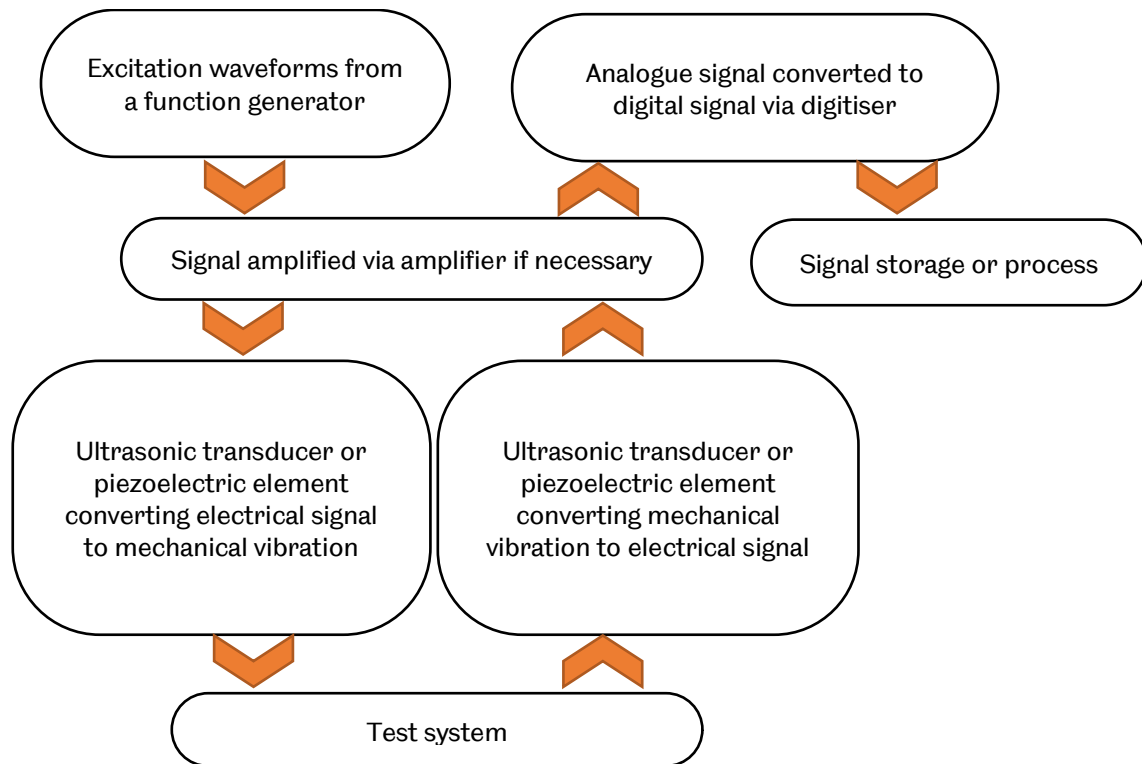


Figure 4.12 ultrasonic measurement process and configurations.

4.6 Conclusion

In this chapter, the apparatus used in the ultrasonic technique is introduced, including the means of generating the ultrasonic wave, amplifying the wave and acquiring the ultrasonic signals. In the current research work, the normal incidence shear wave transducer is used to transmit and receive the ultrasonic signals due to its good ultrasonic characteristics. The gated amplifier is selected due to its ability to produce a high-power ultrasonic signal with the least harmonic distortion.

5 MODELLING OF ULTRASONIC NONLINEARITY AT A FRICTIONAL INTERFACE

When a high-power ultrasound wave meets a frictional interface, the nonlinear nature of the stick-slip phenomenon distorts the high-power ultrasound wave. In this chapter, a numerical method is used in conjunction with an analytical approach to understand the nonlinearity generation of a distorted high-power shear polarised ultrasonic wave after the interaction with a frictional interface. Parameters affecting the nonlinearity generation such as amplitude of incident ultrasound, contact stress and coefficient of friction are investigated in detail.

5.1 Analytical Model

5.1.1 Mathematical Model of Ultrasound at Interface

The same approach used in (Richardson, 1979; O'Neill et al., 2001) is followed here. A schematic diagram of the interaction is depicted in Figure 5.1. Two identical homogeneous, isotropic elastic materials, *I* and *II* are defined at the left and right half space, respectively. Two half-space materials are brought to contact under a normal contact pressure, σ . At the interface ($x = 0$), friction is characterised by Coulomb's law with a constant friction coefficient, μ and the friction force is proportional to the applied normal contact pressure.

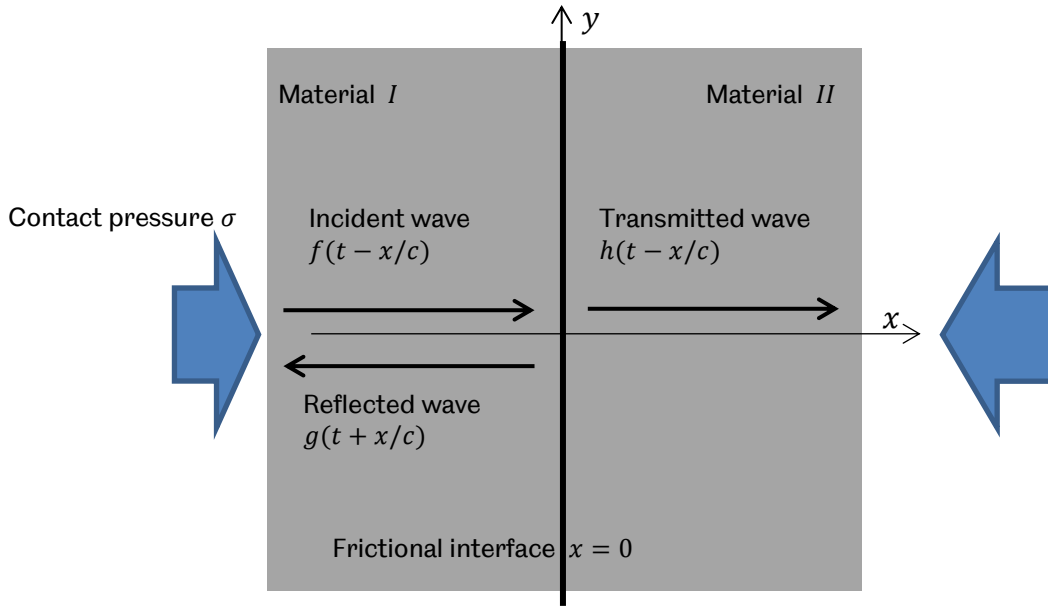


Figure 5.1 Simplified contacting interface and shear polarised ultrasound wave.

In Material I (defined by $x < 0$), the forward incident shear vertically polarised wave is described by $f(t - x/c)$ and the backward reflected wave is $g(t + x/c)$. The transmitted wave defined by $h(t - x/c)$ propagating in Material II. The propagation of incident, reflected and transmitted waves are governed by the wave equation:

$$c^2 \frac{\partial^2 u}{\partial x^2} = \frac{\partial^2 u}{\partial t^2}, \quad (5.1)$$

where $u(t, x)$ is the displacement of the shear wave along the direction y and c is the speed of sound in the both left and right half spaces.

In Material I and II, the total displacement is given as:

$$u^I(x, t) = f\left(t - \frac{x}{c}\right) + g\left(t + \frac{x}{c}\right), \quad (5.2)$$

$$u^{II}(x, t) = h\left(t - \frac{x}{c}\right). \quad (5.3)$$

The corresponding shear stress induced by ultrasound in the material, τ is obtained as (Achenbach, 1973):

$$\tau^I(x, t) = G \frac{\partial u(x, t)}{\partial x} = \frac{G}{c} \left[-f'\left(t - \frac{x}{c}\right) + g'\left(t + \frac{x}{c}\right) \right], \quad (5.4)$$

$$\tau^{II}(x, t) = \frac{G}{c} \left[-h' \left(t - \frac{x}{c} \right) \right], \quad (5.5)$$

where G is the shear modulus of the material and prime is the derivative with respect to its argument.

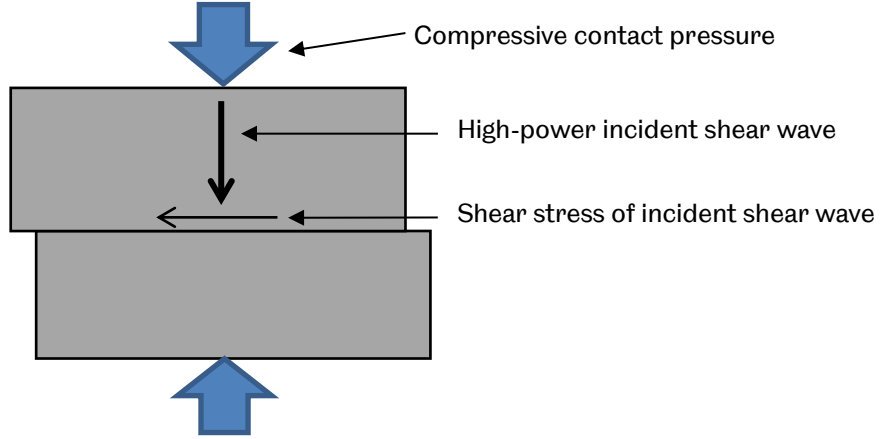


Figure 5.2 Contacting interface slips under high-power incident shear ultrasound and remains closed under compressive contact pressure.

Here the displacement amplitude of the normally incident shear polarised ultrasound is assumed to be sufficiently large. As shown in Figure 5.2, when the high-power shear ultrasound strikes at the frictional interface, the contact state switches between 'stick' and 'slip' motion. Due to the constant compressive contact pressure applied at the interface, the interface always remains closed even during the alternation of 'stick' and 'slip' state. The boundary conditions are defined as:

$$u^I(x, t) = u^{II}(x, t) + \Delta u, ('stick'), \quad (5.6)$$

$$\tau^I(x, t) = \tau^{II}(x, t), ('stick' \text{ and } 'slip'), \quad (5.7)$$

$$\tau^I(x, t) = -sgn \left(\frac{\partial u^I}{\partial t} \right) \mu \sigma, ('slip'), \quad (5.8)$$

where Δu is the displacement difference, $((\partial u^I)/\partial t)$ the total velocity left of the interface and $sgn()$ the sign function. Equation (5.7) describes the stress continuity at the interface regardless of contact state. The friction force described in Equation (5.8) is in an opposite direction of the velocity left of the interface.

At the interface ($x = 0$), the average displacement $\Sigma(t)$ and the relative displacement $\Delta(t)$ are then given as:

$$\Sigma(t) = \frac{1}{2}(u^I(0, t) + u^{II}(0, t)) = \frac{1}{2}[f(t) + g(t) + h(t)], \quad (5.9)$$

$$\Delta(t) = \frac{1}{2}(u^{II}(0, t) - u^I(0, t)) = \frac{1}{2}[-f(t) - g(t) + h(t)]. \quad (5.10)$$

The corresponding derivatives with respect to time are derived as:

$$\dot{\Sigma}(t) = \frac{\partial \Sigma(t)}{\partial t} = \frac{1}{2} \frac{c}{G} [\tau^I(t) - \tau^{II}(t)] + f'(t), \quad (5.11)$$

$$\dot{\Delta}(t) = \frac{\partial \Delta(t)}{\partial t} = \frac{1}{2} \frac{c}{G} [-\tau^I(t) - \tau^{II}(t)] - f'(t). \quad (5.12)$$

The reflected wave and transmitted wave at the interface can be solved by substituting Equation (5.4)-(5.8) into the time derivative of the averaged and relative displacement in Equation (5.11) and (5.12) and then integrating over time, which is given as:

$$g(t) = -\Delta(t) - f(0), \quad (5.13)$$

$$h(t) = f(t) - \Delta(t) - f(0), \quad (5.14)$$

where $f(0)$ is the initial condition of incident wave at the interface and $\Delta(t)$ is a piecewise function depending on the contact state, which is given in Equation (5.15):

$$\Delta(t) = \begin{cases} \Delta(t_c), ('stick') \\ \Delta(t_c) + \frac{c}{G} \left[-sgn \left(\frac{\partial u^I}{\partial t} \right) \mu \sigma \right] (t - t_c) - [f(t) - f(t_c)], ('slip') \end{cases} \quad (5.15)$$

where t_c is the critical time when the contact changes from 'stick' to 'slip' state.

Nonlinearity generation of a high-power shear ultrasound interacting at a frictional interface can be solved by defining an incident wave function (e.g. an incident time-harmonic waveform in Section 5.1.2) and analysing the distortion of the waveform.

5.1.2 Time-Harmonic Waveform

In general, any incident waveform can be used to analyse the nonlinearity generation at an interface. A single frequency time-harmonic waveform is widely used in research (O'Neill et al., 2001; Blanloeuil et al., 2014c) due to its frequency feature. An incident time-harmonic waveform consists of only a single frequency component and any distortion on the reflected and transmitted waves after interacting with the

interface leads to the appearance of extra frequency components, which can be employed to examine the nonlinearity generation.

A pure sinusoidal waveform is exploited here. A shear polarised incident ultrasound and its induced shear stress at the interface are defined as follows:

$$f(x, t) = A_0 \sin(\omega t - kx), \quad (5.16)$$

$$\tau(x, t) = GkA_0 \cos(\omega t - kx), \quad (5.17)$$

where ω and k are the angular frequency and wavenumber of the ultrasound wave, respectively.

The frictional contact is assumed to be in 'slip' motion at $t = 0$ and the shear stress of ultrasound is greater than the friction force at the interface. The critical time t_c is when contact switches from 'slip' to 'stick' state once the shear stress of ultrasound is less than the friction, as shown in Equation(5.18). When the shear stress of ultrasound evolves greater than the friction force, contacting surfaces slip again. The shear stress of ultrasound periodically changes and the contact state alternates between 'stick' and 'slip', as illustrated in Figure 5.3.

$$GkA_0 |\cos(\omega t_c)| = \mu\sigma \quad (5.18)$$

$$t_c = \cos^{-1} \frac{\mu\sigma}{GkA_0} \quad (5.19)$$

Table 5.1 Critical time of contact state alternation.

Contact state	slip→stick	stick→slip	slip→stick	stick→slip	slip→stick
Critical time	$t_{c1} = t_c$	$t_{c2} = \frac{\pi}{\omega} - t_c$	$t_{c3} = \frac{\pi}{\omega} + t_c$	$t_{c4} = \frac{2\pi}{\omega} - t_c$	$t_{c5} = \frac{2\pi}{\omega} + t_c$

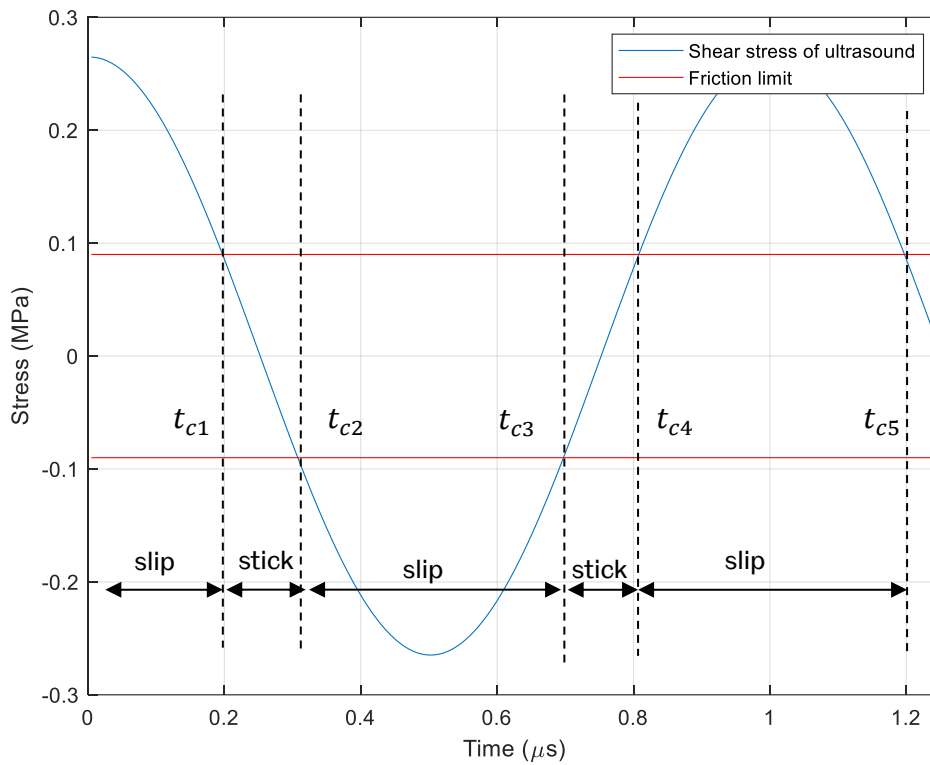


Figure 5.3 At interface, shear stress of ultrasound, friction force, contact state alternation and critical time as in Table 5.1. The amplitude of incident shear wave is 5nm and corresponding shear stress is 0.26MPa .

5.1.3 Analytical solution

The reflected and transmitted waves are solved following the steps in Section 5.1.1. The 'stick' and 'slip' state need to be treated separately. An example of incident, reflected and transmitted waves after interaction at the frictional contact are illustrated in Figure 5.4 and the parameters applied are listed in Table 5.2.

It is noted that due to the interaction at the frictional interface, reflected and transmitted waves are distorted compared with the incident wave. The plateau feature observed on the reflected wave is due to that when the contact surfaces stick, the incident wave propagates through the interface with no wave reflected and the displacement remains unchanged. The 'clipped' feature is not shown on the transmitted waves in the 'stick' state in Figure 5.4 as in this state, the transmitted wave is not distorted. In the 'slip' state, transmitted wave is distorted, which is better illustrated in Figure 5.5.

Table 5.2 Parameters used in time-harmonic signal study.

Material property of Aluminium	
Shear modulus G	26.32GPa
Ultrasound parameters	
Working mode	Continuous wave
Frequency f	1MHz
Speed of sound c	3122m/s
Wavenumber k	2012.6rad · m ⁻¹
Incident ultrasound amplitude A_0	5nm
Shear stress of ultrasound τ	0.264MPa
Interface parameter	
Contact pressure σ	0.3MPa
Friction coefficient μ	0.5

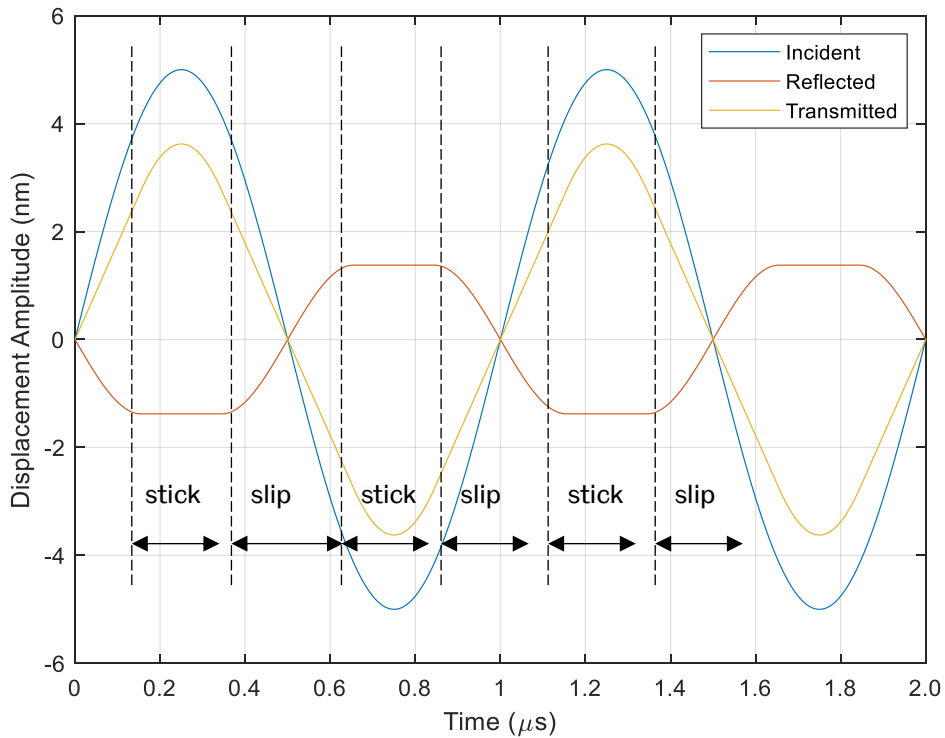


Figure 5.4 At interface, displacement incident, reflected and transmitted waves after interacting with the frictional interface.

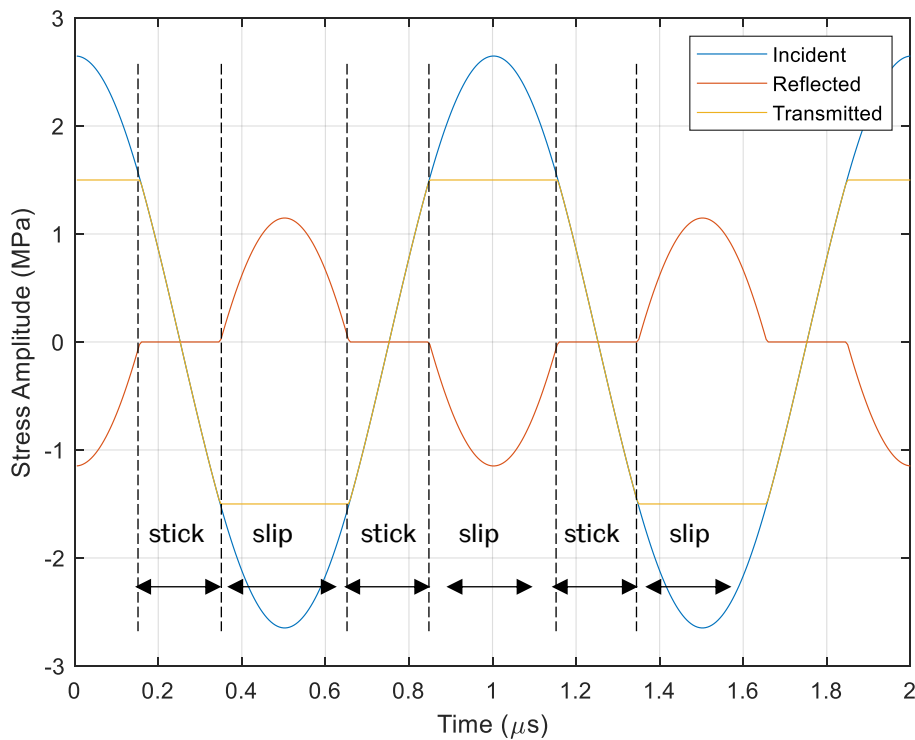


Figure 5.5 At interface, stress of incident, reflected and transmitted waves after interacting with the frictional interface.

Figure 5.5 depicts the stress of incident, reflected and transmitted waves at the interface. In contrast to the displacement in Figure 5.4, transmitted waves also show the 'clipped' feature. When contact is in 'slip' state, the maximum shear stress supported at the contact is limited to the frictional force and transmitted stress remains unvaried during the 'slip' duration. As stress is continuous at the interface even during the 'slip' motion, the unsupported stress is then reflected, resulting in the reflected waveform shown in Figure 5.5. Similar results are also obtained in a previous study (Meziane et al., 2011).

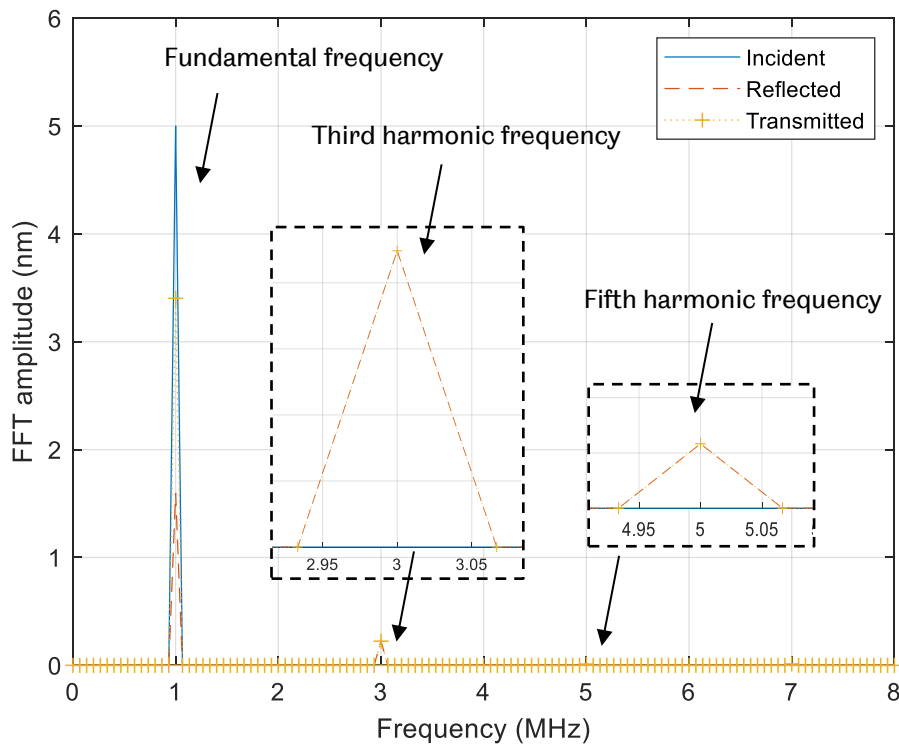


Figure 5.6 Frequency spectrum of incident, reflected and transmitted waves after interacting with the frictional interface.

Frequency spectra are obtained by taking Fast Fourier Transform (FFT) on 15 cycles of the incident, reflected and transmitted waves depicted in Figure 5.4 and are shown in Figure 5.6. Due to the limited data points used in FFT, i.e. 3000 points, the frequency resolution is approximately 66.7kHz. Despite this coarse frequency resolution, extra frequency components are still observed in the reflected and transmitted waves in contrast to the single frequency component of the incident wave. Three points are noted.

- In both reflected and transmitted wave frequency spectrum, only the odd order harmonics, i.e. third, fifth, seventh order etc., are observed and this is mainly due to FFT of the 'clipped' features of the waveform (O'Neill et al., 2001; Meziane et al., 2011). No even harmonics are generated.
- The amplitude of the third harmonic and the fifth harmonic are much smaller than the amplitude of their corresponding fundamental frequency component.
- The third order harmonic amplitude of both reflected and transmitted waves are equal, so are the fifth and higher order harmonics as a result of energy conservation.

Such extra frequency generation is due to the distortion of the reflected and transmitted waves after the interaction with the frictional interface. The non-linear feature of the frictional interface is transferred to cause the ultrasound waves to be distorted and nonlinearity generated. Since no other nonlinearity source is considered in the analytical work, the frictional interface is the sole cause for the harmonic generation of the ultrasound waves.

5.2 Numerical Study

The analytical study in Section 5.1 reveals the interaction of the ultrasound wave with a frictional interface and consequently the waveform distortion and harmonic generation of the ultrasound. The analytical work mainly focuses on the interaction at the interface. The propagation of ultrasound after striking the frictional interface, especially subject to varying contact conditions is studied using a simple finite difference method. Although other more advanced numerical methods and tools are available, the finite difference method is capable of capturing the physical phenomenon reasonably (Blanloeuil et al., 2014c).

5.2.1 Numerical Model

A simple one-dimensional model, used in Blanloeuil and co-workers' study (Blanloeuil et al., 2014c; Blanloeuil et al., 2017), is applied here as depicted in Figure 5.7. To simplify the process, a half space material and a rigid wall are in contact at $x = 0$, under a normally applied compressive stress. The interface is defined as a frictional interface and characterised by classical Coulomb's Law with a constant friction coefficient. Ultrasound wave is excited, propagates towards the interface, at the location $x = -L$, where a transparent boundary is also defined so that waves are not reflecting and only transmitting through towards $x = -\infty$.

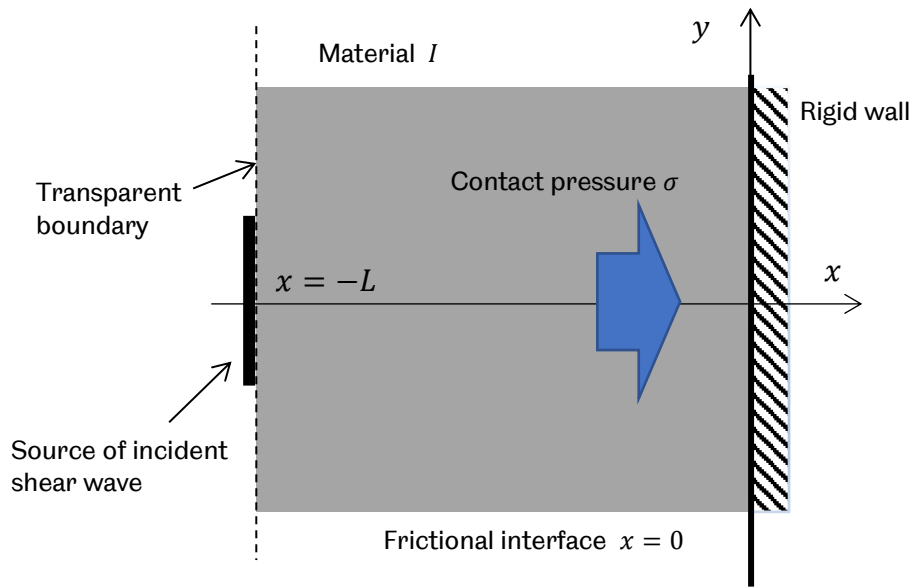


Figure 5.7 Simplified one-dimensional model system.

Derivations given in Section 5.1 still apply here and the terms of Material II vanishes as the rigid wall is used instead. The relative displacement is thus given by Equation (5.2) and the velocity of relative displacement is given as:

$$\dot{u}^I(x, t) = \frac{\partial u}{\partial t} = f' \left(t - \frac{x}{c} \right) + g' \left(t + \frac{x}{c} \right). \quad (5.20)$$

Equation (5.20) and (5.4) are combined to obtain the expression for the derivative as follows:

$$f' \left(t - \frac{x}{c} \right) = \frac{1}{2} \left(\dot{u}^I(x, t) - \frac{c}{G} \tau^I(x, t) \right), \quad (5.21)$$

$$g' \left(t + \frac{x}{c} \right) = \frac{1}{2} \left(\dot{u}^I(x, t) + \frac{c}{G} \tau^I(x, t) \right). \quad (5.22)$$

At the interface, Coulomb's Law in Equation (5.6)-(5.8) is redefined as:

$$'stick': \begin{cases} |\tau^I(0, t)| < \mu \sigma \\ \dot{u}^I(0, t) = 0 \end{cases}, \quad (5.23)$$

$$'slip': \begin{cases} |\tau^I(0, t)| = \mu \sigma \\ \tau^I(0, t) \dot{u}^I(0, t) \leq 0 \end{cases}. \quad (5.24)$$

It is worth noticing that the static friction coefficient μ is applied here. When the dynamic friction coefficient μ_k is employed at the 'slip' state, it replaces the friction coefficient μ in Equation (5.24).

5.2.2 Numerical Implementation

The classic Euler scheme is applied to discretise the wave equation in Equation (5.1). The Material I along $y = 0$ is then discretised in space and time and the subscript i and j denotes the space and time index, respectively, as illustrated in Figure 5.8.

The discretised wave equation is thus given as:

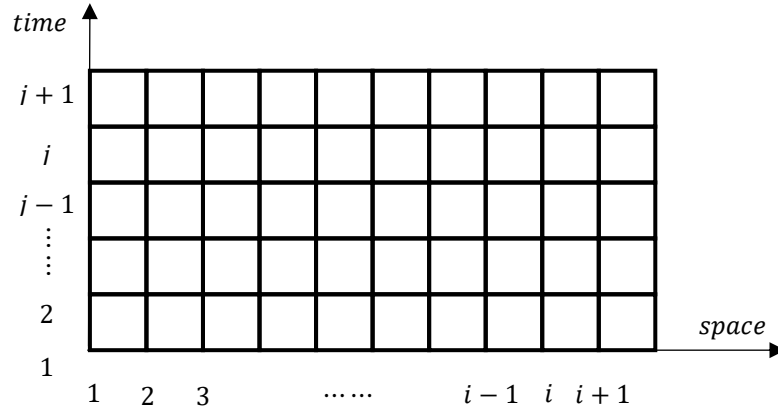


Figure 5.8 Space and time discretisation for one-dimensional system.

$$c^2 \frac{u_{i+1,j} - 2u_{i,j} + u_{i-1,j}}{\delta x^2} = \frac{u_{i,j+1} - 2u_{i,j} + u_{i,j-1}}{\delta t^2}, \quad (5.25)$$

where δx and δt are the space and time increment respectively. Generally, the next time step solution is thus obtained by rearranging Equation (5.25) as:

$$u_{i,j+1} = \frac{1}{2} [r^2 u_{i+1,j} + (2 - 2r^2) u_{i,j} + r^2 u_{i-1,j}], \quad (5.26)$$

$$r = c \frac{\delta t}{\delta x}. \quad (5.27)$$

The term $c (\delta t / \delta x)$ is commonly known as Courant-Friedrichs-Lewy (CFL) condition and for stable numerical solutions, this term should be less than 1.

$$f' \left(t - \frac{-L}{c} \right) = s(t) \quad (5.28)$$

The left boundary $x = -L$, in Figure 5.7 is defined in Equation (5.28). $s(t)$ is the excitation source and thus defining the incident wave. This equation also defines the transparent boundary condition. Using the expression in Equation (5.23), Equation (5.28) can be written in a form (Equation (5.29)) in which discretisation can be operated. The discretisation is thus obtained using the second order upwind

scheme, as shown in Equation (5.30). The next time step solution is thus given in Equation (5.31).

$$\frac{1}{2} \left(\frac{\partial u(x, t)}{\partial t} - c \frac{\partial u(x, t)}{\partial x} \right) = s(t) \quad (5.29)$$

$$\frac{1}{2} \left(\frac{u_{1,j+1} - u_{1,j}}{\delta t} - c \frac{-3u_{1,j} + 4u_{2,j} - u_{3,j}}{2\delta x} \right) = s(t) \quad (5.30)$$

$$u_{1,j+1} = \left(1 - \frac{3}{2}r \right) u_{1,j} + 2ru_{2,j} - \frac{1}{2}ru_{3,j} + 2\delta t s(t) \quad (5.31)$$

The right boundary $x = 0$, in Figure 5.7 is the frictional interface. The contacting interface is assumed to be in 'stick' mode initially and the shear stress is discretised using the second order upwind scheme. If the calculated shear stress is less than the frictional force at the interface, the contact is in 'stick' mode and boundary condition in Equation (5.32) applies. If the shear stress is greater than the friction, contact is in 'slip' mode and the frictional force at the interface equals to the shear stress. Regardless of the contact state, the next time step solution at the boundary $x = 0$ is only determined after shear stress at the interface is computed.

$$'stick' = \begin{cases} \tau_{i,j} = G \frac{3u_{i,j} - 4u_{i-1,j} + u_{i-2,j}}{2\delta x} \\ u_{i,j} = u_{i,j-1} \end{cases} \quad (5.32)$$

$$'slip' = \begin{cases} \tau_{i,j} = \pm\mu\sigma \\ u_{i,j} = \frac{2\delta x\tau_{i,j}/G + 4u_{i-1,j} - u_{i-2,j}}{3} \end{cases} \quad (5.33)$$

The entire procedure of computing the shear ultrasound wave interaction at the frictional interface is summarised in Figure 5.9.

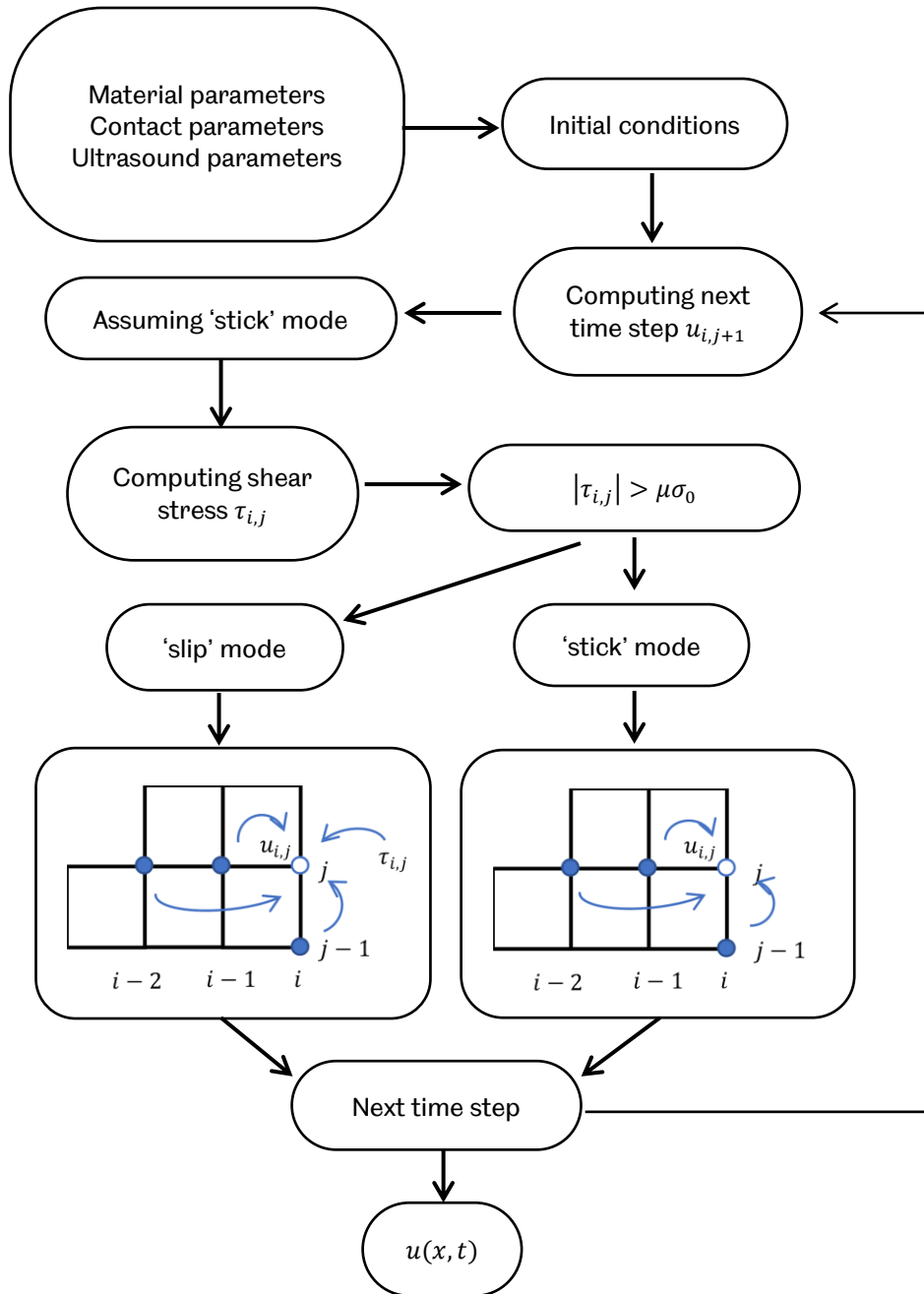


Figure 5.9 Numerical computation procedure.

5.2.3 Numerical Simulation Results

5.2.3.1 Time Evolution

An example of the numerical solution computed using parameters listed in Table 5.3 is given in Figure 5.10. The incident wave starts from the left boundary and propagates towards the frictional interface. After interaction with the frictional boundary, distortion clearly occurs on the waveform.

Table 5.3 Parameters used in numerical study.

Material property of Aluminium	
Shear modulus G	26.92GPa
Ultrasound parameters	
Working mode	5-cycle burst
Frequency f	1MHz
Speed of sound c	3122m/s
Wavenumber k	2019rad · m ⁻¹
Incident ultrasound amplitude A_0	2.5nm
Shear stress of ultrasound τ	0.135MPa
Interface parameters	
Contact pressure σ	0.3MPa
Friction coefficient μ	0.3
Numerical setup parameters	
Space resolution δt	4.5ns
Time resolution δx	20 μ m
CFL condition ($c \delta t / \delta x$)	0.702

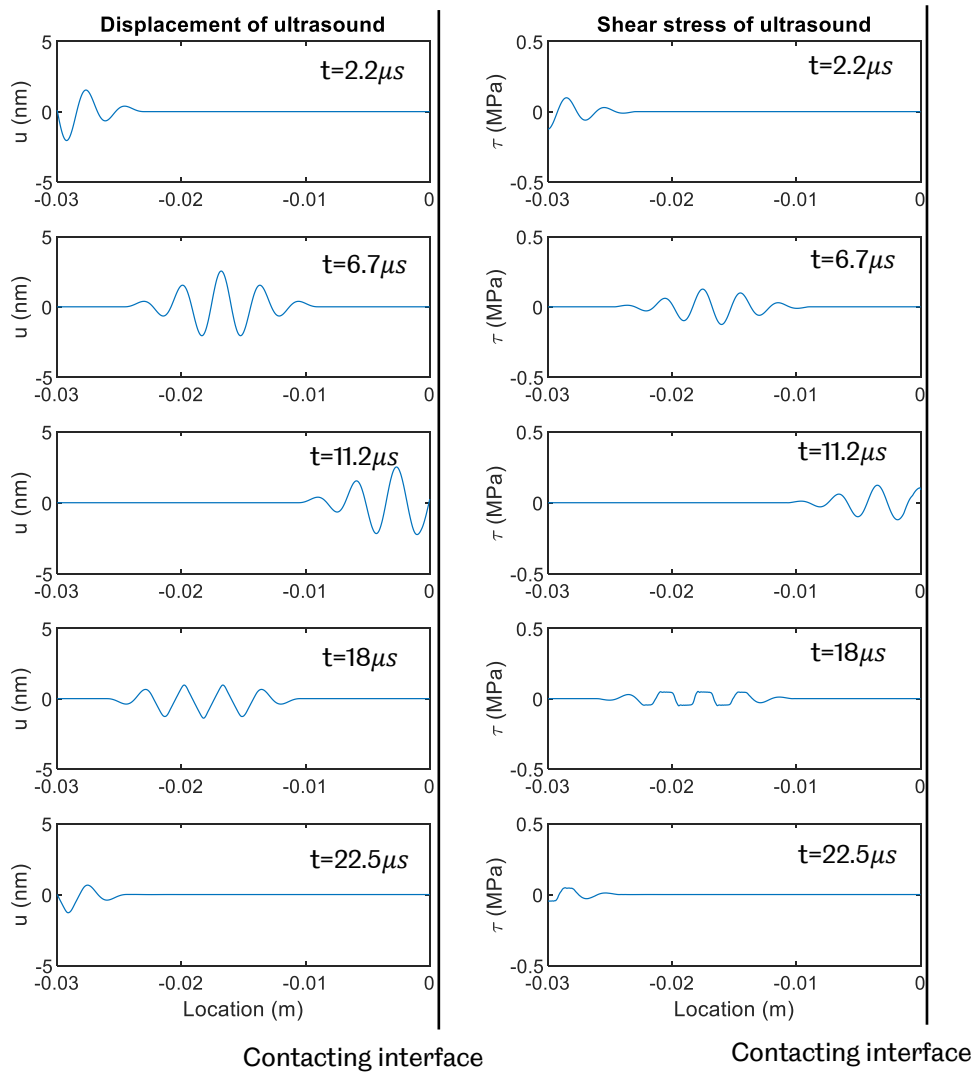


Figure 5.10 Example of numerical solution of ultrasonic wave striking a frictional interface.

At $x = -L$ the displacement and shear stress evolution are given in Figure 5.11. Compared with the incident wave, the reflected waveform is distorted after interaction with the interface when ‘stick-slip’ occurs. The frequency spectrum of the incident wave and ‘reflected’ wave subject to ‘stick-slip’ motion is shown in Figure 5.12. It is noted that when ‘stick-slip’ motion occurs, the distortion on the ‘reflected’ wave leads to the appearance of the harmonic frequency components. As mentioned in 5.1.3, only odd higher order harmonics, i.e. third, fifth, seventh order etc., appear in the frequency spectrum after FFT operations on a distorted waveform.

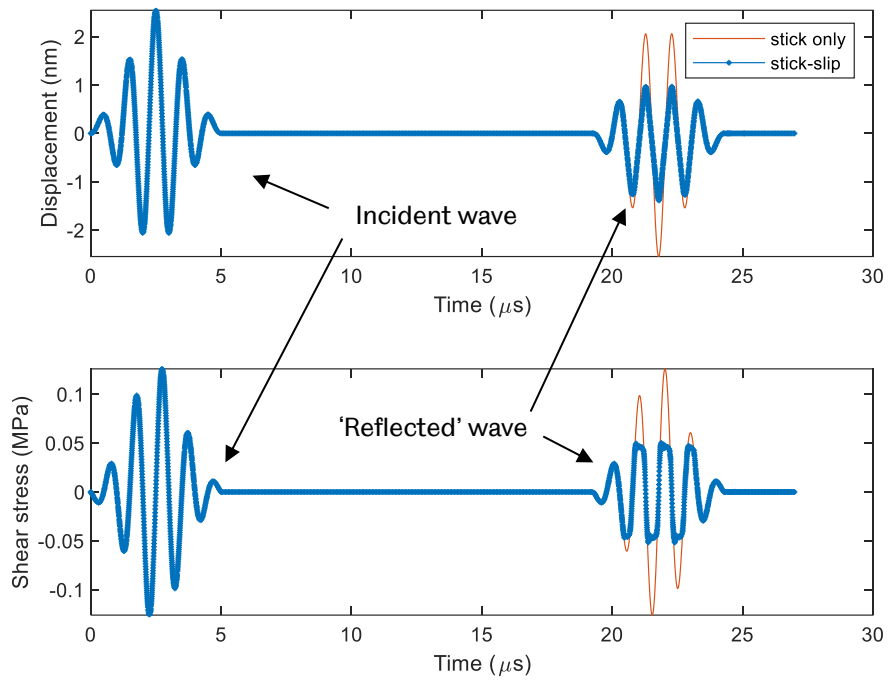


Figure 5.11 Time evolution of displacement and shear stress at $x = -L$.

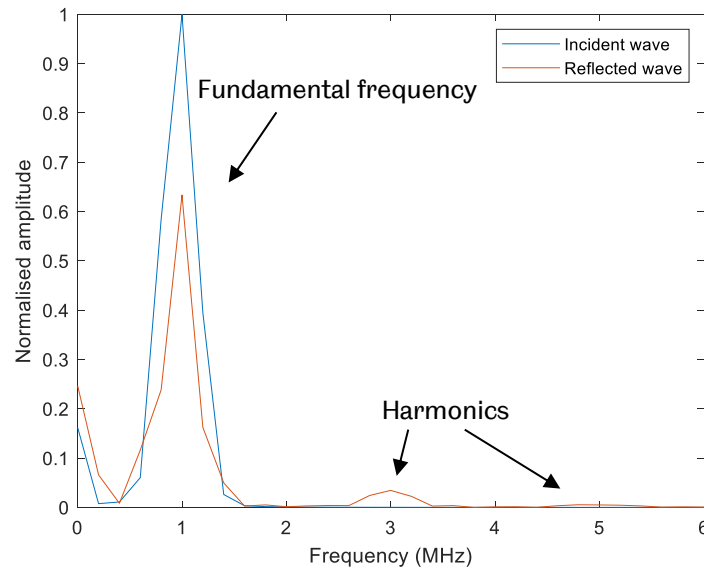


Figure 5.12 Frequency spectrum of displacement at $x = -L$.

Compared with 'clipped' feature in the analytical study (Figure 5.4 and Figure 5.5), The 'reflected' wave in Figure 5.11 is computed as the true transmitted wave due to the algorithm used in Equation (5.32) and (5.33). The true reflected wave can be computed using the Equation (5.13) and (5.14). The displacement and stress of the

incident wave, the computed 'reflected' wave i.e. the true transmitted wave and the computed reflected wave are illustrated in Figure 5.13. Compared with the displacement and stress waveform shown in Figure 5.4 and Figure 5.5. the computation solution ensures the waveforms are preserved. Despite this, the numerical solution still shows good agreement with the analytical solution, shown in a later section.

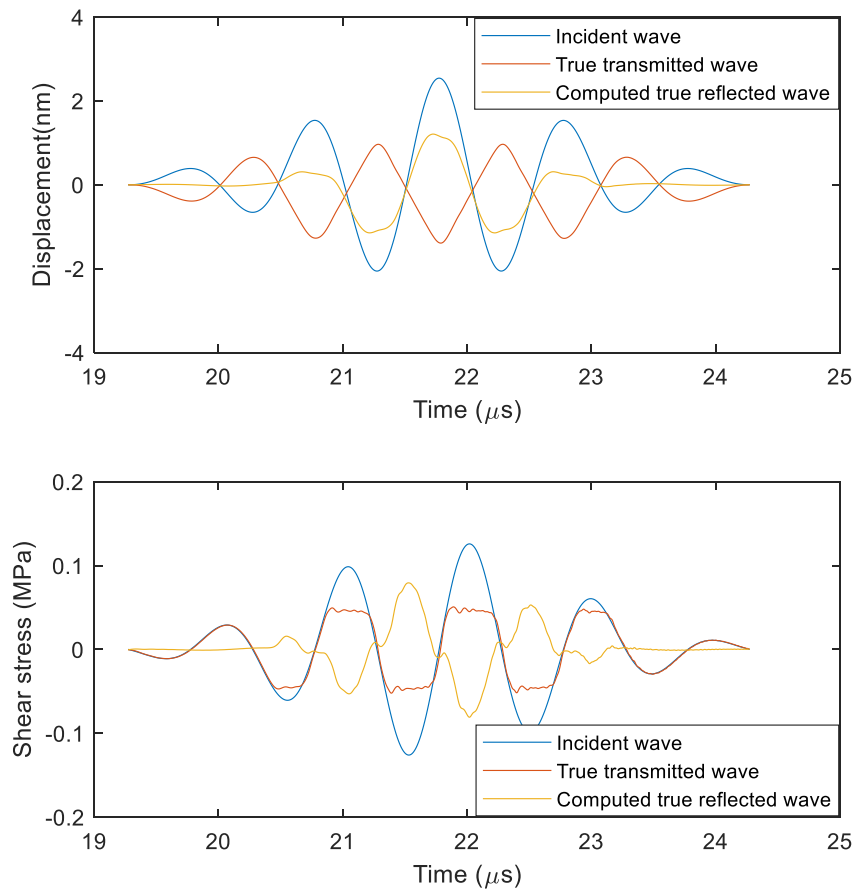


Figure 5.13 Incident wave, computed 'reflected' wave as the true transmitted wave and computed true reflected wave at $x = -L$.

5.2.3.2 Dimensionless Stress

To assess the dependence of the nonlinearity generation of a shear ultrasound at a frictional interface on the ultrasound and contact parameters (such as amplitude of incident wave, contact pressure and friction coefficient), a dimensionless parameter, ξ is introduced (Hirose, 1994; O'Neill et al., 2001; Meziane et al., 2011; Blanloeuil et al., 2014c). It is defined as the ratio of the applied tangential stress to

the maximum shear stress at the interface. Equivalently, it is the ratio of the frictional force to the incident shear stress by ultrasound (Equation (5.34)).

$$\xi = \frac{\mu\sigma}{GkA_0} \quad (5.34)$$

This dimensionless stress indicates the contact state when a shear polarised ultrasound striking at the frictional interface, as illustrated by Equation (5.35). $\xi = 0$ indicates a frictionless interface. When $\xi \geq 1$, ultrasonically induced shear stress is less than the applied tangential stress and consequently the contacting surfaces stick without any relative motion. Within the bounds of (0,1), shear stress exceeds the applied tangential stress and interfaces start to move relative to the other. The contacting interface switches between 'stick' and 'slip' mode depending on the frictional force and ultrasonically induced shear stress and the nonlinearity generation occur.

$$contact\ state = \begin{cases} frictionless\ contact, & \xi = 0 \\ stick - slip\ alternation, & 0 < \xi < 1 \\ stick, & \xi \geq 1 \end{cases} \quad (5.35)$$

5.2.3.3 Comparison with Analytical Solutions

Numerical solutions computed as shown in Figure 5.9 are compared with analytical solutions (Meziane et al., 2011). A 1MHz sinusoidal wave is computed as the incident wave. At the interface, various normal contact stresses are applied so that the 'stick-slip' alternation occurs conditionally. The dimensionless stress, ξ is computed using Equation (5.34). Amplitude of the fundamental frequency, the third and the fifth order harmonics are calculated from the frequency spectrum. The results are illustrated in Figure 5.14 and it is noted that numerical solutions agrees with the analytical solutions for the fundamental, the third and the fifth harmonics subject to various loading conditions, particularly when dimensionless parameter ξ approaches unity. It should be noted that there is still differences between the numerically computed results and the analytical solution. The discrepancy is mainly because continuous sinusoidal wave is used in the analytical model, which is free from envelope or window effect whereas in the numerical study, a burst of 5 cycles sinusoidal wave is employed. Despite this, the fundamental frequency amplitude shares the same trend as the analytical solution for the reflected wave subject to various loading conditions.

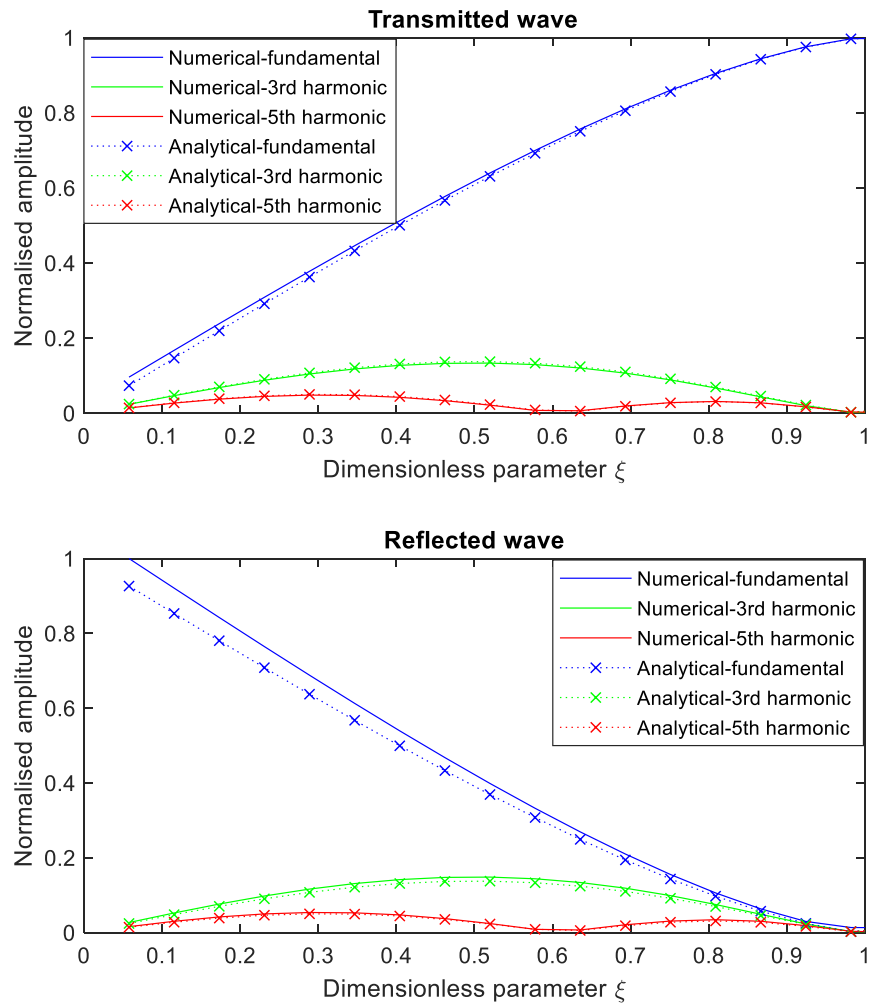


Figure 5.14 Numerical and analytical solutions comparison of ultrasound wave interaction with frictional interface, subject to varying contact stress.

The good agreement between the numerical and analytical solutions enables that various ultrasonic parameters and contact parameters can be employed to investigate the interaction of an ultrasound wave at a frictional interface and corresponding harmonic generation using this numerical tool.

5.2.3.4 Energy Conservation Energy Dissipation

The energy transported by ultrasound is considered here, especially for the presence of a frictional contact which is energy dissipative. The energy carried by

ultrasound at a certain point over a time interval is determined using the following equation as:

$$E_u = \int_{t_{end}}^{t_{start}} \tau(x, t) \dot{u}(x, t) dt. \quad (5.36)$$

At the interface, Equation (5.36) determines the energy dissipation at the interface.

The energy transported by the incident, reflected, transmitted waves at the left boundary $x = -L$ and the energy dissipation at the frictional interface $x = 0$ are computed and depicted in Figure 5.15. As defined in Section 5.2.3.2, dimensionless stress ξ greater than unity indicates contact sticks and no relative motion occurs at the frictional interface. Energy of the incident wave transfers into the transmitted wave and no energy is dissipated at the interface. When ‘stick-slip’ motion occurs at the interface when ultrasound strikes the interface, initial energy carried by the incident wave splits into reflected and transmitted waves whereas the remainder is dissipated at the frictional interface. Maximum energy dissipation occurs at $\xi \approx 0.4$, which agrees well with literature (O’Neill et al., 2001; Meziane et al., 2011). The total energy of reflected wave, transmitted wave and the dissipated portion due to friction equals to the total energy of the incident wave, which indicates the numerical model is energy conservative.

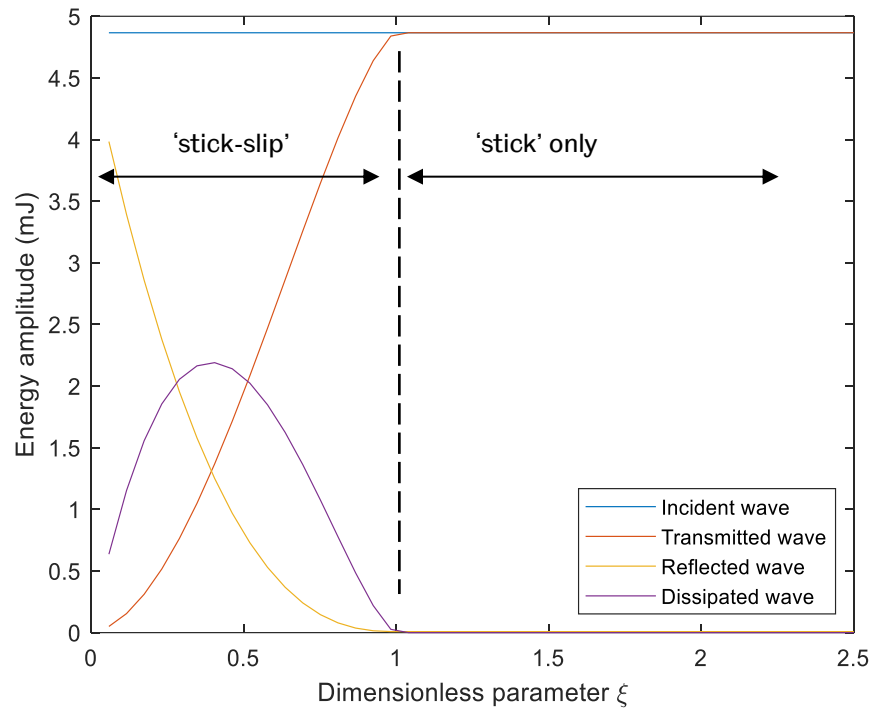


Figure 5.15 Energy transported by incident, transmitted and reflected wave and energy dissipated at the friction interface, subject to various contact stress.

5.2.3.5 Effect of Amplitude of Incident Ultrasound and Contact Stress

The numerical method is employed to investigate the effect of the incident amplitude of ultrasound and the normally applied contact stress on the nonlinearity generation when a shear ultrasound wave strikes at a frictional interface. Parameters employed are listed in Table 5.4. Dimensionless stress ξ is computed for each contact condition. The results are illustrated as follows.

Table 5.4 Parameters used in numerical study. Varying amplitude of incident ultrasound and contact stress.

Ultrasound parameters	
Working mode	5-cycle burst
Frequency f	1MHz
Incident ultrasound amplitude A_0	1.6, 2.4, 3.2, 4.8nm
Shear stress of ultrasound τ	0.08, 0.13, 0.17, 0.26MPa
Interface parameters	
Contact pressure σ	0.05 – 2MPa
Friction coefficient μ	0.3

Figure 5.16 illustrates the transmitted wave amplitude of fundamental frequency (1MHz) A_1 , the third harmonic (3MHz) A_3 and the ratio A_3/A_1 , subject to varying incident ultrasound amplitude and the normally applied contact stress. Regardless of the incident amplitude, large contact stress permits more ultrasound transmission through the interface, as shown for the fundamental frequency A_1 . When the transmitted wave reaches the maximum subject to even higher contact stress, the interface stick and all incident energy is transformed into transmitted waves. The third order harmonic amplitude A_3 , regardless of the incident amplitude, shows a 'rise-drop' dome shaped trend along the increasing contact stress. The rising trend is at the low normal stress region, where two surfaces are in contact and the ultrasound starts to interact with the frictional interface, initiating the 'stick-slip' motion. Increasing the normal contact stress makes the ultrasound wave further entangled with the interface and consequently, nonlinearity is significantly generated. Further compressing the interface, however, start to make the contacted surfaces 'bonded' or 'stuck'. The nonlinear interaction of the ultrasound with the interface by friction, i.e. 'stick-slip' alternation, is impeded and the harmonic generation begins to fall and leaves a peak. Any further increase in the contact stress, however, makes the contact fully 'stick' and no more nonlinear interaction is allowed. The ratio A_3/A_1 , then shows a combined result, increasing and decreasing with the applied normal stress.

For the incident wave, larger amplitudes appear to permit the fundamental frequency component to continue over a wider applied normal stress range. It does the same to the third harmonic component and the nonlinearity generation can occur over a broader stress range with the peak observed at a higher stress.

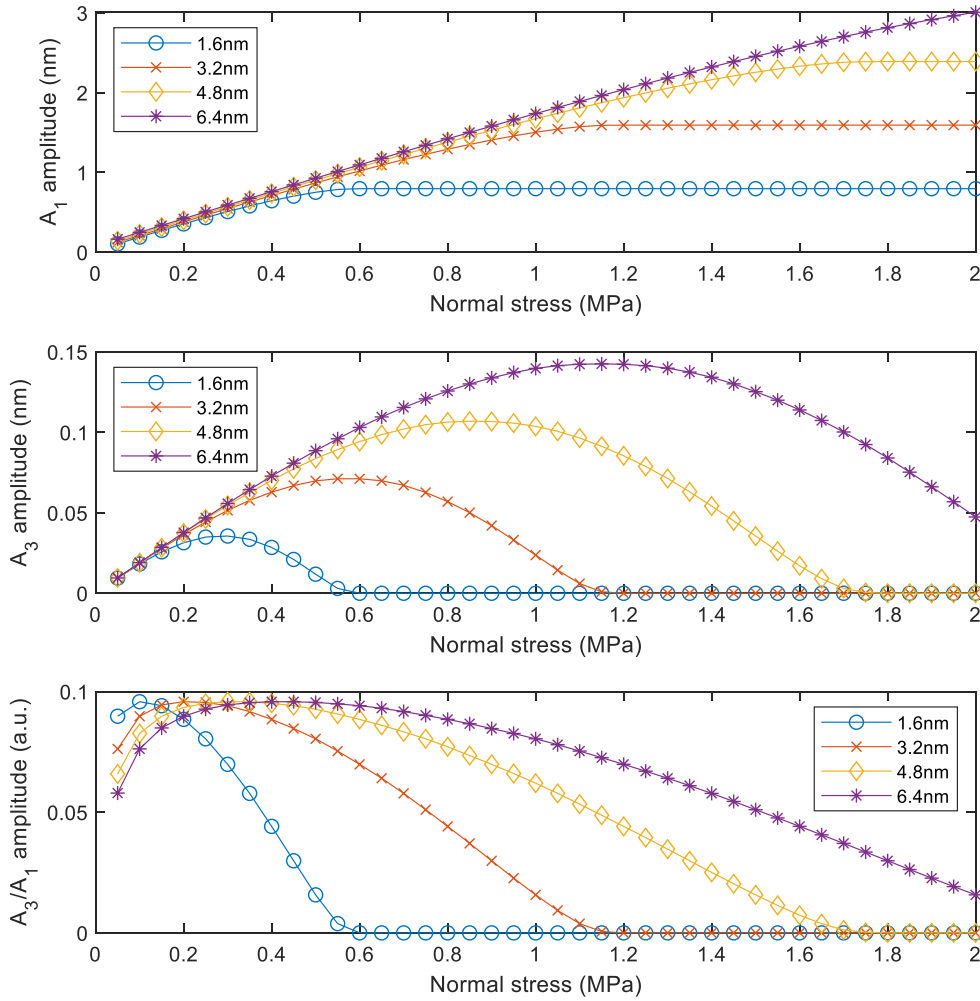


Figure 5.16 Fundamental and third harmonic amplitude of transmitted wave subject to varying amplitude of incident ultrasound and normally applied contact stress.

Figure 5.17 depicts the fundamental frequency, the third harmonic and their ratio of the reflected wave under various contact stresses and amplitudes of incident wave. In contrast to that of the transmitted wave, the reflected wave fundamental frequency amplitude falls along the increasing normal stress for the reflected wave as the higher contact stress allows more wave transmission and less reflection. It is worth noting that the third harmonic amplitude A_3 are identical to that of the transmitted wave in Figure 5.16, which demonstrates the nonlinearity generation occurs in both reflected and transmitted wave equally. Under the combined effects, the ratio A_3/A_1 shows a 'rise-drop' shape as well.

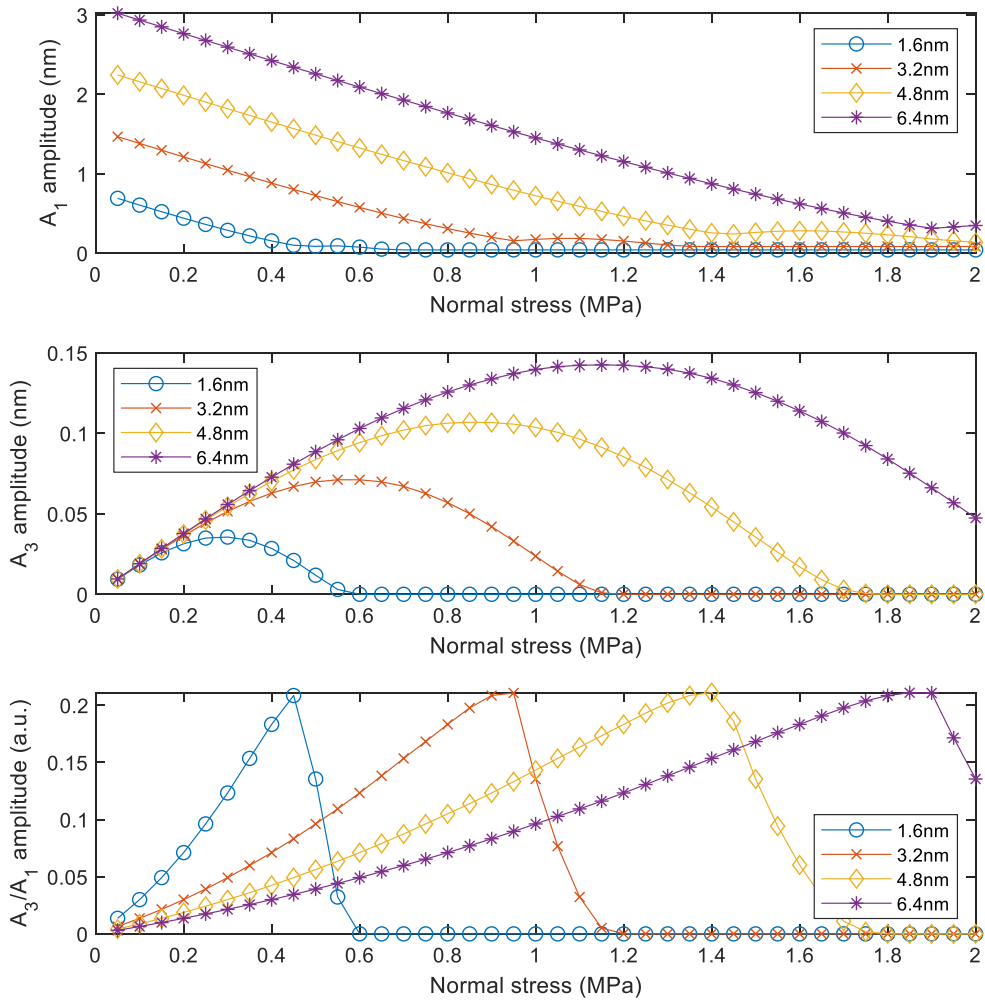


Figure 5.17 Fundamental and third harmonic amplitude of reflected wave subject to varying amplitude of incident ultrasound and normally applied contact stress.

The fundamental frequency, the third harmonic and their ratio of both transmitted and reflected waves are replotted with respect to the dimensionless stress ξ , as shown in Figure 5.18. Any ξ value less than unity indicates a 'stick-slip' region and nonlinearity can be generated. It is noted that regardless of the incident amplitude, the peak in the third harmonic A_3 occurs at $\xi = 0.5$. The ratio A_3/A_1 , similarly show a unique peak for both transmitted and reflected waves in regardless of the amplitude of incident wave. Any ξ value greater than unity, contact sticks and no harmonic generation is initiated.

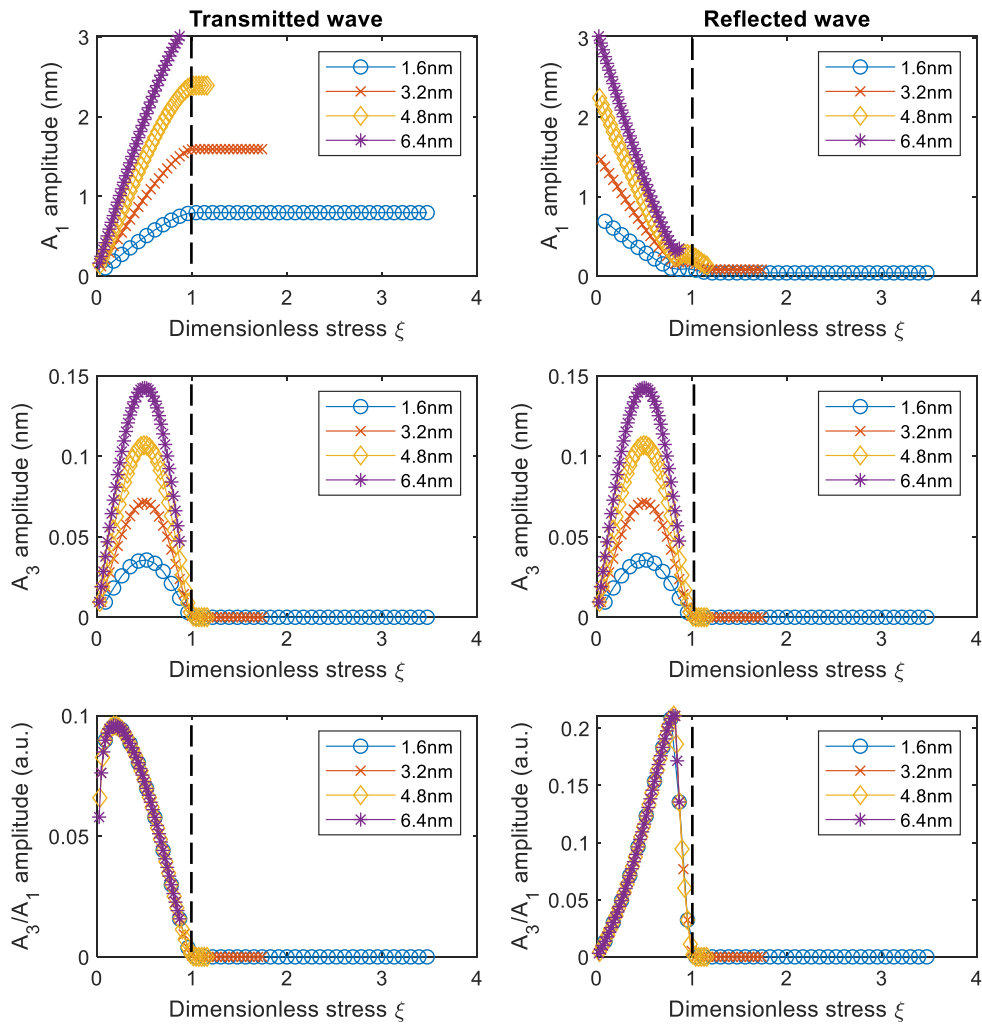


Figure 5.18 Fundamental and third harmonic amplitude of both transmitted and reflected waves vs dimensionless stress ξ .

5.2.3.6 Effect of Friction Coefficient

The effect of friction coefficient is investigated computationally using the numerical method. Various static friction coefficients are defined at the interface and other parameters employed are listed in Table 5.5. Dimensionless stress ξ is computed for each contact conditions. The results are illustrated as follows.

Table 5.5 Parameters used in numerical study. Varying static coefficient of friction.

Ultrasound parameters	
Working mode	5-cycle burst
Frequency f	1MHz
Incident ultrasound amplitude A_0	3.2nm
Shear stress of ultrasound τ	0.17MPa
Interface parameters	
Contact pressure σ	0.04 – 1.6MPa
Friction coefficient μ	0.2, 0.3, 0.4, 0.5

For both reflected and transmitted waves, the fundamental frequency, the third harmonic and their ratio share a similar pattern in Figure 5.16 and Figure 5.17, respectively, as illustrated in Figure 5.19. It is noticed that increasing the static friction coefficient makes the dome-shape harmonic generation occur over a narrower stress range. At the interface with a lower static friction coefficient, the threshold for the 'stick-slip' switch, i.e. the friction force or the applied tangential stress, $\mu\sigma_o$ at the contact is less than the ultrasound induced shear stress τ , given an unchanged amplitude of incident wave. Under a higher contact stress, the tangential force is still less than the shear stress, so the 'stick-slip' occurs. At the interface with a larger static friction coefficient, the allowance between the tangential force and the shear stress is reduced and then only a narrower range of contact stress permit the relative motion between contact surfaces. For the larger static friction coefficient, 'stick-slip' occurs only at lower stress region compared to a higher stress range for a lower static friction coefficient. The nonlinearity generation therefore reaches a maximum at a lower contact stress for the larger friction coefficient and peaks at higher stress for a low friction coefficient.

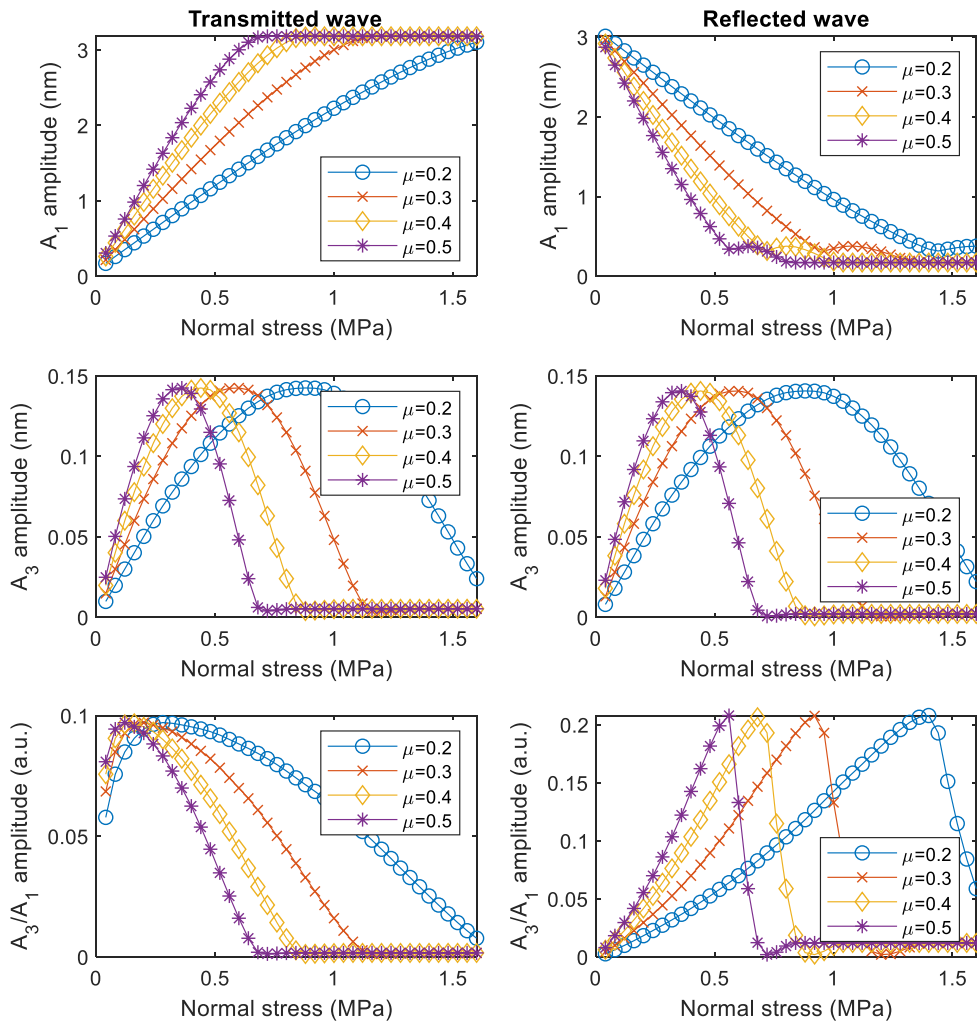


Figure 5.19 Fundamental and third harmonic amplitude of both transmitted and reflected waves subject to varying static friction coefficient.

When the dimensionless stress is used, as shown in Figure 5.20, the fundamental frequency, the third harmonic and the ratio show identical trend for varying static friction coefficient. This is mainly because that the effect of friction coefficient counteracts that of the contact stress applied. It is demonstrated that the harmonic generation peaks at $\xi = 0.5$ for the third harmonic A_3 .

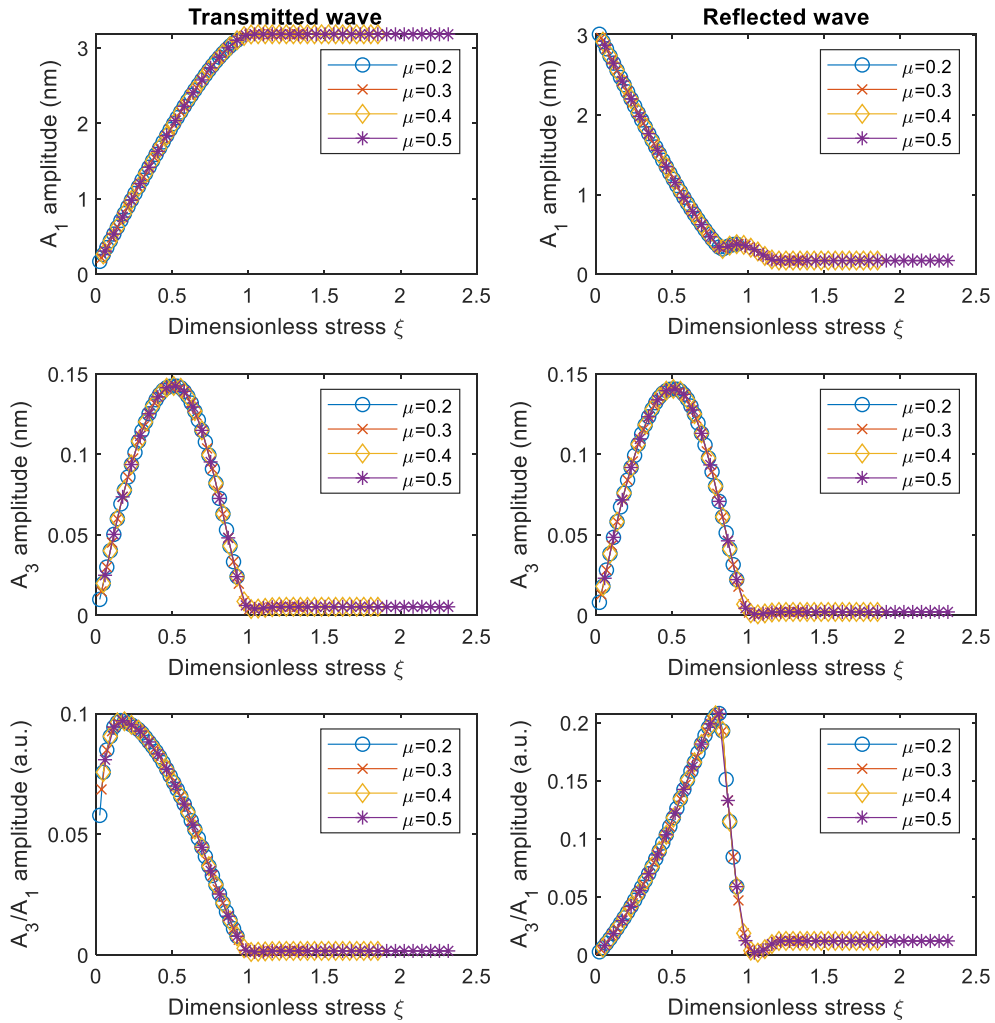


Figure 5.20 Fundamental and third harmonic amplitude of both transmitted and reflected waves vs dimensionless stress ξ , subject to varying static friction coefficient.

The effect of the dynamic friction coefficient μ_k is also investigated computationally using the numerical method. When the dynamic friction coefficient is considered, it replaces the static friction coefficient μ previously employed in Equation (5.24). Various dynamic friction coefficients are defined at the interface and other parameters employed are listed in Table 5.6. Dimensionless stress ξ is computed for each contact conditions. The results are illustrated as follows.

Table 5.6 Parameters used in numerical study. Varying dynamic friction coefficient.

Ultrasound parameters	
Working mode	5-cycle burst
Frequency f	1MHz
Incident ultrasound amplitude A_0	3.2nm
Shear stress of ultrasound τ	0.17MPa
Interface parameters	
Contact pressure σ	0.04 – 1.6MPa
Static friction coefficient μ	0.4
dynamic friction coefficient μ_k	0.4, 0.37, 0.34, 0.31

For both reflected and transmitted wave, the fundamental frequency, the third harmonic and their ratio show the trend, as depicted in Figure 5.21. Given the same static friction coefficient at the interface, varying the dynamic friction coefficient does not affect the fundamental frequency, the third harmonic and their ratio significantly. At the interface, the static friction permits the same normally applied stress for the occurrence of ‘stick-slip’ motion and thus the harmonic generation. With varying dynamic friction coefficient, the critical time for the interface switch from ‘slip’ to ‘stick’ is affected and thus the resultant stress and displacement waveforms are further distorted. It is noted that a larger difference between static and dynamic friction coefficient tends to skew the harmonic generation and peaks shifts towards high stresses.

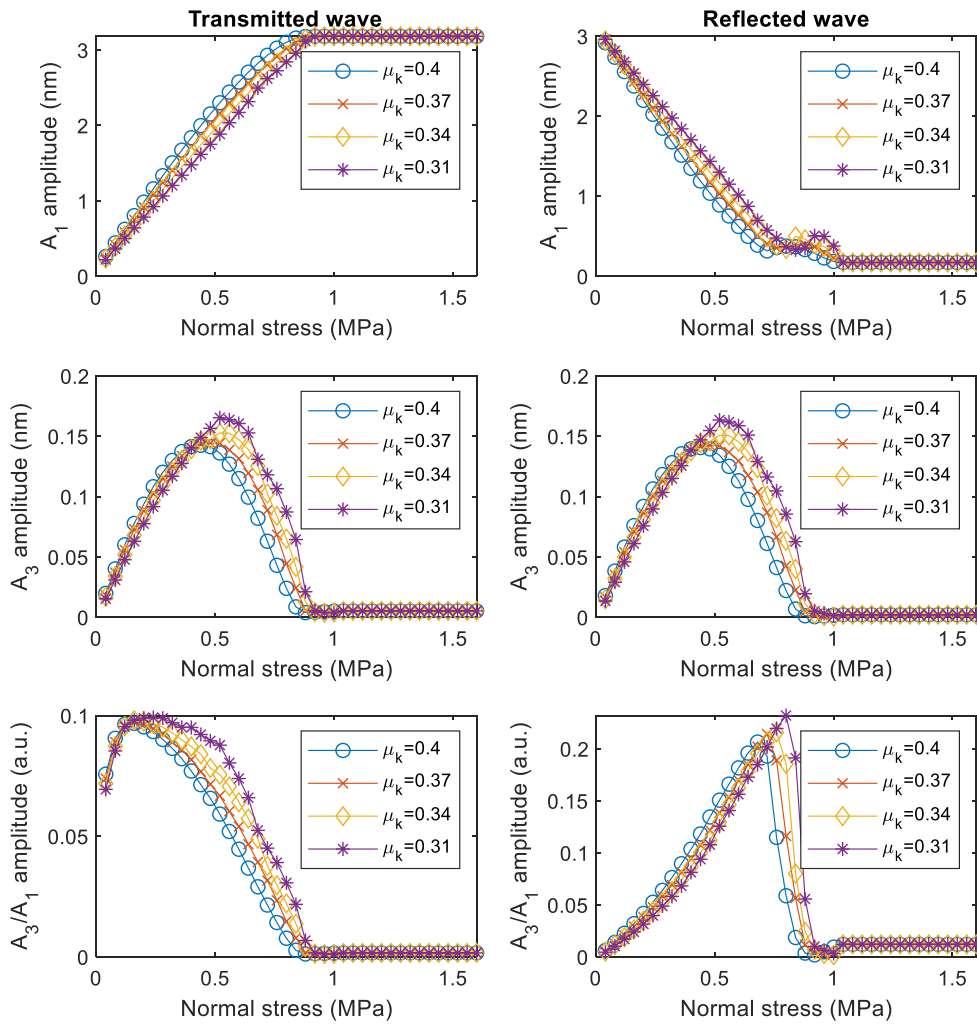


Figure 5.21 Fundamental and third harmonic amplitude of both transmitted and reflected waves subject to varying dynamic friction coefficient.

When the dimensionless stress is employed in Figure 5.22, fundamental frequency, the third harmonic and their ratio show an identical trend as in Figure 5.21. The effect of varying dynamic friction coefficient is still discernible. The nonlinearity generation peaks from $\xi = 0.5$ and shift to a high value when the dynamic friction coefficient decreases.

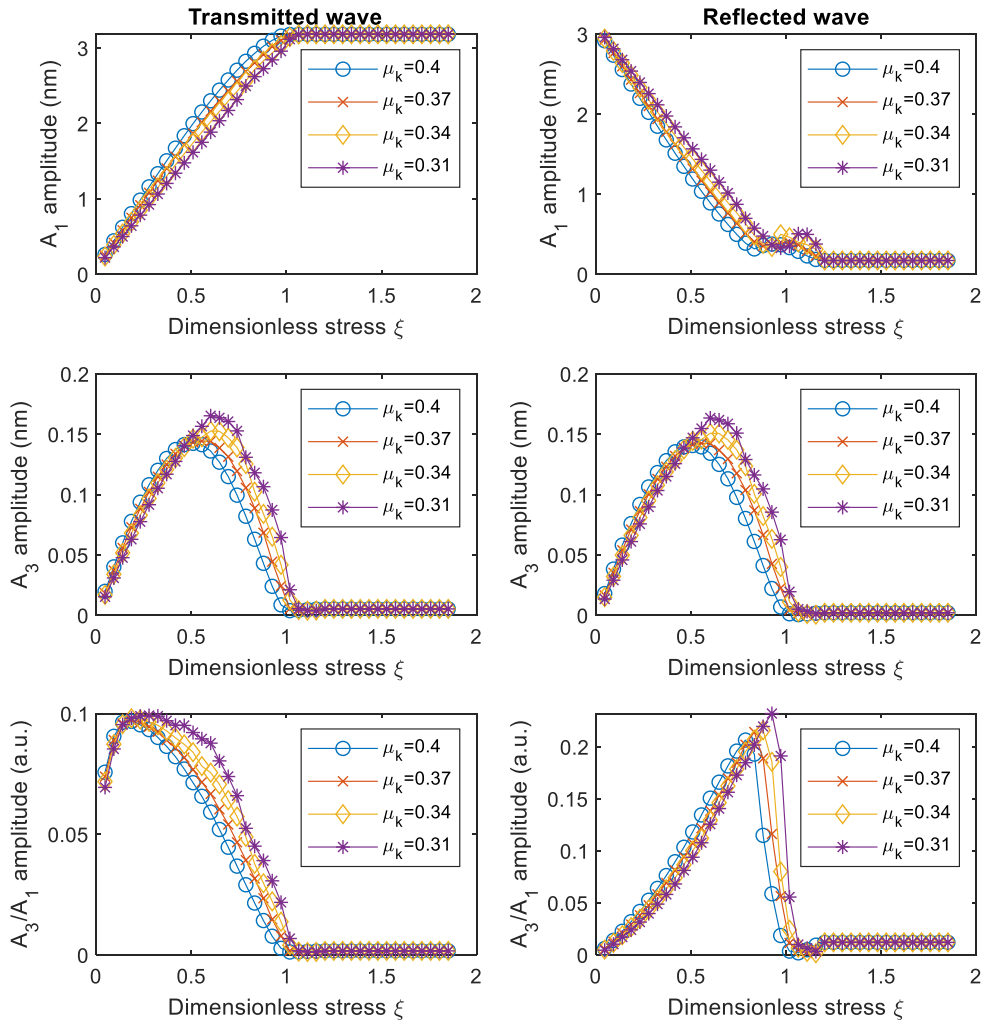


Figure 5.22 Fundamental and third harmonic amplitude of both transmitted and reflected waves vs dimensionless stress ξ , subject to varying dynamic friction coefficient.

5.3 Conclusions

The interaction of a shear polarised wave interacting with a frictional interface was investigated using both analytical and numerical methods. Nonlinearity generation occurs at the interface when a shear ultrasound wave strikes the interface and forces 'stick-slip' motion take place. Such interaction imposes distortion on the reflected and transmitted ultrasound wave and results in the extra frequency components being generated. Compared to the previous work using numerical

models, in this research work the numerical computation was extended to harmonics generation of the distorted reflected wave, which is particularly linked with the following experimental pitch-catch reflection configuration.

The effects of the normally applied contact stress, the amplitude of incident shear wave and friction coefficient at the interface were investigated numerically and are summarised as follows.

- Nonlinearity generation is due to the 'stick-slip' motion at the interface.
- 'stick-slip' motion only occurs at a relatively low contact stress range. High contact stress can prevent the 'slip' motion and does not result in nonlinearity generation.
- Large incident amplitude of ultrasound broadens the contact stress range which allows 'stick-slip' to take place.
- Large static friction coefficient reduces the contact stress range where 'stick-slip' occurs.
- Regardless of ultrasound incident amplitude and the static friction coefficient, harmonic generation is maximised when the dimensionless stress $\xi = 0.5$.
- A dynamic friction coefficient different from the static friction coefficient can skew the peak location of harmonic generation.

Both analytical and numerical models employed in this section are simplified. However, it still provides an insight into the physical phenomenon of the interaction of a shear polarised ultrasound at a frictional interface. The results from the numerical study can be used as guidance in the experimental work for detecting nonlinearity generation in later sections.

6 EXPERIMENTAL CONFIGURATION FOR MEASURING ULTRASONIC NONLINEARITY AT ROUGH CONTACTS

In this chapter, the nonlinearity generation due to shear polarised ultrasound interacting with a rough contact interface is experimentally investigated, following the analytical and numerical work in the previous chapter. The test configurations are shown in detail, including measurement technique and signal processing method. Experimental variables which could influence the measurement of harmonic generation are considered. Optical measurement of the shear wave amplitude is also carried out as test preparation.

6.1 Introduction

Researches on nonlinear ultrasound at a contact interface have mainly focused on longitudinal incidence and its harmonics (Buck et al., 1978; Barnard et al., 1997; Biwa, et al., 2006; Yan et al., 2009; Blanloeuil et al., 2017). Studies on harmonic generation of shear ultrasound are mainly at analytical and numerical analysis stages (O'Neill et al., 2001; Meziane et al., 2011; Delrue et al., 2018) and experimental investigation using shear wave, however, is inadequate (Solodov, 1998; Blanloeuil et al., 2014c). In this

experimental work, the appropriate method to measure the nonlinearity generation due to an ultrasonic wave interacting with rough contact surfaces is investigated.

6.2 Experimental Configurations

The experimental approach used in the previous research can be adopted. Details of the experimental configuration are given as follows.

6.2.1 High Frequency Nonlinear Ultrasonic Technique

It is worth pointing out that when detecting or measuring the nonlinearity generation from a contact interface experimentally, the frequency of both ultrasonic transmitter and receiver need to be carefully selected based on the featured frequency. Nonlinearity generation, or more precisely referred in this work, the harmonic generation, means that high order frequency components are considered. In terms of measuring harmonic generation of a longitudinal wave, the second order harmonic is mainly the target (Barnard et al., 1997; Biwa et al., 2006; Yan et al., 2009; Yuan et al., 2015; Jiao et al., 2014; Liu et al., 2011). In cases of a shear wave, the third order harmonic is the primary target frequency (Solodov, 1998; Blanloeuil et al., 2014c).

A specific experimental method for detecting the harmonic generation applied in these researches is adopted here. This method utilises a frequency ultrasonic transmitter, primarily working at the fundamental frequency, and a wideband ultrasonic transducer as the receiver. The bandwidth of the receiver should be wide enough to cover both the fundamental frequency and the third order harmonic components. This technique is known as high frequency nonlinear ultrasonic technique. This is unlike the conventional ultrasonic measurement techniques where a single probe is employed for the pulse-echo configuration and two probes with the same frequency bandwidth for the pitch-catch method. A schematic diagram of the technique is given in Figure 6.1.

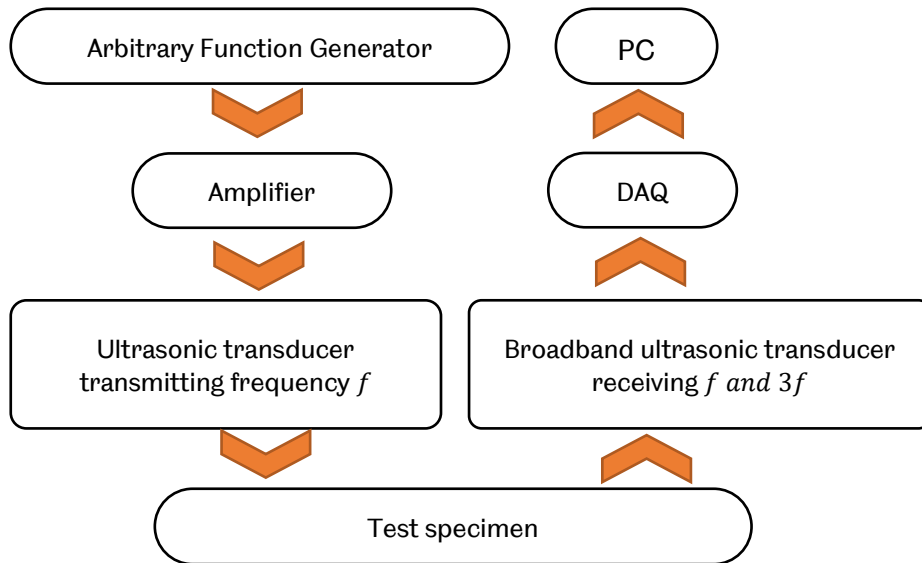


Figure 6.1 Schematic diagram of the high frequency nonlinearity ultrasonic technique applied in this work.

6.2.2 Ultrasonic Apparatus

The ultrasonic apparatus employed in this experiment work is described in detail separately in Chapter 4. The summary of key features of the main ultrasonic apparatus is listed in Table 6.1. A tone burst of a number of cycles of sinusoidal wave was excited and amplified using a RITEC gated amplifier to drive a 1MHz ultrasonic transducer V153 or V152. Returning signals were received using a 5MHz broadband transducer V155 and digitised using a PicoScope. A 1MHz ultrasonic transducer (V153 or V152, Olympus) was used as the transmitter and it was driven at its nominal frequency 1MHz. The harmonic of interest was the third order, i.e. 3MHz. Therefore, a broadband transducer (5MHz V155, Olympus) with the bandwidth (−6dB) from 3MHz to 6.79MHz was used as the receiver in the high frequency nonlinear ultrasonic technique.

Table 6.1 Summary of the ultrasonic apparatus applied in this experiment work.

Ultrasonic function generator: RITEC RAM 5000	
Working mode	N-cycle burst
Waveform	Sinusoidal
Frequency	1MHz
High power amplifier: RITEC RAM 5000	
Working mode	Gated amplifier
Power output	up to 5kW
Voltage output	140V to 1500V (peak-peak)
Duty cycles	0.3%
Burst width	Max. 60 cycles for 1MHz
Ultrasonic transmitter: Panametrics V153 (V152)	
Nominal frequency	1MHz (1MHz)
Bandwidth	1.04MHz (0.82MHz)
Ultrasonic receiver: Panametrics V155	
Nominal frequency	5MHz
Bandwidth	3.79MHz
Ultrasonic digitiser: PicoScope 5444B	
Sampling rate	200MHz
Vertical resolution	12 bits

6.2.3 Loading Equipment

In the experimental work, test specimens were placed in a loading frame, as depicted in Figure 6.2. A hydraulic cylinder was placed between the test specimen and the loading frame to generate a compressive normal load at the contact interface. The valve on the hydraulic cylinder was closed to ensure a constant load was applied. A load cell was placed on top of the upper test specimen to monitor the load during tests.

The load cell used in the research work, was calibrated using a pre-calibrated loading machine to ensure accuracy in the force measurement. The load cell measures the force applied to it and gives a voltage reading as output. The calibration data is given in Figure 6.3.

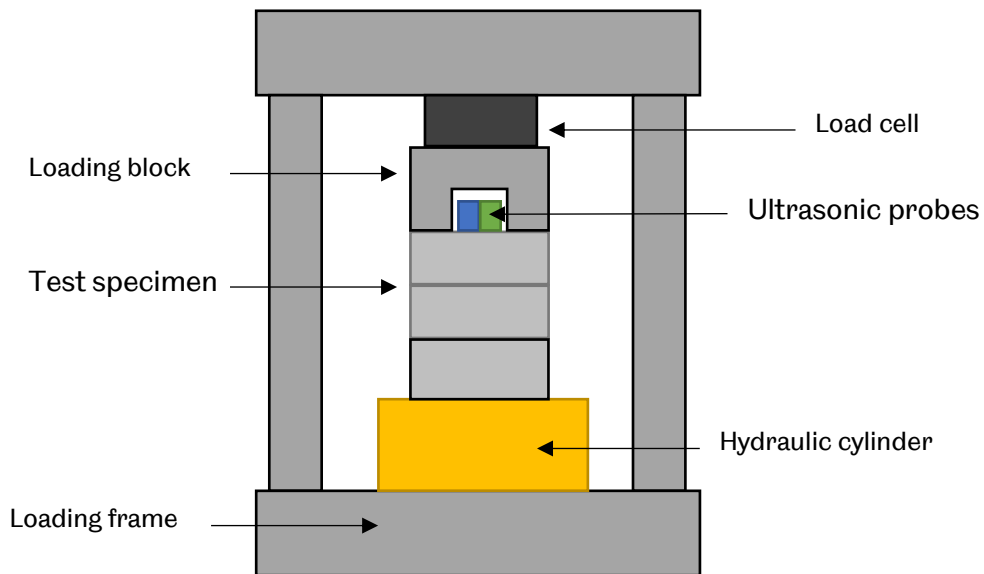


Figure 6.2 Schematic diagram of the loading configuration.

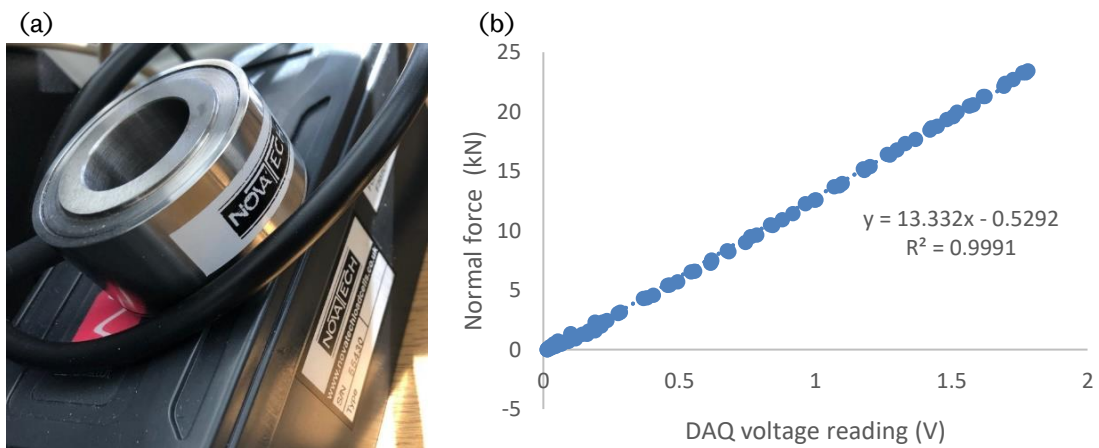


Figure 6.3 (a) NOVATECH loadcell and amplifier. (b) Loadcell calibration relationship.

6.2.4 Test Specimens

Aluminium alloy 6082 is a commonly used engineering material so it was used as the test material. The material was machined to several sets of cylinders with different dimensions, as shown in Figure 6.4. After the specimens were machined, the contact surfaces were polished on a grinding machine using polishing papers with various

grades. The surface roughness of contacting faces was measured using an optical profilometer (ALICONA).



Figure 6.4 Aluminium alloy test specimens with various dimensions.

Dimensions and surface roughness of test specimens are listed in Table 6.2. The surface roughness of test specimens used in nonlinear acoustic response from imperfect interfaces was less than $1\mu\text{m}$ (Pecorari, 2003; Pecorari and Poznić 2005; Biwa et al., 2006; Blanloeuil et al., 2014c). Therefore roughness of test specimens used in the following research work was measured from $0.3\mu\text{m}$ to $1\mu\text{m}$. Test specimens with different diameters were used to achieve various normal compressive stresses at the contacting interface in the following experimental work in Section 7. Various thicknesses of specimens were used in the experimental configuration investigations in Section 7.1.

Table 6.2 Aluminium alloy specimens dimension and surface roughness.

Aluminium alloy test specimen	Dimensions (mm) (diameter, thickness)	Surface roughness of selected area Rq (μm)
S1	74, 28.5	0.373
S2	74, 28.5	0.586
S3	74, 28.5	0.874
S4	74, 28.5	0.483
L1	74, 57	0.453
L2	74, 57	0.847
L3	74, 57	0.954
A11	50, 32	0.469
A12	50, 32	0.728
AL3	50, 32	0.530
A14	50, 32	0.620
H1	74, 82	N/A

6.3 Extra Experimental Considerations

To measure the nonlinearity generation experimentally, extra care must be paid as many experimental variables can affect the true measurement and also may introduce unwanted nonlinearity (Liu et al., 2011). Some factors influencing the detection of nonlinearity generation from the contact interface are investigated here.

6.3.1 Piezoelectric Element or Ultrasonic Probe

In the nonlinearity generation measurement using the high frequency nonlinear ultrasonic technique with the longitudinal waves (Buck et al., 1978; Yan, et al., 2009; Liu et al., 2011; Liu et al., 2012), the piezoelectric element was employed as the transmitter. As previously discussed, when a piezoelectric element is excited, not only the fundamental natural frequency ($1f$) but also the odd harmonics ($3f, 5f, \text{etc.}$) are excited and normally these harmonics are undesired in the actual measurement. This feature has little influence on the detection of harmonic

generation from a longitudinal wave as the nonlinearity generation of a longitudinal wave at an interface is an even order harmonic ($2f, 4f, etc.$). However, for the nonlinearity generation of a shear wave interacting at a contacting interface, the piezoelectric element introduced high order frequency components that imposed side effects on the measurement as the harmonic generation from the interaction of a shear wave and the interface is also an odd order ($3f, 5f, etc.$).

Responses of shear polarised piezoelectric elements are demonstrated in Figure 6.5 and Figure 6.6. Piezoelectric elements were bonded on a test specimen and the pulse-echo configuration was used where the piezoelectric element was working as a transmitter and a receiver alternatively. A short duration pulse was triggered to excite piezoelectric elements using a Film Measurement System (FMS, Tribosonics) (Howard, 2016) and the reflected signal was digitised and recorded using FMS as well. The first reflected signal was extracted and Fast Fourier Transform (FFT) was applied to yield the frequency response. In Figure 6.6, the nominal fundamental frequency as well as high order harmonics were excited regardless of the nominal natural frequency of the piezoelectric element. It is also noticed that the harmonic frequency amplitudes are comparable to that of the fundamental frequency component for some shear polarised piezoelectric elements.

Several reasons may cause this high order harmonic generation from the piezoelectric element. The dimension of a shear polarised piezoelectric element plays a role. The thickness of the piezo element should be much less than the length or width so that the natural resonant frequency of the shear element is dominant. It is critical for the low-frequency elements because to have dominant fundamental frequency, the length or width of the shear element is large. The shear element with nominal frequency of 3MHz and 5MHz in Figure 6.6 (c) and (d) are in an appropriate dimension and the fundamental frequency shows a dominant amplitude. The dominant harmonic amplitude from 1MHz and 2MHz piezo elements are due to their inappropriate dimensions. Damping of the piezoelectric element and the pulsing method also affect the harmonic generation from the element. A heavy damped piezoelectric element with an N-cycle burst excitation waveform can suppress the high order harmonics.

Although undamped piezoelectric element gives larger amplitude, as mentioned in Section 4.1.3, using the shear polarised piezoelectric element in the high frequency nonlinear ultrasonic technique is practically challenging. Despite that ultrasonic probes still produce undesired harmonics when driven by high power, which is discussed in the following Section 6.3.2, the ultrasonic probes help in reducing the piezoelectric element introduced harmonics and it is widely adopted in the

measurement of nonlinearity generation from both longitudinal and shear waves (Biwa et al., 2006; Blanloeuil et al., 2014c; Jiao et al., 2014; Yuan et al., 2015). Therefore, normal incidence shear probes were employed in the research.

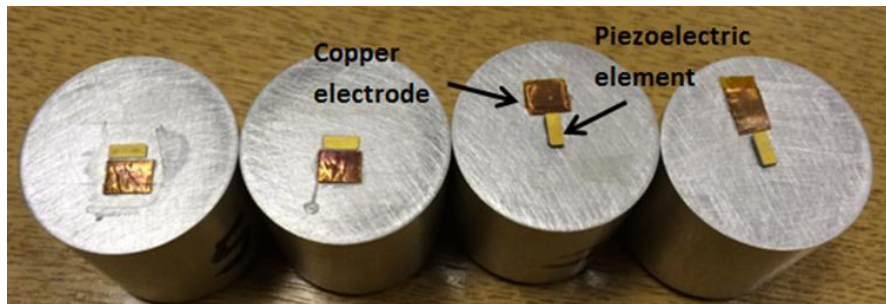


Figure 6.5 Aluminium alloy test specimen with shear polarised piezoelectric element

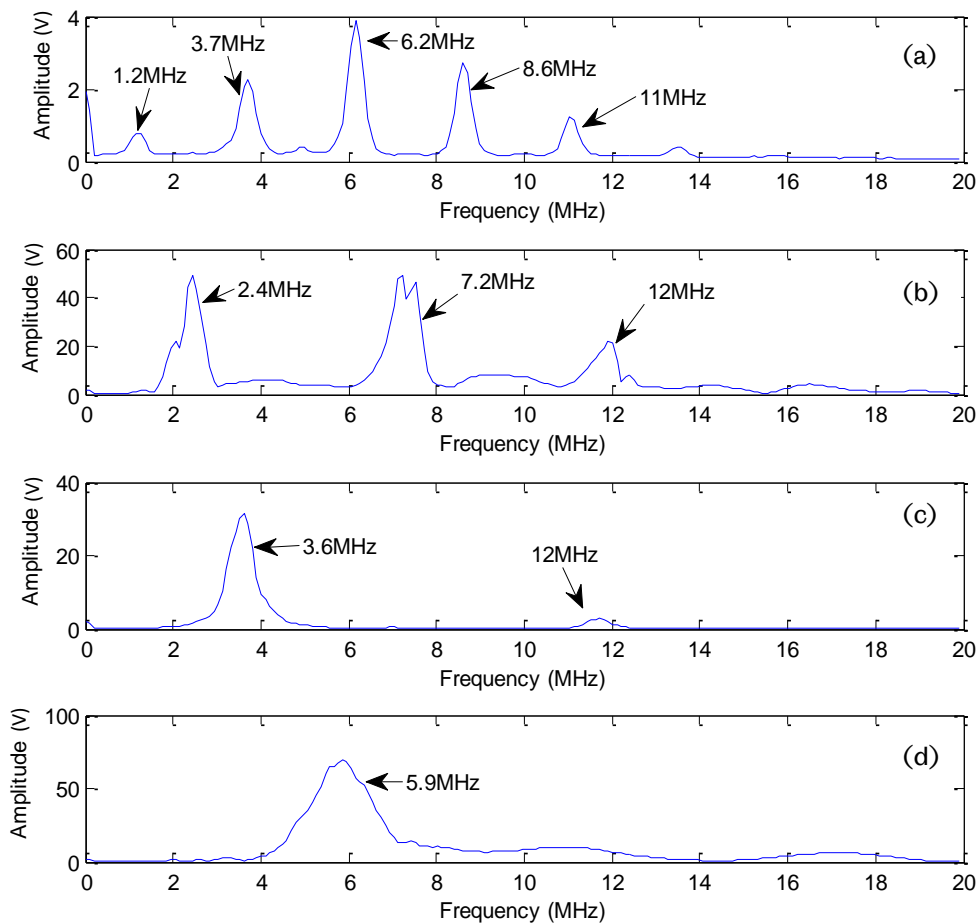


Figure 6.6 Frequency response of shear polarised piezoelectric element subject: (a) nominal 1MHz; (b) nominal 2MHz; (c) nominal 3MHz and (d) nominal 5MHz. Elements were excited with short-duration pulse and the first reflected signal were selected for FFT operation.

6.3.2 Amplifier and Amplification Level

Regardless of using longitudinal wave or shear wave as the incident wave, a high-power amplifier is critical to the nonlinearity generation measurement. The amplitude from the ultrasonic probe needs to be considerable so that either the normal stress induced from a longitudinal wave or the shear stress induced by a shear ultrasound is sufficiently large enough to open the closed interface or activate the 'slip-stick' motion of the interface. This normally requires high voltage to excite either the piezoelectric element or ultrasonic probe.

When high voltage is applied, the undesired harmonics are also generated and it is even worse when an improperly damped piezoelectric element is excited, providing that the element are prone to these odd harmonics generation. The voltage across a piezoelectric element is also limited. For a 1MHz shear polarised element, the safe excitation voltage is approximately smaller than 100V, which is not practically sufficient in some tests.

For an ultrasonic probe, the excitation voltage can be potentially around 600V (Olympus NDT Inc, 2006). Such excitation voltage range is more practically feasible to activate the contact interface 'slip-stick' motion. When subject to such high power, the probe also shows undesired high order frequency components. With careful configuration, the harmonic amplitudes can be maintained at a minimum level.

Example of the harmonic generation subject to various amplification level is shown in Figure 6.7. A 1MHz ultrasonic probe (V153, Olympus) and a 5MHz transducer (V155, Olympus) was mounted on a test specimen S1 and were used as the transmitter and receiver, respectively. A tone burst of 15-cycle sinusoidal wave was excited to drive the transmitter. Various excitation voltages were applied. The first received signal was selected for FFT operation.

In Figure 6.7 (a), when a low excitation voltage, i.e. 4V(peak-peak) is applied to a normal incidence shear wave probe, the third order harmonic is excited as well, but the amplitude is relatively low compared to its neighbouring frequencies. When a high excitation voltage is applied using an amplifier, i.e. 280V(peak-peak), both fundamental and the third order harmonic are amplified. Compared with its adjacent frequencies, the third order harmonic are discernible. The ratio of the third order harmonic to its fundamental frequency under varying excitation voltage is illustrated in Figure 6.7 (b). The third order harmonic generation is generally increasing with rising excitation voltage. The amplitude of A_3/A_1 is still reasonably low (less than 0.15%, i.e. -56dB) even at the high excitation voltage. Such third order

harmonics are not easily suppressed practically so extra care should be paid when considering the harmonic generation from the contacting interface.

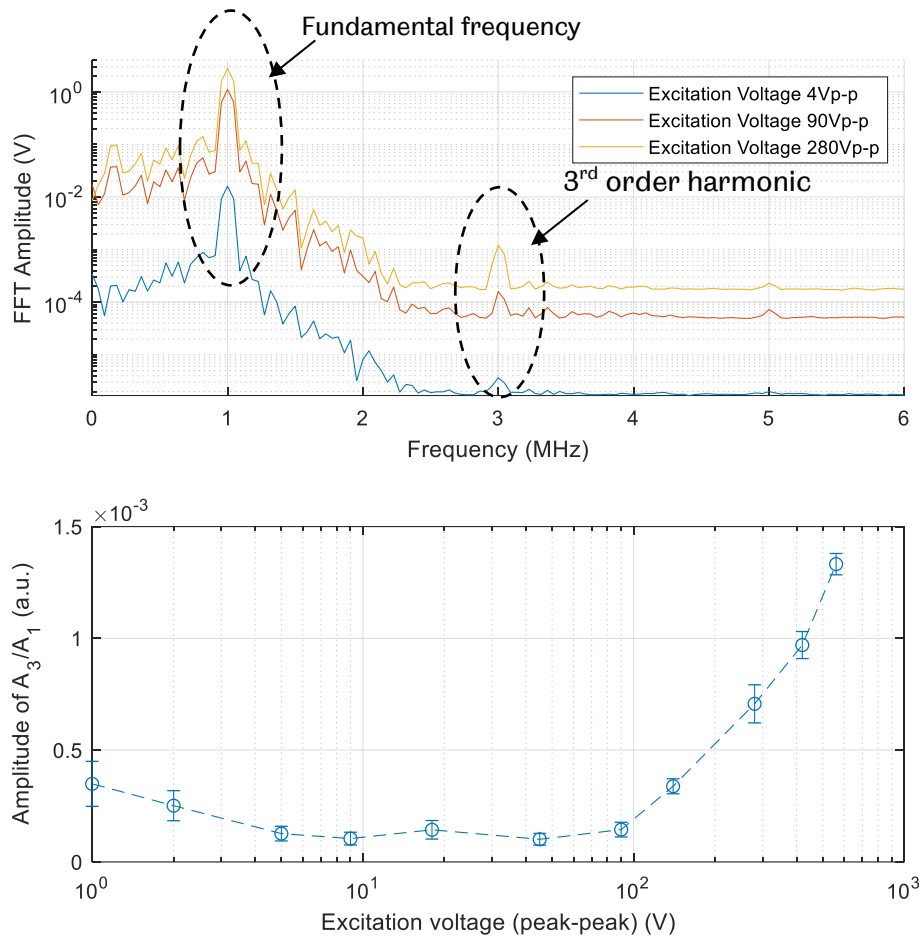


Figure 6.7 (a) Frequency response of a normal incidence shear wave transducer subject to $4V_{p-p}$, $90V_{p-p}$ and $280V_{p-p}$ excitations. (b) 3^{rd} order harmonic relative to fundamental frequency amplitude subject to various excitation voltages (100 repetitions).

6.3.3 Shear Wave Couplant

The measurement of nonlinearity generation at a rough interface uses the normal incidence shear wave probes as the transmitter and receiver. Care is required when mounting the probe on test specimens. Unlike a shear polarised piezoelectric element being bonded on a test specimen or angle beam transducer using the mode conversion method and coupled with test specimens using a general gel, high viscosity shear wave couplant must be applied between the probe and the test specimen.

Several points were noticed practically when applying the shear couplant in tests. The amount of shear couplant applied was just sufficient to cover the contacting face of the transducer and any excessive couplant applied potentially reduced the amplitude of transmitted through the coupling layer as shear wave also attenuates in the couplant. After the couplant was used between the contact probe and test specimen, a gentle force was applied to the specimen for a decent spell to allow a minimum coupling layer to form. During this period, tests were not taken as the optimal coupling layer was in formation and the shear wave amplitude was gradually increasing. Pulse-echo method was employed to check the shear wave amplitude intermittently to ensure a stabilised amplitude reading was reached.

The high viscosity shear wave couplant plays a vital role in harmonic generation detection. A normal incidence shear wave probe mounted with shear wave couplant enables the maximised shear wave component with the minimised longitudinal component in the measurement. A shear ultrasound probe was mounted using a general ultrasound gel and a shear wave couplant (SWC-2, Olympus), respectively. A tone burst of 10-cycle sinusoidal wave was excited at 20V. Time domain responses are shown in Figure 6.8. An improperly mounted shear wave transducer cannot give a clear reflection signal. The shear component only shows a comparable amplitude to the longitudinal component Figure 6.8 (a). While the reflected signals are clearly observed from a properly mounted probe, in Figure 6.8 (b). The shear component is at least 30 times larger than the longitudinal component.

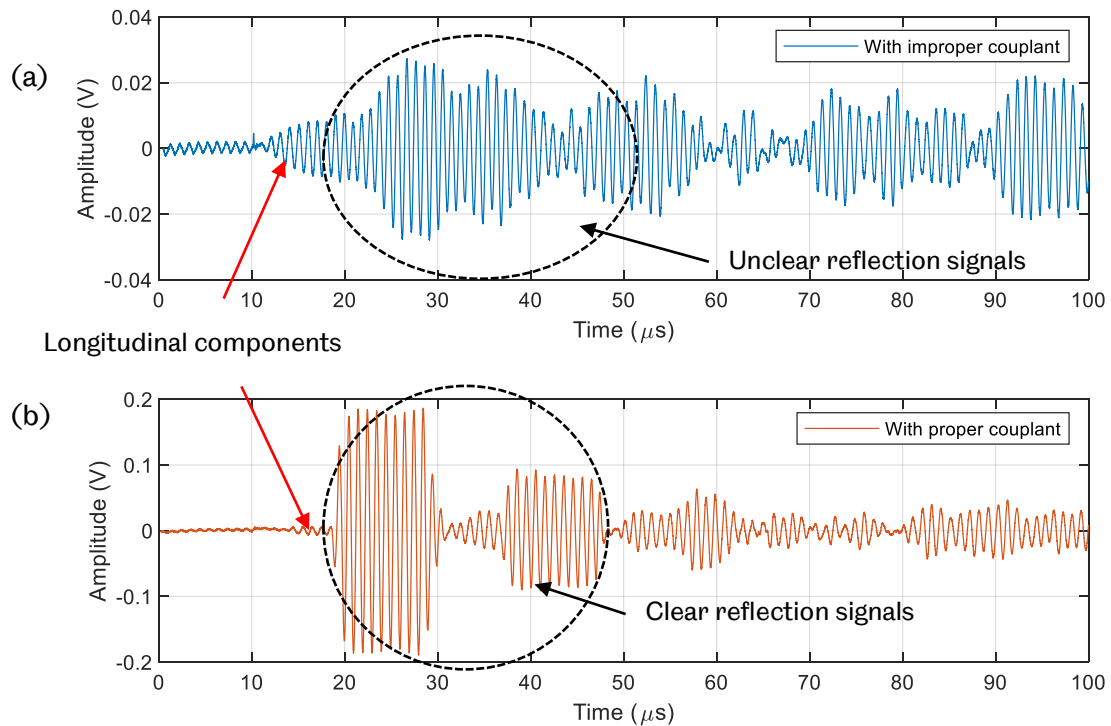


Figure 6.8 Comparison of couplant effect in shear wave signal measurement. Shear transducer mounted (a) with improperly couplant and (b) with proper couplant, subject to $20V_{p-p}$ excitation of a 10-cycle tone burst (100 repetitions).

6.3.4 Transducer Alignment

When the high frequency nonlinear ultrasonic technique is carried out using two ultrasonic transducers, locations of the probes affect the nonlinearity measurement in the harmonic generation detection using longitudinal probes (Liu et al., 2011). It holds true for the harmonic generation detection using shear waves. Shear wave polarisation being perpendicular to its propagation direction, the alignment of two normal incidence shear transducers must be taken into considerations.

As depicted in Figure 6.9 the alignment of two normal incidence shear wave ultrasonic probes is considered. Two probes (V153 and V155, 12.7mm diameter, Olympus) were placed on the top and bottom of a test specimen and a tone burst of sine wave was excited at 90V. The polarisation direction was changed from aligned condition (0° difference) to 90° difference, clockwise and anti-clockwise. When both probes were aligned with 0° difference, locations were varied in two directions, one along the polarisation direction (i.e. 'vertical offset') and the other normal to the polarisation direction (i.e. 'horizontal offset'). Pitch-catch configuration, where

ultrasound signal was transmitted from one probe and received from a separate receiver, as illustrated in Figure 6.9, was employed.

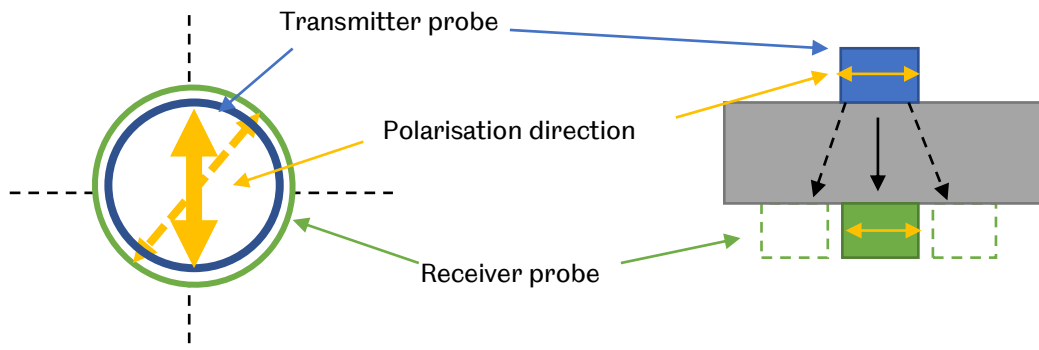


Figure 6.9 Schematic diagram of alignment of normal incidence shear wave ultrasonic sensors.

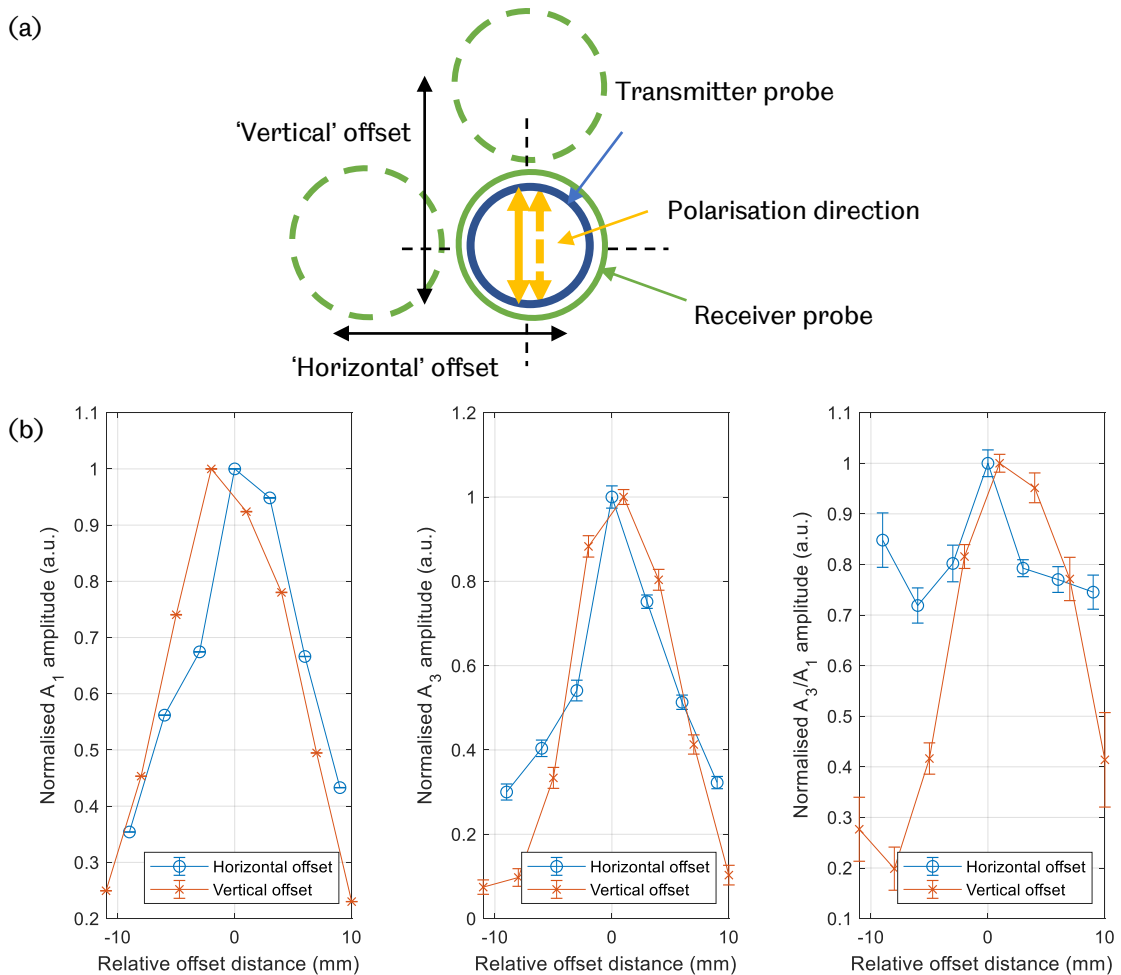


Figure 6.10 (a) Schematic diagram of locations of normal incidence shear wave ultrasonic sensors. (b) Measurement of fundamental A_1 , third order harmonic frequency A_3 and the ratio A_3/A_1 (50 repetitions).

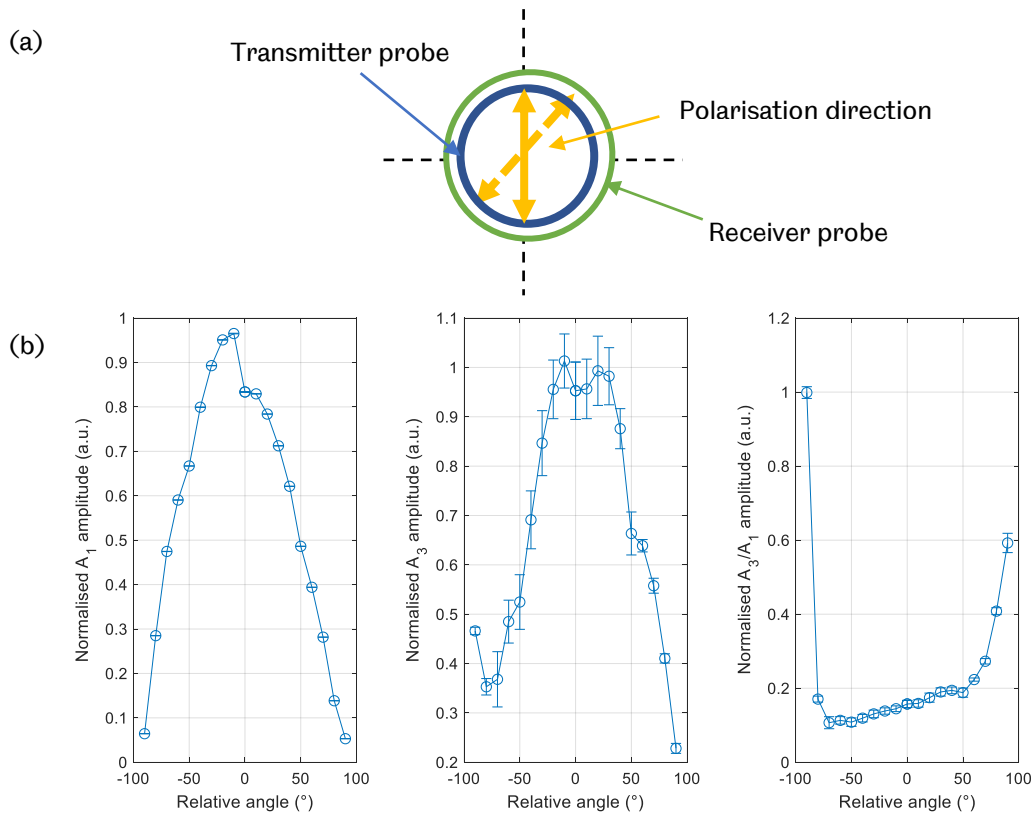


Figure 6.11 (a) Schematic diagram of angle alignment of normal incidence shear wave ultrasonic sensors. (b) Measurement of fundamental A_1 , 3rd order harmonic frequency A_3 and their ratio A_3/A_1 (50 repetitions).

When two normal incidence shear wave probes are offset in both ‘horizontal’ and ‘vertical’ directions, as illustrated in Figure 6.10 (a) and (b), both fundamental frequency A_1 and the third harmonic component A_3 drop dramatically. Their ratio A_3/A_1 also shows the similar dependence on the location.

When the angle of these two shear wave transducers are misaligned from -90° to 0° and to $+90^\circ$ (Figure 6.11 (b)) strong dependence of fundamental frequency, A_1 and the third order harmonic A_3 on the alignment angle. Their ratio, A_3/A_1 however, remains reasonably constant over the angle range from -20° to $+20^\circ$.

Both sets of the transducer alignment investigation indicate that the alignment of the transducers is critical in the high frequency nonlinear ultrasonic technique. Ideally two normal incidence shear wave probes are perfectly aligned, without ‘horizontal’ and ‘vertical’ offset and angle misalignment of polarisation direction of the transducers. The ‘perfect’ alignment arrangement is practically difficult to achieve. To ensure the minimum side effect from the transducer alignments, the same alignment conditions are kept throughout the measurement.

6.3.5 Data Acquisition

In the high frequency nonlinear ultrasonic technique, the primary signal is the higher order frequency components ($3f, 5f$ etc.) rather than the fundamental frequency ($1f$). Therefore, when the returning signal is received and digitised, extra care is needed and two aspects are taken into account, the number of captures recorded in the test and the digitiser voltage scale or sensitivity, respectively.

Tests were carried out using two normal incidence shear transducers (V153 and V155, 12.7mm diameter, Olympus) mounted on the same side of an aluminium test specimen S1 (as in Table 6.2), as shown in Figure 6.12. The specimen only made contact with air to ensure that the received signal was free from the effect due to the actually solid-solid contact. A tone burst of 90V 15-cycle sine wave was applied to excited the transmitter. The first reflection signal from the solid-air interface was received and used in the following analysis.

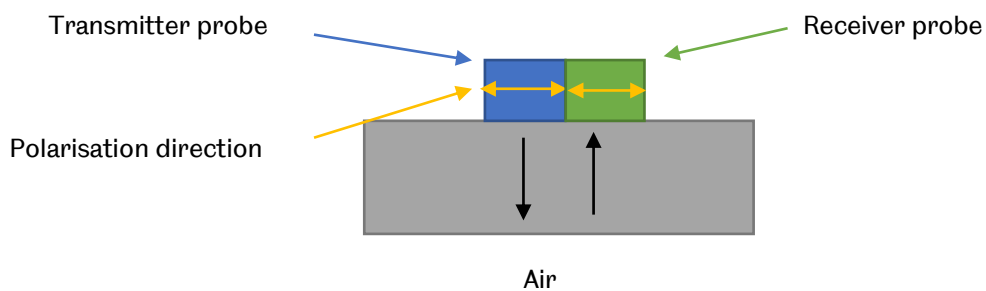


Figure 6.12 Schematic diagram of signal acquisition.

6.3.5.1 Number of Captures (Repetition)

In the test, the measurement of harmonics may be affected by random noise. A number of captures or repetitions are therefore required to reduce such noise. Various number of captures were used in the received signal acquisition subject to the same test conditions. The averaged frequency domain signal is illustrated in Figure 6.13. The averaged fundamental frequency amplitude A_1 shows little variation when various number of captures are applied while larger variations are observed for the third order harmonic A_3 with various number of captures.

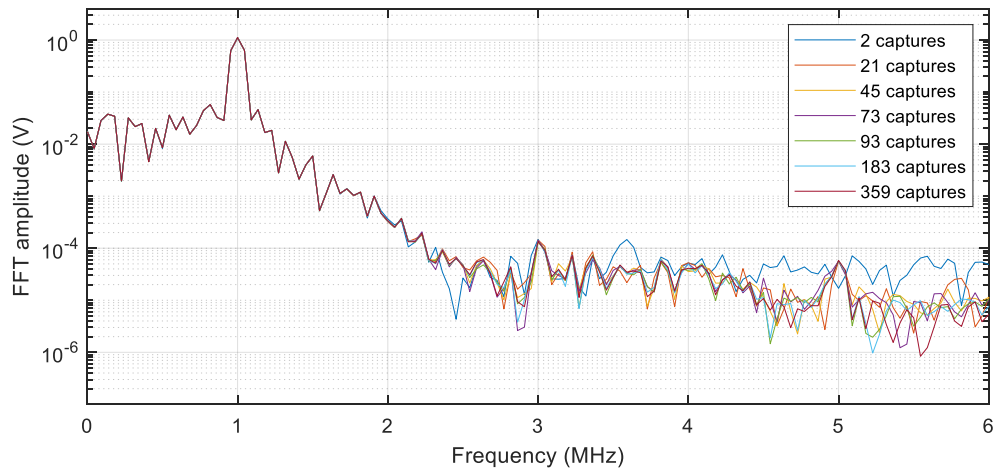


Figure 6.13 Averaged frequency spectra subject to various number of captures (repetitions). A tone burst of 15-cycle sine wave sent to test specimen S1 and the reflected signal received.

The mean and standard deviation of both the fundamental and the 3rd order harmonic are depicted in Figure 6.14 (a) and (b), respectively. The fundamental frequency remains constant for different number of captures with standard variation of less than 1% due to its high signal strength. For the 3rd order harmonic frequency, it remains reasonably constant with the increasing number of captures, although with some slight variations. The standard variation is approximately 20% and such high value is mainly due to that in the solid-air arrangement, the third order harmonic is mainly the inherent nonlinearity noise in the system, including amplifier, couplant, transducer and test specimen.

Although results illustrated in Figure 6.14 demonstrate that the fundamental frequency and the third order harmonic remains reasonably constant at various number of captures, in the actual tests, a sufficient number of captures should still be employed to reduce the random noise occurred in the experiment.

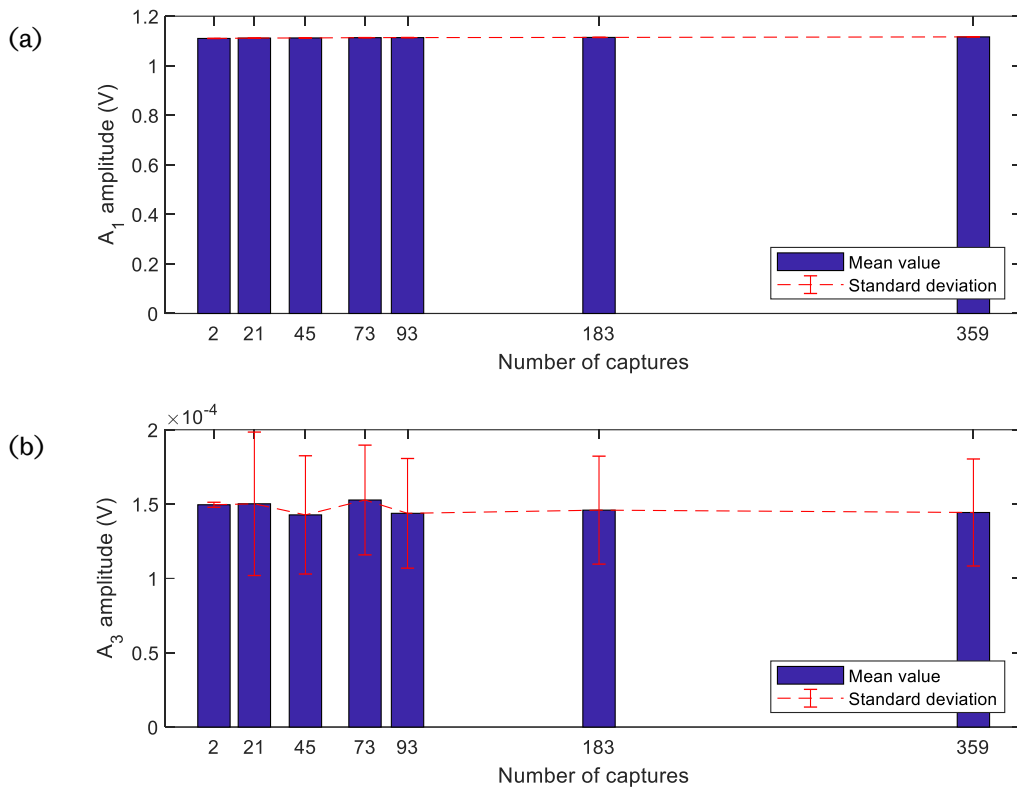


Figure 6.14 (a) Mean and standard deviation of fundamental A_1 . (b) Mean and standard deviation of the 3rd order harmonic frequency A_3 .

6.3.5.2 Digitising Voltage Scale and Sensitivity

Various digitising voltage scales were used on the received signal from the solid-air contact interface subject to the same test condition alterations. A 12-bit digitisation was used, as discussed in Section 4.4. The time domain signals received are depicted in Figure 6.15. When a sufficient voltage scale is used in digitising (Figure 6.15(a) and (c)), the corresponding third order harmonic is not affected (Figure 6.15(b) and (d)). However, if the digitising voltage scale is not adequate (Figure 6.15(e), (g) and (i)), the target signal, e.g. the first reflection signal, cannot be fully captured and digitised, leaving a 'clipped' signal. Such clipped feature causes the odd harmonic components to emerge (Figure 6.15(f), (h) and (j)).

The amplitude of both fundamental frequency and the 3rd order harmonic is shown in Figure 6.16(a) and (b), respectively. Due to the digitising voltage scale limit, the fundamental frequency, A_1 is capped. For the voltage scale sufficiently covers the target signal, the amplitude reasonably agrees. However, the third order harmonic

amplitude, A_3 is at least two orders of magnitude greater digitised using insufficient voltage scales, compared to those using an adequate scale.

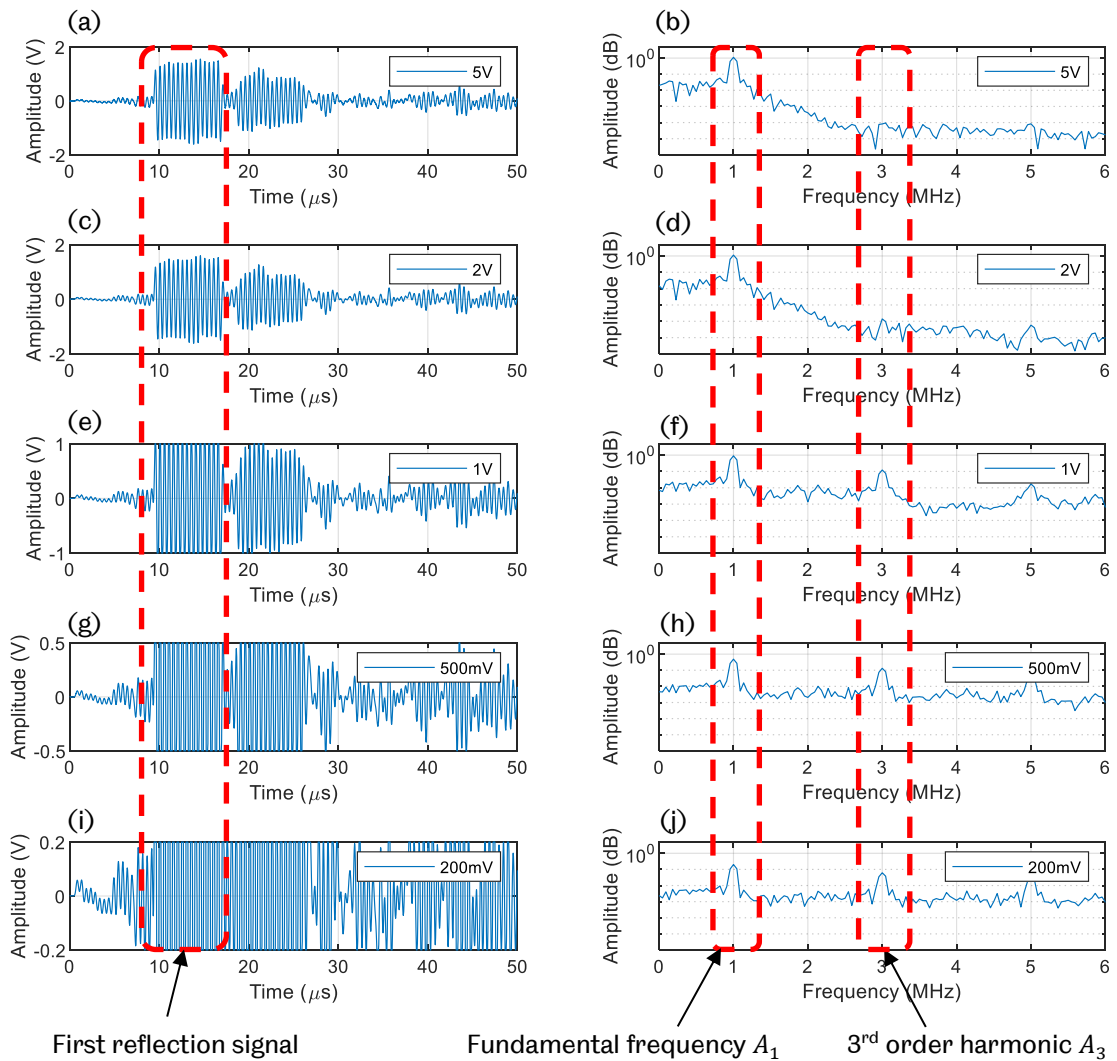


Figure 6.15 Effect of various digitising voltage scale on harmonics measurement (12-bit digitisation). (a) Time domain using 5V scale. (b) Frequency spectrum of the first reflection signal captured using 5V scale. (c) Time domain using 2V scale. (d) Frequency spectrum of the first reflection signal captured using 2V scale. (e) Time domain using 1V scale. (f) Frequency spectrum of the first reflection signal captured using 1V scale. (g) Time domain using 500mV scale. (h) Frequency spectrum of the first reflection signal captured using 500mV scale. (i) Time domain using 200mV scale. (j) Frequency spectrum of the first reflection signal captured using 200mV scale.

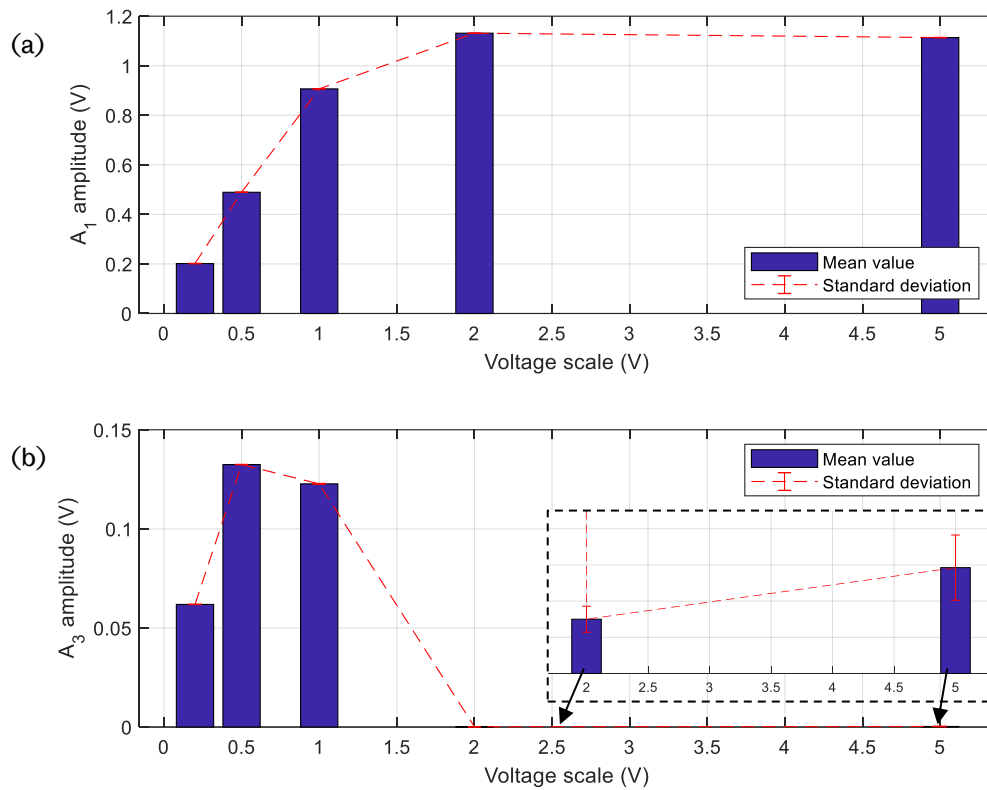


Figure 6.16 (a) Mean and standard deviation of fundamental A_1 subject to various digitising voltage scales. (b) Mean and standard deviation of the 3rd order harmonic frequency A_3 subject to various digitising voltage scales.

It is illustrated that the inadequate digitising voltage scale produces significant nonlinearities which could potentially overwhelm the target nonlinearity generated at the contact interface.

The sufficient digitising voltage scale does not indicate that the larger voltage is better. A tone burst of 4V 15-cycle sinusoidal wave was applied to excited the transmitter. A range of adequate digitising voltage scales was used on the same reflected signal subject to the same condition alterations. The averaged frequency spectrum of the first reflection signal is given in Figure 6.17. Due to the sufficient digitising voltage scales that are applied, time domain signals are not clipped off. The fundamental frequency A_1 overlaps when different digitising scales are used and while the 3rd order harmonic A_3 shows variations.

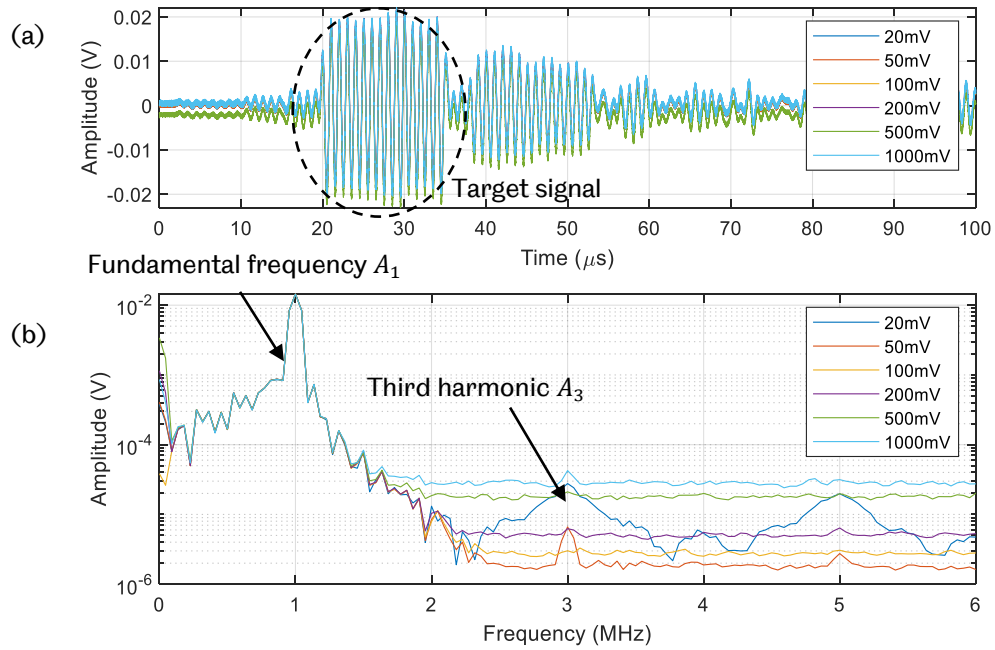


Figure 6.17 (a) Averaged time domain signal subject to various digitising voltage scales (b) Averaged frequency spectra. A tone burst of 15-cycle sine wave sent to test specimen S1 and reflected signal received and digitised (50 repetitions).

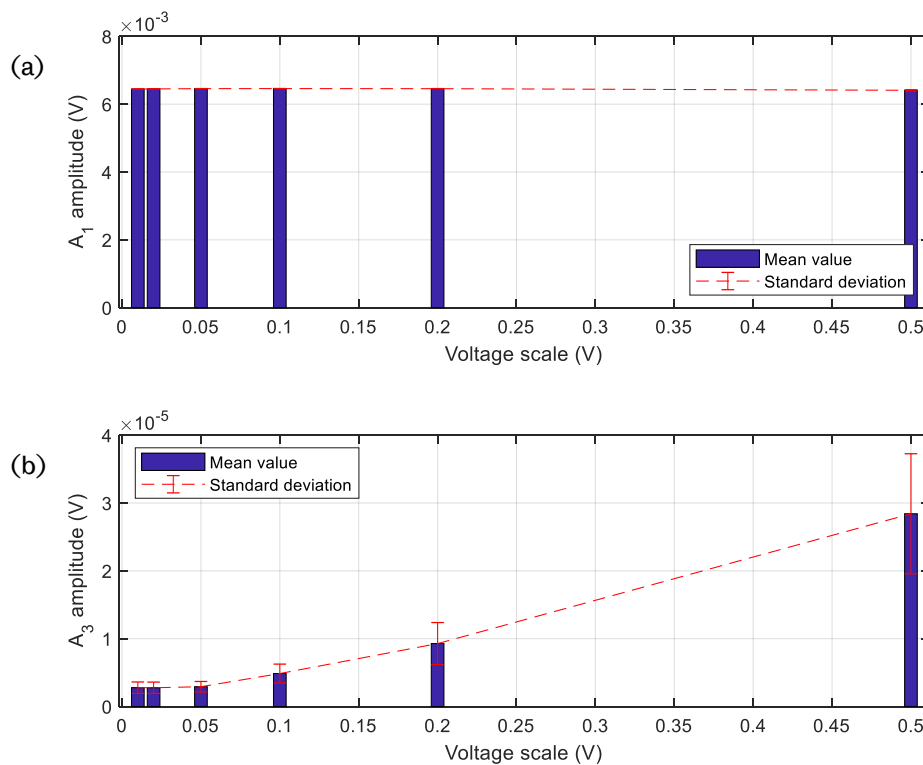


Figure 6.18 (a) Mean and standard deviation of fundamental A_1 subject to various digitising voltage scales. (b) Mean and standard deviation of the 3rd order harmonic frequency A_3 subject to various digitising voltage scales.

The mean fundamental frequency and the third harmonic component are shown in Figure 6.18 (a) and (b), respectively. The fundamental frequency amplitude remains constant regardless of the voltage scales. The third harmonic amplitude shows an increasing trend when a larger voltage scale is used with yet a tenfold difference. The large enough digitising voltage scale loses the sensitivity due to its coarse digitisation resolution, resulting in the false nonlinearity detection.

It is clear that the digitising voltage scale plays a significant role in the high frequency nonlinear ultrasonic technique as either insufficient or excessive voltage scales cause a false nonlinearity in the signal, which would influence the detection of the true harmonic generation at the frictional contact interface.

6.4 Signal Processing Method

The post-processing method, compared with the experimental factors considered in Section 6.3, may not crucially affect the detection of the higher order harmonics. However, it still plays a significant role in proper measurement of the nonlinearities as these high order frequency components are generally at least 40dB less than the fundamental frequency amplitude (Liu et al., 2011).

6.4.1 Method of Extracting Frequency Amplitude

Practical routines of extracting the high order harmonics are employed for longitudinal waves (Yan et al., 2009) and for shear waves (Blanloeuil et al., 2014c). A similar routine is adopted in this research work, as shown in Figure 6.19. Figure 6.20 (a) illustrates an example of time domain signal received. Shear wave transducers were placed on the top and bottom face of the test specimen H1 (as in Table 6.2) so that only the system inherent nonlinearity was considered. A tone burst of 90V 15-cycle sine wave was applied to excite the transmitter. The target signal was of the interest so that it was extracted from the received signal and a window function was applied to the extracted signal, as shown in Figure 6.20 (b).

Different operations are applied to the windowed signal to obtain both the fundamental frequency and the third harmonic frequency information. The most applied method is the Fast Fourier Transform (FFT). The windowed truncated signal is converted from time domain to frequency domain (Figure 6.21 (a)). Both fundamental frequency and high order harmonics are discernible in this frequency

spectrum and their amplitude can be obtained. In the second method, bandpass filters with passband around 1MHz and 3MHz, respectively are applied to the truncated time domain signal, which provides the time domain waveform of the passband only. The blue line indicates the time domain waveform around 1MHz and the red is for the time domain of the 3rd harmonic, as shown in Figure 6.21 (b). The envelope amplitude of these time domain signals is taken as the fundamental and the 3rd harmonic amplitude. The third method to extract the frequency information is the total harmonic distortion analysis, as depicted in Figure 6.21 (c). This MATLAB built-in function enables measurement of nonlinearity of a time domain signal providing that the fundamental frequency is dominant.

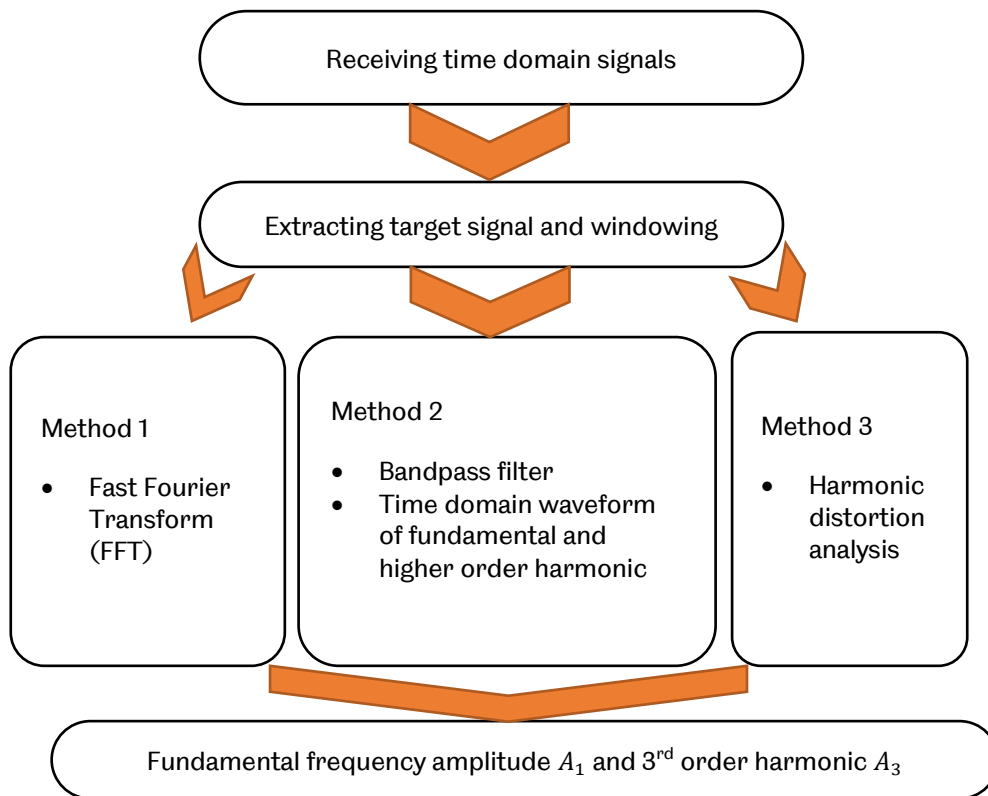


Figure 6.19 Schematic diagram of the signal processing method to extract high order harmonics.

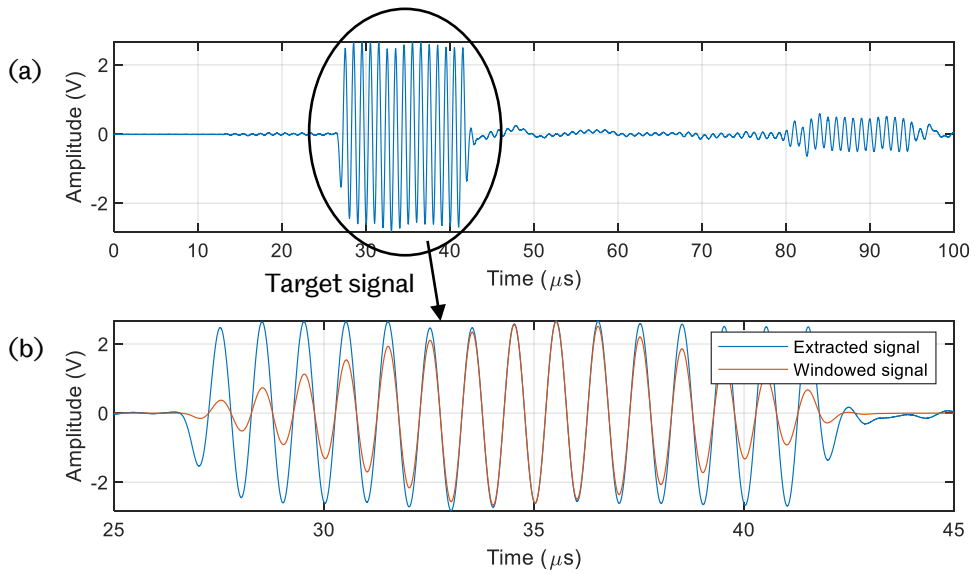


Figure 6.20 (a) Original time domain signal (b) Extracted target signal with and without windowing. A tone burst of 15-cycle sine wave propagating through test specimen H1 (50 repetitions).

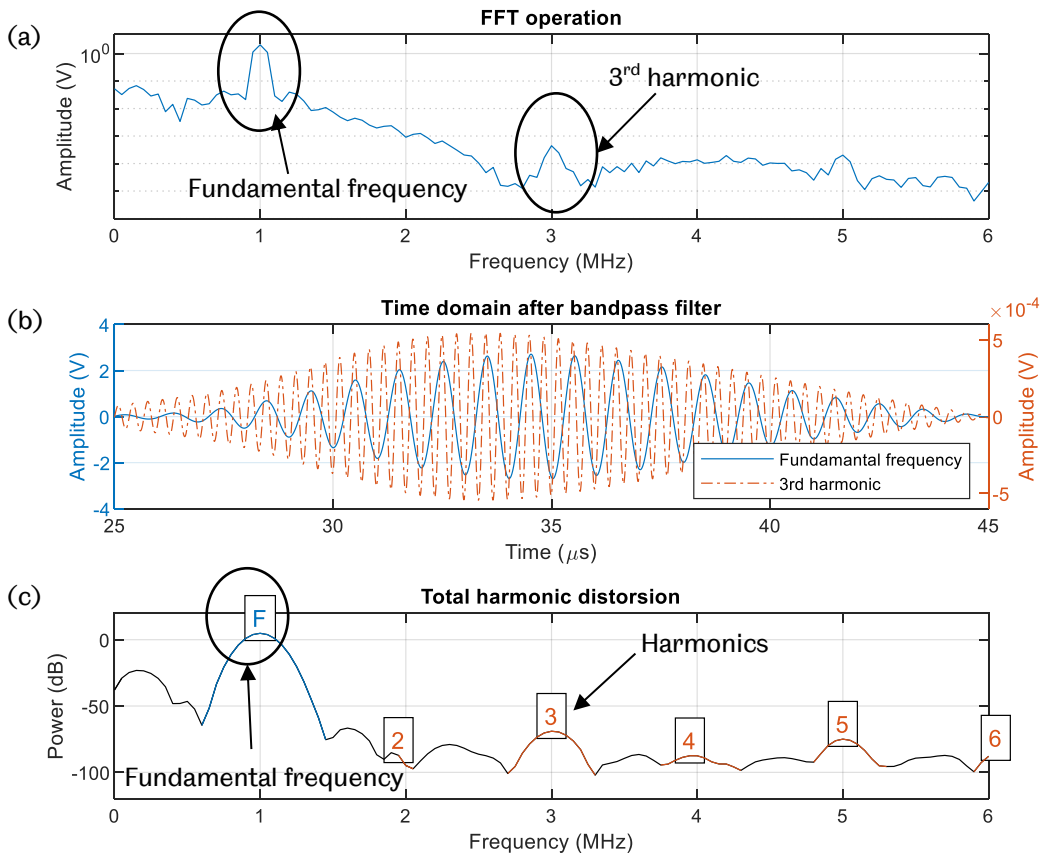


Figure 6.21 (a) Frequency spectrum using FFT. (b) Time domain signal using bandpass filter. (c) Total harmonic distortion analysis. A tone burst of 15-cycle sine wave propagating through test specimen H1 (50 repetitions).

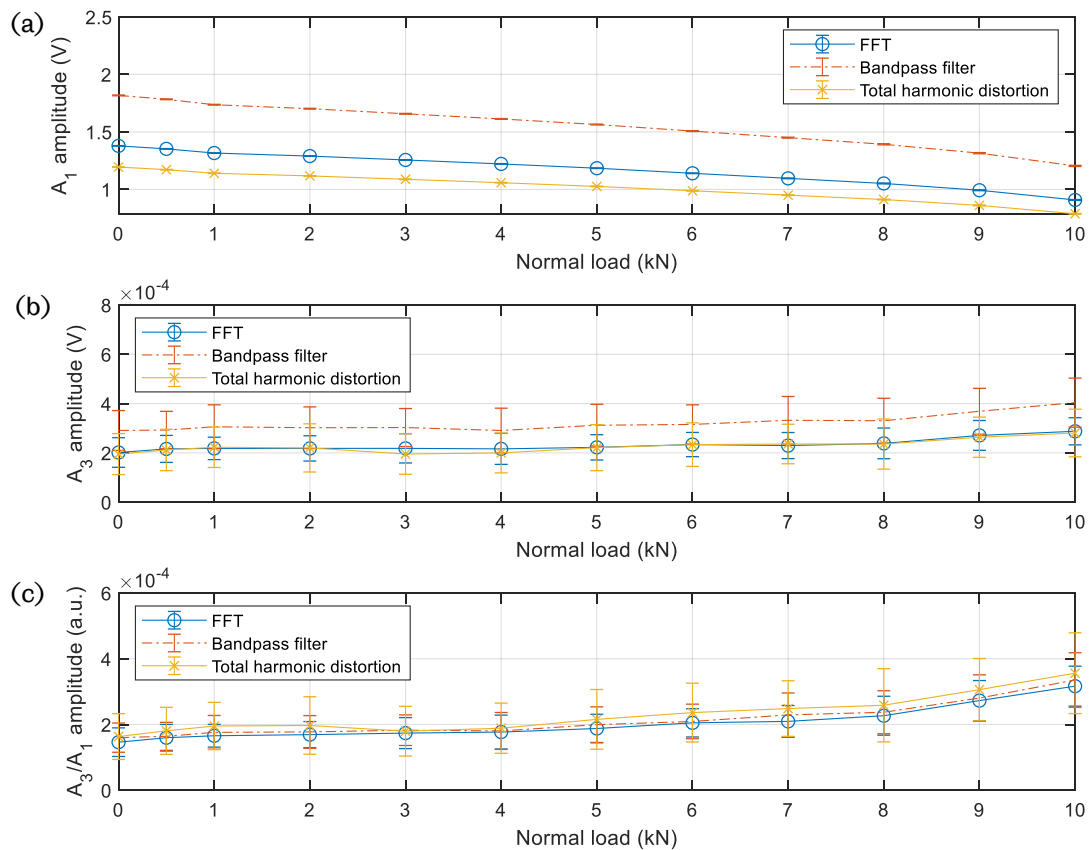


Figure 6.22 (a) Fundamental frequency amplitude, A_1 (b) The 3rd harmonic amplitude, A_3 (c) The ratio A_3/A_1 subject to various normal loads and extracted using three methods. A tone burst of 15-cycle sine wave propagating through test specimen H1 (50 repetitions).

The comparison of these three methods to extract the harmonic amplitudes is illustrated in Figure 6.22. A range of normal loads was applied to the test specimen. In Figure 6.22 (a) the fundamental frequency A_1 extracted using the three method shows similar decreasing trend despite that amplitudes does not agree. The third harmonic amplitude A_3 follows the same trend although the absolute amplitude is not alike. However, for the amplitude ratio A_3/A_1 overlaps regardless of the method applied.

All three methods can detect the information of harmonics. Although the amplitudes of the harmonics may not be identical using these three methods, the trend subject to change in test parameters, e.g. various normal loads, is still discernible regardless of the method employed.

6.4.2 Effect of Signal Truncation and Windowing

Regardless of methods of extracting the harmonic amplitude, the truncated signal plays an important role. For the actual measurement data, the length of the truncated target time domain signal and the window function applied to the truncated signal would potentially influence the high order harmonics measurement. The effect of truncation and windowing is investigated for harmonic generation with longitudinal waves (Liu et al., 2011). Such effect on the nonlinearity generation of shear waves is discussed here.

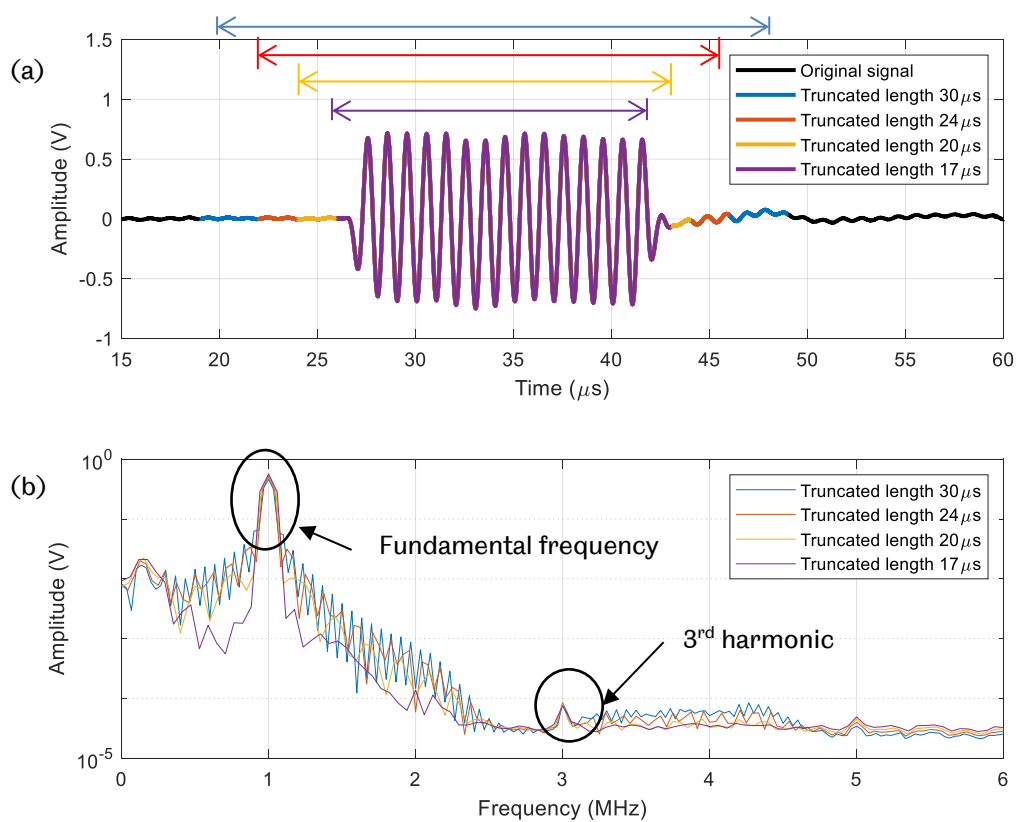


Figure 6.23 (a) Original time domain signal and truncated signal with various length. (b) Frequency spectrum of the various truncated length. A tone burst of 15-cycle sine wave propagating through test specimen H1 (50 repetitions).

As shown in Figure 6.23 (a) the target signal is separated using various truncation lengths and the corresponding frequency spectrum is illustrated in Figure 6.23 (b). At both fundamental frequency and the third order harmonic, the peak appears overlapping for various truncation length while at other frequency components, smaller truncation length shows a smoother frequency spectrum. Large truncation tends to cover not only the target signal but also the other reverberations or echoes,

which result in spikes in the frequency spectrum. In Figure 6.24, the fundamental amplitude A_1 decreases with the increasing truncation window length as large truncation also contains more portion of signal without little ultrasonic energy and lows the 'averaged' amplitude. The third order harmonic amplitude A_3 remains reasonably unaffected when the truncation length becomes several cycles wider than the actual target signal. It decreases as well as the fundamental frequency when the truncation length is more than sufficient.

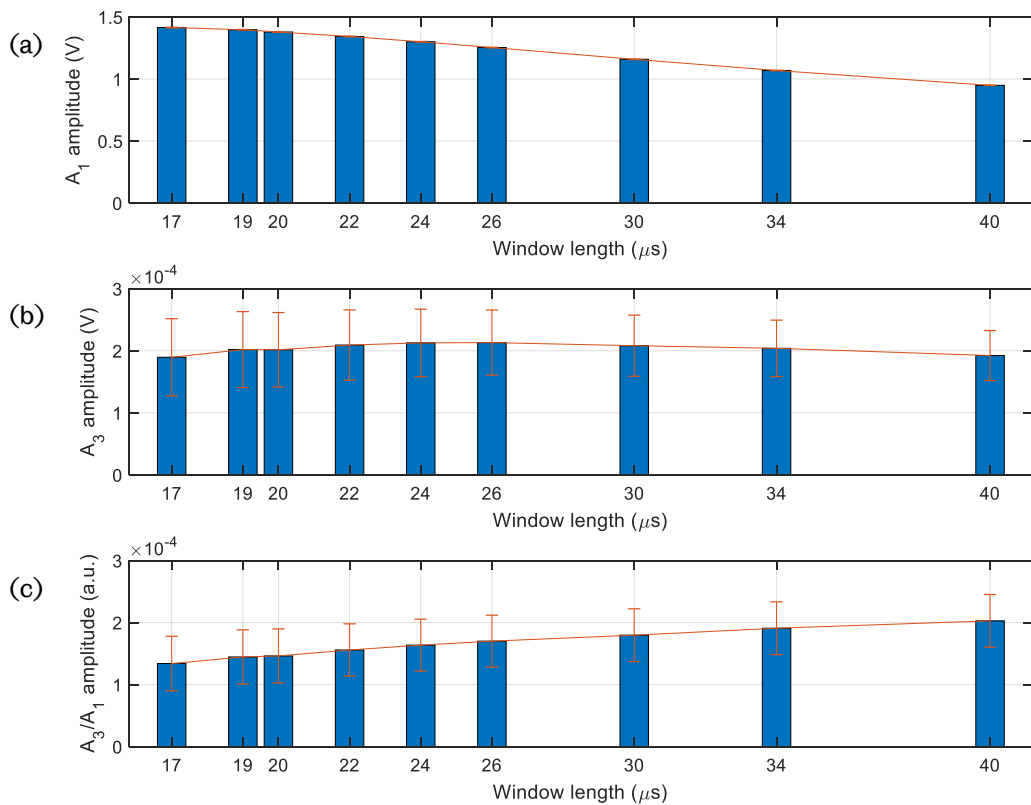


Figure 6.24 (a) Fundamental frequency amplitude, A_1 (b) The 3rd harmonic amplitude, A_3 (c) The ratio A_3/A_1 subject to various truncation length. A tone burst of 15-cycle sine wave propagating through test specimen H1 (50 repetitions)

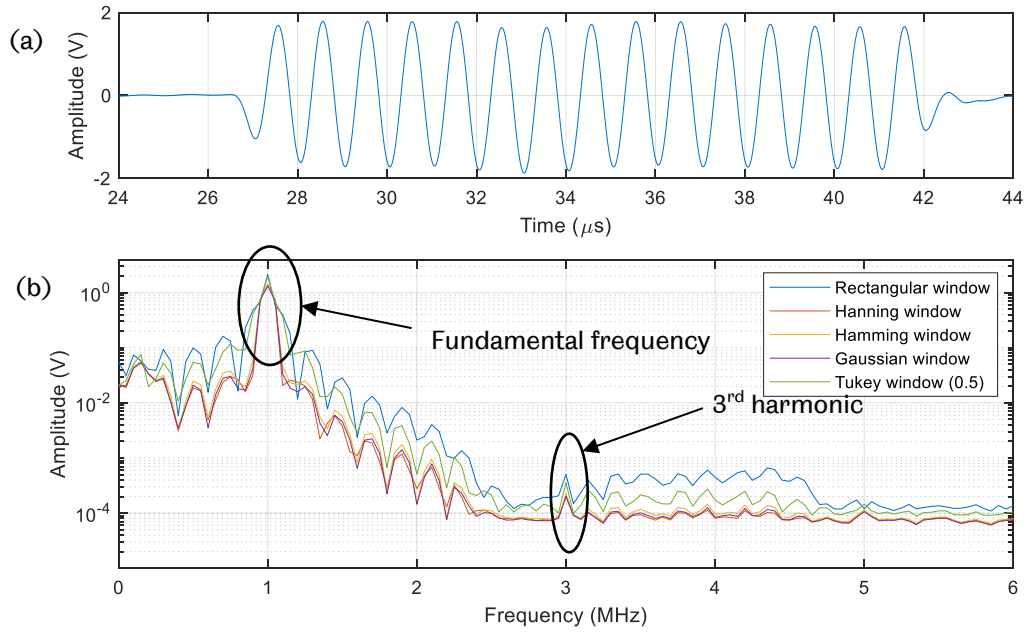


Figure 6.25 (a) Averaged target signal of 15-cycle sinusoidal wave. (b) Frequency spectrum of the target signal in (a) subject to different window functions. A tone burst of 15-cycle sine wave propagating through test specimen H1 (50 repetitions).

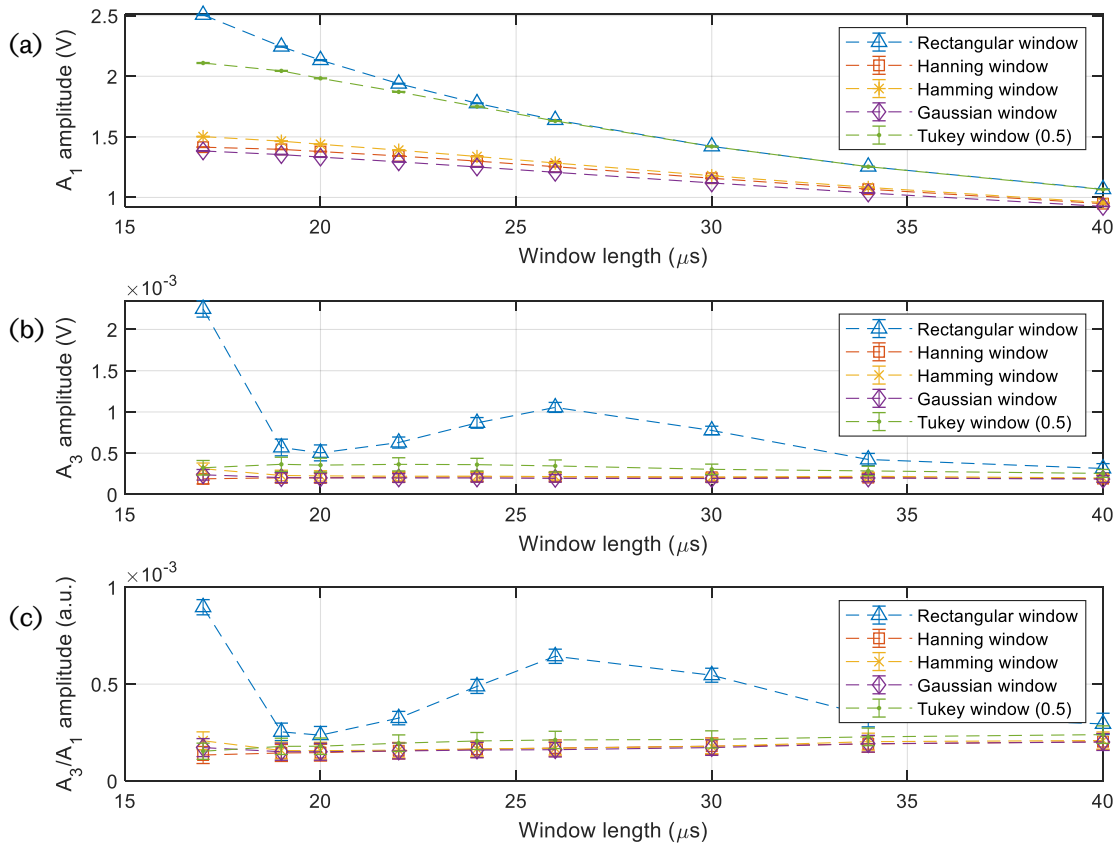


Figure 6.26 (a) Fundamental frequency amplitude, A_1 (b) The 3rd harmonic amplitude, A_3 (c) The ratio A_3/A_1 subject to various truncation length and window functions. A tone burst of 15-cycle sine wave propagating through test specimen H1 (50 repetitions).

Window function also influences the measurement of the higher order harmonics. With all other factors unaltered, the effect of window function is depicted in Figure 6.25 and Figure 6.26. It is noticed that when rectangular window is applied, the higher order frequency component is less discernible compared with other window functions (Figure 6.25 (b)). The amplitude of fundamental frequency A_1 , the third order harmonic A_3 and their ratio A_3/A_1 measured using rectangular window is also greater than those of other window functions, regardless of the truncation length (Figure 6.26 (a)). Results from Hann, Hamming and Gaussian window show little discrepancy. The Hann window function is adopted as it gives the least false nonlinearity (Liu et al. 2011) and the rectangular window should not be applied.

It should be noted that zeros are often padded on the time domain signal before time domain signal is converted to frequency spectrum using FFT operation, particular for a time domain signal with insufficient data points. However, zero-padding only works as interpolation in the frequency domain and improves merely the appearance of the frequency spectrum (Shin and Hammond, 1993). The true resolution in frequency domain is not improved. In this research work, a 15-cycle target signal with 2ns time domain resolution results in typically 10000 data points and a frequency resolution of 50kHz. With such resolution, the fundamental and harmonic components are resolvable. Therefore, in the following work, zero-padding is not applied with FFT operation.

The signal process method, despite insignificant, still affect the true nonlinearity measurement. Such influence could be compensated to yield the true nonlinearity. In a more practical approach, the same signal processing should be applied to all the tests, regardless of the harmonic amplitude method, truncation length and window function, so that the harmonics of interest due to test conditions can be revealed.

6.5 Laser Vibrometer Measurement

To understand the nonlinearity generation from the frictional contact interface, knowledge of the ultrasonically induced shear stress is of significance. Only sufficiently large shear stress can activate the 'stick-slip' mode at the pre-compressed contact interface and results in measurable nonlinearity. Inadequate ultrasonically induced shear stress is unable to trigger the slip motion at the contact interfaces. Although large stress can be obtained using an amplifier to output an enlarged incident wave, the stress level is still unavailable from either the amplifier settings or the measured ultrasound signal. Therefore, direct measurement of the

shear stress is critical and such measurement is carried out using a laser vibrometer and then measured displacement is converted to the stress (Liu et al., 2011; Blanloeuil et al., 2014c).

6.5.1 Laser Measurement Equipment

POLYTEC laser sensor head (OFV 354) was employed in conjunction with the vibrometer controller (OFV 2500), as shown in Figure 6.27. As the primary frequency used in this research work is 1MHz, the velocity decoder was employed as this configuration enabled the measurable frequency up to 3MHz.



Figure 6.27 Polytec laser sensor head and vibrometer controller (Reproduced from Polytec datasheet).

6.5.2 Laser Measurement Configurations

Generally using laser vibrometer to measure the displacement of longitudinal ultrasound can be carried out at the contact face without too much difficulty. As longitudinal wave produces an out-of-plane displacement, positioning the laser vibrometer in a way that the laser beam is perpendicular to the contacting face and parallel to ultrasonic propagation direction enables the longitudinal displacement measurement. However, it is challenging to measure the displacement of a shear polarised ultrasound at a contact face as the displacement direction is parallel to the contact face. Three approaches were attempted here.

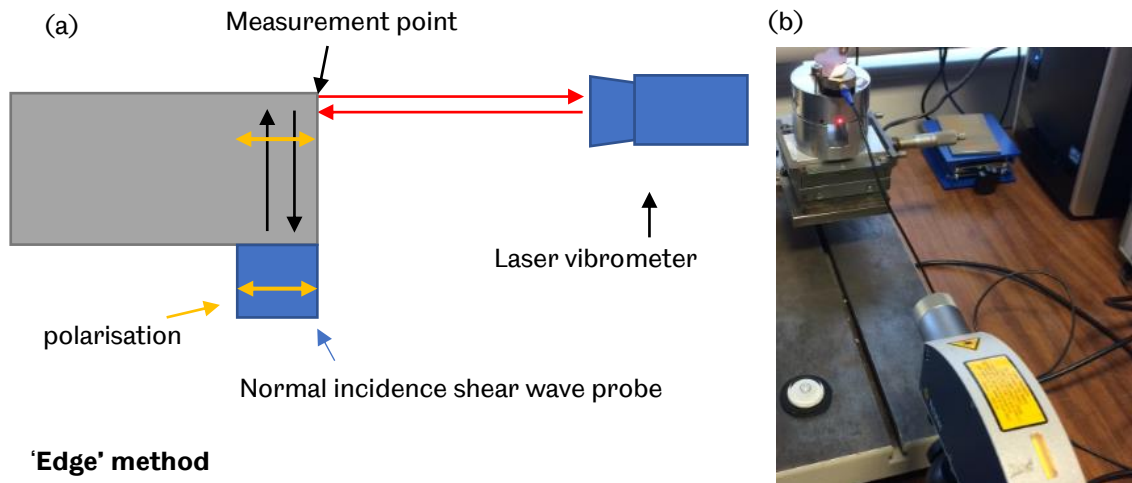


Figure 6.28 (a) Schematic diagram of displacement amplitude measurement using laser vibrometer: transducer on the edge of specimen ('Edge' method). (b) Measurement arrangement.

The first measurement configuration attempted is shown in Figure 6.28. A normal incidence shear wave transducer was placed close to the edge of the specimen and the laser measurement was carried out at the top end on the circumferential face. In this configuration, the displacement measured on the edge of specimen was assumed to be the same as the ultrasound displacement at the contact face of the specimen. However, as the size of transducer was finite and during propagation the ultrasound beam spread the measured ultrasound on the edge was far more complex. The displacement measured using this configuration did not represent the true displacement at the centre of the specimen.

The second approach attempted is illustrated in Figure 6.29. A small reflective prism was bonded at the centre of the contact face. The normal incidence shear wave probe was placed in the centre. The displacement at the bottom of the reflective prism was assumed the same as the displacement at the contact face as the in-place shear motion was converted to the out-of-plane motion of the reflective prism. Using this arrangement, the true displacement at the specimen was measured as the ultrasound propagation was not affected by the confined geometry as in the first configuration (Figure 6.28). However, practically the laser measurement was still influenced by the dimension, location and the bonding of the reflective prism.

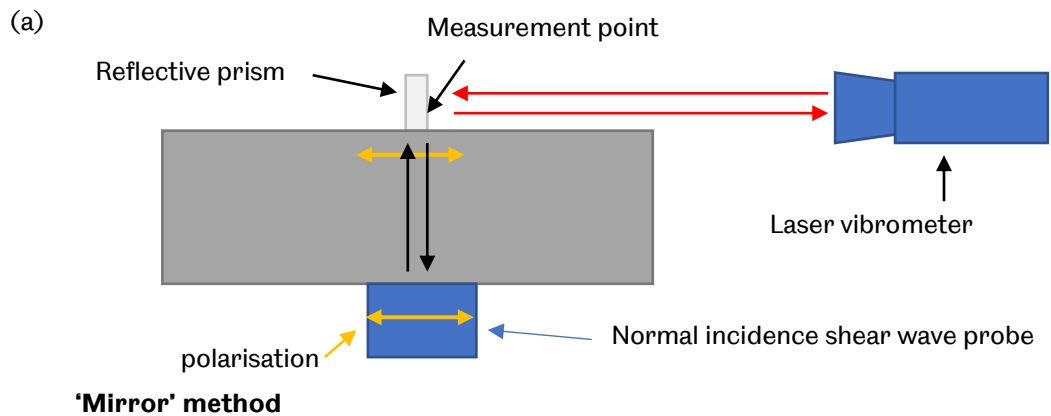
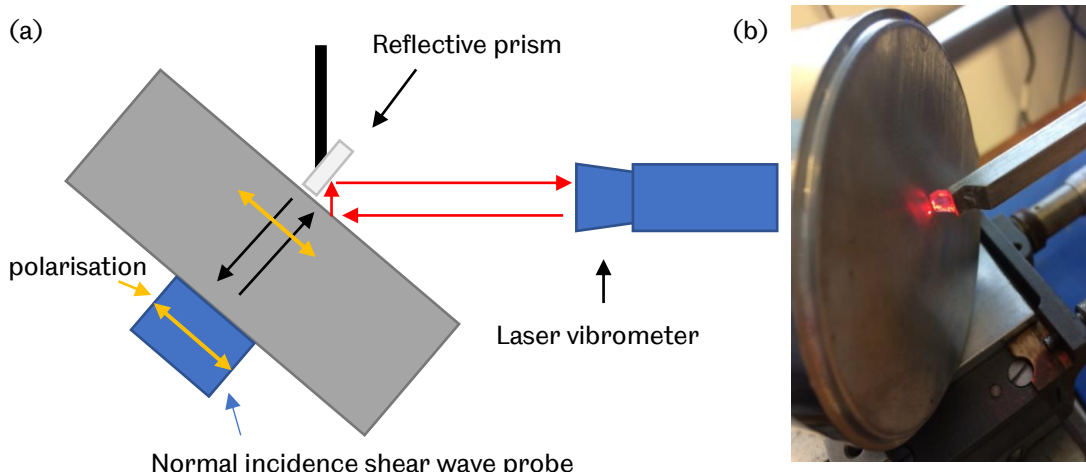


Figure 6.29 (a) Schematic diagram of displacement amplitude measurement using laser vibrometer: reflective prism bonded at the centre of specimen ('Mirror' method). (b) Reflective prism bonded on the specimen.

The approach used in literature (Blanloeuil et al., 2014c) was adopted as the third configuration of measuring the displacement of shear polarised ultrasound (Figure 6.30). The normal incidence shear wave probe was mounted in the centre of a test specimen and the specimen was placed at 45° angle to the laser beam. A removable reflective prism was positioned close to the contact face where the measurement was taken. The displacement along the tangential direction was decomposed in x and y directions as shown in Figure 6.30 (c). The x-direction component of the displacement can be detected by the laser vibrometer. The main advantage of this approach was that the ultrasound displacement at the contact face was not affected by the confined geometry and the target measurement surface was free from other factors, such as the bonded reflective prism.



'45-degree angle' method

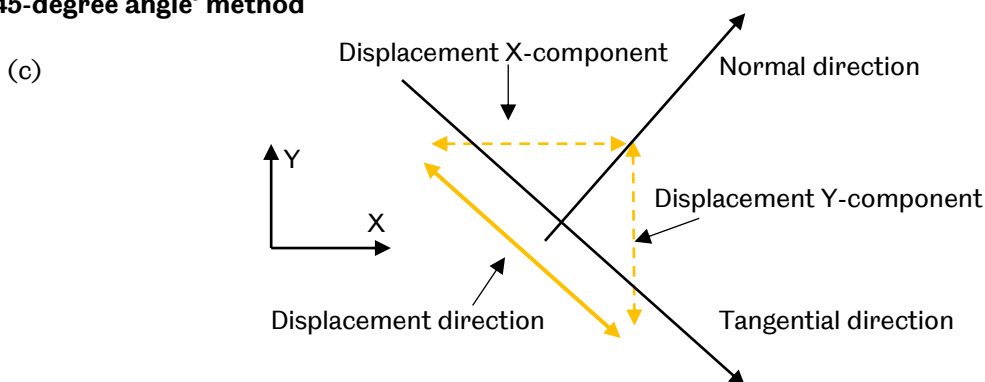


Figure 6.30 (a) Schematic diagram of displacement amplitude measurement using laser vibrometer: 45° oriented reflective prism. (b) Adjustable reflective prism at the centre of specimen (45-degree angle method). (c) Displacement decomposition in x and y directions.

The displacement measurement using laser vibrometer was carried out in the arrangement as shown in Table 6.3. A tone burst of 5-cycle sinusoidal wave was used to excite the transmitter (V153, Olympus) at various excitation levels. The ultrasonic signal was also recorded using the pulse-echo method simultaneously.

Table 6.3 Summary of the displacement measurement arrangement using laser vibrometer.

Test Specimen Arrangement			
V152 (1MHz, Olympus)		V153 (1MHz, Olympus)	
Specimen S	Specimen L	Specimen S	Specimen L
Amplifier(RITEC) excitation voltage (peak-peak) (V): 90, 140, 280, 420, 560, 700, 840			

6.5.3 Laser Measurement Results

An example of laser measurement is demonstrated in Figure 6.31. The shear wave was triggered from the ultrasonic transducer and when it struck the target contact face, the out-of-plane shear component was detected by the laser vibrometer Figure 6.31 (b). After another same time duration, the reflected signal was captured by the transducer Figure 6.31 (a). Due to relationship of time-of-flight, the signal captured by the laser vibrometer was the shear polarisation introduced motion. It is noted that in Figure 6.31 (b) there was no apparent signal detected before the shear wave arrived at the target contact face. This means that longitudinal wave with faster travelling speed was unable to cause any significant out-of-plane motion and the normal incidence shear wave transducers functioned properly under high excitation amplitudes, propagating primarily the shear polarised ultrasound.

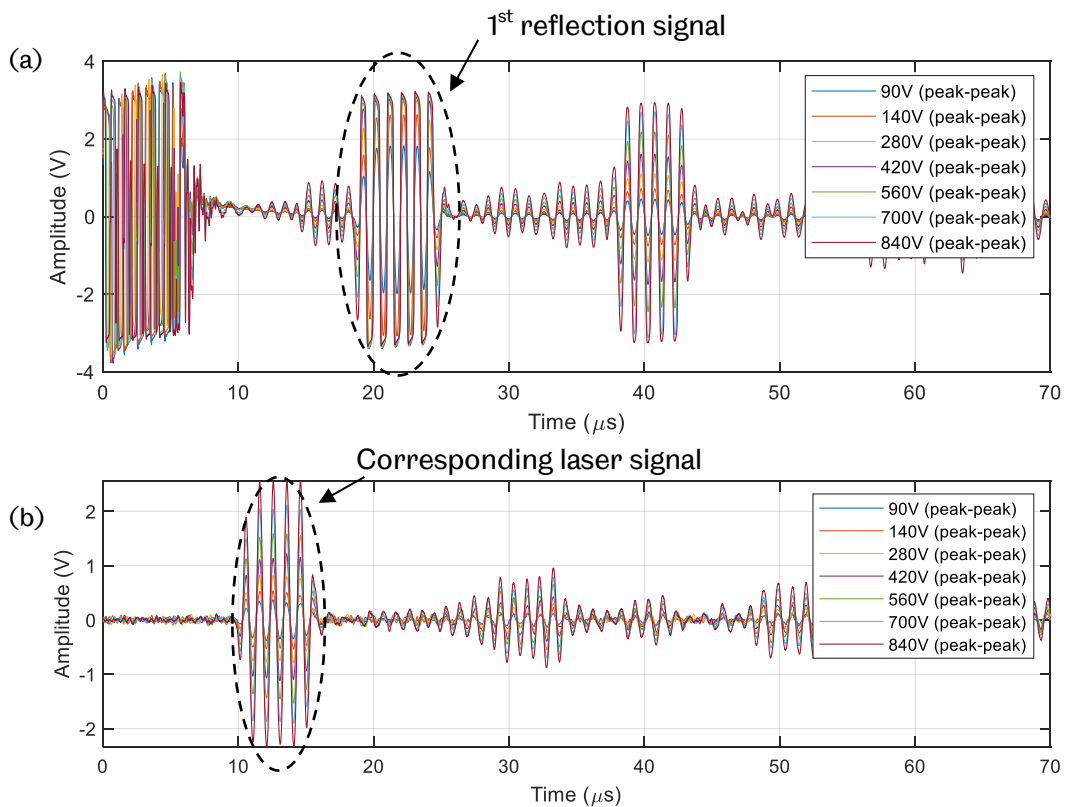


Figure 6.31 (a) Ultrasonic measurement using pulse-echo method for test specimen S with probe V153, subject to varying excitations. (b) Corresponding simultaneous laser vibrometer measurement. Signal encircled received first by laser vibrometer and then by ultrasound digitiser. (75 repetitions).

The signal encircled in Figure 6.31 (b) was converted into velocity as the velocity decoder was employed, as depicted in Figure 6.32 (a). Integration operation was

performed to obtain the displacement (Figure 6.32 (b)). The maximum of the displacement was taken and the amplitude of the displacement at the target contact face was worked out using the following trigonometrical rule.

$$Displacement = Displacement_{45^\circ} / \cos(45^\circ) \quad (6.1)$$

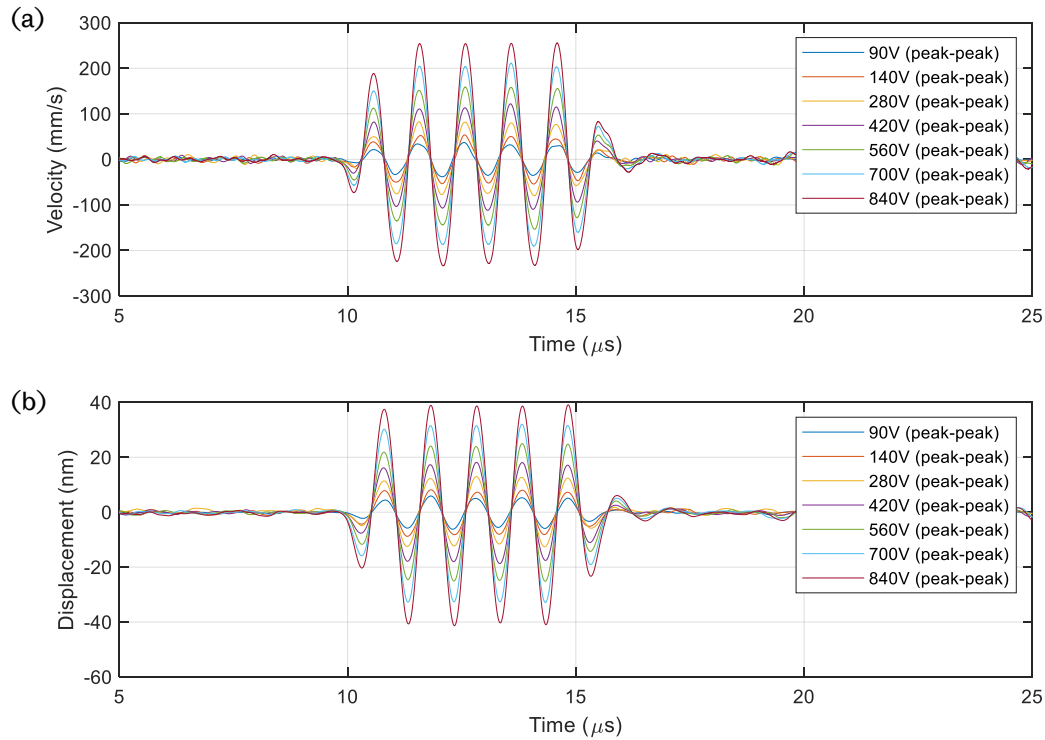


Figure 6.32 (a) Laser measured velocity and (b) laser measured displacement of test specimen S with probe V153, subject to varying excitations. (75 repetitions).

For various test specimens, the displacement at the contact face measured using laser vibrometer is illustrated in Figure 6.33. Results from all three measurement configurations show an increasing trend with the increasing excitation amplitude. The '45° angle' method gives the largest shear polarised displacement and the 'Edge' method gives the least displacement.

As mentioned previously in Section 6.5.2, in the 'Edge' method configuration, the transducer was placed close to the edge of the test specimen and shear wave propagation was influenced by the confined geometry of the test specimen. The displacement measured using this method was not as same as the wave travelling through the centre of the specimen. In the 'Mirror' method, displacement measured was affected by the geometry of the reflective prism and the bonding, which

resulted in smaller measured displacement. The displacement measured using these two methods were not used.

In the '45° angle' method, the target contact face was not influenced by bonding of extra materials and measurement using laser vibrometer was at the centre of the contact face. The displacement measured using this method was therefore adopted in the following research work.

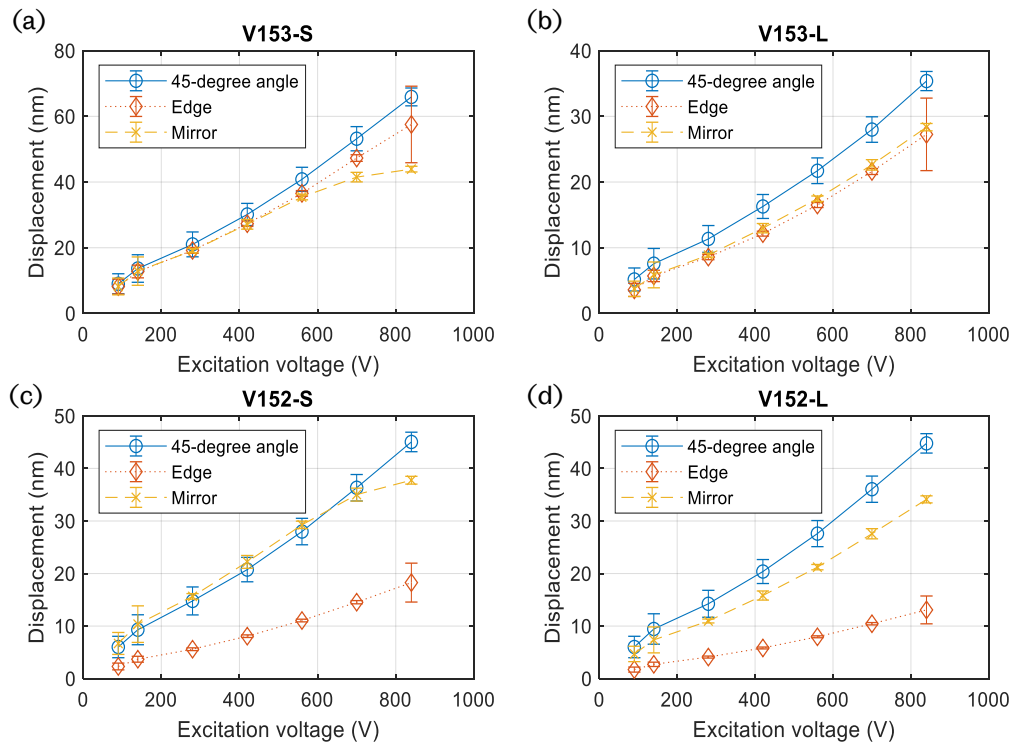


Figure 6.33 Shear polarised ultrasound displacement measurement using different laser vibrometer configurations subject to amplification levels. (a) Probe V153 on Specimen S. (b) Probe V153 on Specimen L. (c) Probe V152 on Specimen S. (d) Probe V152 on Specimen L. (75 repetitions).

It is also worth looking at the displacement measured using laser vibrometer compared with the ultrasonic measurement using the pulse-echo method (Figure 6.34). The displacement dependence on the excitation levels resembles that of the ultrasonic pulse-echo amplitude. It is reasonable that within the possible maximum excitations (840V peak-peak due to the amplifier and transducer specification), such dependence is linear. For different transducer and specimen combinations, the linear trends between the ultrasound pulse-echo amplitude and the displacement are shown in Figure 6.35.

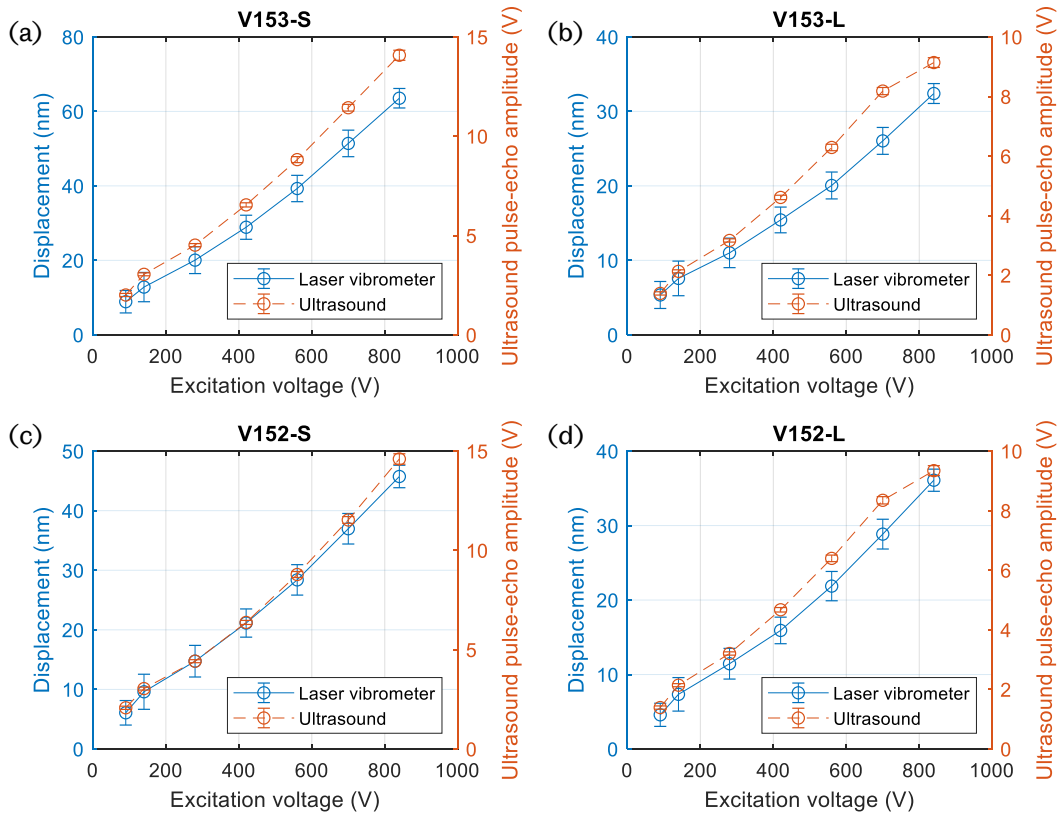


Figure 6.34 Shear polarised ultrasound displacement measurement using 45° angle subject to excitations versus the pulse-echo ultrasonic measurement. (a) Probe V153 on Specimen S. (b) Probe V153 on Specimen L. (c) Probe V152 on Specimen S. (d) Probe V152 on Specimen L. (75 repetitions).

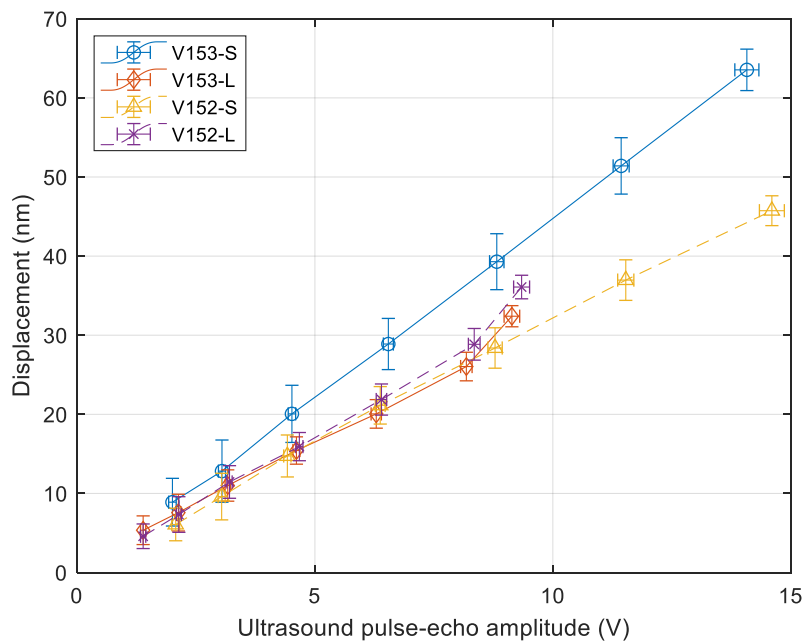


Figure 6.35 Shear wave ultrasound displacement and its corresponding ultrasonic pulse-echo amplitude for transducer V153 and V152 and test specimen S and L. (75 repetitions).

The ultrasound introduced shear stress at the target contact face is calculated using the Equation (6.2):

$$\tau_{ultrasound} = GkA_{contact}, \quad (6.2)$$

where G is the shear modulus of the test specimen, k the wave number and $A_{contact}$ the displacement of shear wave at the interface. Given that 1MHz shear wave employed, the possibly maximum shear stress introduced by ultrasound is obtained for each transducer and test specimen combination, as illustrated in Figure 6.36. It is noticed that the maximum shear stress is less than 5MPa for transducer V153 on specimen S and less than 2MPa for specimen L, 2.5MPa for V152-S and less than 2MPa for V152-L.

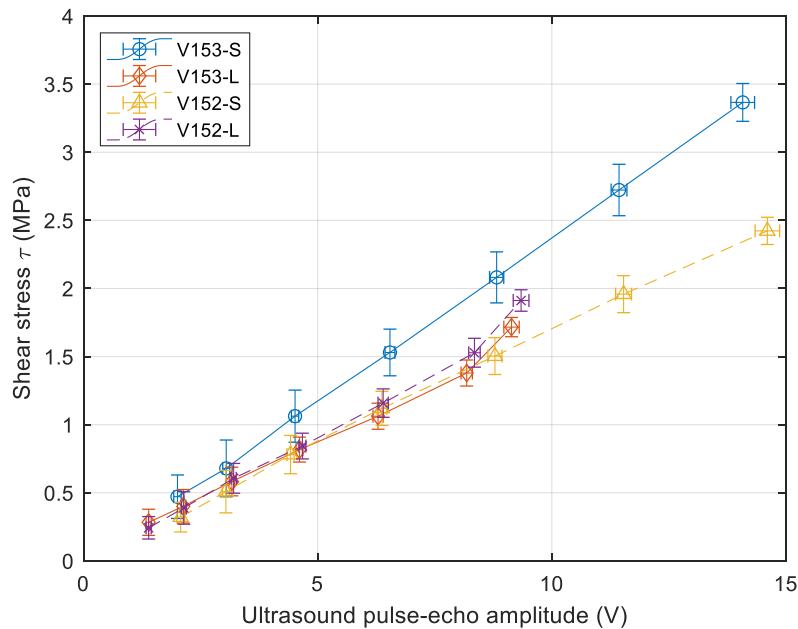


Figure 6.36 Shear polarised ultrasound introduced shears stress and its corresponding ultrasonic pulse-echo amplitude for transducer V153 and V152 and test specimen S and L. (75 repetitions).

Results in Figure 6.36 provides sufficient information on the shear stress introduced by the shear polarised ultrasound at the target contact face. Although the displacement (or shear stress) measurement are of limited accuracy due to the experiment setup and configurations, it still enables a reasonable knowledge of the shear stress arising from ultrasound, which was unavailable previously. The unique 'excitation amplitude-ultrasonic pulse echo amplitude-shear stress' relationship of each transducer and specimen (Figure 6.36) enables the stress level under a certain excitation and the corresponding ultrasonic pulse-echo amplitude to be estimated, within the practical limit of amplification level (e.g. 840V of RITEC amplifier).

6.6 Conclusion

In this chapter, experimental configurations for measuring harmonics at the rough contacts are investigated. High frequency nonlinear ultrasonic technique is employed throughout the investigation. Considerations also focus on the experimental variables, including transducer alignment, coupling, amplification and data acquisition sensitivity, which affect either the test implementation or the true measurement of the nonlinearity. The system inherent nonlinearity may cause false harmonics being detected if experiments are not carefully conducted. A practical approach to ensure the true measurement of harmonic generation from the rough contacts is to keep test configuration, data acquisition and signal processing consistent so that even the system inherent or false nonlinearity cannot be compensated or minimised, it remains at a reasonably unaltered.

The incident shear stress is critical in the activation of the nonlinear 'stick-slip' motion at a rough interface but it is difficult to measure. Measurement of the shear stress is carried out using a laser vibrometer and an angle test configuration. Using proper amplification setup, the displacement of the incident shear wave at the interface is approximately tens of nanometres and the shear stress is less than 5MPa. Despite the limited accuracy, the shear stress measured with laser vibrometer provides guidance on the following detection of contact nonlinearity in experiments.

7 MEASUREMENT OF ULTRASONIC NONLINEARITY AT ROUGH CONTACTS

In this chapter, experimental configurations discussed in the previous section are adopted in the measurement of nonlinearity generation due to shear polarised ultrasound interacting with a rough contact interface. Transmission test configuration and a novel reflection test configuration are first discussed and a method of removing the system inherent nonlinearity is followed. The experimental results show that the contact, nonlinearity is generated and is detectable. Influence of several factors affecting the nonlinear interaction at the contact interface is investigated including the ultrasonic incident amplitude and the normal stress. The contact nonlinearity measurement using subsequent echoes is also discussed.

7.1 Normally Incident Shear Wave Experiment Configuration

As mentioned previously, most researches on the nonlinearity generation of the interaction between a shear wave and a rough interface focus on numerical study and experimental investigation is lacking. The experimental configurations used in the nonlinearity generation when a longitudinal wave strikes the contact interface can be applied here. The most applied experimental configuration is the pitch-catch

approach where the transmission signal is used. In this work, an alternative novel approach is studied where the reflection signal is employed. Details of both arrangements are shown as follows.

7.1.1 Pitch-Catch Transmission Configuration

The test configuration using pitch-catch transmission arrangement is illustrated in Figure 7.1. Two normal incidence shear wave transducers were employed. The transducer with the centre frequency of the fundamental frequency $1f$ mounted on the top test specimen was working as the transmitter. The probe with the centre frequency at the 3rd order harmonic $3f$ was clamped on a second test specimen and works as the receiver. Two test specimens were brought to contact under the normally applied load by the hydraulic cylinder. The ultrasonic signal travelled from the transmitter, through the top test specimen, interacting at the interface, transmitted through the second test specimen and received by the second shear wave probe.

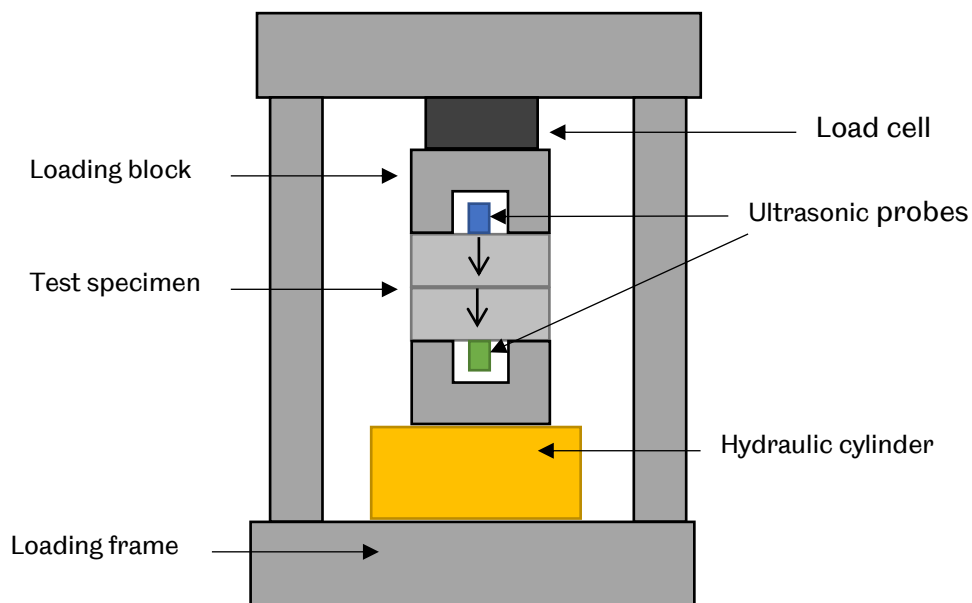


Figure 7.1 Schematic diagram of the test configuration: pitch-catch transmission arrangement.

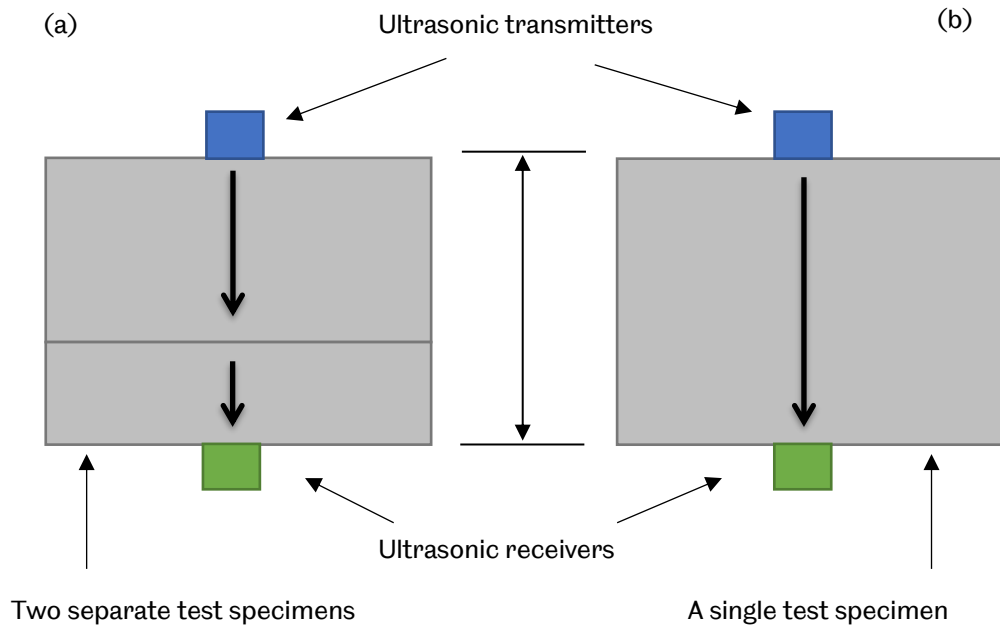


Figure 7.2 Pitch-catch transmission arrangement comparison. (a) two separate test specimens with contact interface. (b) a single test specimen without contact interface.

Comparison tests were carried out using the pitch-catch transmission arrangement as illustrated in Figure 7.2. Two test specimens with short length were brought to contact under the normally applied force and a solid-solid contact interface formed (Figure 7.2 (a)). In Figure 7.2 (b) a single specimen with a length equal to the total length of the two separate short test specimens was loaded. Transducers were placed on top and bottom faces of the long test specimen. In this arrangement, the contact interface was excluded, and the ultrasound travelled directly from the transmitter to the receiver through the material without any interaction with the contact interface. Test conditions for both arrangements are summarised in Table 7.1.

Table 7.1 Test conditions in pitch-catch transmission arrangement.

	With contact interface	Without contact interface
Test specimen	Al Alloy 6082 L1-S4	Al Alloy 6082 H1
Transmitter	V152 1MHz	V152 1MHz
Receiver	V155 5MHz	V155 5MHz
Waveform	15-cycle 1MHz sine wave	15-cycle 1MHz sine wave
Excitation voltage	90V, 280V	90V, 280V
Normal force	0 – 40 kN	0 – 40 kN

The time domain signals of both two-specimen and a single specimen are depicted in Figure 7.3 and Figure 7.4, respectively. Due to the existence of the contact interface in the two-specimen arrangement, several echoes are received by the wideband transducer. The first signal is the transmitted ultrasound through the contact interface. The second and third signals are the reflections within the bottom test specimen. For the single test specimen without the contact interface, the time domain signal is clearer. The first signal is the transmission and the second signal is the reflection from the top face of the test specimen. Due to the significant amplitude, the first transmitted signal is used for the following analysis. The same signal processing method is applied to both test data to ensure the consistency.

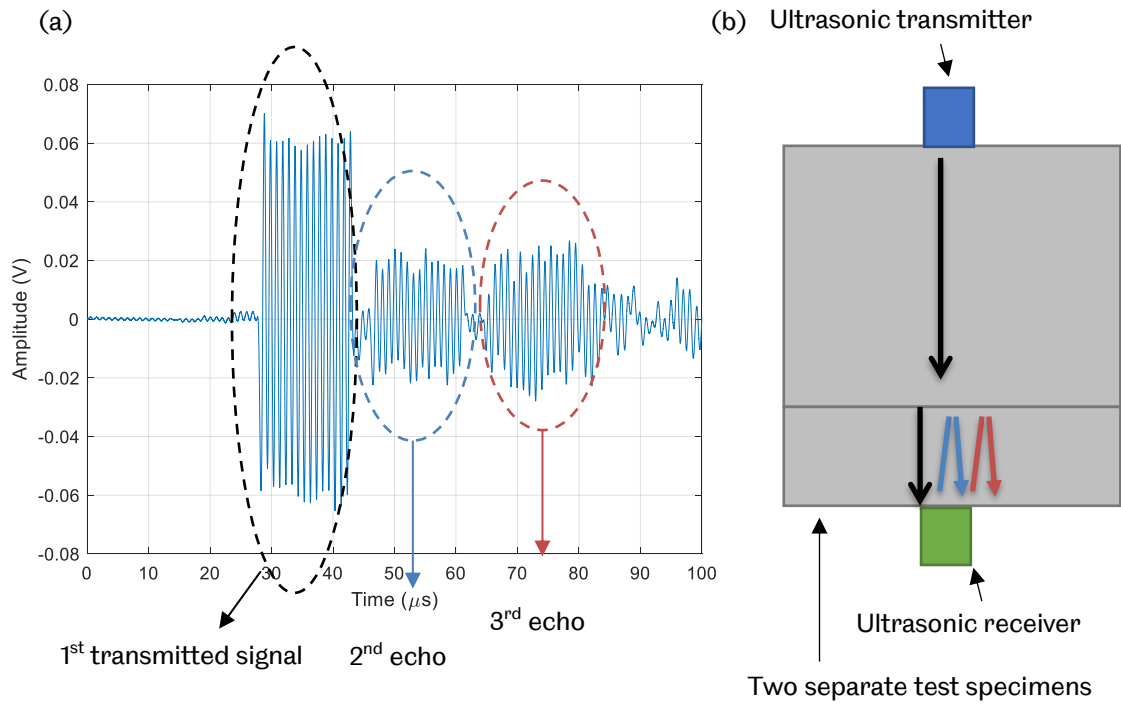


Figure 7.3 (a) Time domain signal in the test with contact interface (L1-S4, excitation 90V, normal stress 0.12MPa, 100 repetitions). (b) Schematic diagram of two separate test specimens with contact interface.

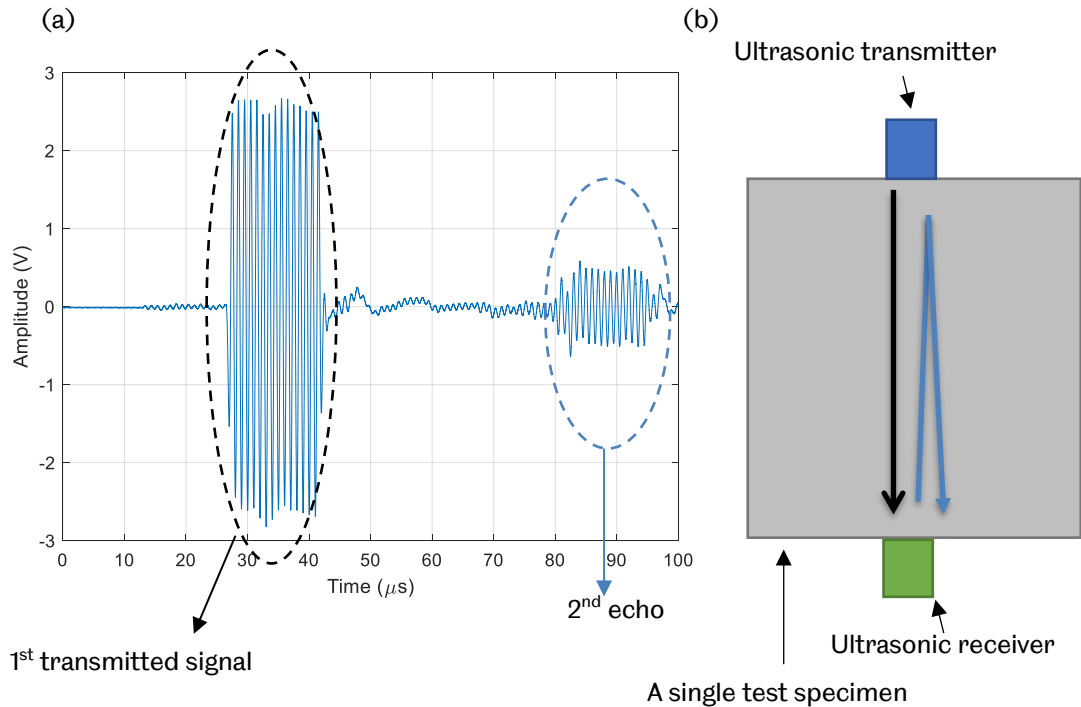


Figure 7.4 (a) Time domain signal in the test without contact interface (H1, excitation 90V, normal stress 0.12MPa, 100 repetitions). (b) Schematic diagram of a single test specimen without contact interface.

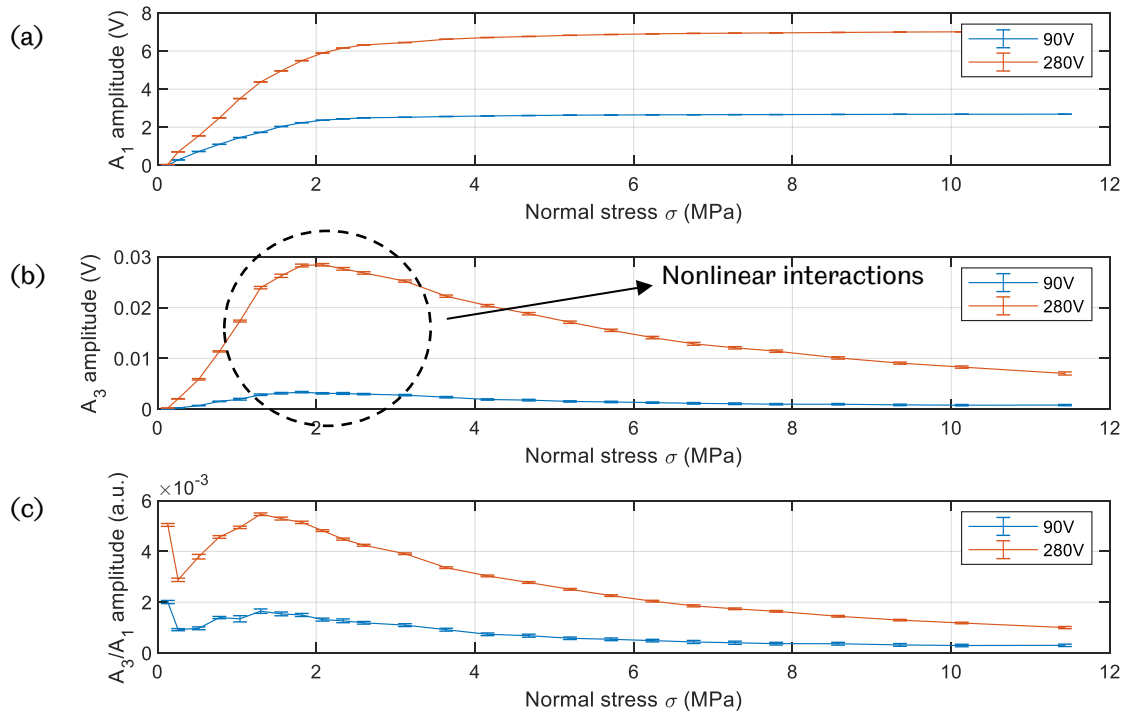


Figure 7.5 (a) Fundamental frequency amplitude A_1 , (b) The third order harmonic A_3 , (c) The ratio A_3/A_1 subject to various normal stresses and incident amplitudes of the two separate test specimens with contact interface (L1-S4, 100 repetitions).

The fundamental frequency amplitude A_1 , the third harmonic A_3 and the ratio A_3/A_1 of the test with contact interface formed by two separate test specimens are illustrated in Figure 7.5, subject to different incident amplitudes (90V and 280V excitation) and a range of normal stress. The fundamental frequency amplitude, A_1 rises when the normally applied stress starts to increase and reaches and remains approximately constant when the normal stress is high. When two separate test specimens are brought to contact under the increasing loads, a higher portion of ultrasound is transmitted through the contact interface. Most of the ultrasonic energy transmitted is through when the contact interface is compressed at higher loads.

As discussed in Chapter 5, only odd harmonics (3rd and 5th, etc.) are generated from a rough contact and in this work the third harmonic is considered. The third order harmonic amplitude A_3 , shows a different trend over the increasing load. As the normal stress starts to increase, the shear wave can interact with the contact interface nonlinearly. The shear wave introduced tangential stress, which begins to overcome the frictional force at the contact interface and initiates slip of the contact faces, resulting in the distortion of the waveform transmitted through, in the form of odd order harmonics, as shown in Figure 7.6 (a). When normal stress applied to

the contact interface is further increasing, the friction force becomes difficult to overcome by the ultrasound introduced shear stress, so the slips occur but with reduced extent and consequently the odd order harmonic amplitude drops. Further compressing the interface restricts the occurrence of the slip motions as the frictional force is sufficiently large for the incident shear stress to overcome. As a result, the transmitted waveform is least distorted, and the third order harmonics remains at the minimum values at high stresses, as illustrated in Figure 7.6 (b).

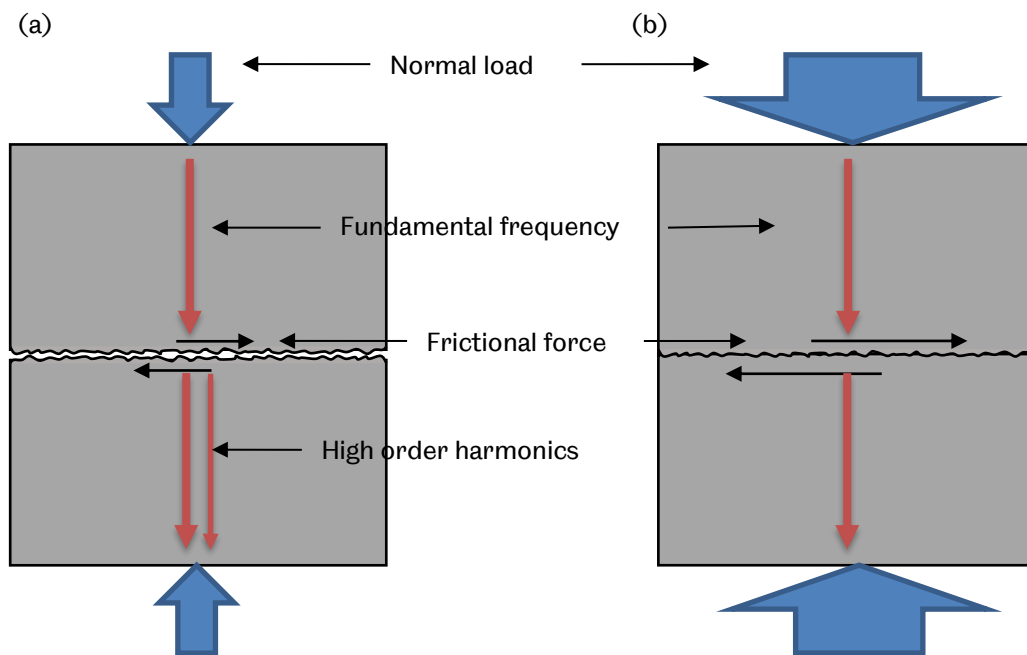


Figure 7.6 (a) Two separate test specimens with contact interface under low normal load. (b) Two separate test specimens with contact interface under high normal load.

The amplitude ratio A_3/A_1 shows a similar dependence as the third order harmonic, increasing to a peak and falling along with rising normal stress applied at the contact.

For the comparison test without the contact interface, the fundamental frequency amplitude A_1 , the third harmonic A_3 and the ratio A_3/A_1 , show a distinct trend over the varying normal stress, as demonstrated in Figure 7.7. As there is no interface, the ultrasound travel directly from one face of the specimen to the other face. The varying loads applied normally have no influence on the fundamental frequency amplitude. It is not surprising that the third order harmonic amplitude remains reasonably constant, indicating little variation over the normal stress. Even increasing the incident amplitude of shear wave to a higher excitation, the third harmonic amplitudes still shows independence over the applied normal load. This

third harmonic A_3 mainly from the test system itself (transducer, couplant and test specimen) as no contact interface is involved. It is noticed that compared to Figure 7.5, amplitudes of A_1 and A_3 in Figure 7.7 are smaller subject to the same excitation level and it is possibly caused by mounting the transducers on test specimens. Despite this amplitude difference, test results still show that the higher order frequency component merely comes from the system (previously discussed in Chapter 6) and no more extra nonlinearity is generated inside the test specimen.

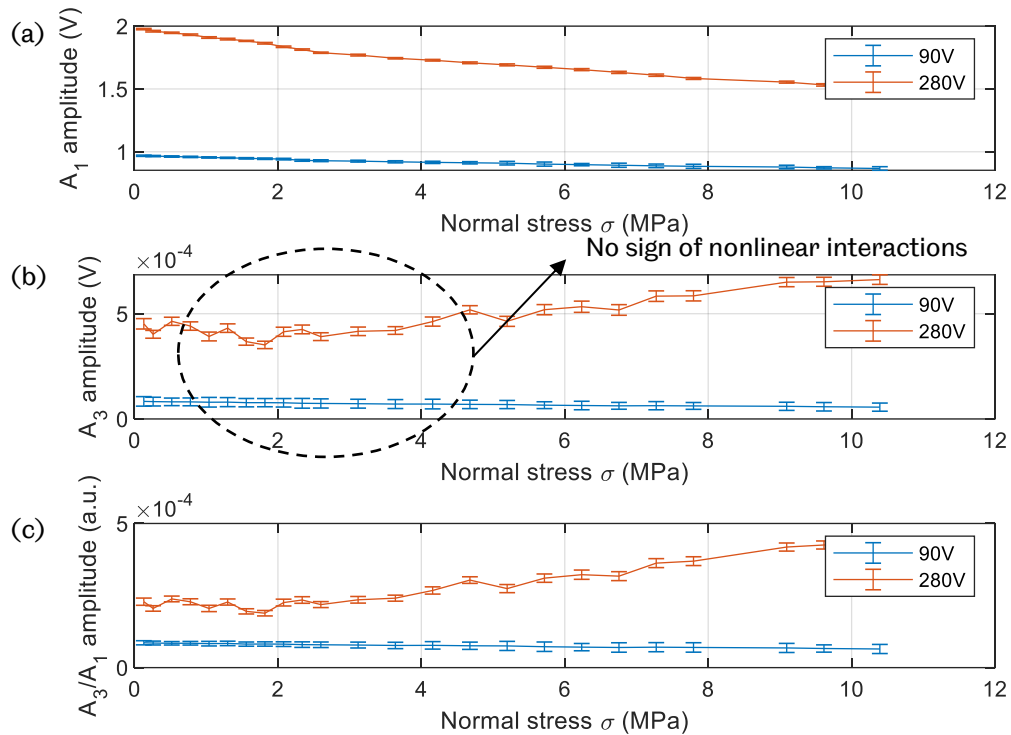


Figure 7.7 (a) Fundamental frequency amplitude A_1 , (b) The third order harmonic A_3 , (c) The ratio A_3/A_1 subject to various normal stresses and incident amplitudes of a single test specimen without contact interface (H1, 100 repetitions).

7.1.2 Pitch-Catch Reflection Configuration

In this work, a novel reflection measurement configuration is investigated in the measurement of the nonlinearity generated from the contact interface. As shown in Figure 7.8, the low-frequency transmitter and the high-frequency receiver were placed side by side on the top face of a test specimen. A second test specimen was brought to contact with the top specimen under normally applied load. Shear polarised ultrasound travelled from the transmitter and after striking the contact interface, received by the wideband receiver.

Comparison tests were also carried out using the reflection configuration as depicted in Figure 7.9. In Figure 7.9 (a), two specimens were brought to contact and a solid-solid contact interface forms. In Figure 7.9 (b) only the top single specimen was loaded which formed a solid-air contact interface. In this arrangement, the solid-solid contact interface was ruled out and no interaction of the ultrasound occurs at the contact interface. Table 7.2 summarises the test conditions for these two comparison tests.

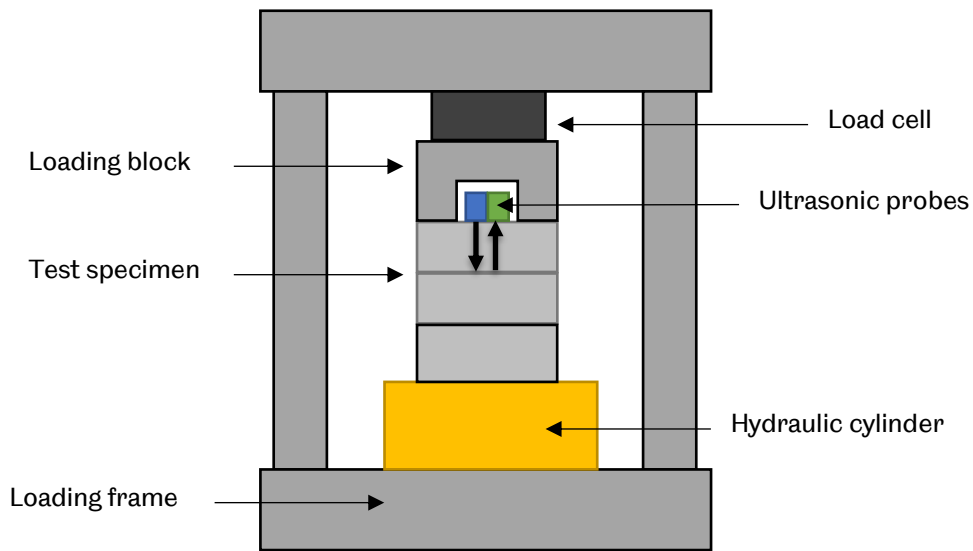


Figure 7.8 Schematic diagram of the test configuration: pitch-catch reflection arrangement.

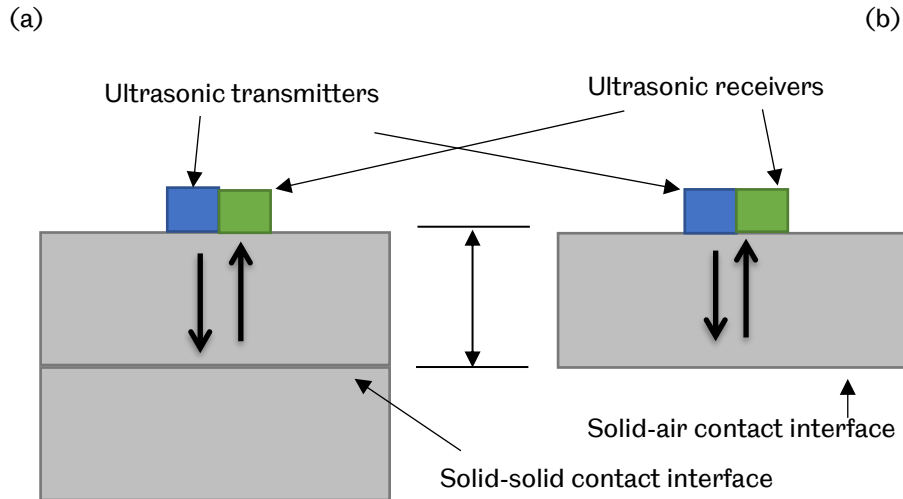


Figure 7.9 Pitch-catch reflection arrangement comparison. (a) Two separate test specimens with solid-solid contact interface. (b) A single test specimen with solid-air contact interface.

Table 7.2 Test conditions in pitch-catch reflection arrangement.

	Solid-solid interface	Solid-air interface
Test specimen	Al Alloy 6082 S1-S4	Al Alloy 6082 S1
Transmitter	V153 1MHz	V153 1MHz
Receiver	V155 5MHz	V155 5MHz
Waveform	15-cycle 1MHz sine wave	15-cycle 1MHz sine wave
Excitation voltage	90, 280, 560V	90, 280, 560V
Normal force	0 – 45 kN	0 – 45 kN

The time domain signal using the pitch-catch reflection configuration is shown in Figure 7.10. In both solid-solid contact interface test and the solid-air contact interface, the same top test specimen with ultrasonic transducers is used and the reflected signals (first, second and third reflections) shows the same time of flight in both arrangements. Due to the relatively large amplitude, the first reflection signal is truncated for the further frequency analysis.

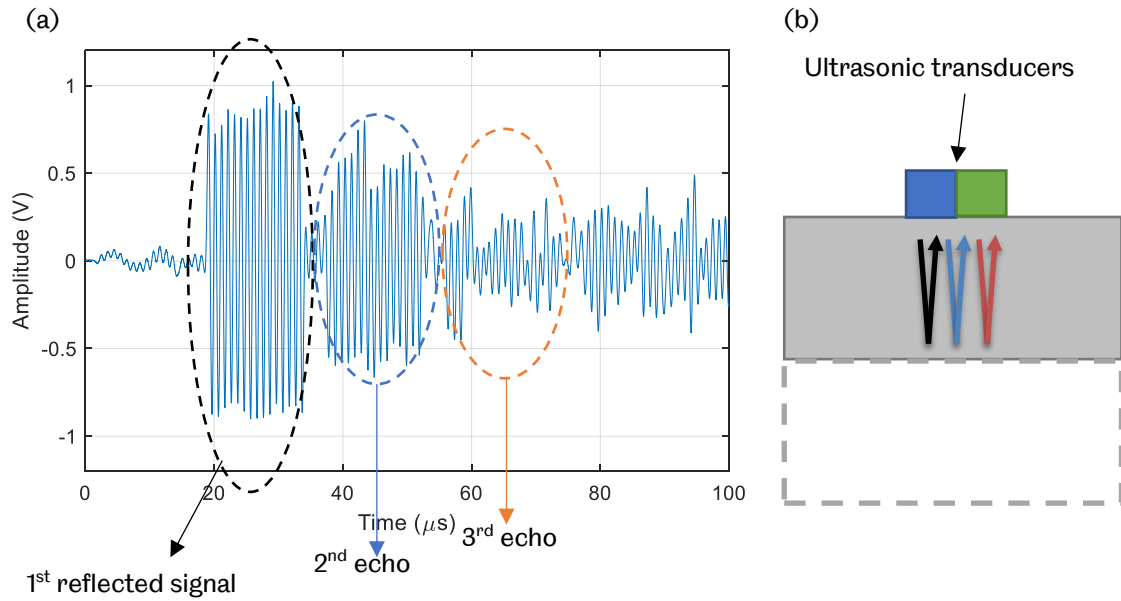


Figure 7.10 (a) Time domain signal in the test using reflection configuration (S1-Air, excitation 90V, 100 repetitions). (b) Schematic diagram of pitch-catch reflection test with solid-solid or solid-air contact interface.

The fundamental frequency amplitude A_1 , the third harmonic A_3 and the amplitude ratio A_3/A_1 of the reflection arrangement with the solid-solid contact interface are depicted in Figure 7.11. The fundamental frequency amplitude, A_1 drops when the normally applied stress starts to increase and reaches and remains approximately constant when the normal stress is high Figure 7.11 (a). When two separate test specimens are brought to contact under the increasing force, more ultrasound transmitted through the contact interface and less is reflected. When the contact interface is compressed at higher load, minimum level of ultrasound is reflected.

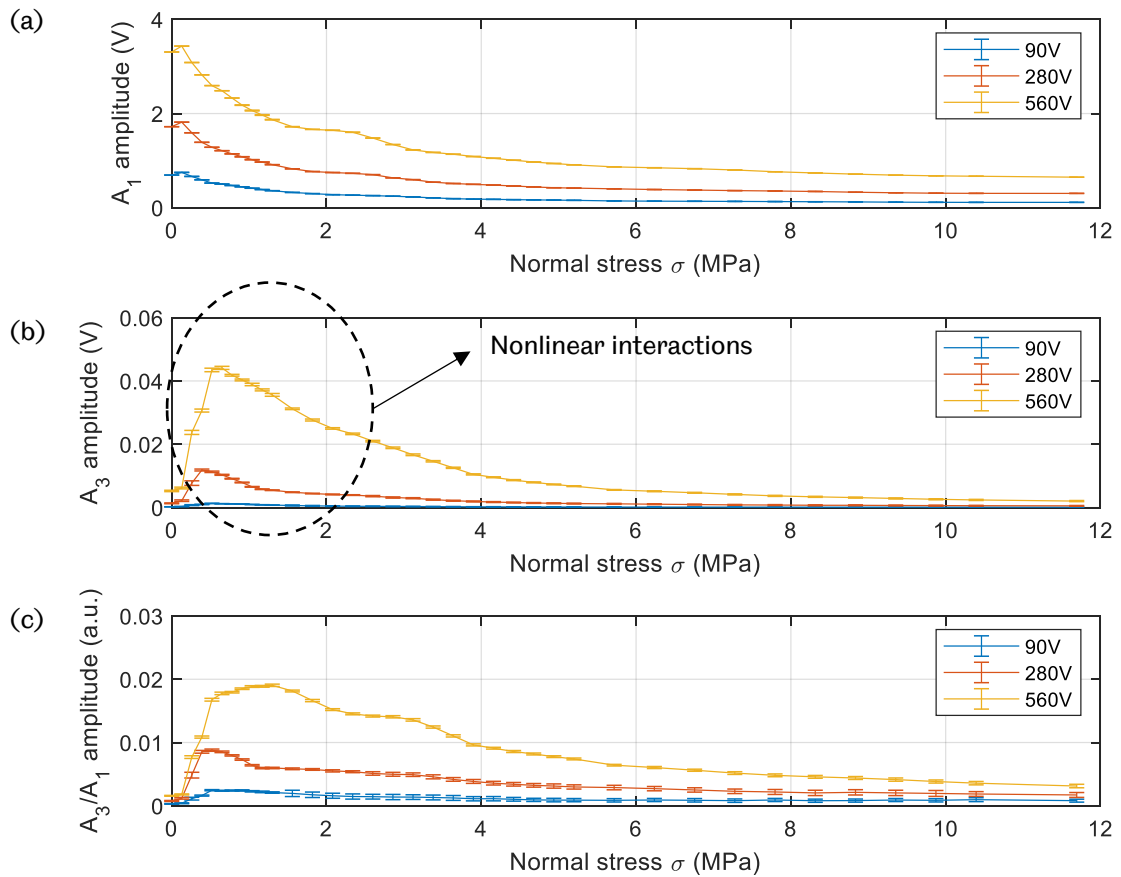


Figure 7.11 (a) Fundamental frequency amplitude A_1 , (b) The third order harmonic A_3 , (c) The ratio A_3/A_1 subject to various normal stresses and incident amplitudes of the test with solid-solid contact interface (S1-S4, 100 repetitions).

The third order harmonic amplitude A_3 , however, rises and falls with the increasing loads, as in Figure 7.11 (b). As the normal stress starts to increase, shear wave can overcome the frictional force at the interface, activating the 'slip-stick' motion. Such nonlinear interaction of the ultrasound wave with the interface causes the distortion of the waveform reflected backwards. Further compressing the interface, the incident shear stress becomes gradually unable to overcome the friction force, which leads to a reduced extent of 'slip-stick' motion and falling odd order harmonic. When the contact interface is heavily compressed, the nonlinear interaction between shear wave and frictional contact faces are impeded under the high friction force and the high order harmonics are suppressed. The amplitude ratio A_3/A_1 also shows a 'rise-fall' trend with increasing normal stress applied at the contact interface Figure 7.11 (c).

For the comparison test with the solid-air interface, the fundamental frequency amplitude A_1 , the third harmonic A_3 and the ratio A_3/A_1 all show little change with

varying normal stress, as demonstrated in Figure 7.12. Due to the non-existence of the solid-solid interface, the ultrasound reflects without any interaction at the solid-air interface. The normally applied loads have no influence on the fundamental frequency and the third harmonic, regardless of the incident amplitude of shear wave. The measured high order frequency component is only the systems built-in nonlinearity.

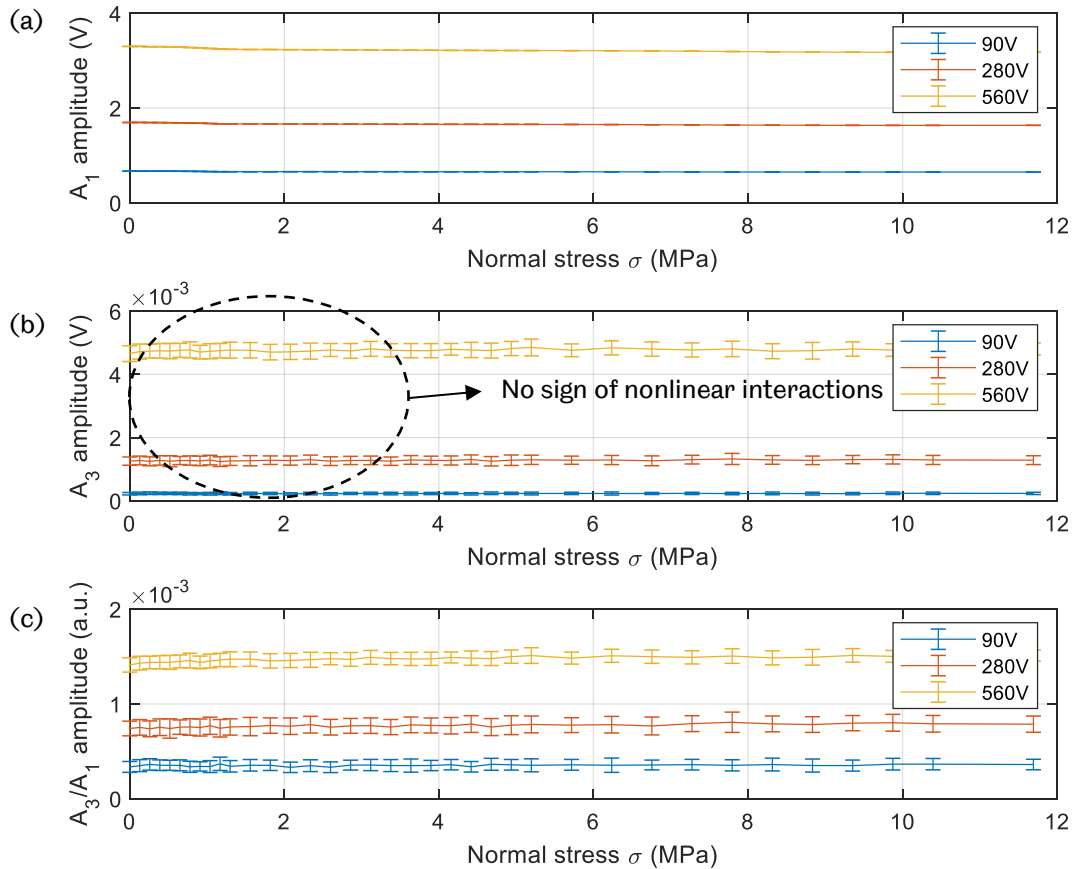


Figure 7.12 (a) Fundamental frequency amplitude A_1 , (b) The third order harmonic A_3 , (c) The ratio A_3/A_1 subject to various normal stresses and incident amplitudes of test with solid-air contact interface (S1-Air, 100 repetitions).

7.1.3 Comparison of Pitch-Catch Transmission and Reflection Configurations

Combining the pitch-catch transmission test with contact interface and without contact interface, as shown in Figure 7.13, it is reasonable to conclude that the third harmonic generation originates from the interface and the interaction of the shear wave with the frictional interface, e.g. the 'slip-stick' motion, is the source of the

nonlinearity. Although some systems inherent nonlinearity is measured in the single test specimen, the amplitude is much less than that from the interface. In the pitch-catch transmission configuration, the nonlinearity originates from the interface is detectable.

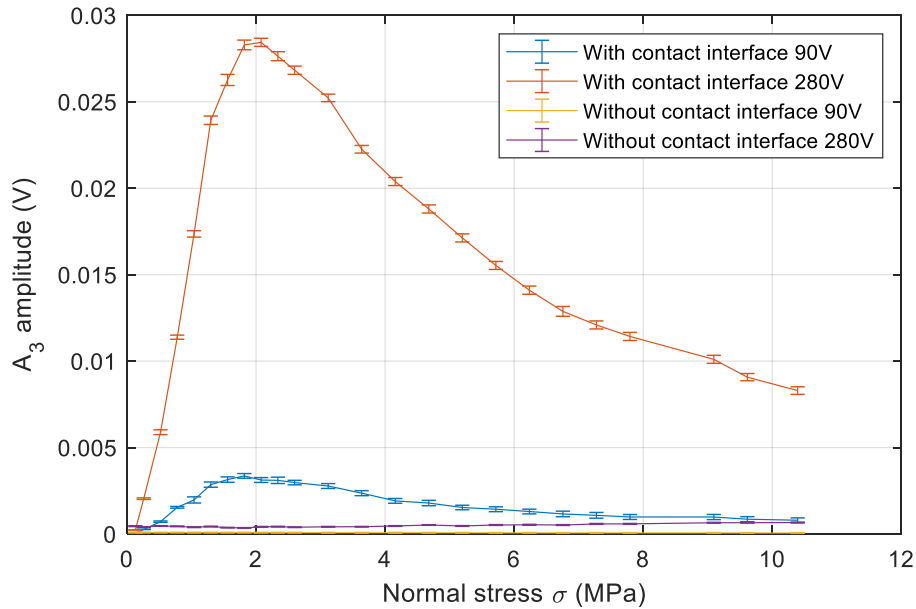


Figure 7.13 The third harmonic amplitude A_3 of test with contact interface (L1-S4) and without contact interface (H1) using pitch-catch transmission configurations (100 repetitions).

For the pitch-catch reflection test with solid-solid and solid-air interface, (Figure 7.14) it also concludes that the third harmonic generation occurs due to the interaction of the shear wave with the frictional contact interface, e.g. the 'slip-stick' motion. In the pitch-catch reflection configuration, that nonlinearity originates from the interface is detectable.

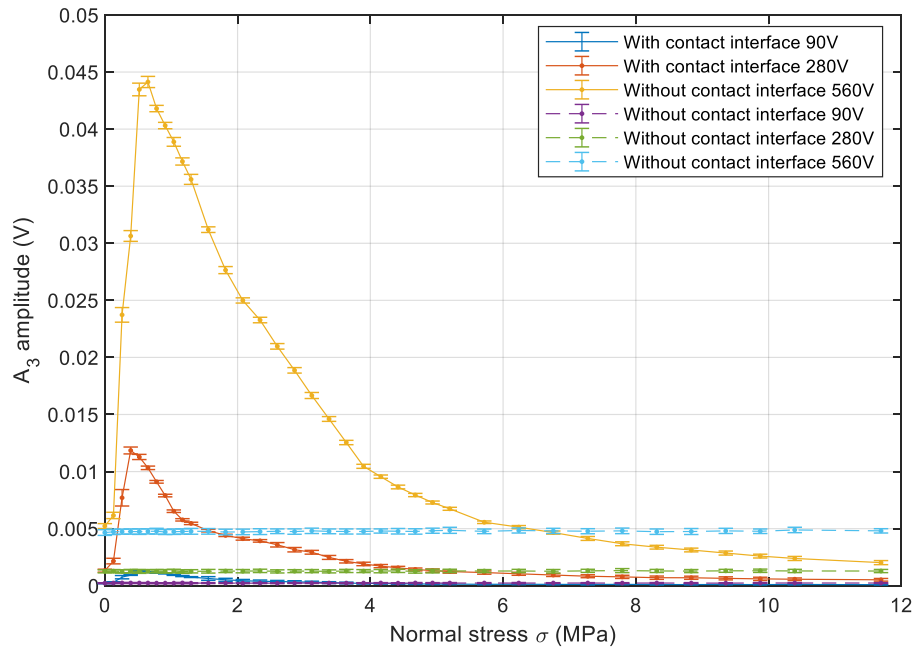


Figure 7.14 The third harmonic amplitude A_3 of test with solid-solid interface (S1-S4) and solid-air interface (S1-Air) using pitch-catch reflection configuration (100 repetitions).

Both pitch-catch transmission and reflection configurations are applicable to the measurement of the harmonic generation originating from a rough interface. Such results also agree with the finding from previous theoretical and numerical study, that higher order harmonics appear in both transmission and reflection (O'Neill et al., 2001). Both test arrangements following the high frequency nonlinear ultrasonic technique prove their usefulness in measuring the contact nonlinearity due to interaction of a shear wave and a frictional interface.

However, practically that the pitch-catch transmission configuration is more challenging to achieve test results, compared to the reflection configuration. In both transmission arrangement (Figure 7.13) and reflection configuration (Figure 7.14), the peak of the third order harmonic occurs at low contact stress region. At such regions, conformal contact is not fully developed as the asperities still deform and yield, which result in an increased transmission and reflection decrease. Figure 7.15 schematically shows how the gaps between the contact asperities hinder the transmission of ultrasound. Although an ultrasonic wave with distortion can travel through the interface, the transmitted wave fails to carry much information of the nonlinear interaction at the interface. When the normal stress is large, and the contact is developed, where the transmission and reflection remain stabilised, the harmonic generation, however, is impeded to occur because the likelihood of slip is reduced.

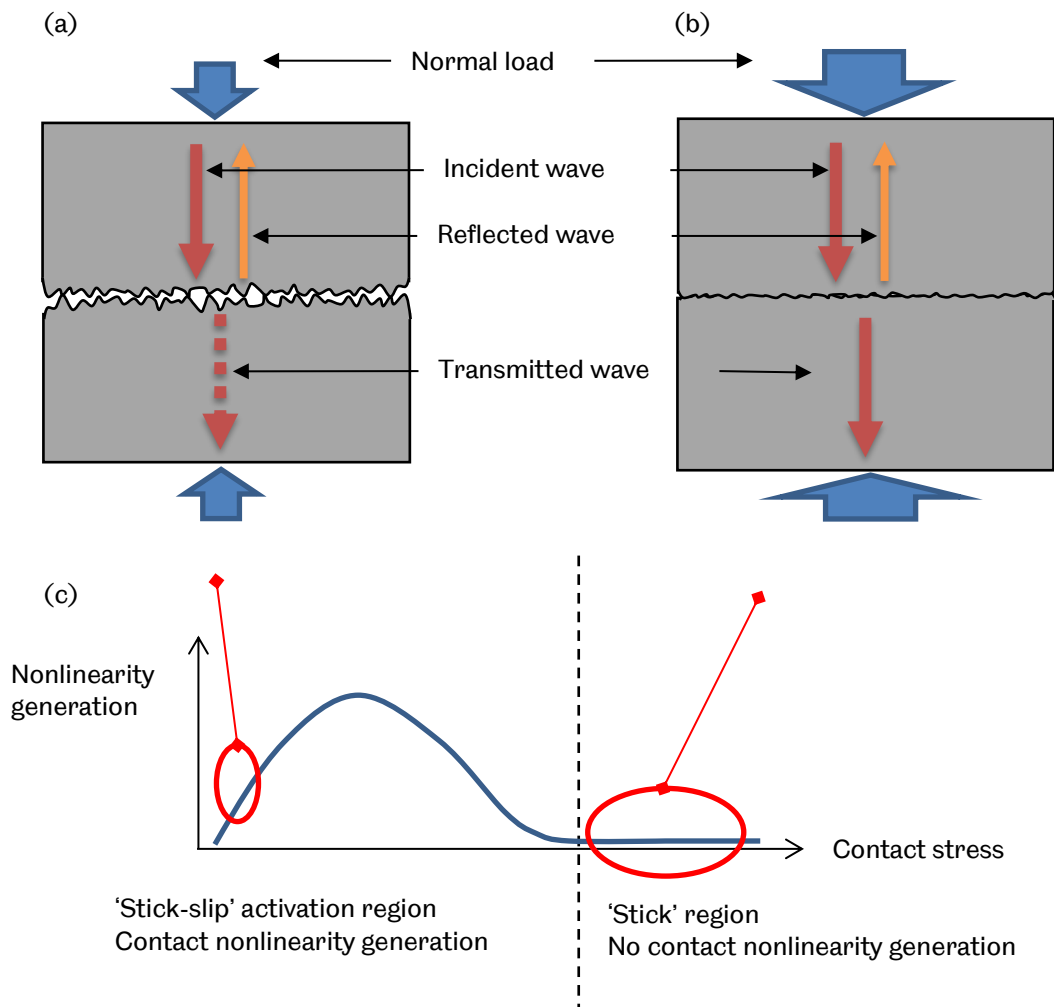


Figure 7.15 (a) Two test specimens with contact interface under low normal loads. (b) Two test specimens with contact interface under high normal loads. (c) Contact nonlinearity generation region for (a) and (b).

An example of such case is illustrated in Figure 7.16. In the sensitive region of the contact nonlinearity generation (low normal stress), both first and third harmonic frequency amplitudes are hardly noticeable. The third harmonic amplitude A_3 does not show apparent 'rise-fall' trend. Even though the nonlinear interaction of the shear polarised ultrasound with the rough interface occurs, the transmitted signal is weak, and the harmonic generation is missed unintentionally (Figure 7.17 (a)).

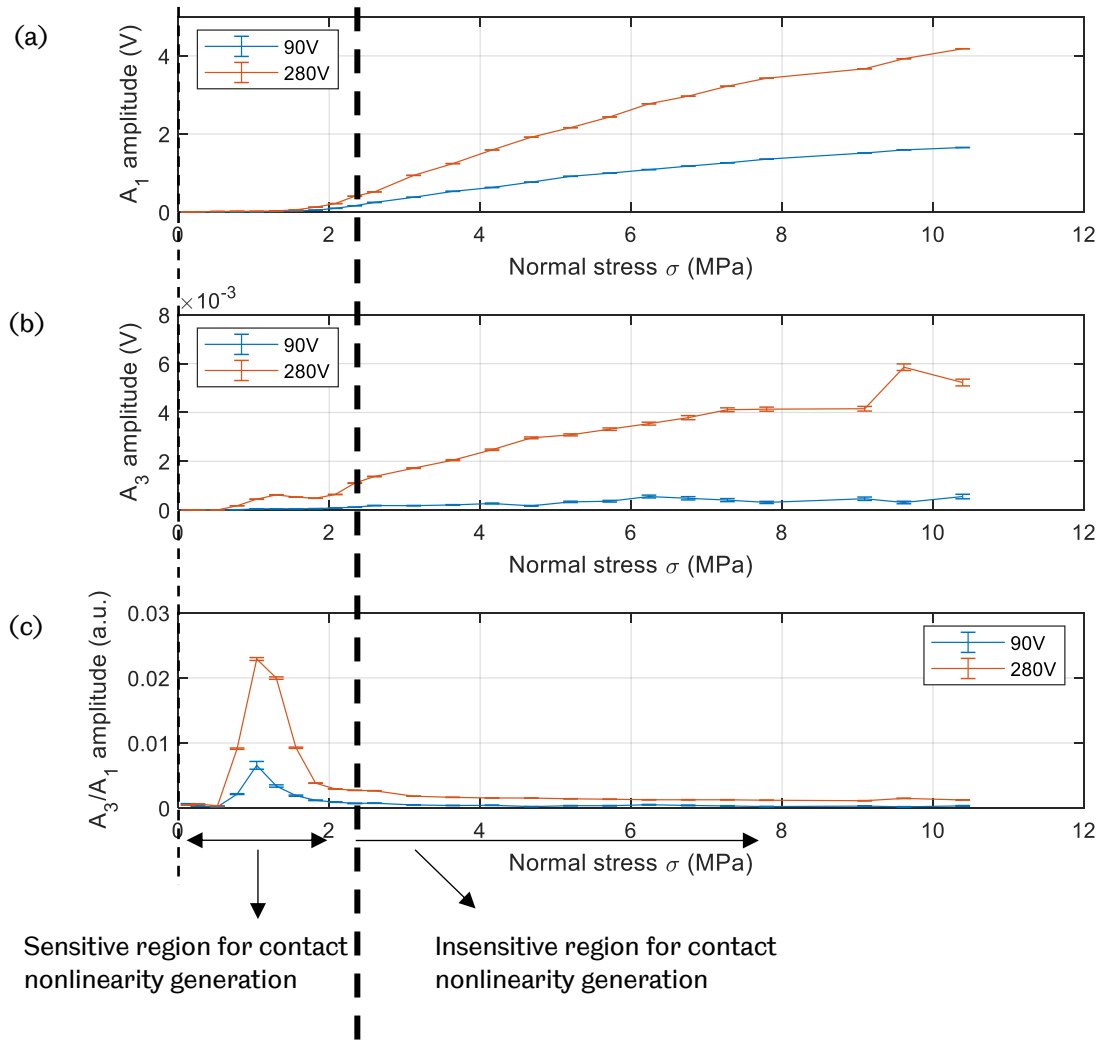


Figure 7.16 (a) Fundamental frequency amplitude A_1 , (b) The third order harmonic A_3 , (c) The ratio A_3/A_1 subject to various normal stresses and incident amplitudes of the pitch-catch transmission arrangement (L1-S4, 100 repetitions).

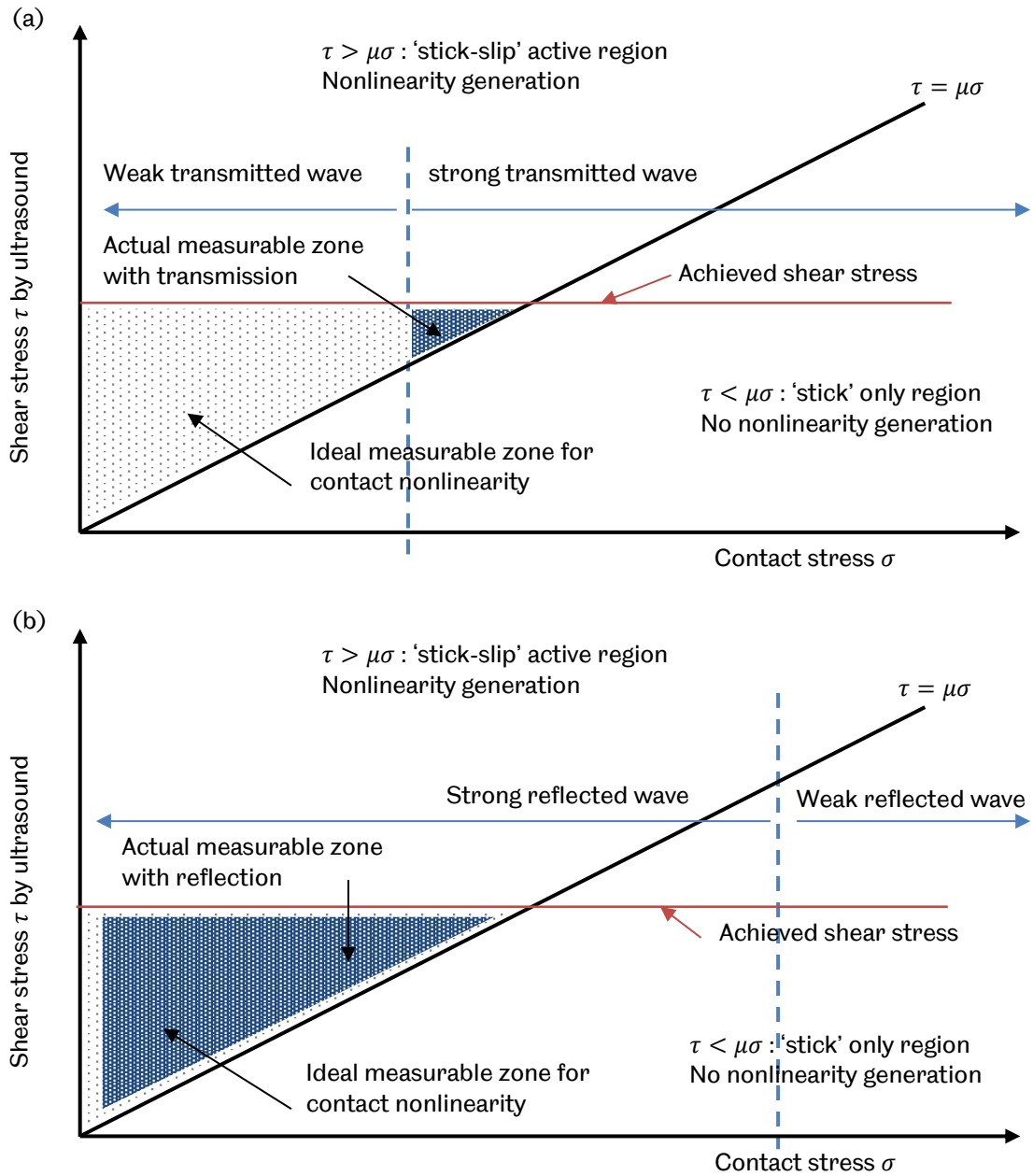


Figure 7.17 Contact nonlinearity measurable zone. (a) Limited measurable zone for transmission configuration. (b) Measurable zone for reflection configuration.

With the novel reflection arrangement, although it is decreasing when normal stress is increasingly applied, the 'always'-noticeable reflected signal ensures the detection of the contact-generated harmonics (Figure 7.17 (b)).

The other practical advantage of the pitch-catch reflection configuration over the transmission is that it provides the feasibility of taking measurement from one side of the contact interface. In the laboratory condition, access to the contact interface from both sides by placing one transducer on each side can be achieved without much difficulty. However, in most mechanical components only one-side access is practically possible. In such cases, the transmission configuration is not useful at all while the reflection arrangement shows its flexibility of placing ultrasonic transducers on the same side of a contact interface.

Due to the practical benefits of the good contact harmonics generation detection and flexibility of instrumentation, the novel pitch-catch reflection configuration is therefore applied for all the following tests.

7.2 Method of Removing Nonlinearity from Other Sources

From previous test results it is noticed that the third order harmonic amplitude is non-zero for both the single test specimen in the transmission arrangement and the solid-air contact interface in the reflection configuration, where no solid-solid interface is formed. Clearly the measurement harmonic cannot be generated from the contact interface because there isn't one. The only source of such nonlinearity is the measurement system. It is of significance to understand the influence of the system built-in harmonics to the nonlinearity originated at the rough interface. As discussed previously, the pitch-catch reflection configuration is employed in the following tests.

7.2.1 Solid-Air Contact Interface

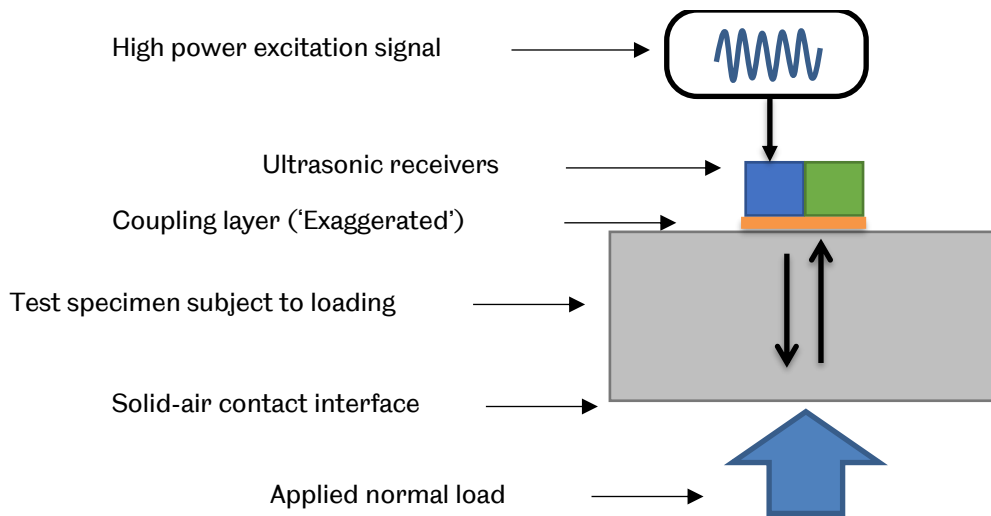


Figure 7.18 Possible source of system built-in nonlinearity from in the solid-air contact interface test using pitch-catch arrangement.

Table 7.3 Possible source of nonlinearity in the solid-air contact interface using pitch-catch reflection arrangement.

Ultrasonic transducer	Higher order harmonics are also generated even when it is driven at its main resonant frequency, e.g. the fundamental frequency.
High power amplifier	When the fundamental frequency is amplified, the higher order odd harmonics are also amplified to some extent.
Coupling layer	Coupling material may behave nonlinearly due to the internal structure, when subject to high stress.
Test specimen	Test specimen may behave nonlinearly due to the internal structure, when subject to high stress.
Loadings	Load may change the material behaviour from linear to nonlinear.

In the pitch-catch reflection arrangement, it is straightforward to use the solid-air contact interface to account for the system built-in nonlinearity. Figure 7.18 indicates several possible sources of the system built-in nonlinearity, which are listed in Table 7.3. The effect of each source cannot easily be investigated individually

as they are coupled. It is reasonable to treat these sources as a single source of harmonic generation.

Table 7.4 Test conditions in solid-air contact interface.

	Solid-air contact interface
Test specimen	Al Alloy 6082 S1
Transducer	V153-V155
Waveform	15-cycle 1MHz sine wave
Excitation voltage	1V – 420V (peak-peak)
Normal force	0 – 45 kN

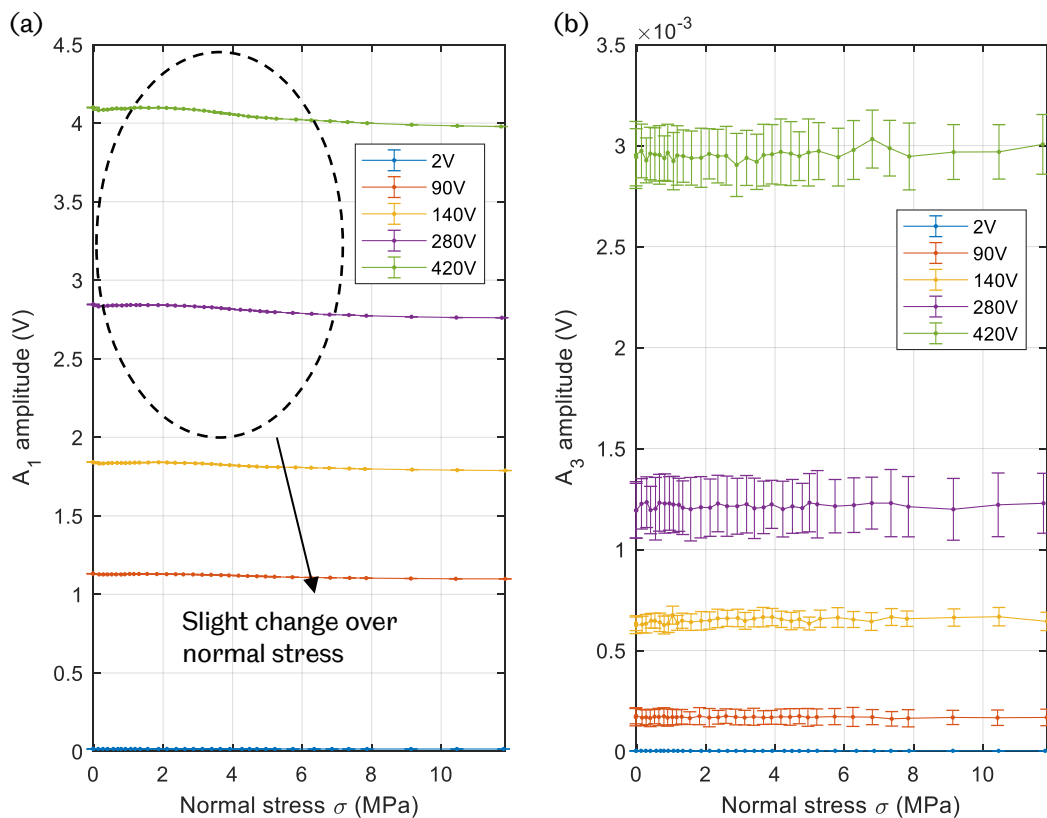


Figure 7.19 (a) The fundamental frequency amplitude A_1 , (b) The third harmonic amplitude A_3 of solid-air contact interface (S1-Air) subject to various amplification levels and normally applied loads (100 repetitions).

Test conditions are summarised in Table 7.4. Figure 7.19 shows the fundamental frequency A_1 and the third harmonic amplitude A_3 of the solid-air contact interface subject to various normal stresses and excitation levels. It is noticed that the fundamental frequency amplitude A_1 drops slightly with the increasing normal stress, although the test specimen contacts only with air. The third harmonic amplitude A_3 , although showing slight fluctuations, is reasonably constant over the normal stress, even under the high amplification is applied. Relatively large deviations (10%) for the third harmonics are shown in Figure 7.19 (b) for solid-air interface as there is no extra harmonic from the contact and it measures the system inherent nonlinearity.

As the fundamental frequency A_1 is still affected by the normal stress, the third harmonic A_3 can be treated as independent of the normal stress (Equation (7.1)) and the fundamental frequency A_1 (Equation (7.2)). It is only influenced by the excitation levels used, i.e. the amplitude of the incidence wave (Equation (7.3)).

$$A_3^{system} \neq f(\sigma) \quad (7.1)$$

$$A_3^{system} \neq f(A_1) \quad (7.2)$$

$$A_3^{system} = f(A_{inc}) = f(Voltage) \quad (7.3)$$

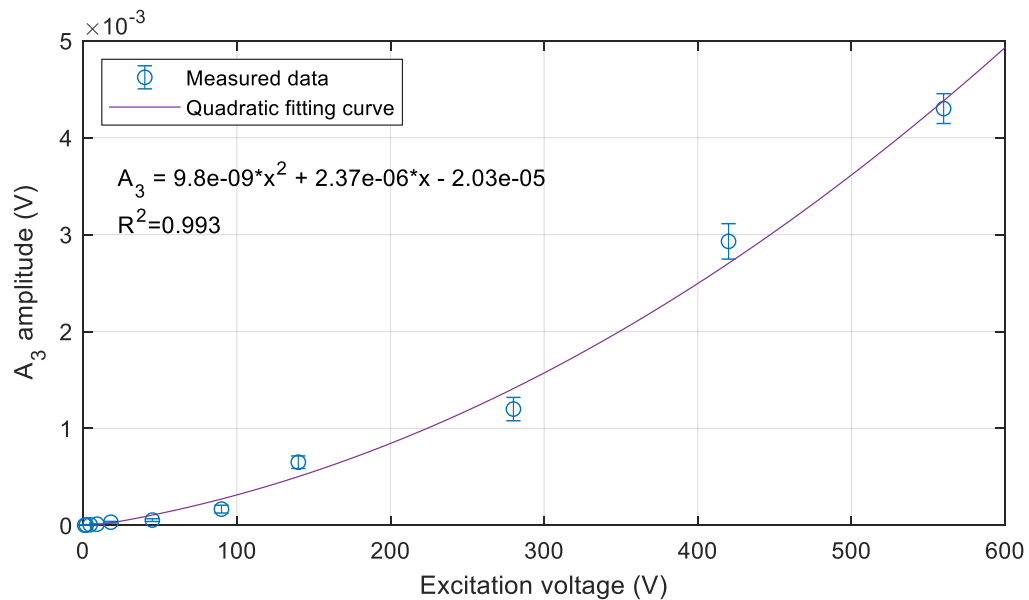


Figure 7.20 The third harmonic amplitude A_3 of solid-air contact interface (S1-Air) subject to various excitation voltages (100 repetitions).

The dependence of averaged third harmonic amplitudes A_3 on the excitation voltage is clearly depicted in Figure 7.20. At low excitation voltage, the third harmonic increases reasonably linearly with the rising voltage. When high excitation voltage is applied (greater than 100V), the harmonic amplitude rises dramatically. This may be due to the high excitations used. The third harmonic amplitude increases with excitation voltages approximately quadratically as the quadratic fitting function shown in Figure 7.20. High voltage excitation not only triggers the higher order frequency of an ultrasonic transducer, the resulted high amplitude ultrasound wave also increasing the likelihood of occurrence of some intrinsic material nonlinearities. From the solid-air interface test, the system built-in nonlinearity shows independence of the normal load applied and it is heavily affected by the excitation voltage or the amplitude of the incidence wave.

7.2.2 Solid-Solid Contact Interface with Low Power Input

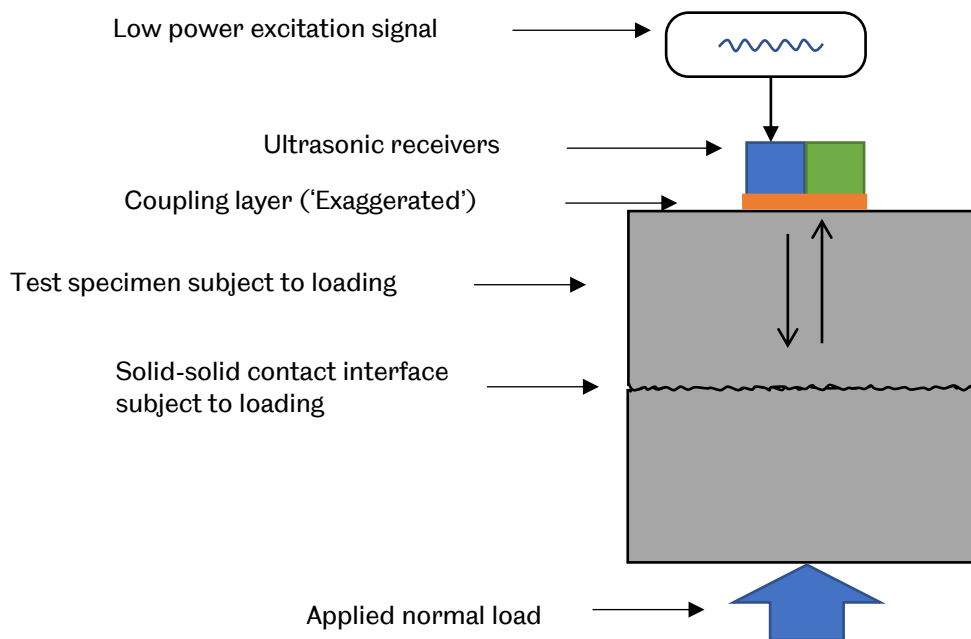


Figure 7.21 Possible source of system built-in nonlinearity from in the solid-solid contact interface test using pitch-catch arrangement subject to low power input.

A more practically case to consider the source of nonlinearity generation is the solid-solid interface subject to low power input, as shown in Figure 7.21. The possible sources are listed in Table 7.5. The rough interface is taken into account so the effect

of normal applied stress can be better understood. The low excitation voltage is applied to ensure that with such low power input, the nonlinear interaction of the shear wave with the frictional contact interface, e.g. ‘stick-slip’ motion is highly unlikely to occur.

Table 7.5 Possible source of nonlinearity in the solid-solid contact interface under low power input using pitch-catch reflection arrangement.

Ultrasonic transducer	Higher order harmonics are also generated even when it is driven at its main resonant frequency e.g. the fundamental frequency.
Coupling layer	Coupling material may behave nonlinearly due to the internal structure, when subject to high stress.
Test specimen	Test specimen may behave nonlinearly due to the internal structure, when subject to high stress.
Loadings	Load may change the material behaviour from linear to nonlinear.
Solid-solid contact interface	Potentially source of harmonic generation when subject to stresses.

Table 7.6 Test conditions in solid-air contact interface.

	Solid-solid contact interface
Test specimen	Al Alloy 6082 S1-S2, S3 and S4
Transducer	V153-V155
Waveform	15-cycle 1MHz sine wave
Excitation voltage	2V (peak-peak)
Normal force	0 – 45 kN

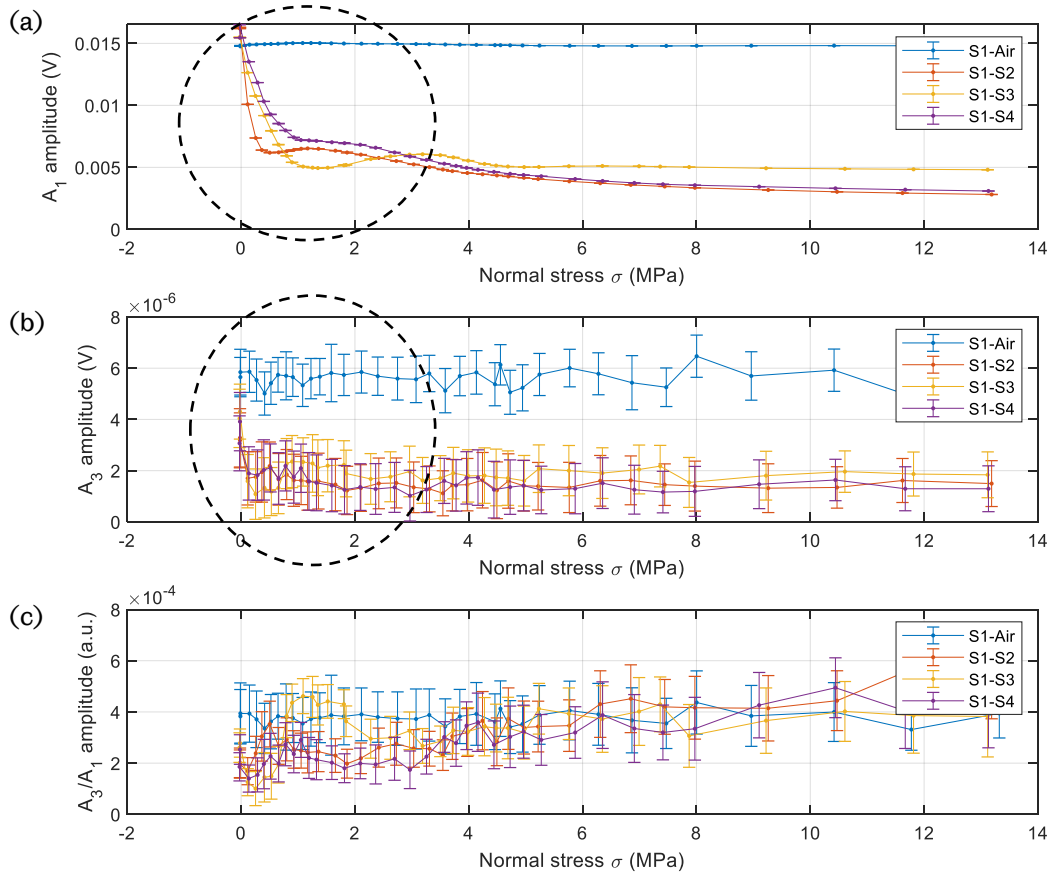


Figure 7.22 (a) The fundamental frequency amplitude A_1 , (b) The third harmonic amplitude A_3 , (c) The ratio A_3/A_1 of reflected signal from solid-solid contact interface subject to low amplification (2V peak-peak) and normally applied loads (100 repetitions).

Test conditions of the solid-solid interface are listed in Table 7.6. The fundamental frequency A_1 and the third harmonic A_3 are depicted in Figure 7.22 with the low power input. The effect of loadings at the interface is significant even the amplitude is low. Due to the presence of the interface and the increasing of the normally applied stress, less ultrasound is reflected, which result in the drop of both fundamental and the third harmonic amplitude. The third harmonic amplitude falls quickly when the contact stress starts to increase. At higher contact loadings, both signal reaches the minimum and stabilise. The amplitude ratio A_3/A_1 also shows increasing trend with the applied normal stress.

As a comparison, the solid-air interface is also plotted in Figure 7.22 and fundamental, the third order frequency and their ratio remain unchanged when subject to the same range of normal contact stresses.

Due to the existence of the contact interface, the harmonic amplitude contains both the system built-in nonlinearity and the nonlinearity due to the contact at low power

input. The relationship previously shown in Equation (7.1)-(7.3) can be modified as follows:

$$A_3^{system} + A_3^{low-power Contact} = f(\sigma) = f(A_1), \quad (7.4)$$

$$(A_3^{system} + A_3^{low-power Contact})/A_1 = f(\sigma). \quad (7.5)$$

7.2.3 Input Power Evolution

It is worth looking into the solid-solid interface when the input power gradually increases. The test conditions are listed in Table 7.7. The fundamental frequency A_1 decreases with the increased normal contact stress, as shown in Figure 7.23, regardless of input powers or the excitation voltages. The third harmonic amplitude A_3 and the amplitude ratio A_3/A_1 demonstrates distinct behaviour under different input excitation voltages, as depicted in Figure 7.24.

Table 7.7 Test conditions in solid-solid contact interface: power evolution.

	Solid-solid contact interface
Test specimen	Al Alloy 6082 S1- S4
Transducer	V153-V155
Waveform	15-cycle 1MHz sine wave
Excitation voltage	2, 5, 9, 45V (peak-peak)
Normal force	0 – 45 kN

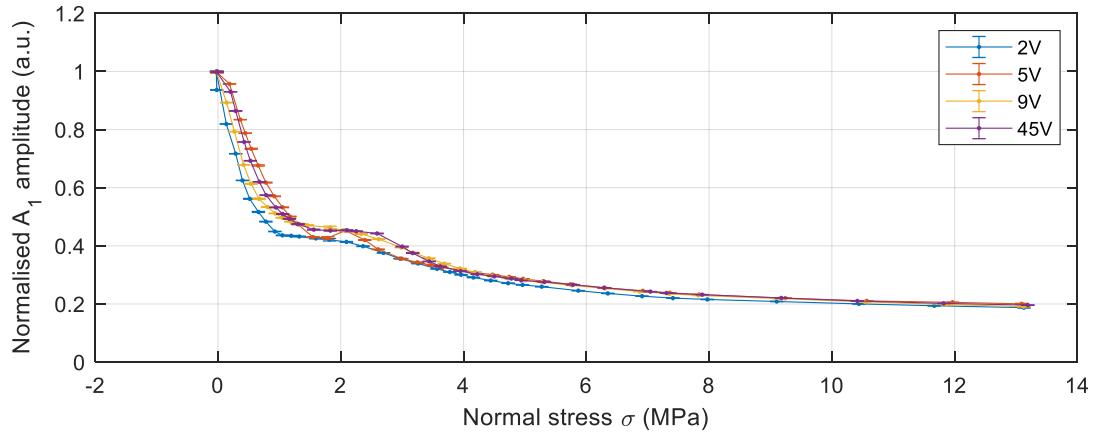


Figure 7.23 The normalised fundamental frequency amplitude A_1 of reflected signal from solid-solid contact interface (S1-S4) subject to various amplification and normally applied loads (100 repetitions)

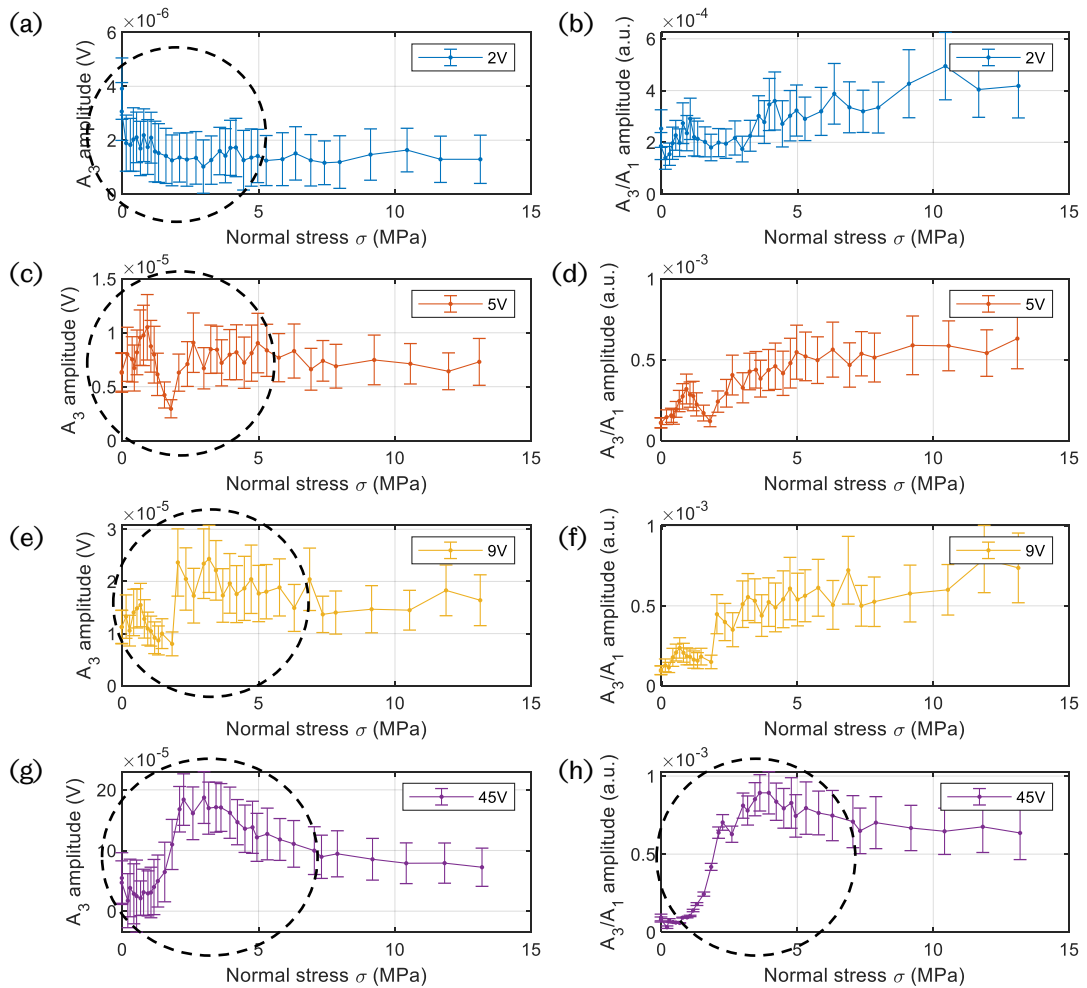


Figure 7.24 The third harmonic amplitude A_3 and the ratio A_3/A_1 of reflected signal from solid-solid contact interface (S1-S4) subject to various normally applied loads at excitation voltage (a) and (b): 2V; (c) and (d): 5V; (e) and (f) 9V; (g) and (h): 45V. (100 repetitions).

When the input power is low (Figure 7.24 (a)), the third harmonic still follows a similar trend as the fundamental frequency illustrated in Figure 7.23. When increasing the excitation slightly (Figure 7.24 (c) and (e)), the third harmonic A_3 shows no reduction when the contact interface starts to compress. The amplitude ratio when such relatively low excitation voltage is applied shares a resembling linearly increasing tendency. When a higher amplification is used, the third order harmonics, however, exhibit a 'rise-fall' pattern with the increasing normal contact stress. In such case, the power is large enough to activate the nonlinear interaction of the shear ultrasound and the rough interface.

In the input power evolution test, nonlinearity from two origins, the system built-in nonlinearity and the contact interface introduced nonlinearity involve in the harmonic generation. At the low excitation voltage, the system inherent nonlinearity dominates. When the input power is increased, more system built-in nonlinearity is also generated. The contact nonlinearity gradually becomes significant rises and outpaces the system intrinsic nonlinearity. When high power is used, nonlinearity originates from the contact interface dominates the total nonlinearity generated.

7.2.4 Reference Consideration and Contact Harmonic Estimation

As shown in the previous section, when high power ultrasound is used, both system inherent nonlinearity and the harmonic originating from rough contacts are measured. Although the amplitude is insignificant, compared to the nonlinearity generation due to contact, the system built-in harmonic still needs to be separated and eliminated. The harmonic amplitudes obtained at high normal contact stress and the low power input is treated as the nonlinearity arisen inside the system (Blanloeuil et al., 2014c) as under such conditions, the nonlinear 'slip-stick' motion is not activated as the frictional force is considered significant than the ultrasound introduced shear stress.

7.2.4.1 Estimation Using Low Power Solid-Solid Contact

As shown in Section 7.2.2 the system inherent nonlinearity in the solid-solid contact interface at low power shows the dependence on the normal applied load, it is reasonable to make the assumption that at high ultrasonic input amplitude which allows the activation of 'slip-stick' motion, the system built-in nonlinearity follows the same trend as in the low power case where the 'slip' motion is not triggered. A scaling factor, C_a is defined in Equation (7.6).

$$C_a = (A_3^{system} + A_3^{low-power Contact})/A_1$$

$$= \frac{A_3^{measured}}{A_1^{measured}} \Big|_{low-power Contact} \quad (7.6)$$

$$A_3^{system} \Big|_{high-power Contact} = C_a \times A_1 \Big|_{high-power Contact} \quad (7.7)$$

$$A_3^{contact} = A_3^{measured} \Big|_{high-power Contact} - A_3^{system} \Big|_{high-power Contact} \quad (7.8)$$

The system built-in nonlinearity is estimated by multiplying the scaling factors a with the measurement fundamental frequency amplitude A_1 (Equation (7.7)) and it is then subtracted from the measured third harmonic A_3 , which leads to the contact nonlinearity.

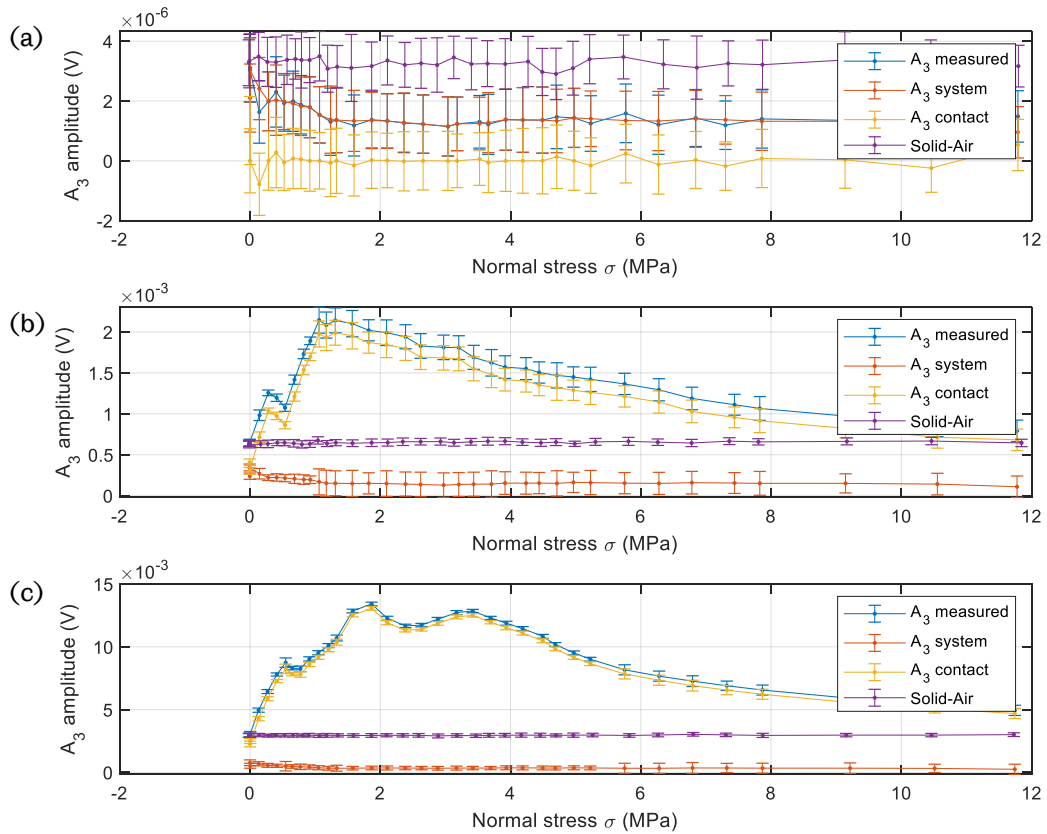


Figure 7.25 The measured third harmonic of a reflected signal, the system harmonic and the contact harmonic subject to various loads at (a) 2V, (b) 140V and (c) 420V. (S1-S4, 100 repetitions).

The measured third harmonic, $A_3^{measured}$ the system built-in harmonic, A_3^{system} and the contact harmonic, $A_3^{contact}$ are depicted in Figure 7.25. When low input power is applied, the harmonic generation is assumed inactivated and the contact harmonic is approximately zero Figure 7.25 (a). In Figure 7.25 (b) and (c), higher power ultrasound is applied to the solid-solid contact interface and the nonlinear ‘slip-stick’ interaction is enabled. The contact harmonic still able to show the typical ‘rise-fall’ shaped trend.

Although the contact harmonic, $A_3^{contact}$ is estimated at various input ultrasonic power, the effect of the input ultrasonic amplitude is not accounted properly. At ‘zero’ stress condition, the contact is intentionally configured as solid-air interface and the contact harmonic should be zero, while it is non-zero in Figure 7.25 (b) and (c).

7.2.4.2 Estimation Using Solid-Air Contact

In this approach the effect of incident amplitude is considered using the solid-air contact interface measurement, as shown in Section 7.2.1. The scaling factor, C_b and contact harmonic estimation is shown in Equation (7.9)-(7.11):

$$C_b = \frac{A_3^{system} |_{high\ power\ solid-air}}{A_3^{system} |_{low\ power\ solid-air}} = \frac{A_3^{measured} |_{high\ power\ solid-air}}{A_3^{measured} |_{low\ power\ solid-air}}, \quad (7.9)$$

$$A_3^{system} |_{high-power\ Contact} = C_b \times A_3 |_{low-power\ Contact}, \quad (7.10)$$

$$A_3^{contact} = A_3^{measured} |_{high-power\ Contact} - A_3^{system} |_{high-power\ Contact} \quad (7.11)$$

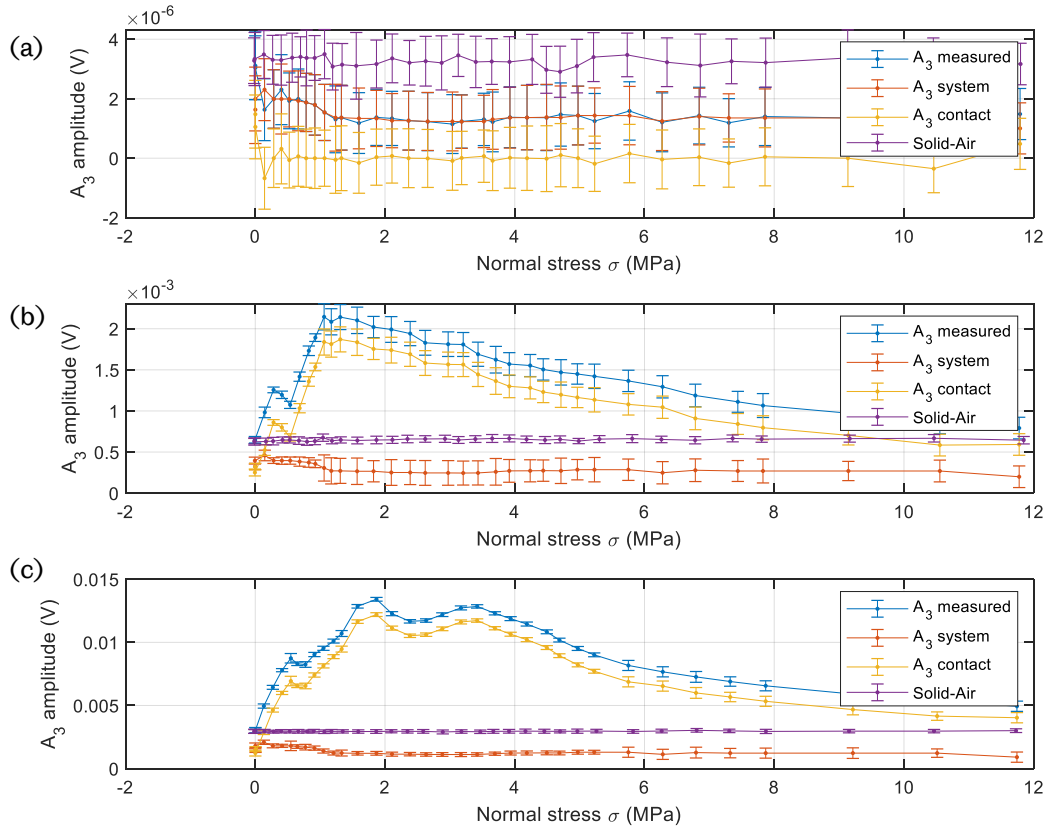


Figure 7.26 The measured third harmonic of a reflected signal, the system harmonic and the contact harmonic subject to various loads at (a) 2V, (b) 140V and (c) 420V. (S1-S4, 100 repetitions).

The measured third harmonic, $A_3^{measured}$ the system built-in harmonic, A_3^{system} and the contact harmonic, $A_3^{contact}$ using the revised equations are illustrated in Figure 7.26. Similar information as demonstrated in Figure 7.25 is obtained. It is worth noticing that at 'zero' stress condition where the contact is in solid-air status, the contact harmonic, is approaching zero compared with that estimated using previous approach. The system harmonic also accounts more in the measured third harmonic.

7.2.4.3 Estimation Using Solid-Air Contact with Low Power Solid-Solid Contact

It is reasonable to combine the previous two approaches to estimate the nonlinearity from the contact interface. Scaling factor C_a and C_b are then applied to the measured third harmonic in the meantime. Equations for estimating both system and contact nonlinearity are modified as follows:

$$\begin{aligned}
A_3^{system} \Big|_{high-power\ Contact} &= C_a \times C_b \times A_1 \Big|_{high-power\ Contact} \\
&= \frac{A_3^{measured}}{A_1^{measured}} \Big|_{low-power\ Contact} \\
&\times \frac{A_3^{measured} \Big|_{high\ power\ solid-air}}{A_3^{measured} \Big|_{low\ power\ solid-air}}
\end{aligned}
\tag{7.12}$$

$$\begin{aligned}
A_3^{contact} &= A_3^{measured} \Big|_{high-power\ Contact} \\
&- A_3^{system} \Big|_{high-power\ Contact}
\end{aligned}
\tag{7.13}$$

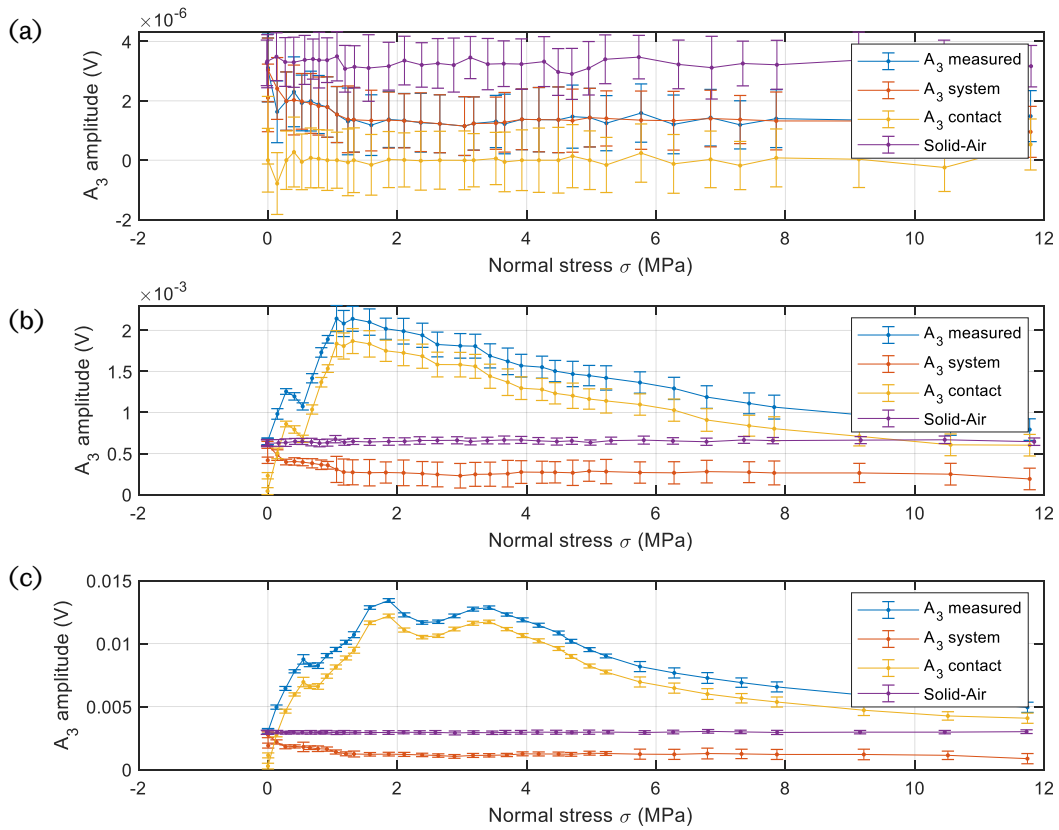


Figure 7.27 The measured third harmonic of a reflected signal, the system harmonic and the contact harmonic subject to various loads at (a) 2V, (b) 140V and (c) 420V. (S1-S4, 100 repetitions).

Using the revised approach, at higher ultrasonic input amplitudes, the harmonic follows the same trend as the measured third harmonic (Figure 7.27). At the ‘zero’ stress condition (solid-air interface), the third harmonic approaches zero,

indicating no system harmonic is considered. When the contact is gradually compressed, the third harmonic only indicates the nonlinearity originating from the rough interface.

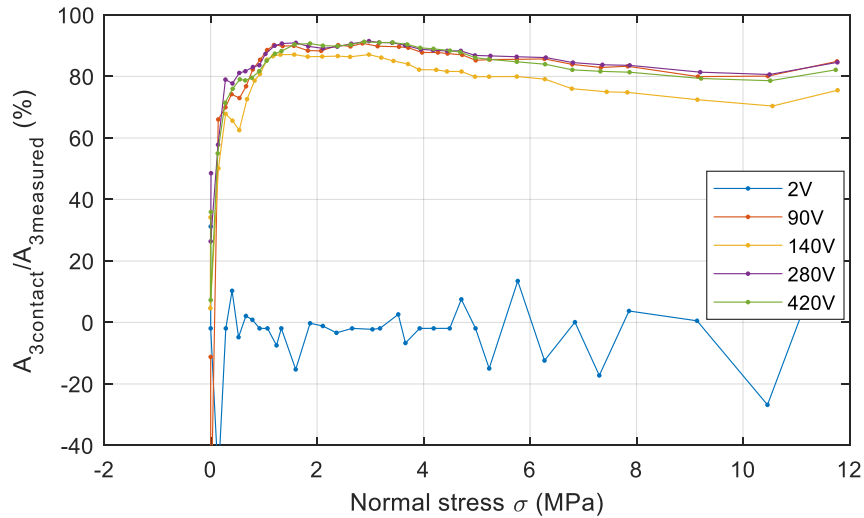


Figure 7.28 Percentage of contact harmonic in the total measured third harmonic amplitude of test specimen S1-S4.

The weight of the contact harmonic to the total measured third harmonic amplitude is depicted in Figure 7.28. When high input power is used, i.e. above 90V, as the interface is compressed, the contact nonlinearity increases to approximately 90% of the total measured harmonics and then falls to 80% when the normal contact stress is high. For the low input power, i.e. 2V, the low amplitude incident shear wave is unable to trigger the ‘stick-slip’ motion the contact and no harmonic is generated from the contact. Therefore contact nonlinearity remains 0% for low input power.

The approach of estimating contact harmonic using the solid-air interface and the low-power solid-solid interface enables the separation of the system built-in nonlinearity from the nonlinearity arising from the rough interface. This approach is used in the following tests.

7.3 Normally Incident Shear Wave Results

Using the pitch-catch reflection arrangement and the contact harmonic estimation method described in previous sections, the effect of the amplitude of incident

ultrasound and the normally applied contact stress on the ultrasonic nonlinearity generation at a rough interface is studied.

7.3.1 Varying Incident Amplitude

As discussed in Section 7.2.3, when the incidence ultrasound amplitude is increased gradually from a low-power condition where the nonlinear interaction is inactivated, to a high incident amplitude where ‘stick-slip’ motion is triggered, the third harmonic amplitude A_3 starts to show the ‘rise-fall’ feature along with the applied normal contact stress. The contact harmonic is depicted in Figure 7.29. The at low incidence amplitude, e.g. $1V_{p-p}$ and $5V_{p-p}$, the contact harmonic is approximately zero (Figure 7.29 (a)) and the corresponding normalised amplitudes fluctuate without a clear trend (Figure 7.29 (b)). With the higher input power where the ‘stick-slip’ occurrence is enabled, the typical ‘rise-fall’ tendency clearly shows ($45V_{p-p}$ and $90V_{p-p}$ in Figure 7.29).

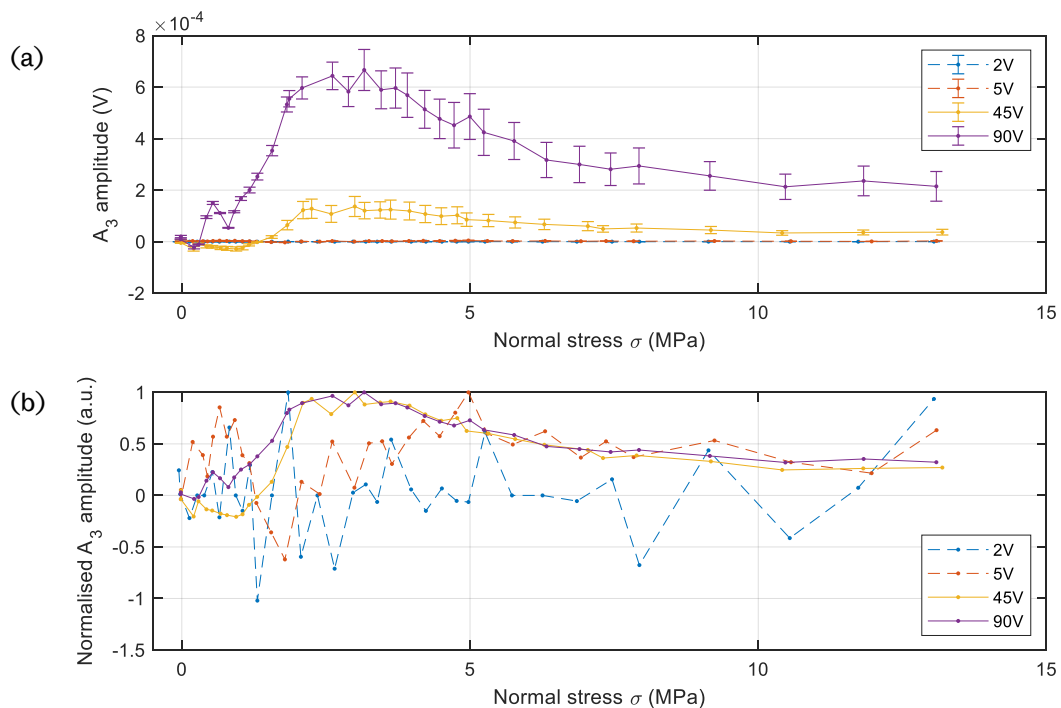


Figure 7.29 (a) Contact harmonic amplitude; (b) normalised contact harmonic amplitude subject to lower power inputs.

It is worth looking at the effect of the incidence amplitude when the higher power ultrasound is employed to strike the interface and in such case the source of the contact nonlinearity - 'stick-slip' motion activation is always enabled, as illustrated in Figure 7.29. Shear wave ultrasound was triggered with higher excitation voltages, from $90V_{p-p}$ to $450V_{p-p}$ and the representative 'rise-drop' pattern is observed on the contact nonlinearity for all incidence amplitudes.

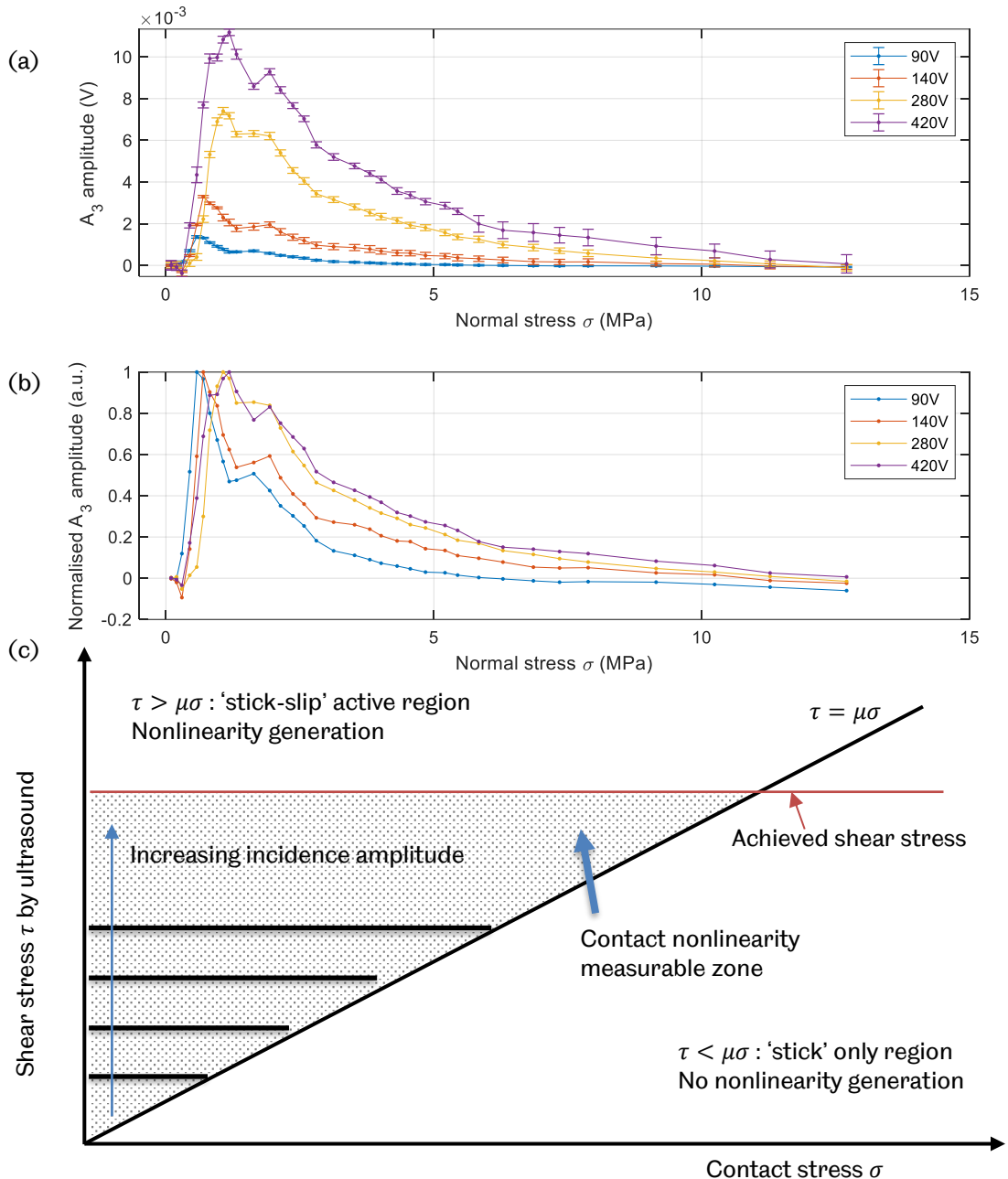


Figure 7.30 (a) Contact harmonic amplitude; (b) Normalised contact harmonic amplitude subject to higher power inputs. (c) Measurable zone for increasing incidence amplitude.

Larger contact nonlinearity is generated when a higher incident amplitude is applied and the interface is compressed at that same stress. Larger incidence amplitudes appear to allow the nonlinearity originated over a wider stress range in Figure 7.30 (a), as the higher input power would potentially trigger the 'slip' motion when the frictional force is larger at the interface. In Figure 7.30 (b) the dependence of the activation stress range on the input power is unclear and for different incidence amplitudes, the normalised contact harmonic overlap. The peak of the contact nonlinearity under varying incident amplitudes are shown in Figure 7.31. Larger incident amplitude results in the contact nonlinearity generation over a wider stress range. The contact nonlinearity peaks at a larger normal stress.

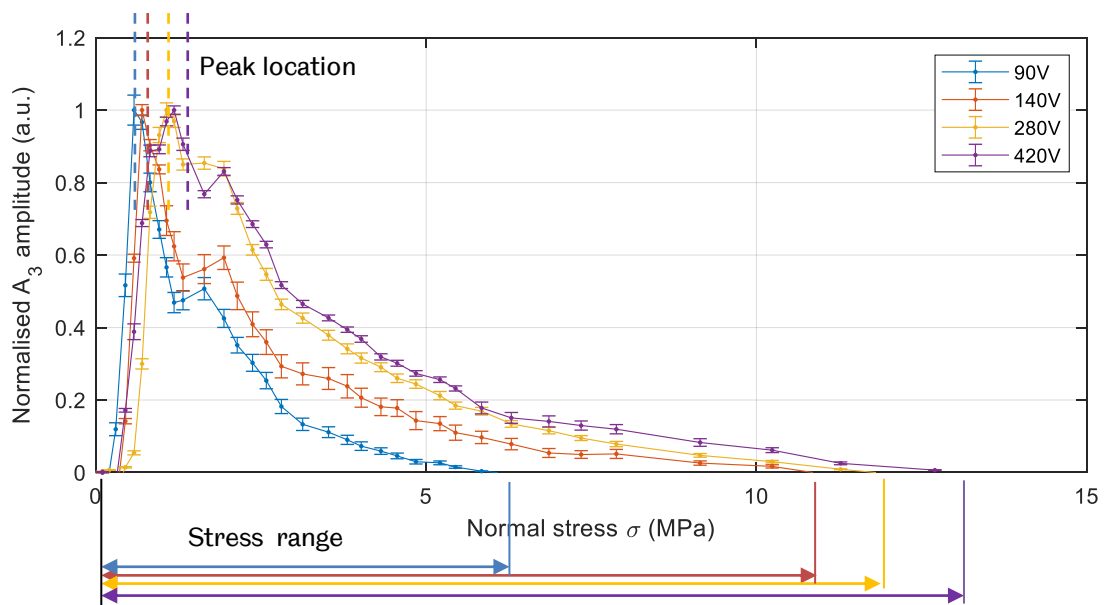


Figure 7.31 Normalised contact harmonic amplitude and fitting curve subject to higher power inputs (Test specimen S1-S4, 100 repetitions).

7.3.2 Varying Contact Stress

The effect of varying normal contact stress has been discussed in the previous sections. As shown in Figure 7.32 (b), when a sufficiently large incident amplitude is applied and 'slip-stick' occurs, the contact nonlinearity shows the 'rise-fall' trend with the applied normal stress. At low contact stress (Figure 7.32 (a)), a contact interface is just formed between the two test specimens, and only a few asperity contacts occur. The nonlinear 'slip-stick' motion may only be triggered at a low

extent. When the contact is increasingly compressed, more asperities are brought to contact which is in favour of the nonlinearity generation at the contact interface (Figure 7.32 (b)). In this development, the contact nonlinearity generation reaches a peak where the interaction of the high-power shear wave with the rough contact is maximum (Figure 7.32 (b)). Further higher normal stress applied to the contact results in more asperities sticking and the resulting frictional force is too high for the shear wave introduced shear stress to overcome. Then, the 'slip-stick' motion is suppressed, which leads to a decreasing contact harmonic at high normal stress.

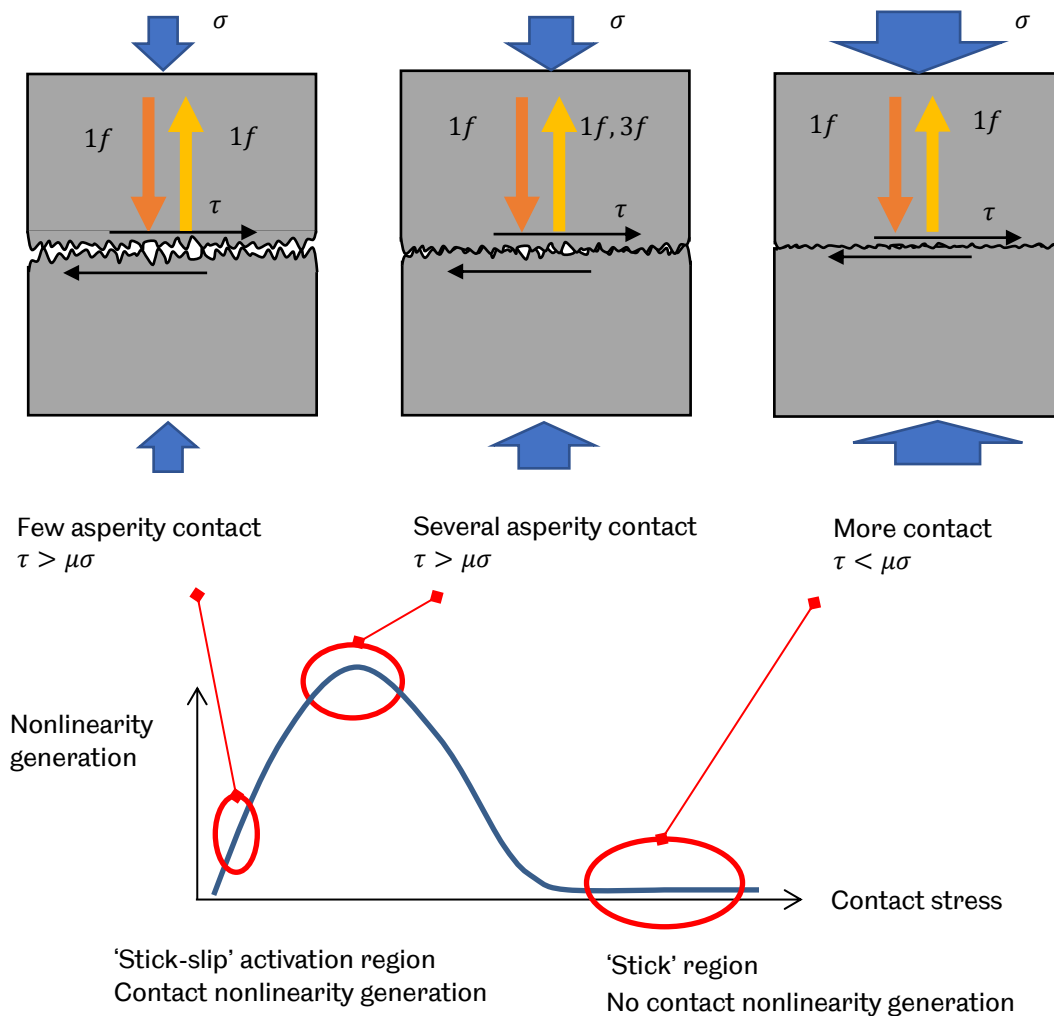


Figure 7.32 Two test specimens with contact interface under (a) low normal stress; (b) higher normal stress and (c) high normal stress.

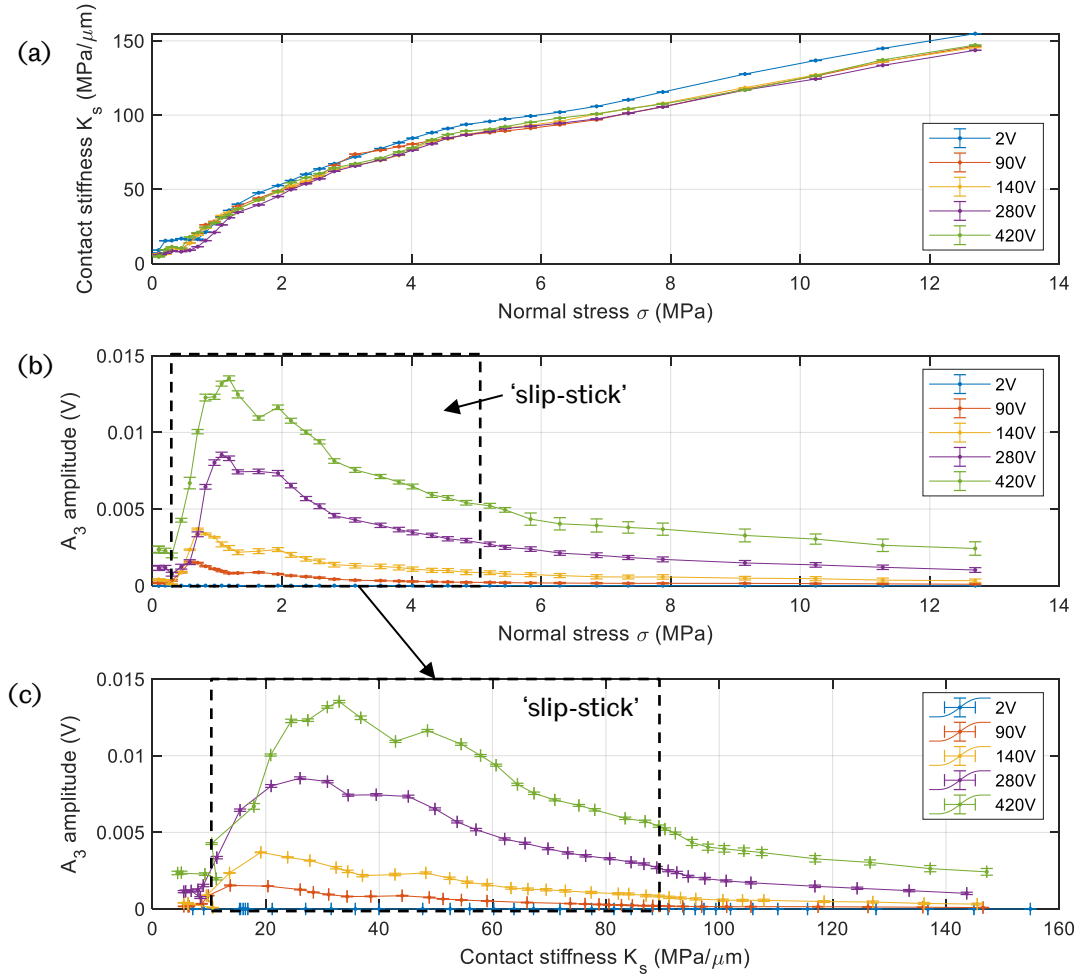


Figure 7.33 (a) Contact stiffness (b) contact harmonic A_3 amplitude subject to higher power inputs and varying normal contact stresses. (c) Contact stiffness and contact harmonic A_3 amplitude subject to higher power inputs. (Test specimen S1-S4, 100 repetitions).

The reflection coefficient is dependent on the stiffness of the interface (Baik and Thompson, 1984). This is a method that has widely been used to study rough surface contacts (Dwyer-Joyce et al., 2001). The relationship between stiffness and the reflection is given by the so-called spring model (Nagy, 1992; Królikowski and Szczepiek, 1993; Drinkwater et al., 1996):

$$\frac{\pi f G}{c_s} \sqrt{\frac{1}{R^2} - 1}, \quad (7.14)$$

$$R = \frac{A_1^{\text{solid-solid contact}}}{A_1^{\text{solid-air contact}}}. \quad (7.15)$$

where f is the fundamental frequency of the received ultrasound, G the shear modulus of the specimen, c_s the speed of shear wave in the specimen and R the

reflection coefficient. Stiffness varies from zero for no contact to infinity for an interface that is fully in contact (no air gaps).

The interfacial shear stiffness is depicted in Figure 7.33 (a). For varying incidence amplitudes, the contact interfacial stiffness shares a common trend over the rising contact stress. Larger stiffness indicates that contacting surfaces are more conformal and more ultrasound transmitted through the contact interface. It is noticed that over the normal contact stress range applied, the interfacial stiffness increases and the conformity increases. The contact nonlinearity peaks only at relatively low contact stiffness (Figure 7.33 (a)), which indicates that the nonlinear interaction of a shear ultrasound wave and a rough interface only occurs when relatively low normal stress is applied where contact is still less conformal.

7.3.3 Experimental Results

Test results using the pitch-catch reflection arrangement subject to varying incident amplitude and normal contact stress are illustrated in Figure 7.34 (a), (b), (c) and (d) for test specimen S1-S4, S1-S2, S1-L1, S1-L3 respectively. For all test specimens, contact nonlinearity is preferably generated in the region of low contact stress and high incident shear stress (converted from displacement, as measured with laser vibrometer in Chapter 6). The 'stick-slip' activation region is encircled by the dashed line and contact nonlinearity generation is preferably measured in this region.

Although the contact nonlinearity generation is activated in low normal stress and high incident shear stress region, for different test specimens, the shape of the peak nonlinearity generation (in red in Figure 7.34 (a)-(d)) differs even the same normal stress and incident shear stress is applied. It may indicate the difference of contacting interface of test specimens and the friction of each contacting pair. Contacting face dimension are the same for test specimens S4, S2, L1 and L3. These contacting faces are prepared to various surface roughness and when in contact with specimen S1, friction at the contact varies. A same incident shear wave strikes various contacting faces, the interaction and the contact nonlinearity generation differs. This nonlinearity generation region is useful in contact friction estimation and it is discussed in Chapter 8.

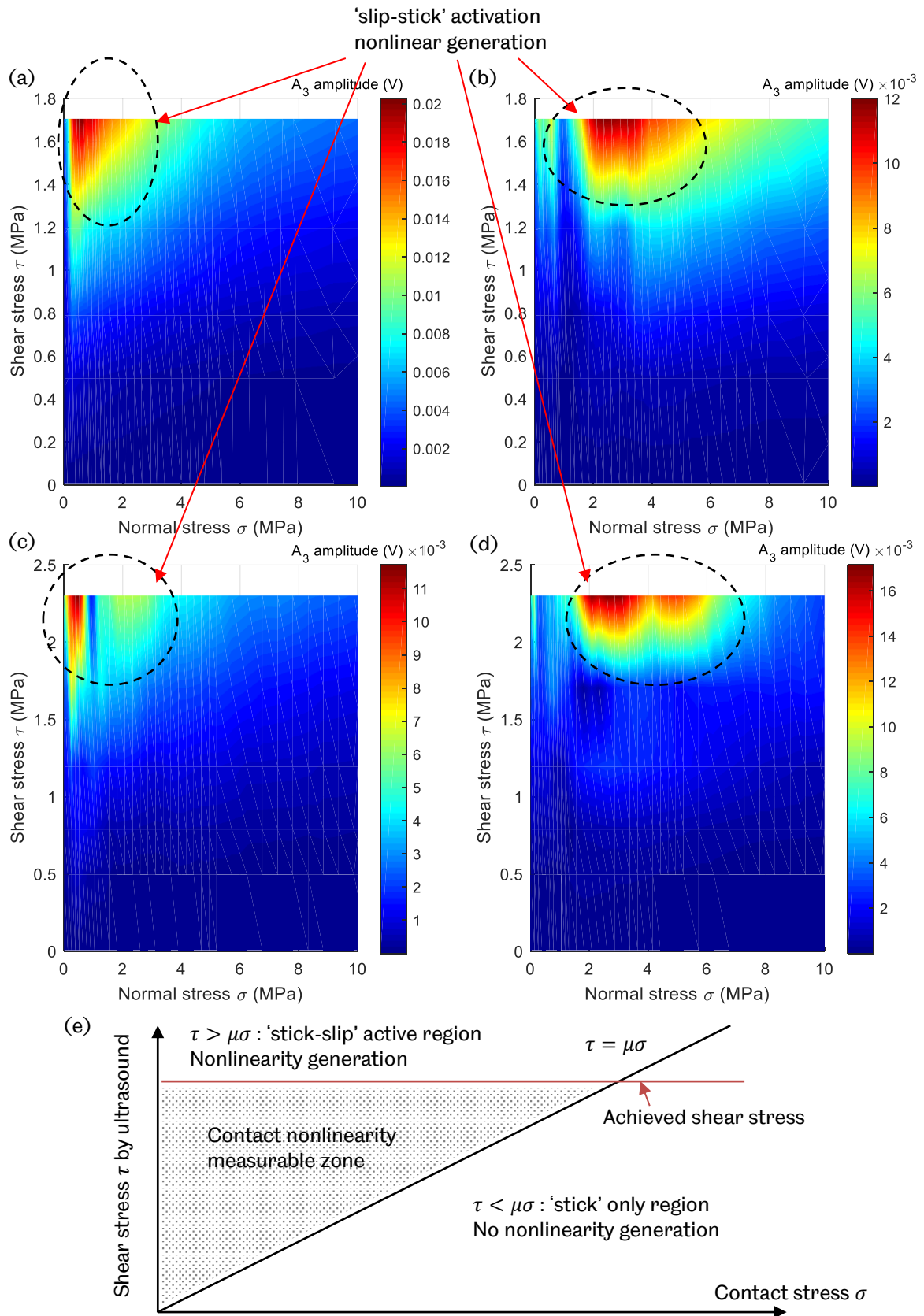


Figure 7.34 Contact nonlinearity amplitude (the third harmonic A_3) subject to varying incident voltage and contact stress: (a) Test specimen S1-S4. (b) Test specimen S1-S2. (c) Test specimen S1-L1. (d) Test specimen S1-L3. (e) Contact nonlinearity measurable zone.

7.4 Measurement of Ultrasonic Nonlinearity at Rough Interface - Subsequent Echoes

In previous sections measurement focuses on the first reflection signal which directly scattered backwards from the contact interface after the nonlinear interaction with the rough interface. Previous numerical work also used the first echo, either the first reflection signal or transmission signal, in the contact harmonics generation analysis (O'Neill et al., 2001; Meziane et al., 2011). In the experiment, contact nonlinearity is also detected in subsequent echoes, i.e. the second and third reflection signals. Details are shown as follows.

7.4.1 Experimental Configuration

The pitch-catch reflection configuration was adopted. Two sets of test specimens were employed. In the first set, two test specimens were with the same length (Figure 7.35 (a)) while for the second set, one specimen was twice the length than the other (Figure 7.35 (b)). The test conditions are listed in Table 7.8.

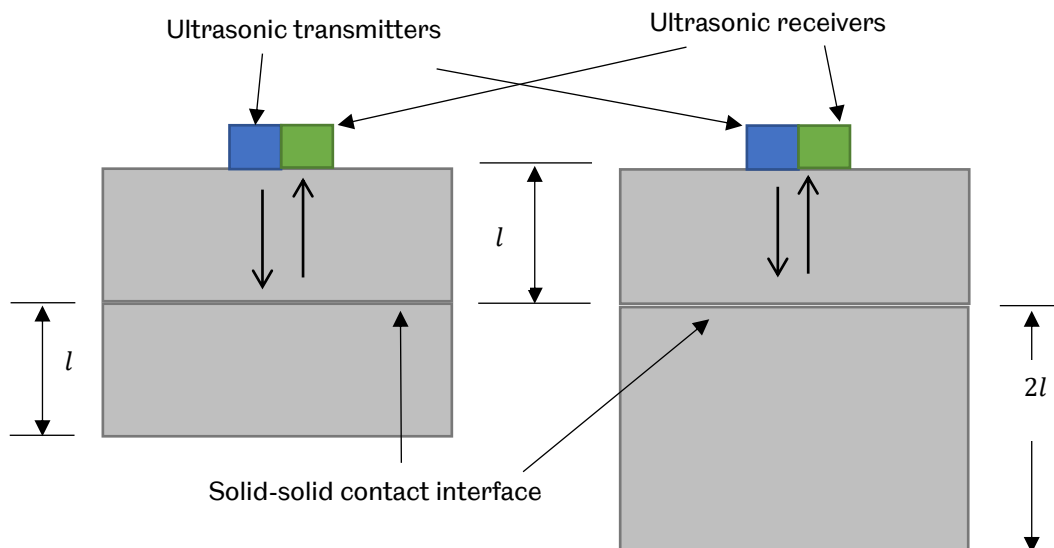


Figure 7.35 Pitch-catch reflection arrangement. (a) two test specimens with same length l . (b) two test specimens with length l and $2l$.

Table 7.8 Test conditions in pitch-catch reflection arrangement.

	Test Set 1	Test Set 2
Test specimen	Al Alloy 6082 S1-S4	Al Alloy 6082 S1-L1
Specimen length	l, l	$l, 2l$
Transducer	V153-V155	V153-V155
Waveform	15-cycle 1MHz sine wave	15-cycle 1MHz sine wave
Amplification	90, 140, 280, 420V	90, 140, 280, 420V
Normal force	0 – 45 kN	0 – 45 kN

The time domain for the first set test specimens (both length l) are illustrated in Figure 7.36. The first echo is the reflected signal and the ultrasound interacts at the rough contact interface only once. After this interaction, some portion of the ultrasound transmits through the contact interface and reflects at the bottom boundary of the lower specimen. This ultrasonic wave propagates upwards, striking the interface, transmitting through to the upper specimen and travelling towards the ultrasonic receiver (dash blue line in Figure 7.36 (b)). After the first ultrasound-contact-interface interaction, some part of the ultrasound bounces within the upper specimen, striking the interface for a second time and received by the transducer (solid blue line in Figure 7.36 (b)). As the upper and lower specimens are the same length, the time-of-flight for both reflected and transmitted ultrasound are equal so that both signals reach the receiver at the same time. So the second echo consists of both reflection and transmission. Similar processes repeat again within the upper and lower test specimens and the third echo contains both reflected signal (dash orange line in Figure 7.36 (b)) and transmitted ultrasound (dash blue line in Figure 7.36 (b)).

The time domain for the second pair of test specimens (upper specimen length l and lower specimen length $2l$) are depicted in Figure 7.37. Due to the lower specimen is of length of $2l$, the first signal received by the ultrasonic transducer is the reflected ultrasound. The second echo received is the twice-reflected wave (solid blue line in Figure 7.37 (b)). The third echo consists of the three-time-reflected wave (solid orange line in Figure 7.37 (b)) and transmitted ultrasound (dash orange line in Figure 7.37 (b)).

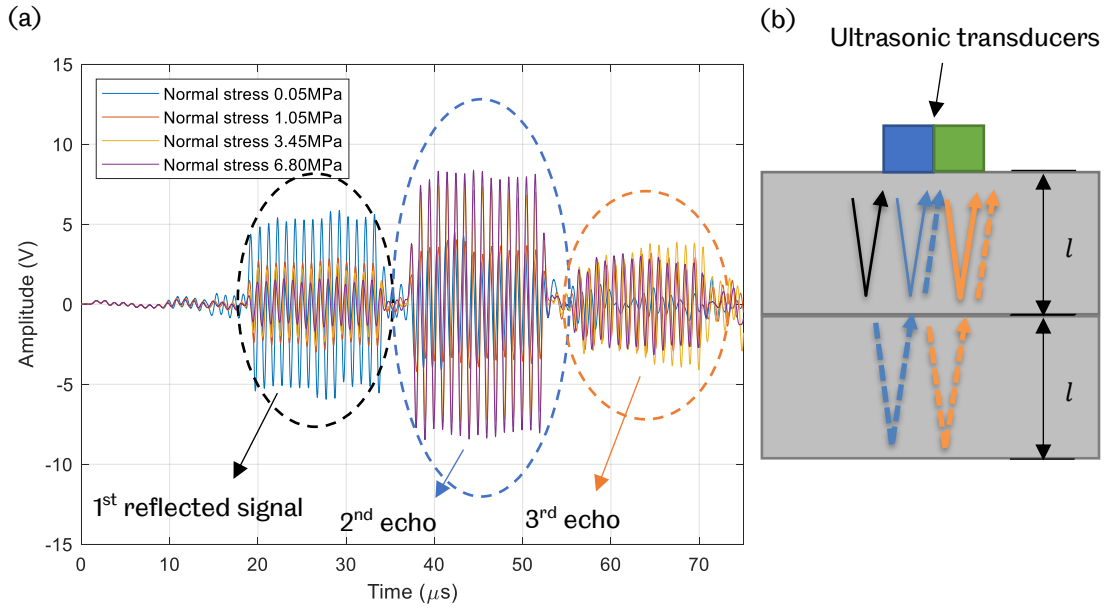


Figure 7.36 Time domain signal in the test specimens (S1-S4, both length l) subject to varied normal force (excitation 420V, 100 repetitions). (b) Schematic diagram of reflected and transmitted signal inside specimens.

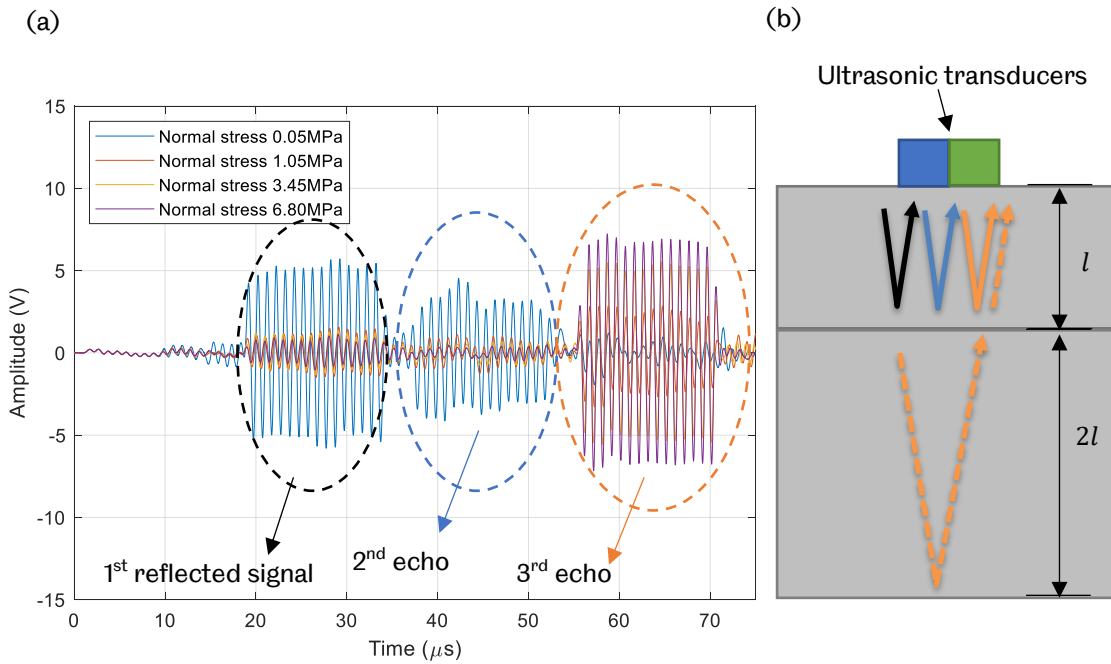


Figure 7.37 Time domain signal in the test specimens (S1-L1, length l and $2l$) subject to varied normal force (excitation 420V, 100 repetitions). (b) Schematic diagram of reflected and transmitted signal inside specimens.

7.4.2 Ultrasonic Nonlinearity in Subsequent Echoes

For the test specimens of length l , the fundamental frequency amplitude A_1 and the third harmonic A_3 in each echo subject to varying normal contact stress are illustrated in Figure 7.38. In Figure 7.38 (a), the fundamental frequency amplitude A_1 decreases when the applied normal stress increases as only reflection signal is received. The behaviour of the third harmonic A_3 follows what has been discussed in previous sections. The 'rise-fall' trend shows occurrence of the nonlinear interaction of high-power ultrasound with a rough interface.

For the second echo, the fundamental frequency amplitude A_1 drops and followed by monotonically increasing trend when the contact interface is further pressed. The fundamental frequency amplitude A_1 in the second echo indicates the transition from reflected wave to the transmitted wave of the captured signal. As the applied normal stress increases, more ultrasound wave transmits through the interface and less reflected ultrasound is received by the transducer. Further compressing the interface makes more ultrasound transmitted through and bouncing back at the bottom boundary of the lower specimen. Consequently, more reflected transmission wave propagates through the interface again with a reversed direction and reaches the receiver. The third harmonic A_3 , however, does not show this 'fall-rise' trend along the increased normal stress. It displays the similar behaviour to the third harmonic in Echo 1, showing the 'rise-drop' pattern when the contact stress is enlarged.

For the third echo, the fundamental frequency amplitude shows a complex trend over the contact stress as mixed multiple reflections and transmissions are detected by the receiving transducer. The third harmonic A_3 , shows the similar trend as in the first and second echoes.

Similar results are achieved in the test specimens with length of l and $2l$, as depicted in Figure 7.39. The fundamental frequency amplitude A_1 indicates that the first and the second echoes are reflected signals and the transmission signal forms the third echo. The third harmonic A_3 in all three echoes increases with the normal contact stress, followed by a decrease tendency when the interface is compressed heavily, indicating the occurrence of the nonlinear interaction of ultrasound with the contact interface.

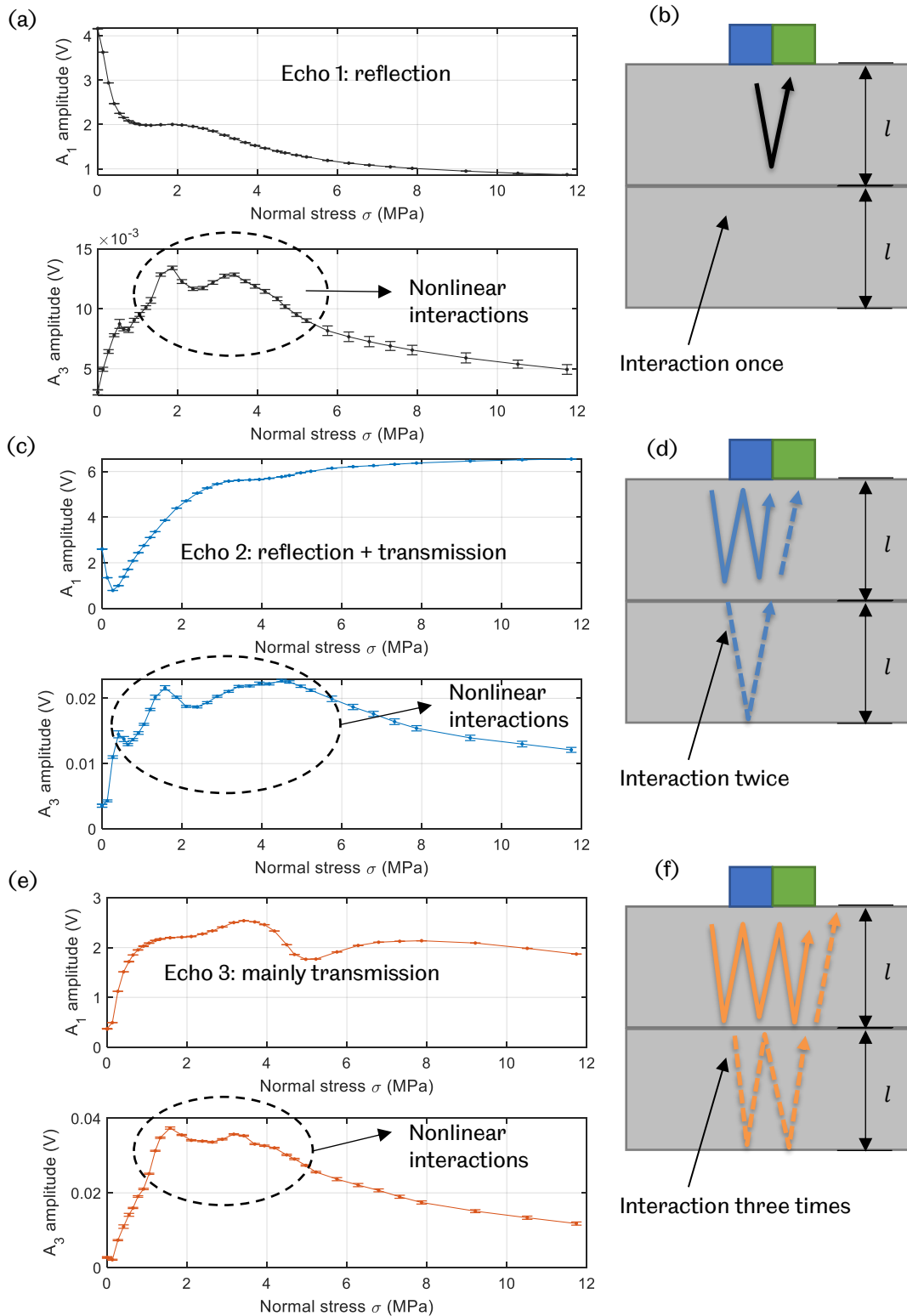


Figure 7.38 Test specimens (length l and l) subject to varying normal stress (Excitation 420V, 100 repetitions). (a) Fundamental frequency amplitude A_1 and the third order harmonic A_3 in Echo 1. (b) Schematic diagram of Echo 1. (c) Fundamental frequency amplitude A_1 and the third order harmonic A_3 in Echo 2. (d) Schematic diagram of Echo 2. (e) Fundamental frequency amplitude A_1 and the third order harmonic A_3 in Echo 3. (f) Schematic diagram of Echo 3.

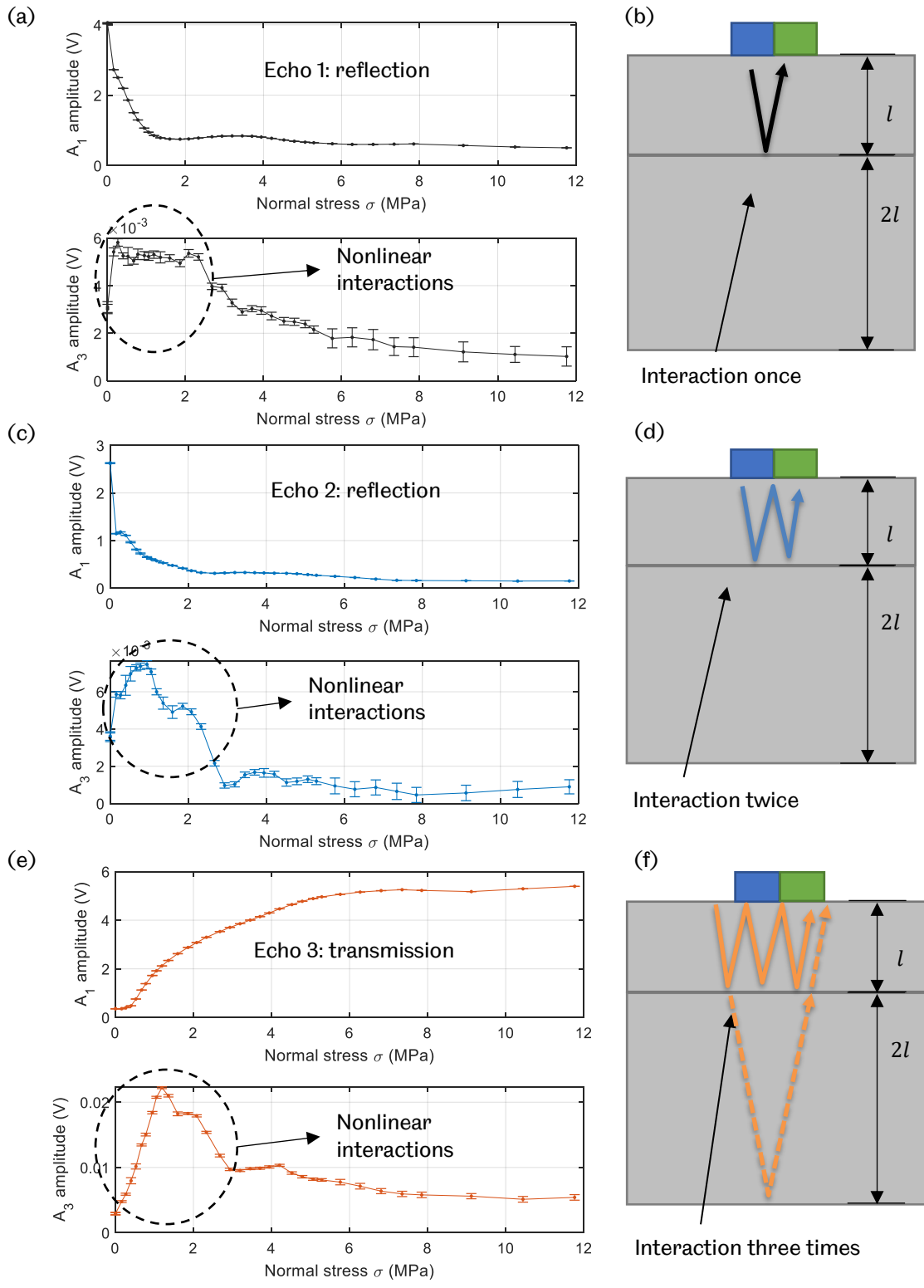


Figure 7.39 Test specimens (length l and $2l$) subject to varying normal stress (Excitation 420V, 100 repetitions). (a) Fundamental frequency amplitude A_1 and the third order harmonic A_3 in Echo 1. (b) Schematic diagram of Echo 1. (c) Fundamental frequency amplitude A_1 and the third order harmonic A_3 in Echo 2. (d) Schematic diagram of Echo 2. (e) Fundamental frequency amplitude A_1 and the third order harmonic A_3 in Echo 3. (f) Schematic diagram of Echo 3.

In both pairs of test specimens, the third harmonic A_3 for the first three echoes all indicates the generation of the nonlinearity at the rough contact interface when the high-power ultrasound interacts with the interface. It is worth noting that the amplitude of the third harmonic A_3 in the first three echoes. As illustrated in Figure 7.40, in both set of test specimens, the third harmonic A_3 in the subsequent echoes are greater than that in the preceding echoes. It may indicate that the nonlinearity generation not only occurs when the ultrasound strikes the rough contact interface for the first time, but also originates in the subsequent interactions.

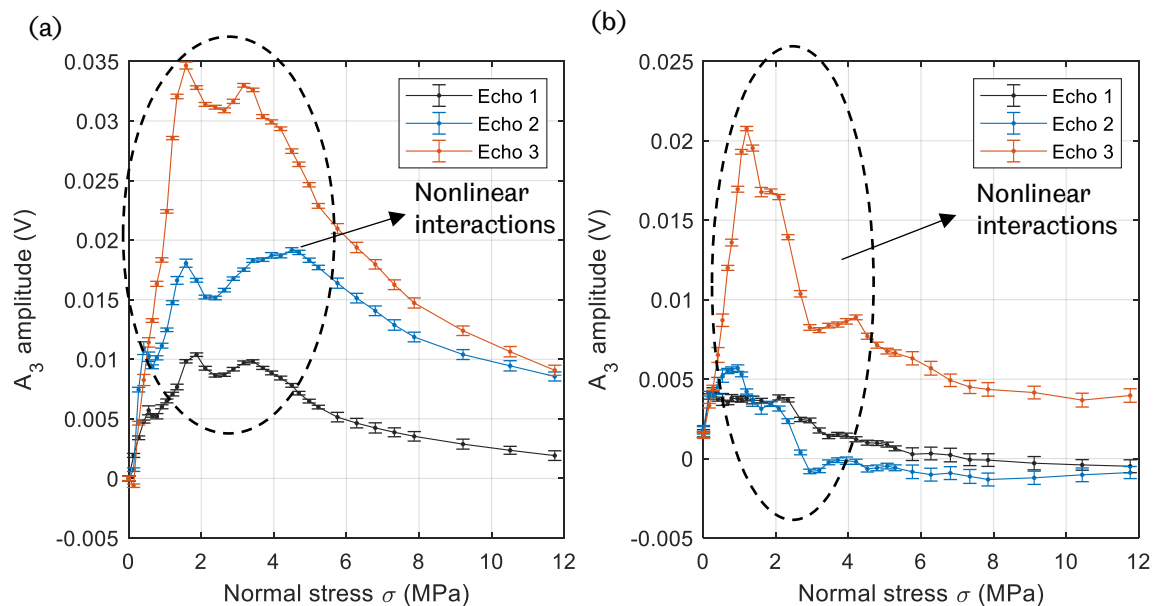


Figure 7.40 The third harmonic A_3 originated at contact interface in all echoes subject to varying normal stress. (a) Test specimens S1-S4 (length l and l , 100 repetitions). (b) Test specimens S1-L1 (length l and $2l$, 100 repetitions).

As depicted in Figure 7.41 (a) and (b), in the experiment, the contact face of the test specimen is rough and consists of asperities with various heights and sizes. After the nonlinear interaction at the rough contact interface, both reflected and transmitted ultrasound is distorted due to the 'stick-slip' motion at the interface. Because of the presence of the asperities, the nonlinear 'stick-slip' motion is activated primarily at the asperities which are in contact, rather than the entire contact interface. Then the ultrasound wave is partially distorted. When the reflected and transmitted wave bounces back at the specimen boundary and strikes the contact interface for a second time, the previously partially distorted ultrasound still enables the nonlinear 'stick-slip' activation at some asperities. The partially contorted ultrasound is further distorted and consequently results in the greater third harmonic A_3 . When the

reflected and transmitted wave meets the contact interface for a third time, more distortion on the ultrasound takes place and even more nonlinearity generation is activated at the rough contact interface.

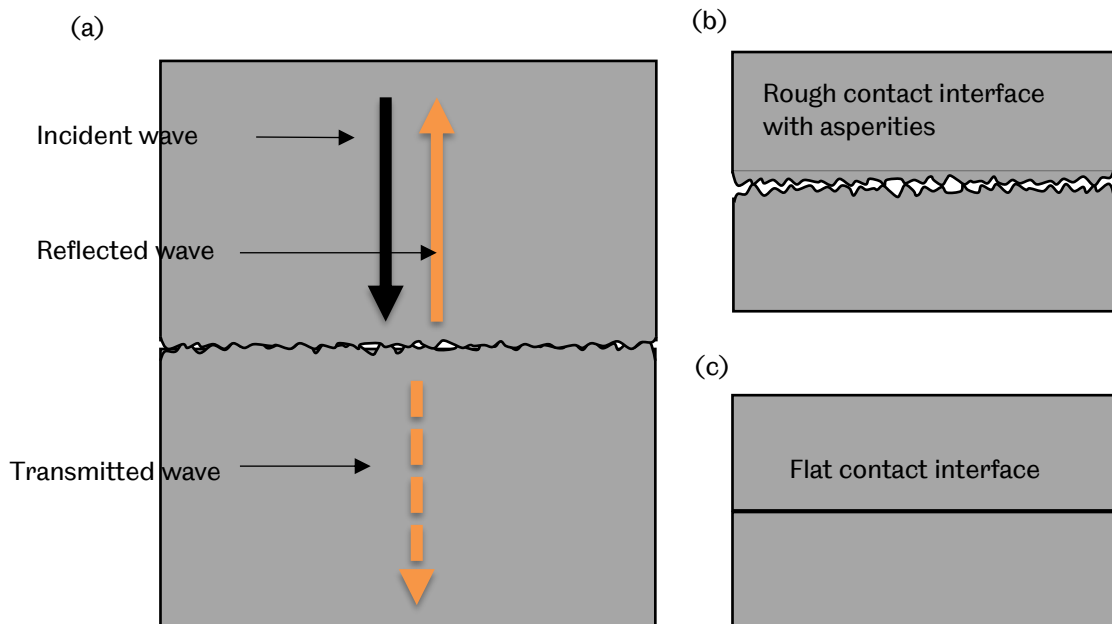


Figure 7.41 (a) Schematic diagram of nonlinear interaction of ultrasound at rough contact interface for multiple echoes. (b) Rough contact interface with asperities in the experiment. (c) Flat contact interface in the numerical work.

The ultrasonic nonlinearity originating at the rough contact interface in subsequent echoes is not observed in the numerical model in Chapter 5. A frictional but flat contact interface is used in the numerical model, as illustrated in Figure 7.41 (c). In the numerical study, the ultrasonic wave is clipped when the high-power wave strikes at the flat contact interface at the first-time interaction. The resulted reflected wave or transmitted wave are not sufficiently powerful to activate the 'stick-slip' motion when it strikes the contact interface for a second time. Therefore, no further distortion is exerted on the ultrasound.

7.5 Conclusion

In this chapter, the experimental arrangement is investigated using the high frequency nonlinear ultrasonic technique. The pitch-catch reflection configuration is employed in the measurement. The measured third harmonic amplitude is split into two parts, the system built-in nonlinearity and the contact nonlinearity. Methods are investigated to separate the targeted contact nonlinearity from the measured third harmonic signal. Two major factors affecting the contact harmonic generation is studied, namely the incidence amplitude and the applied normal contact stress. Experimental results suggest that activation the 'slip-stick' motion and the subsequent contact harmonic generation can occur at the rough interface when the incident amplitude is sufficiently large and the contact stress is relatively low.

The ultrasonic nonlinearity at a rough interface in the subsequent echoes has been studied. Nonlinearity in the subsequent echoes shows the similar 'rise-drop' trend over the applied contact stress. The stronger amplitude of the third harmonic in subsequent echoes indicates that nonlinearity originating from a rough contact interface accumulates and suggests that nonlinear interaction between ultrasound and a rough contact continues in these subsequent echoes.

8 ESTIMATION COEFFICIENT OF FRICTION USING ULTRASONIC NONLINEARITY

In this chapter, the measurement of nonlinearity generation due to shear polarised ultrasound interacting with a rough contact interface using subsequent echoes is discussed first. The contact nonlinearity generation detected experimentally is then compared with the numerical model. Lastly, the two strategies of estimating the coefficient of friction at a rough contact interface are investigated using the contact nonlinearity generation.

8.1 Comparison Experimental Work with Numerical Study

In the numerical study (Section 5.2.3), the contact nonlinearity generation was modelled computationally when a high-power ultrasound strikes a frictional contact interface. The contact nonlinearity was also determined experimentally (Section 7.3) when two rough faces were brought to contact. Before using the ultrasonic nonlinearity generation to estimate the coefficient of friction at the contact, comparison between the numerical and experimental results are first discussed as follows.

8.1.1 Dimensionless Stress

In Section 5.2.3.2, a dimensionless parameter, ξ was introduced to characterise the status of the contact interface under ultrasonic oscillations and is defined by Equation (8.1). It describes the ratio of the frictional stress to the tangential oscillating stress introduced by shear polarised ultrasound at the contact interface. Any dimensionless stress greater than unity value ($\xi \geq 1$) indicates the contact is 'bonded' without any relative motion at the interface. Any value less than unity represents the case that there is relative motion at the contact and the interface alternates between 'stick' mode and 'slip' mode (Equation (8.2)).

$$\xi = \frac{\mu\sigma}{GkA_{contact}} \quad (8.1)$$

$$contact\ state = \begin{cases} stick - slip\ alternation, & 0 < \xi < 1 \\ stick, & \xi \geq 1 \end{cases} \quad (8.2)$$

In the comparison between the numerical and experimental results, the dimensionless stress is used and Equation (8.1) is employed to compute the nondimensional stress ξ for both numerical and experimental results.

8.1.1.1 Coefficient of Friction Measurement Using Sliding Test

To use the dimensionless stress in the comparison between the numerical and experimental results, the coefficient of friction for all contact pairs are required. Due to the size of the test specimens, conventional tribometers are not applicable to determine the static friction coefficient of each contact pair. Alternatively, the primitive sliding test can be employed to determine the static friction coefficient (Blanloeuil et al., 2014c).

The sliding test was adopted in the experiment. As depicted in Figure 8.1 (a), a pair of test specimens were placed the on the supporting frame and the lower test specimen was mounted on the supporting block to prevent its movement. An adjustable screw was used to control the inclination of the tilted base. At the start of the test, the tilted base was set to minimum tilt angle. At this angle, the upper test specimen rested on the lower test specimen. An adjustable screw was then used to gradually increase the tilt angle. When the upper test specimen started to slide over the lower one, the inclination was read from the digital angle gauge. Measurement was repeated a number of times to ensure consistency. It was noted that when the

same pair of test specimens slide repeatedly a number of times, scratches were observed on the contacting faces. Friction coefficient measurement was made prior to the occurrence of these scratches.

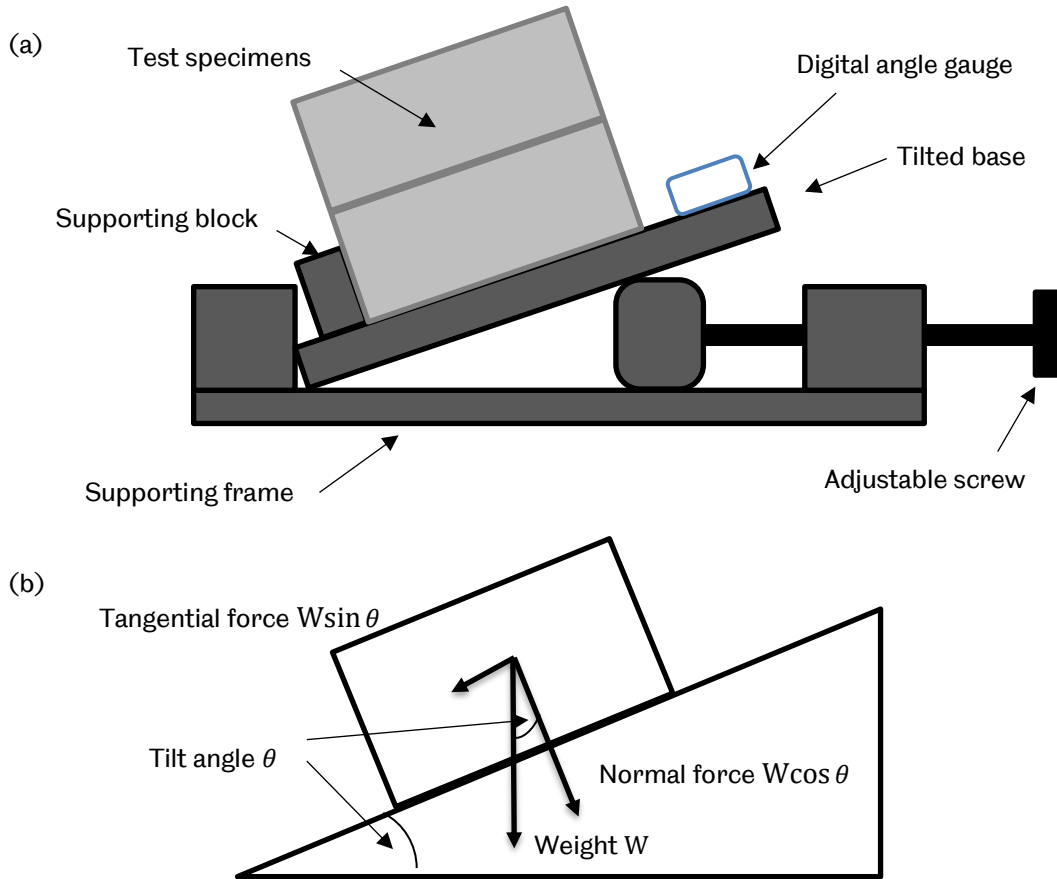


Figure 8.1 (a) Schematic diagram of sliding test for friction coefficient measurement. (b) Measuring friction coefficient using the sliding test.

$$\mu = \frac{W \sin \theta}{W \cos \theta} = \tan \theta \quad (8.3)$$

The static friction coefficient was determined using Equation (8.3). For each pair of contact specimens used, the static friction coefficient is listed in Table 8.1.

Table 8.1 Friction coefficient measurement using sliding test.

Contact pair	Friction coefficient: mean value ± standard deviation (repeated for 30 times)	Surface roughness (μm)
S1-S2	0.423±0.0529	0.586
S1-S3	0.443±0.0746	0.874
S1-S4	0.485±0.0592	0.483
S1-L1	0.385±0.0472	0.453
S1-L2	0.411±0.0302	0.847
S1-L3	0.420±0.0323	0.954
S1-AI1	0.341±0.0428	0.469
S1-AI2	0.464±0.0814	0.728
S1-AI4	0.409±0.0856	0.620

The friction coefficient measured using the sliding test for different specimens are approximately 0.4 and the variation of each contact pair is approximately 10%. Although it is crude, the sliding test still provides the information on the friction of a rough contact.

8.1.1.2 Shear Stress Introduced by Ultrasound at Contact Interface

The shear stress introduced by ultrasound at the interface $\tau_{ultrasound}$, is determined using Equation (8.4). The displacement amplitude of shear polarised ultrasound at the contact interface $A_{contact}$, was determined using the laser vibrometer, as shown in Section 6.5.3. The shear stress introduced by ultrasound in the experiment is listed in Table 8.2.

$$\tau_{ultrasound} = GkA_{contact} \quad (8.4)$$

Table 8.2 Shear stress by ultrasound at contact interface.

Voltage input of RITEC amplifier (V)	Displacement amplitude (nm)	Shear stress (MPa)
90	9.13	0.496
140	14.52	0.789
280	21.97	1.194
420	31.37	1.705
560	42.35	2.302

The maximum achieved shear stress is approximately 2.3MPa, which is sufficient to activate the nonlinear interaction ('stick-slip') at the interface, compared with the normal stress applied in the experiment. It is noticed that the shear stress was measured at a solid-air interface. The shear stress at the solid-solid interface is not known and difficult to measure. Therefore, it is reasonable to use the measured shear stress as the shear stress at a contact interface.

8.1.1.3 Computation of Dimensionless Stress

The dimensionless stress ξ , for each contact pair used in the experiment can be computed using the Equation (8.1). An example of the dimensionless stress for all experiment conditions of contact pair S1-S4 is illustrated in Figure 8.2 ($\mu = 0.48$ from Table 8.1). It is noticed that the dimensionless stress falls within the range of 0 to 1 for higher shear stress and lower normal stress. Under these test conditions, the nonlinear 'stick-slip' motion is activated and contact nonlinearity generation take places.

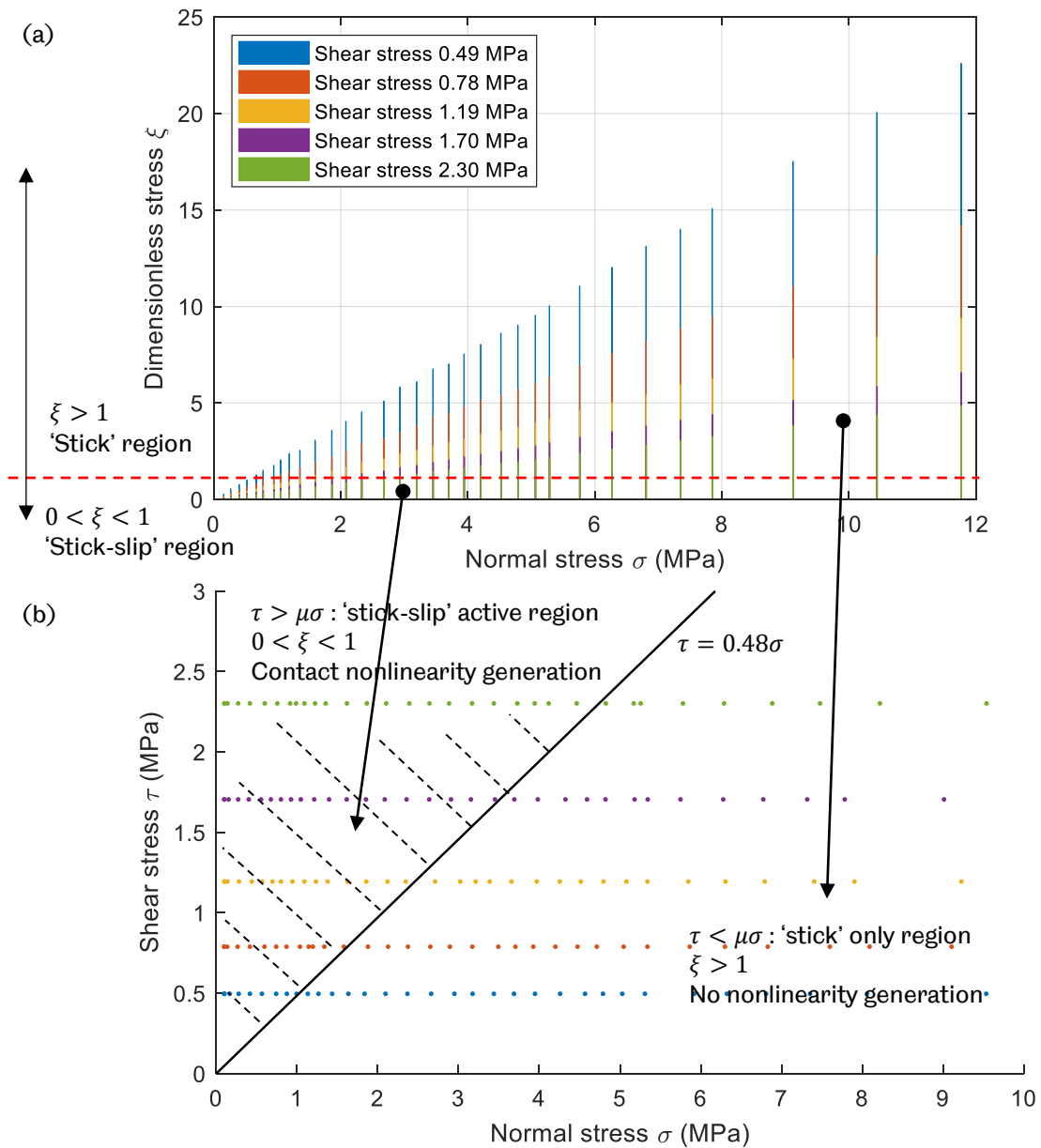


Figure 8.2 (a) Dimensionless stress ξ for all test conditions for test specimen S1-S4. (b) Contact nonlinearity measurable zone for S1-S4.

8.1.2 Comparison Experimental Work with Numerical Study

The test conditions employed in the experiment, such as the applied normal stress, amplitude of displacement of shear ultrasound and the measured coefficient of friction, were applied in the numerical study as the input parameter. This is to ensure that the comparison of the ultrasonic nonlinearity generation at contact interface in both numerical computation and experiment is reasonable and valid.

Test specimens S1-S4 are used as an example in this section. For the experimental results, the third harmonic A_3 was treated using the method previously mentioned in Section 7.2. The system inherent nonlinearity was removed from the measured third harmonic and the remainder was the contact nonlinearity. Because the magnitude and the unit of the third harmonic in the numerical computation was different from that of the experiment, the normalised values were employed to facilitate comparison.

The normalised third harmonic A_3 for both numerical and experimental subject to varying normal and shear stress is illustrated in Figure 8.3. For both numerical and experimental results, the ultrasonic nonlinearity shows similar trend over the increasing dimensionless stress (Figure 8.3 (a)) or normal stress Figure 8.3 (b)), i.e. rising to a peak at lower stress region and then followed by a drop when the normal stress is higher. The peak locations numerically computed and experimentally measured are also close and the 'rise-drop' trend falls approximately within the range from 0 to 1 in Figure 8.3 (a) when plotted against the dimensionless stress. Overall the numerical model shows agreement with the experiment.

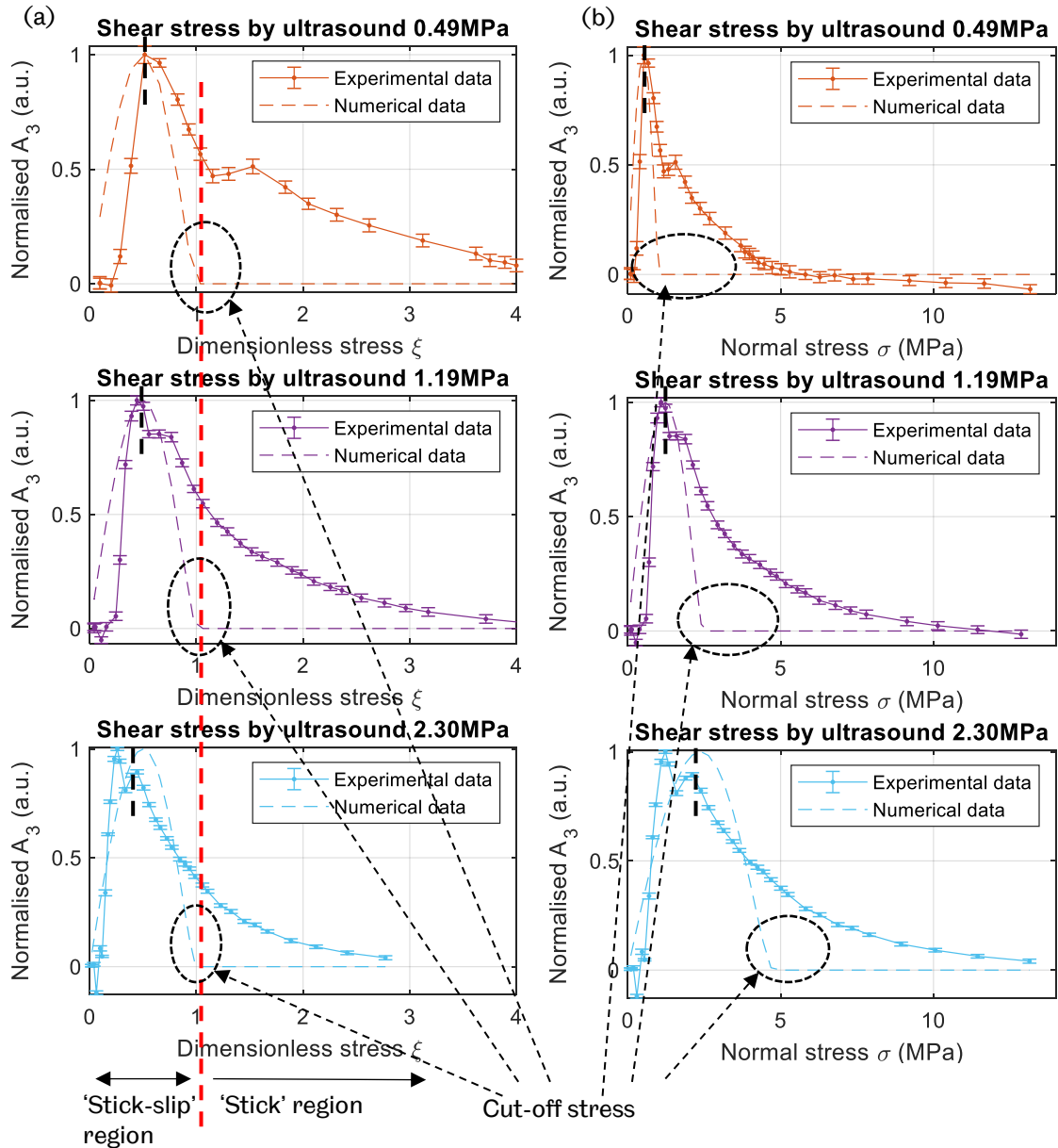


Figure 8.3 Comparison of the third harmonic A_3 originated at contact interface subject to varying normal stress and excitations (90V, 280V and 560V) vs (a) Dimensionless stress ξ . (b) Normal stress σ . (Test specimen S1-S4, 100 repetitions).

Several differences are noticed between the numerical and experimental results. In Figure 8.3 (a), although the peak of the third harmonic is in the range of 0 to 1, numerical study always predicts the maximum harmonic generation occurs at $\xi = 0.5$, while the experimental results shows a shift of the peak when various shear stress is applied at the interface by ultrasound wave. As indicated with black dash line in Figure 8.11 (a), higher shear stress is prone to result in a peak at a lower dimensionless stress. One likely reason is that during ultrasonic displacement

amplitude measurement, at high voltage input, the ultrasonic displacement may be over-estimated whereas under-estimation occurs at low gain level.

It is also noticed that in the numerical study (Figure 8.3 (a)), the harmonic generation occurs only when the dimensionless stress is less than unity. Any nondimensional stress greater than unity cannot activate the 'stick-slip' motion. This defines the 'cut-off' stress where harmonic amplitude stops abruptly and it remains zero above this cut-off stress. However, for experimental results, the third harmonic measured in the experiment fades away gradually and disappears when the contact is compressed sufficiently. It leaves significant difference above the cut-off stress, as encircled in black dash circle in Figure 8.3 (b). In practice, the slow decay of the third harmonic implies that nonlinear interaction (i.e. slip) between a rough interface and ultrasound is still taking place even when the normal stress is greater than the cut-off stress. Asperities on a rough surface play a significant role here because ultrasound wave can only interact with some asperities when it strikes the contact interface. Above the cut-off stress, the partially distorted ultrasound is still able to activate the nonlinear 'stick-slip' movement at the asperity contacts.

The cut-off stress is also observed in the fundamental frequency amplitude, as shown in Figure 8.4. As the contact is gradually compressed, the fundamental frequency amplitude decreases slowly in the experiment while it declines quickly in numerical study to a cut-off stress and remains zero after this stress. As the asperity contact is not realised in the numerical model, the numerical study only works when the nonlinear 'stick-slip' motion is activated at the interface.

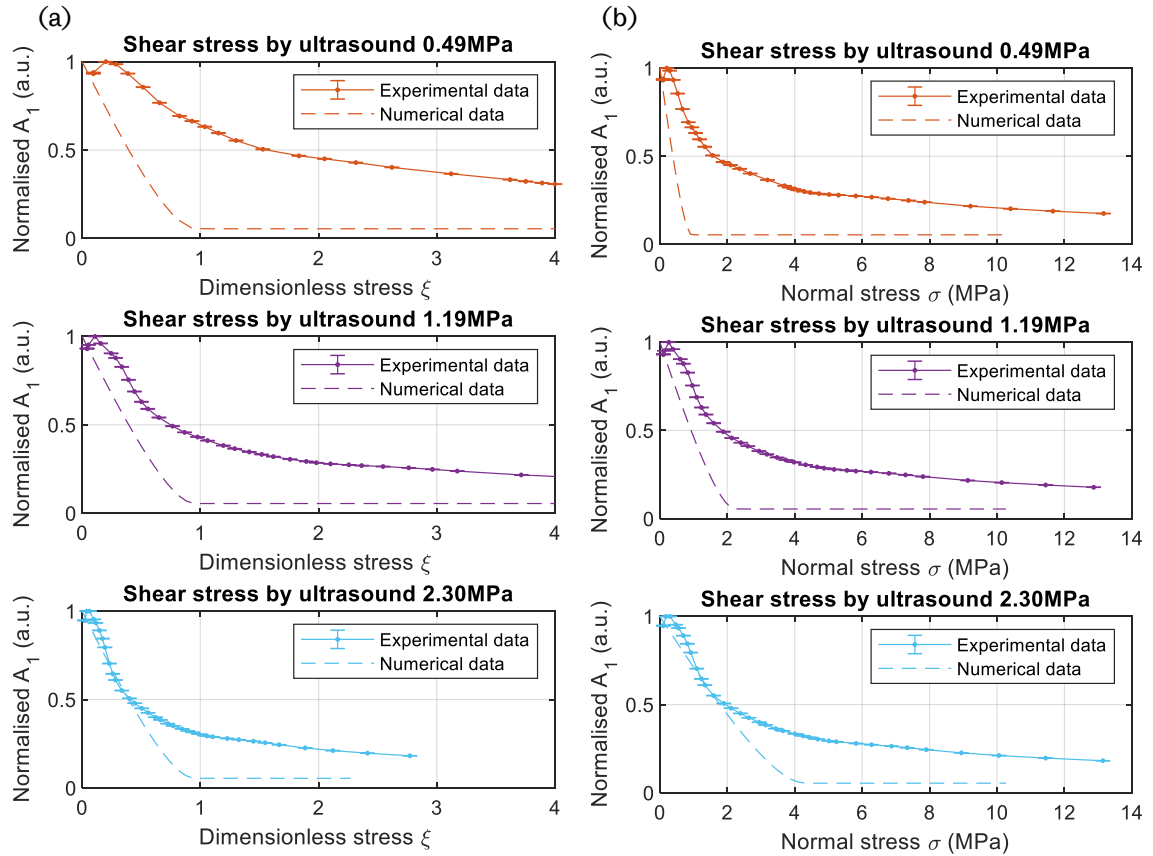


Figure 8.4 Comparison of the fundamental frequency A_1 subject to varying normal stress and excitations (90V, 280V and 560V) vs (a) Dimensionless stress ξ . (b) Normal stress σ . (Test specimen S1-S4, 100 repetitions).

Figure 8.5 illustrates the third harmonic A_3 generation at the rough interface under all the test conditions (for all incident shear and normal stress applied in experiments) in both numerical and experimental study. The colour bar indicates the amplitude of the ultrasonic nonlinearity A_3 . The numerical and experimental results agree qualitatively. Both numerical and experimental work shows a similar region of nonlinear interaction. In Figure 8.6, the results are plotted against the dimensionless stress. The numerical results show that the nonlinear 'stick-slip' takes place only when the dimensionless stress is less than unity. In the experiment, the contact nonlinearity generation takes place in a wider range of dimensionless stress.

The comparison results suggest that the numerical model is capable as a fair approximation of predicting the nonlinearity generation when ultrasound strikes at the frictional contact interface and agrees reasonably well with the experimental results. The numerical model only works when the nonlinear 'stick-slip' phenomenon takes place. Where the nonlinear interaction between the high-power shear wave and the frictional contact interface does not occur, the numerical results show significant difference with the experimental work.

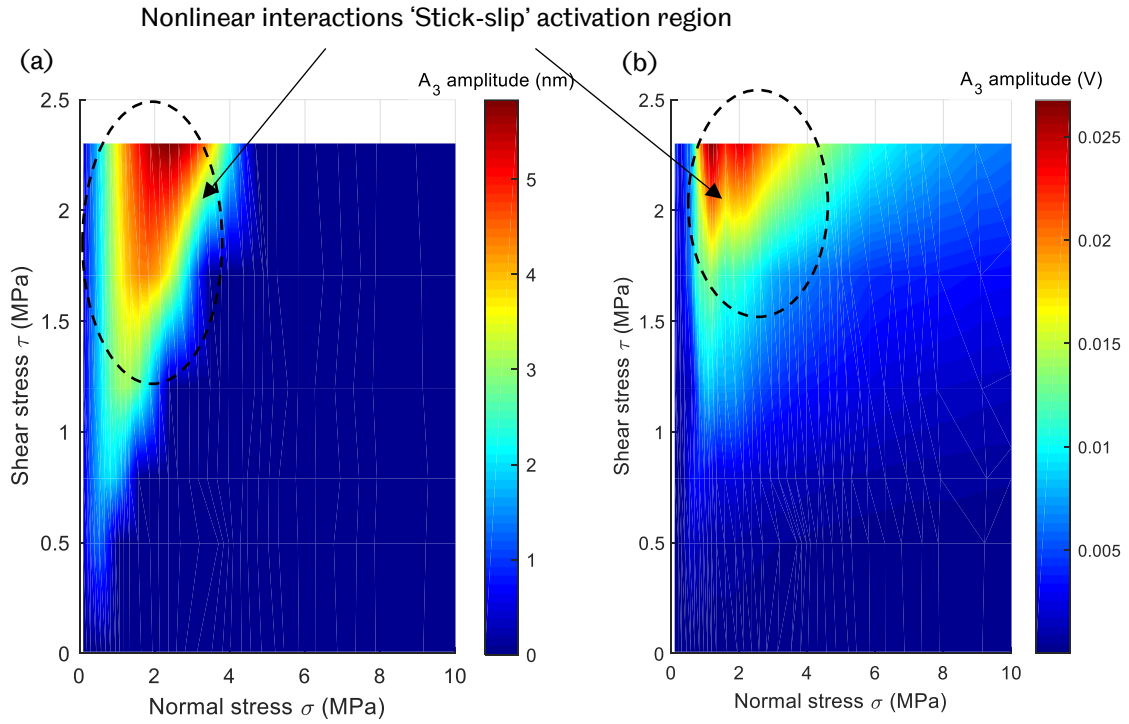


Figure 8.5 Comparison of the third harmonic A_3 vs normal stress. (a) Numerical computation. (b) Experimental result. (Test specimen S1-S4, excitations 90 – 560V).

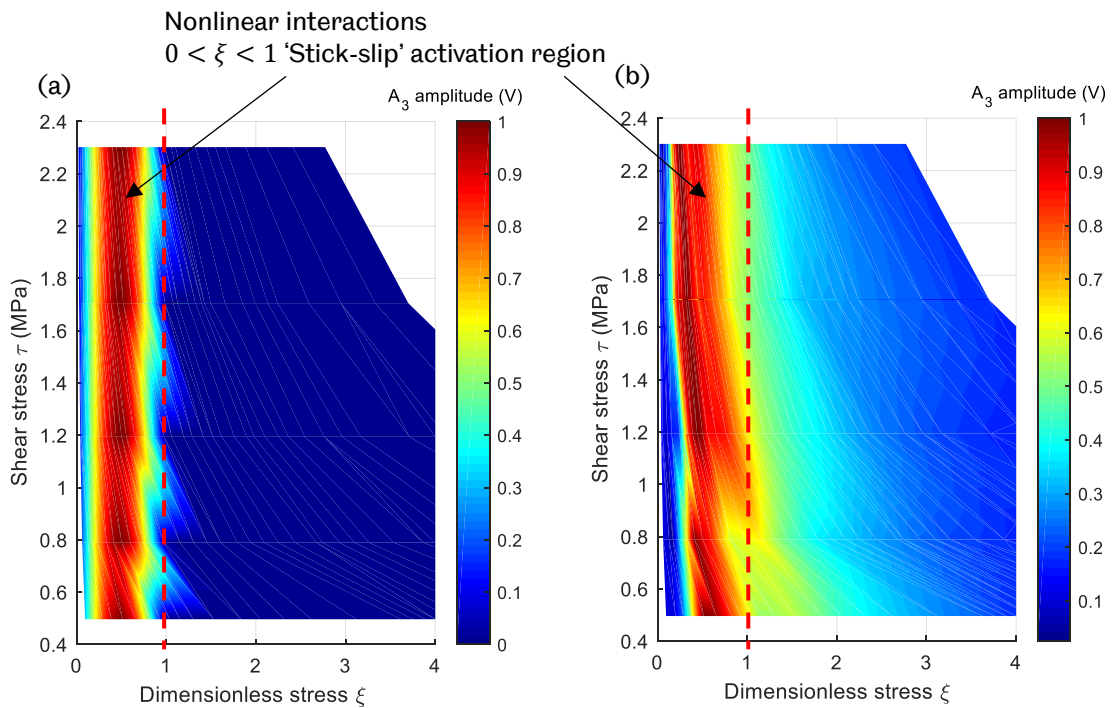


Figure 8.6 Comparison of the third harmonic A_3 vs dimensionless stress. (a) Numerical computation. (b) Experimental result. (Test specimen S1-S4, excitations 90 – 560V).

8.1.3 Ultrasonic Nonlinearity at Rough Contact Interface: From Numerical Model to Experimental Work

As discussed in Section 8.2.2, the numerical results show good agreement with the experiment results in terms of contact ultrasonic nonlinearity generation. The difference between the numerical results and the experimental works shows the drawback of the numerical model used in this research work. The numerical model is simplified, and some assumptions were made to facilitate numerical computation. The main differences between the numerical study and the experimental work are listed in Table 8.3.

The numerical model used here cannot realise the asperities contact and the elastic-plastic deformation at the load-bearing asperities. Since the contact faces are assumed flat but frictional, when the host medium is brought to contact, the entire flat face is in contact with its contact pair and this is illustrated in Figure 8.7 (a). The apparent area is the true contact area and the normal contact stress equal the nominal stress. Assuming the host medium is elastic, no elastic-plastic deformation occurs at the contact interface.

In the experiment, rough contacting faces are taken into account. The real contacting faces consist of numerous asperities with various dimensions are demonstrated in Figure 8.7 (b) and (c). When two test specimens are compressed together, contacts are made on the load-bearing asperities. Contact nonlinearity is generated on these contacts as shown in Figure 8.7 (b). Contact area is much less than the apparent contact area. The contact stress is extremely high at some contact points. When test specimens are compressed further, the load-bearing asperities deform elastically and then yield to plastic deformation. The 'old' contacts stick and no contact nonlinearity generation takes place. Meanwhile, more asperities are newly brought to contact. Therefore, more contact nonlinearity is still generated from the newly developed contacts Figure 8.7 (c).

It is worth noting that because the contact is made on the load-bearing asperities, at lightly loaded condition, the true contact area is very small. Further compressing the contact makes the load-bearing asperities yield plastically and the true contact area develops. In the experiment, the maximum applied normal stress is approximately 12MPa. The true contact area is estimated using the relationship defined in Equation (8.5), as 2% (Kendall and Tabor, 1971).

$$Area\% = \frac{\sigma}{H} = \frac{\text{applied normal stress}}{\text{Hardness of material}} \quad (8.5)$$

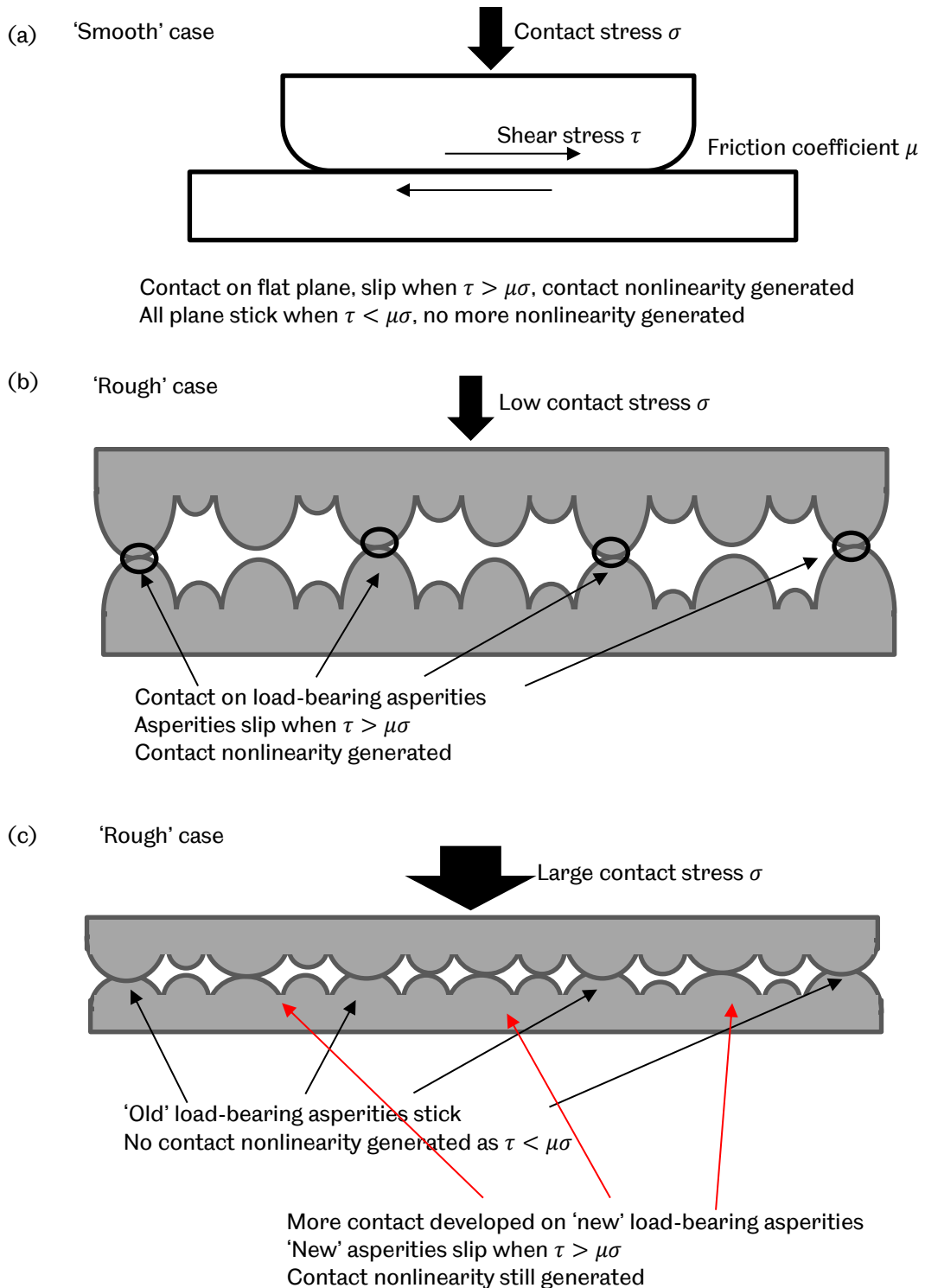


Figure 8.7 Contact nonlinearity generation in different cases. (a) Contact made on smooth plate plane. (b) Rough surfaces under low normal stress, contact on load-bearing asperities. (c) Rough surfaces under high normal stress, contact developed on new load-bearing asperities.

Table 8.3 Difference between numerical and experimental work.

1D Numerical model	Experiment
<ul style="list-style-type: none"> Contacting plane is flat with frictional coefficient. 	<ul style="list-style-type: none"> Contacting faces are rough and consist of numerous asperities.
<ul style="list-style-type: none"> Single value contact stress applies to the entire contact interface. 	<ul style="list-style-type: none"> Single value nominal contact stress applies to the entire contact interface. Due to the contact on asperities, normal stress varies locally.
<ul style="list-style-type: none"> Host medium is elastic. 	<ul style="list-style-type: none"> Test specimen is assumed elastic. At contact interface, elastic-plastic deformation takes places because the contact is made on load-bearing asperities.

8.2 Estimation of the Coefficient of Friction

Regardless of the over-simplification, the numerical model still captures the nature of the nonlinearity generation when a high-power ultrasound strikes a rough contact interface, i.e. the ultrasonic nonlinearity originating from the ‘stick-slip’ motion at the interface. The coefficient of friction plays a significant role in this nonlinear process, as discussed in Section 5.2.3. The experimental results show that the nonlinearity generation at a frictional interface is measurable and the third harmonic A_3 is sensitive to the nonlinear ‘stick-slip’ phenomenon at the rough interface. The friction coefficient of the statically compressed contact pairs can be estimated using the ultrasonic nonlinearity.

In the previous study on the contact nonlinearity generation, Hirose (1994), O’Neill and his colleagues (2001) and Blanloeuil and his colleagues (2014c) suggest that using the nonlinearity generation at a frictional contact enables the friction coefficient to be estimated but no attempts have been carried out. The work of estimating friction coefficient using the ultrasonic nonlinearity is carried out in the following sections.

8.2.1 Contact Nonlinearity Coefficient

In the measurement of contact stiffness (Gonzalez-Valadez et al., 2010), lubricant film thickness (Dwyer-Joyce et al., 2003; Dwyer-Joyce et al., 2004) and viscosity

(Schirru et al., 2015b) using ultrasonic method, a dimensionless parameter reflection coefficient, R is defined as ratio of measured amplitude (fundamental frequency amplitude A_1) of solid-air interface to that of solid-solid or solid-liquid interface, as described in Equation (8.6):

$$R = \frac{\text{measurement}}{\text{reference}} = \frac{A_1^{\text{solid-solid/liquid system}}}{A_1^{\text{solid-air system}}}. \quad (8.6)$$

The similar concept can be adopted here. A dimensionless parameter nonlinearity coefficient, N , is defined as in Equation (8.7). This is the ratio of the harmonic generation A_3 at solid-solid contact interface to that of the solid-air system in the pitch-catch reflection configuration. The solid-air contact interface is taken as the reference as it contains only the system inherent nonlinearity without any nonlinearity from the contact interface (Equation (8.8)). The measured nonlinearity in a solid-solid contact interface consists of both the system inherent nonlinearity and contact nonlinearity (Equation (8.9)).

$$N = \frac{\text{measurement}}{\text{reference}} = \frac{A_3^{\text{solid-solid system}}}{A_3^{\text{solid-air system}}} \quad (8.7)$$

$$A_3^{\text{solid-air system}} = A_3^{\text{system inherent}} \quad (8.8)$$

$$A_3^{\text{solid-solid system}} = A_3^{\text{system inherent}} + A_3^{\text{contact interface}} \quad (8.9)$$

$$\begin{aligned} N &= \frac{A_3^{\text{solid-solid system}}}{A_3^{\text{solid-air system}}} = \frac{A_3^{\text{system inherent}} + A_3^{\text{contact interface}}}{A_3^{\text{system inherent}}} \\ &= 1 + \frac{A_3^{\text{contact interface}}}{A_3^{\text{system inherent}}} \end{aligned} \quad (8.10)$$

The nonlinearity coefficient ranges from unity. When $N = 1$, it means that there is no contact nonlinearity generated at the contact interface. Any nonlinearity coefficient above unity indicates nonlinearity generation takes places.

The nonlinearity coefficient facilitates the post-processing of the measured third harmonic A_3 . Hence the experiment. Only a reference is required before the actual

measurement and there is no necessity to carry out the solid-air contact experiment over the entire loading ranges and to compute the absolute value of the nonlinearity only from the contact. In the following friction coefficient estimation, the nonlinearity coefficient is applied.

8.2.2 Friction Coefficient Estimation Using 'Cut-Off' Stress

The first strategy to estimate the friction coefficient is by using the cut-off normal stress. In the numerical computation, the cut-off stress is where the normal stress applied at the contact interface is just able to prevent the 'stick-slip' motion and the ultrasonic introduced shear stress is just unable to overcome the friction at the contact interface, as illustrated in Figure 8.8.

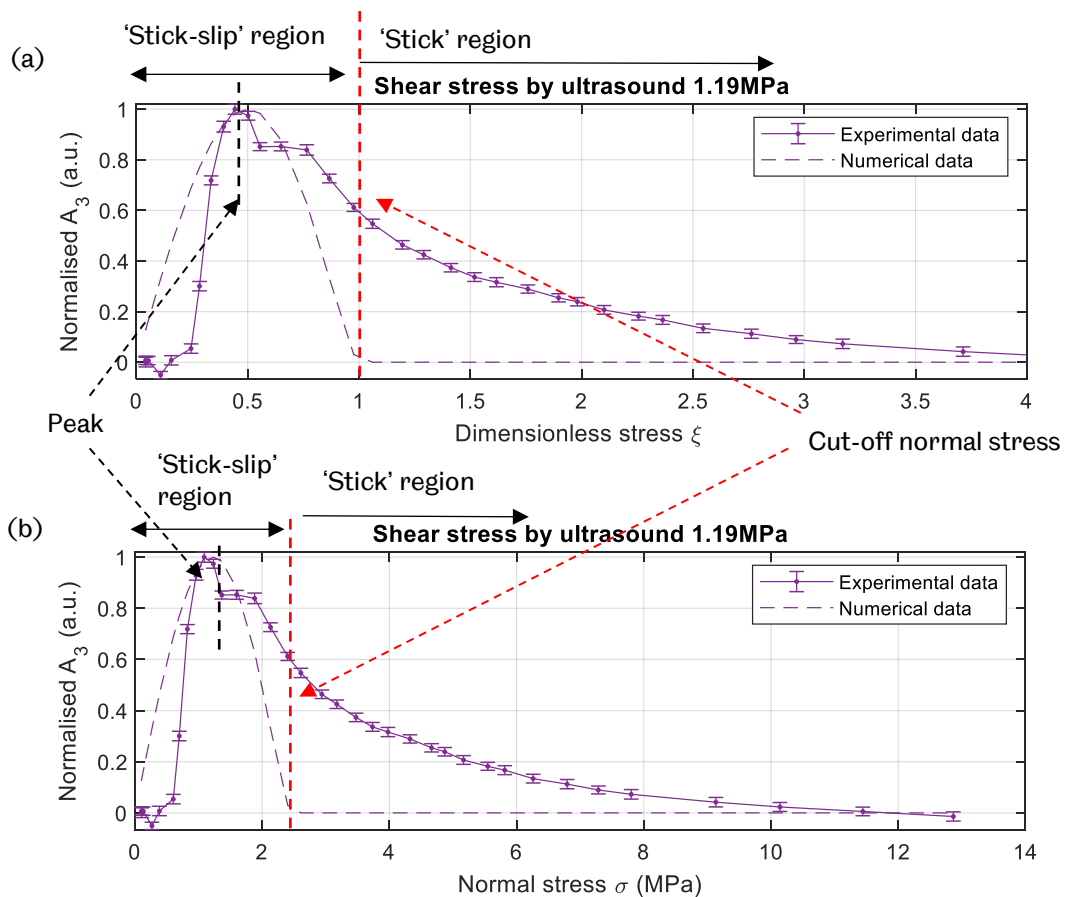


Figure 8.8 Estimation friction coefficient using cut-off stress. Normalised contact nonlinearity A_3 vs Dimensionless stress ξ and (b) Normal stress σ . (Test specimen S1-S4, excitation 280V, 100 repetitions).

8.2.2.1 Normal Stress at The Peak of Ultrasonic Nonlinearity

It is noticed that in Figure 8.8, numerical determination of the cut-off friction is less challenging. However, for the experimental data, to locate the cut-off stress proves difficult. One way to estimate the cut-off stress experimentally is to use the peak location of the harmonic generation.

The peak location (i.e. the contact normal stress) of the experimentally measured and numerically predicted ultrasonic nonlinearity illustrated in Figure 8.3 are listed in Table 8.4. At various test conditions, the normal stress where the harmonic generation reaches the peak, in both numerical and experimental work shows some reasonable agreement. The differences may arise from the practical measurement of the contact normal stress and the ultrasound introduced shear stress.

Table 8.4 Estimated normal stress at the peak position in numerical and experimental work, from Figure 8.3.

Test conditions: shear stress	Normal stress at peak location in numerical study	Normal stress at peak location in experimental study
0.496MPa	0.527MPa	0.527MPa
1.194MPa	1.234MPa	1.089MPa
2.302MPa	2.391MPa	1.563MPa

8.2.2.2 From Normal Stress at The Peak to The Cut-Off Stress

After determination of the contact normal stress where the ultrasonic nonlinearity peaks, the cut-off stress can then be estimated using a coefficient as defined in Equation (8.11):

$$M = \frac{\sigma_{peak}}{\sigma_{cut-off}} = \frac{\xi_{peak}}{\xi_{cut-off}}. \quad (8.11)$$

The coefficient M describes the relationship of the peak of the ultrasonic nonlinearity and the stop point of the harmonic generation. The coefficient is normally determined using the dimensionless stress ξ , as depicted in Figure 8.9. In this numerical study, the peak occurs when dimensionless stress is 0.5 and the cut-off point is always unity.

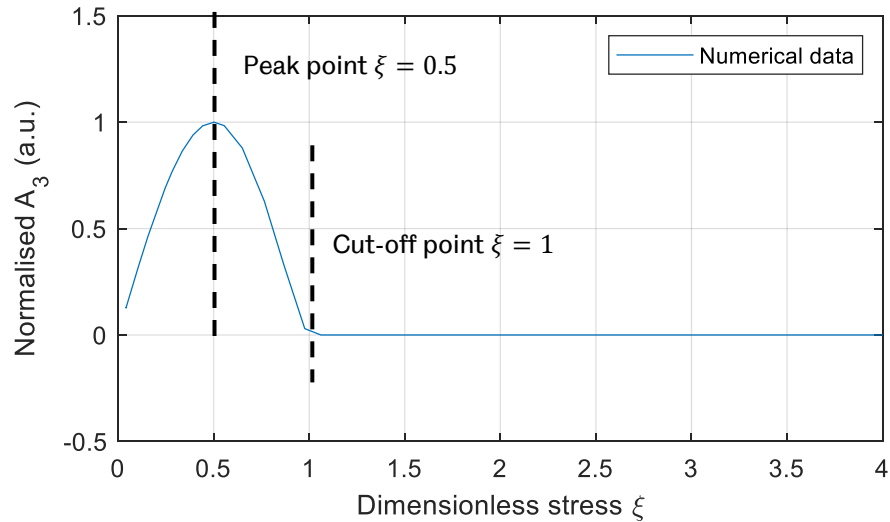


Figure 8.9 Estimation cut-off point using the peak point in numerical study.

It is worth mentioning that in other research, different peak point values are obtained and these are listed in Table 8.5. Although the peak of the ultrasonic nonlinearity is computed as various dimensionless stresses, the variation is insignificant, varying from 0.4 to 0.5. The peak value obtained in this research work $\xi = 0.5$ (Chapter 5) is reasonably applied in the following friction coefficient estimation.

Table 8.5 Various peak point of ultrasonic nonlinearity.

Previous work	Peak point
2-D numerical study (Hirose 1994)	$\xi \approx 0.5$
1-D numerical study with time harmonic sine incidence (O'Neill et al., 2001)	$\xi \approx 0.5$
1-D analytical study with time harmonic sine incidence (Meziane et al., 2011)	$\xi = 0.5$
1-D analytical study with narrow band pulse incidence (Meziane et al., 2011)	$\xi \approx 0.4$
2-D numerical study with non-plane incidence (Meziane et al., 2011)	$\xi \approx 0.4$
1-D numerical study with 5-cyc sine incidence (Blanloeuil et al., 2014c)	$\xi \approx 0.45$

The coefficient M is thus determined to be 0.5 and therefore the cut-off stress is calculated using Equation (8.12):

$$\sigma_{cut-off} = \frac{\sigma_{peak}}{M} = 2\sigma_{peak}. \quad (8.12)$$

8.2.2.3 Estimation of Friction Coefficient Using Cut-Off Stress Strategy

With the cut-off stress strategy estimated using the peak of the nonlinearity generation, the friction coefficient in the experiment can be estimated using Equation (8.13). The estimation process is summarised in Figure 8.10. The shear stress $\tau_{ultrasound}$ is previously defined in Equation (8.4).

$$\mu = \frac{\tau_{ultrasound}}{\sigma_{cut-off}} = \frac{\tau_{ultrasound}}{\frac{\sigma_{peak}}{M}} = M \frac{\tau_{ultrasound}}{\sigma_{peak}} = 0.5 \frac{\tau_{ultrasound}}{\sigma_{peak}} \quad (8.13)$$

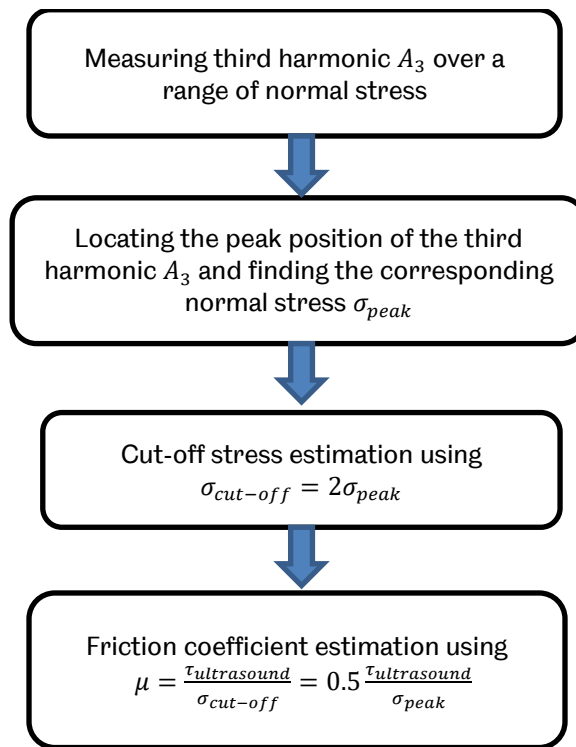


Figure 8.10 Procedure of estimation friction coefficient using cut-off stress strategy.

To locate the peak point of measured third harmonic A_3 and to remove the fluctuation during experiment, a parabolic function is employed to fit the test results around the peak of the measured nonlinearity. One advantage of using the quadratic curve is that it offers a good agreement with both numerical and analytical solution

of the third harmonic (as previously discussed in Chapter 5), as depicted in Figure 8.11. The peak feature is preserved when the quadratic function is used to smooth the experimental data.

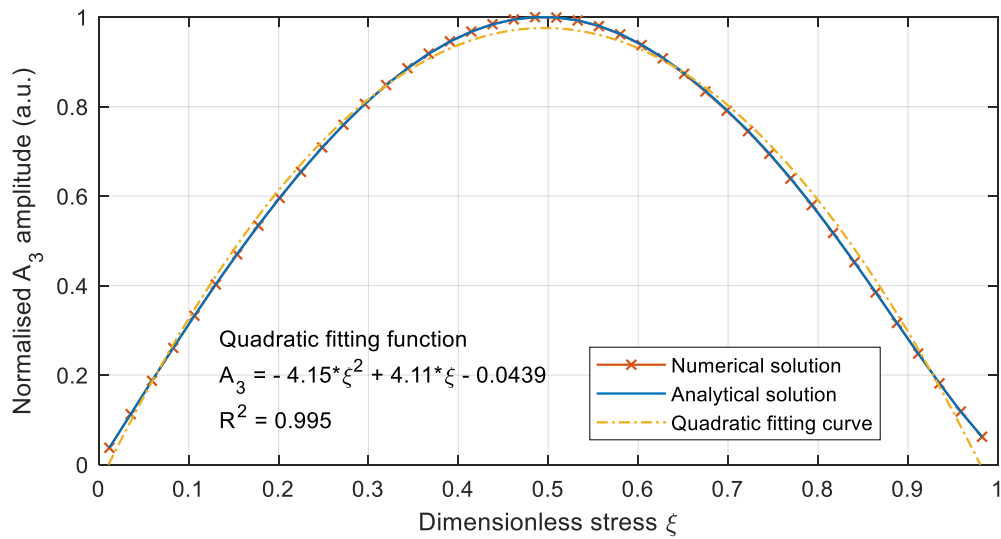


Figure 8.11 Numerical and analytical solution of harmonic generation (from Chapter 5) fitted with quadratic function.

An example of using this strategy is illustrated in Figure 8.12. For test contact pair S1-S4, the friction coefficient is estimated at approximately 0.50 under the shear stress of 1.70MPa and 0.59 under the shear stress of 2.30MPa. The difference as previously discussed may arise from the measurement of the shear stress introduced by ultrasound.

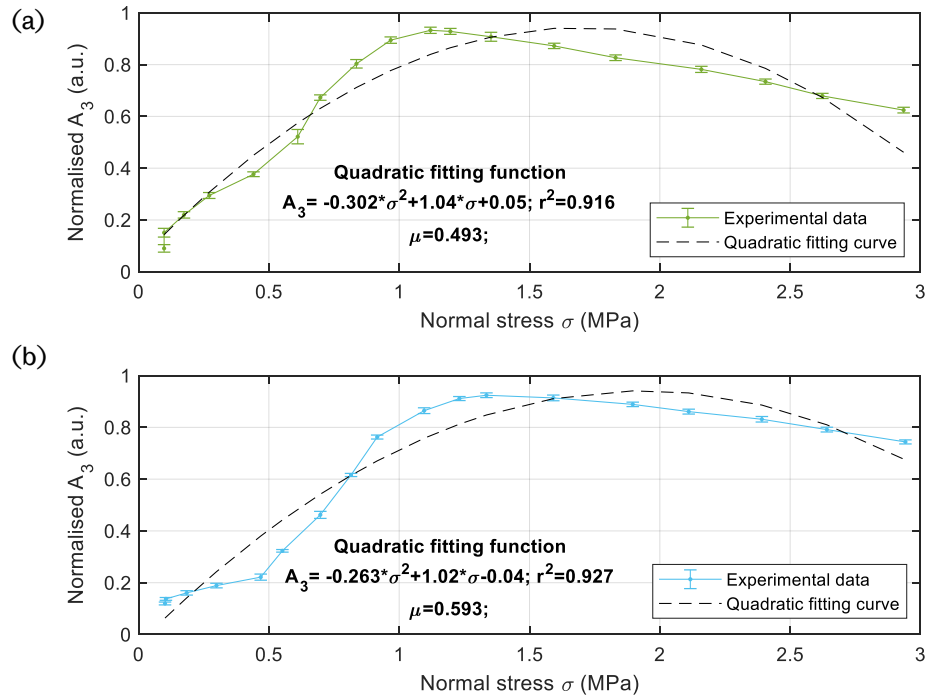


Figure 8.12 Estimation friction coefficient using cut-off stress for test specimens S1-S4. (a) Shear stress by ultrasound 1.70MPa (excitation 420V) (b) Shear stress by ultrasound 2.30MPa (excitation 560V).

This approach is also applicable to all test conditions for various shear and normal stress, as shown in Figure 8.13. The peaks at various conditions are determined using a threshold value, i.e. 0.95, as the 'x' markers in Figure 8.13. The friction coefficient is computed at each peak which satisfies the threshold requirement and the arithmetic average value is calculated as the friction coefficient.

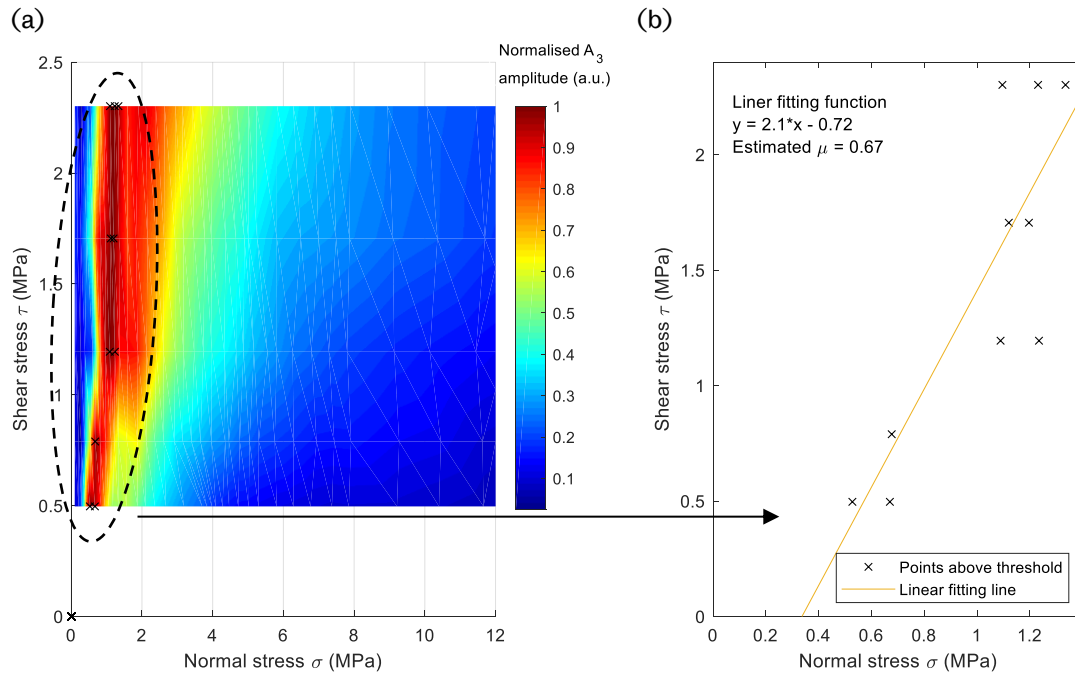


Figure 8.13 Estimation friction coefficient using cut-off stress strategy for test specimens S1-S4. (a) Shear stress by ultrasound vs normal stress at interface (excitations 90 – 560V). (b) Peak points used in friction coefficient estimation.

For the test contact pair S1-S4, the averaged friction coefficient is approximately 0.67, which is in reasonable agreement with sliding test value (0.48). It is noticed that the measurement points ('x') in Figure 8.13 (b), shows a linear relationship between the shear stress and normal stress, which agrees with the Amontons' Law that frictional force is proportional to the normal force (Hutchings and Hutchings, 2017).

8.2.3 Correlation Experiment with Numerical Model

The second strategy to estimate the friction coefficient is using numerical computation to fit the experimental data. One simple approach is to use the correlation of the experimental data with the numerical data subject to the same test conditions. Other more advanced statistical tools are available to estimate the friction coefficient from the experimental data, such as Markov Chain, however, they are out of the scope of current research. In this work, the simple correlation strategy is used.

The same test conditions experimentally applied are set as the input in the numerical computation. The friction coefficient ranges from 0 to 1 is used in the numerical calculation. For each friction coefficient, the nonlinearity computed numerically is compared with the experimental data and the correlation coefficient is calculated for each friction coefficient input. The most correlated friction coefficient is the estimated friction coefficient for the experimental data.

The correlation coefficient is as defined in Equation (8.14):

$$r = \frac{1}{n} \sum_{i=1}^n \left(\frac{A_i - \mu_A}{\sigma_A} \right) \left(\frac{B_i - \mu_B}{\sigma_B} \right). \quad (8.14)$$

where A and B are the contact nonlinearity (i.e. the third harmonic amplitude A_3) in the numerical study and experimental work, respectively, n the length of each data, A_i the element, μ_A the mean and σ_A the standard deviation of A , B_i the element, μ_B the mean and σ_B the standard deviation of B . The frequently used correlation coefficient measures the linear dependence of the data A and B .

The procedure of estimating friction coefficient using the correlation of experimental data with the numerical computation are summarised in Figure 8.14. Examples using this strategy are depicted in Figure 8.15 and Figure 8.16.

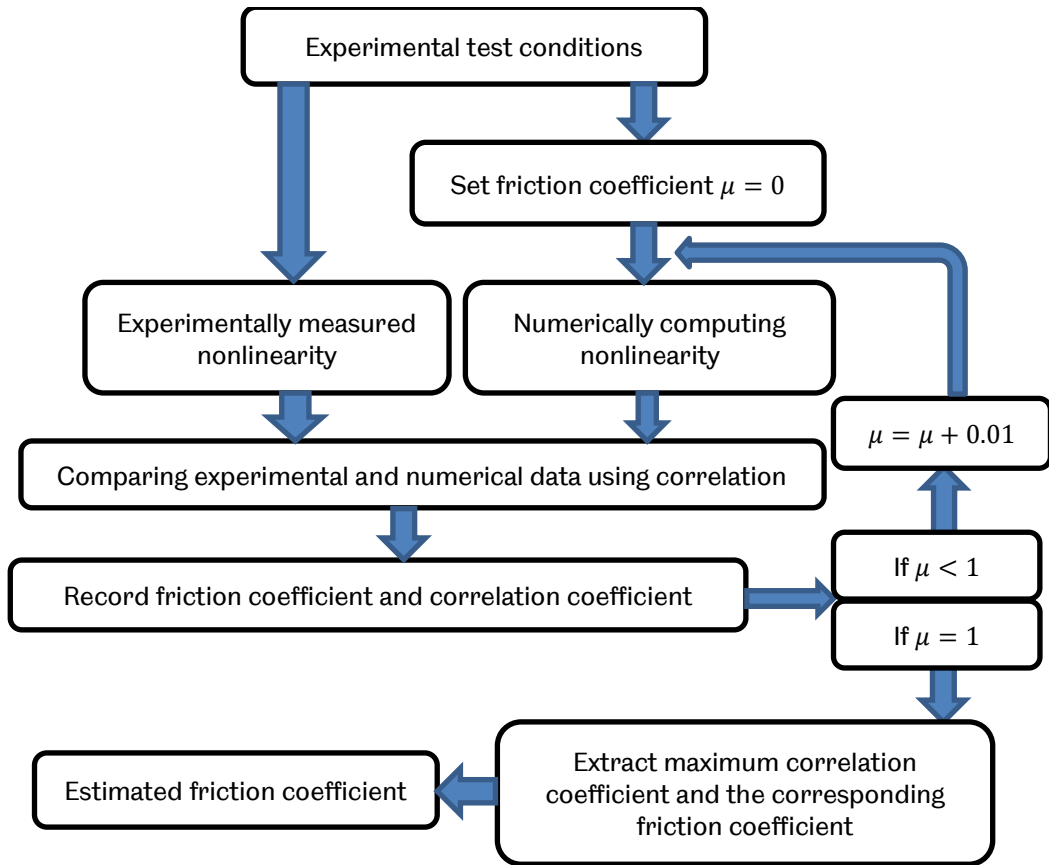


Figure 8.14 Procedure of estimation friction coefficient using correlation strategy: correlation of experimental data with numerical computation.

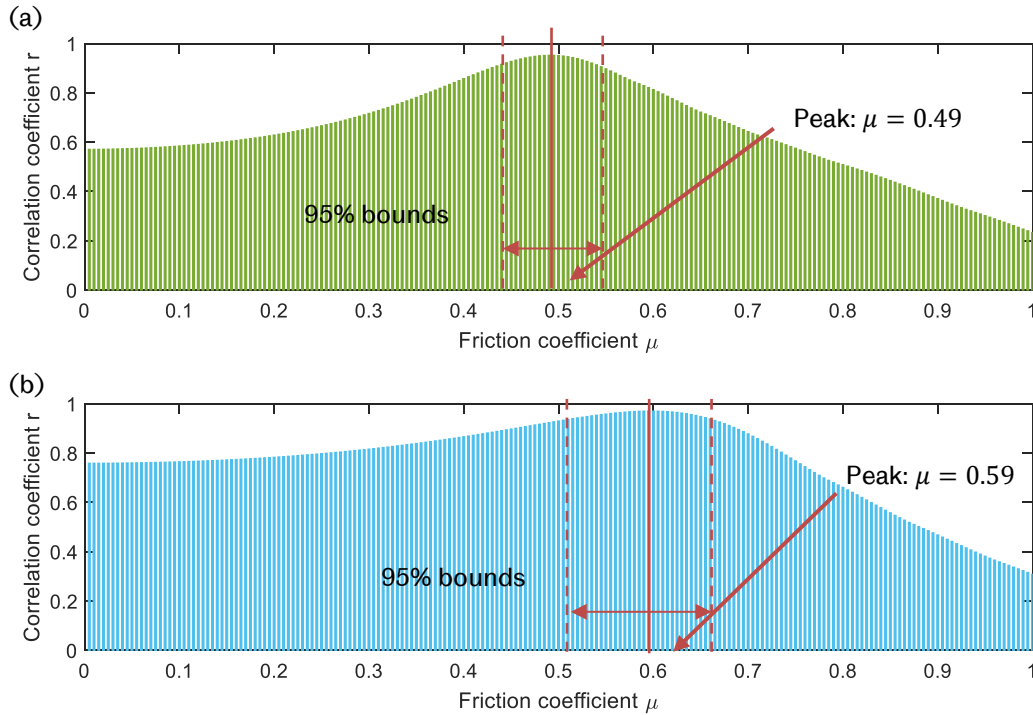


Figure 8.15 Estimation friction coefficient using correlation strategy for test specimens S1-S4. (a) Shear stress by ultrasound 1.70MPa (excitation 420V). (b) Shear stress by ultrasound 2.30MPa (excitation 560V).

It is observed that in Figure 8.15, at the vicinity of the maximum correlation coefficient, several friction coefficients also yield similar correlation coefficient so that the several numerically computed results satisfy the experimental data. It may indicate that friction coefficient of a small localised contact region differs others and the shear wave ultrasound may detect the total resultant friction coefficient in the contact area. Therefore several friction coefficients μ satisfy the experiments.

The friction coefficient with the peak correlation coefficient is used as the estimation and friction coefficient within the 95% peak bounds (red dashed line in Figure 8.15) are used as discrepancies. For the contact pair S1-S4, the friction coefficient is approximately 0.49 (0.49-0.54 as 95% bounds) for a shear stress of 1.70MPa and 0.59 (0.49-0.67 as 95% bounds) for a shear stress of 2.30MPa. The measured incidence shear stress may be the reason for the difference of estimated friction coefficient.

In Figure 8.16 the computation of correlation coefficient is carried out for all the test conditions. When the numerical computation aligns most with the experimental study, the friction coefficient is approximately 0.42 with several similar values (0.34-0.51 95% bounds) also in agreement with experimental work in this vicinity.

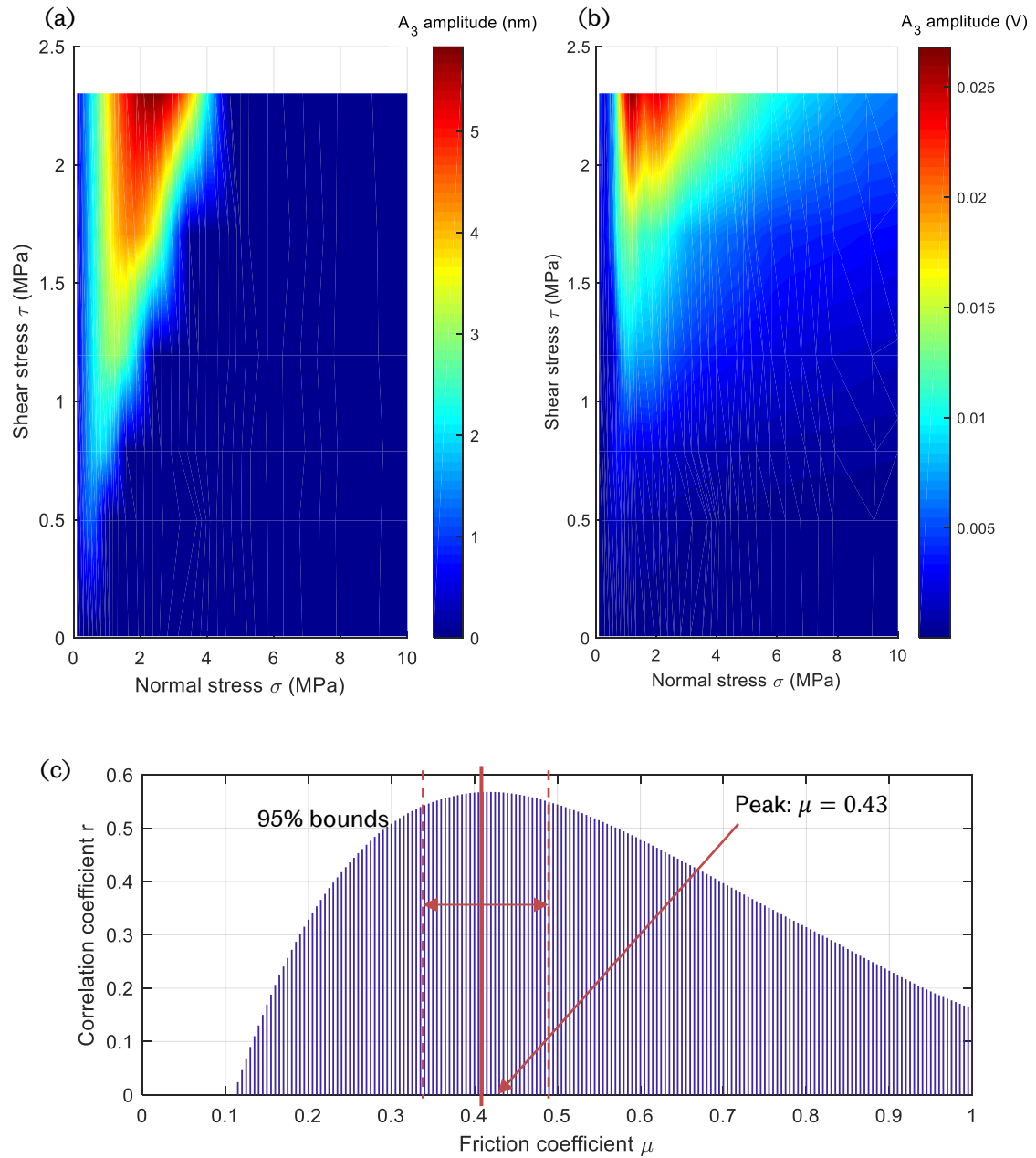


Figure 8.16 Estimation friction coefficient using correlation strategy for test specimens S1-S4. (a) Numerically computed nonlinearity and (b) experimentally measured nonlinearity subject to various excitations (2 – 560V) and normal stress. (c) Friction coefficient estimation.

8.2.4 Coefficient of Friction Estimation Using Ultrasound

8.2.4.1 Estimation Friction Coefficient

For all test specimens and contact pairs employed in this research work, the friction coefficient has been estimated using both strategies previously discussed in Section 8.2.2 and 8.2.3.

The friction coefficient estimated using the cut-off stress strategy is shown in Figure 8.17 and compared with the friction coefficient measured using the sliding test. The black dash lines indicate the maximum and minimum friction coefficients measured in the sliding test. With the cut-off stress strategy, the friction coefficient is shown in blue circles (Figure 8.17 (a)). For all specimens, the magnitude order is the same as that of the sliding test measurement and for some specimens the estimated friction coefficients are within the sliding test bounds (4 out of 9 specimens, 44%). A perfect agreement line (black solid line in Figure 8.17 (b)) is used to check the agreement of friction coefficient measured using ultrasound with sliding test. Although some ultrasound estimated values are distributed in the vicinity of the perfect agreement line, the rest scatter away. These friction coefficient using ultrasound and sliding tests are not well aligned. When all test condition are employed in the estimation, although fewer friction coefficient estimated using ultrasound falls within the bound (3 out of 9 specimens, 33%) (Figure 8.17 (c)), it still yields same magnitude order. Alignment of friction coefficient estimated using ultrasound and sliding test are not improved (Figure 8.17 (d)).

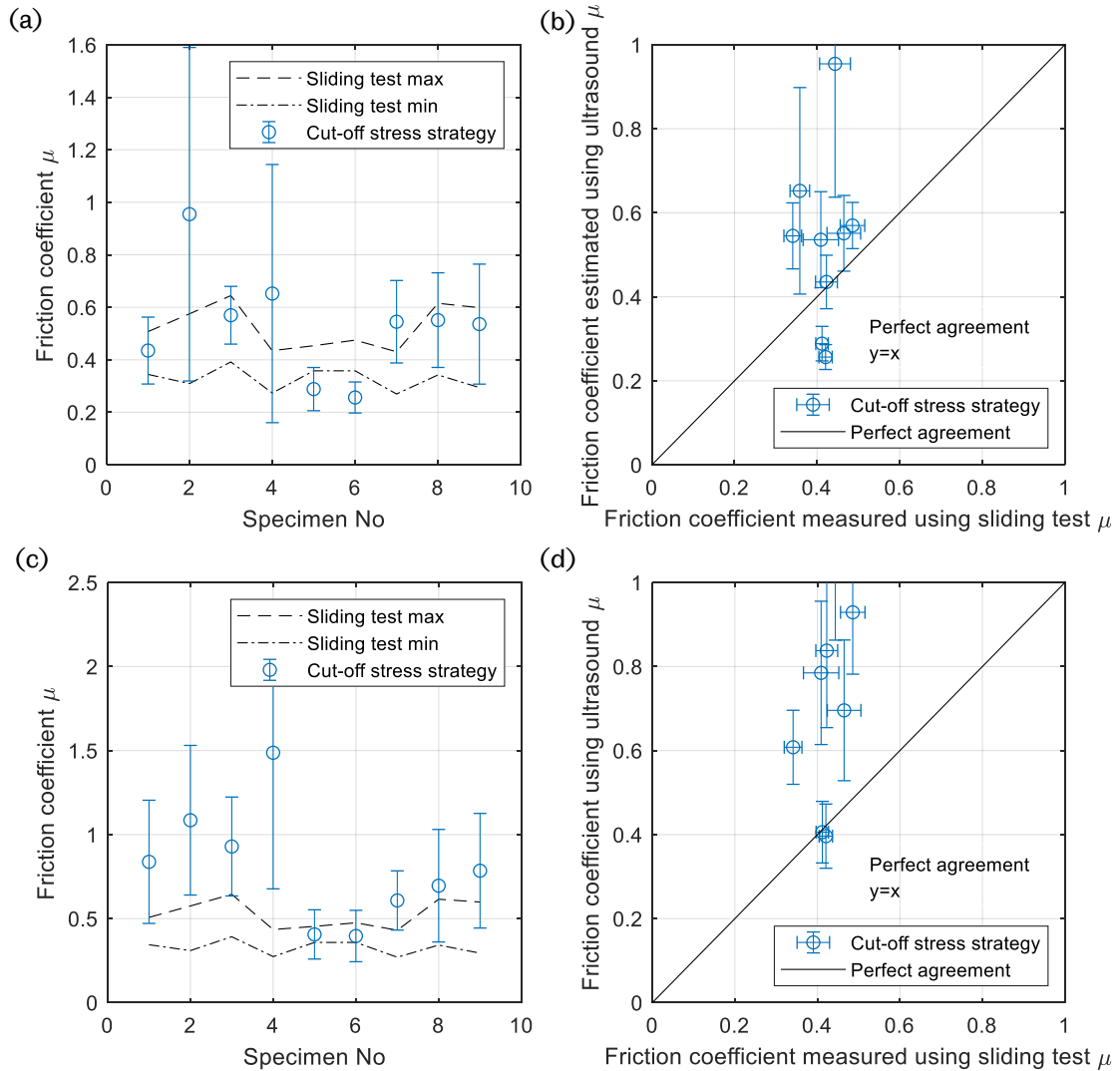


Figure 8.17 Estimation friction coefficient using cut-off stress strategy. (a) Test specimen No. vs friction coefficient. (b) Comparison between friction measurement using sliding test and ultrasound. (c) Test specimen No. vs friction coefficient for all the test conditions. (d) Comparison between friction measurement using sliding test and ultrasound for all the test conditions.

The friction coefficient estimated using correlation strategy is shown in Figure 8.18. Like the cut-off stress strategy, the estimation of friction coefficient using a single test condition shows some agreement (5 out of 9 specimens in the sliding test bounds, 55%) (Figure 8.18 (a) and (b)). The estimated friction coefficient shows the same magnitude with the measured values used in the sliding test. Improvement in estimation is achieved when all the test conditions are used (7 out of 9 specimens in the sliding test bounds, 77%). The ultrasonically estimated friction coefficient shows slightly improved agreement with the sliding test in Figure 8.18 (c) and (d).

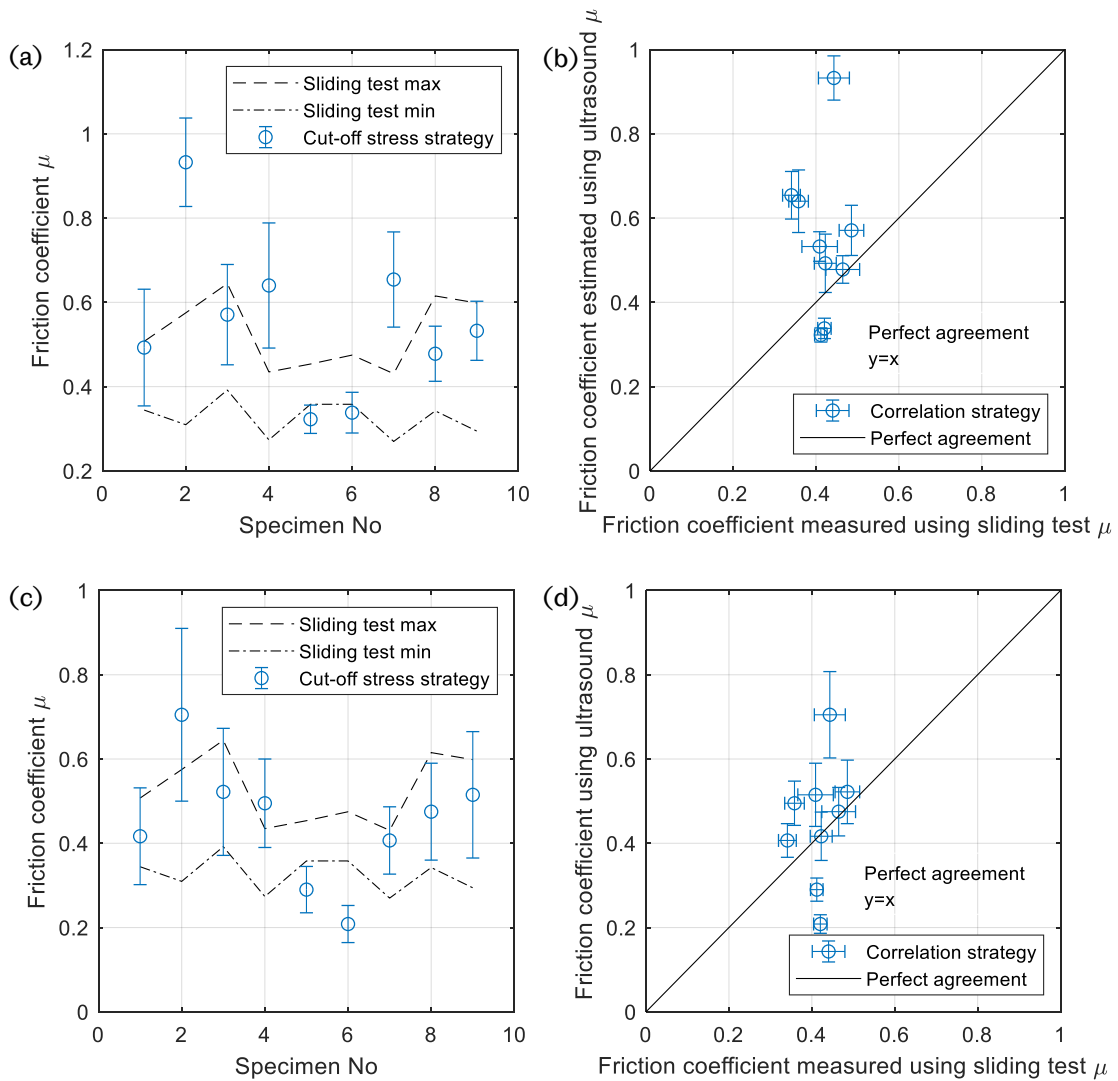


Figure 8.18 Estimation friction coefficient using correlation strategy. (a) Test specimen No. vs friction coefficient. (b) Comparison between friction measurement using sliding test and ultrasound. (c) Test specimen No. vs friction coefficient for all the test conditions. (d) Comparison between friction measurement using sliding and ultrasound for all the test conditions.

8.2.4.2 Friction Coefficient Comparison

The friction coefficient is estimated using an ultrasonic method on aluminium alloy test specimens. The friction coefficient of aluminium on aluminium or similar materials has been previously investigated. For aluminium on aluminium metal contact, the friction coefficient is approximately 1.2 while it decreases to 0.8 if the contact is made of an oxide film (Bowden and Tabor, 1964). With a simple model considering plastic deformation, the friction coefficient is estimated as 0.2 generally for metals (Tabor, 1981). With a centrifugal friction apparatus, the static friction of

aluminium to aluminium contact is approximately 0.5 (Dunkin and Kim, 1996). The comparison of the published friction coefficient with that estimated using ultrasonic method is illustrated in Figure 8.19 (a).

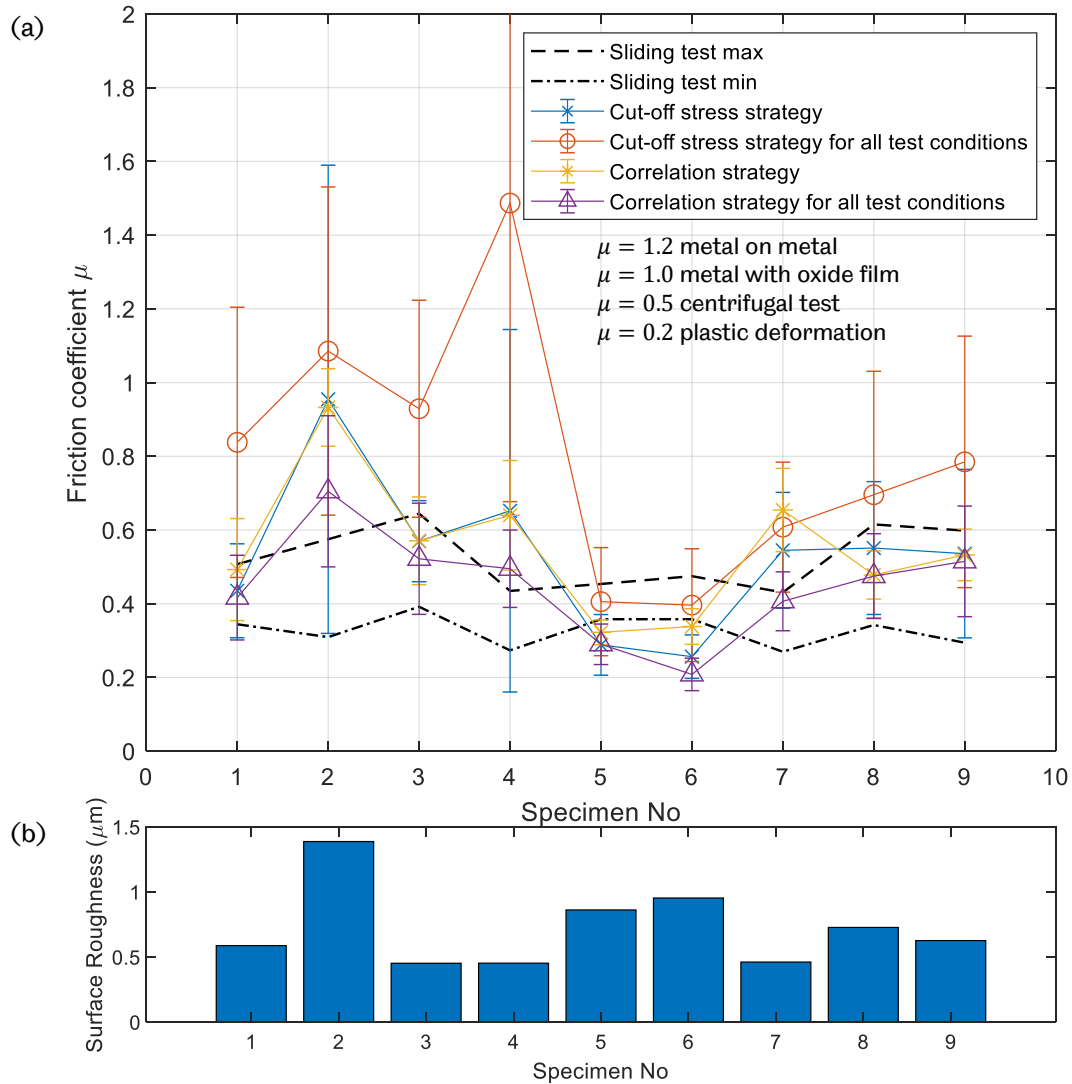


Figure 8.19 (a) Comparison between friction coefficient measured using ultrasonic strategies with sliding test and other published values for aluminium contacts. (b) Surface roughness of test specimens.

The friction coefficient measured using sliding test for all contact specimens ranges from approximately around 0.38-0.48 (10% errors). Using ultrasound contact nonlinearity, friction coefficient is estimated from 0.3-1 (20% error for correlation strategy 95% bounds; 30% for cut-off stress strategy) for various Aluminium Alloy contact pairs. The friction estimated using ultrasound method show some agreement with the primitive sliding test (approximately 40% for cut-off stress

strategy, 67% for correlation strategy; 54% in total). The estimated friction coefficients also fall within the bounds (0.2-1.2) in previous research work. Friction coefficient measurement is affected heavily by test methods, environment conditions and contacting surface conditions. The test method and test conditions used in the ultrasound method differs from those in previous research work, this may result in the variations of the friction coefficient measurement using the ultrasonic methods.

The surface roughness is also depicted in Figure 8.19 (b). It is shown that the friction coefficient measured using ultrasound methods or sliding test is independent on the surface roughness of test specimens.

The accurate measurement of coefficient of friction is quite difficult. The results strongly depend on the test method and environmental conditions. Nevertheless, the friction coefficient measured by in-situ ultrasonic method is comparable with the published values. It is suggested that the ultrasonic method be used as a tool to determine the friction coefficient of a contact interface in-situ.

8.3 Conclusion

In this chapter, the contact nonlinearity generation from experiments was compared with the numerical computation. The experimental work shows reasonably good agreement with the numerical study. The difference between the numerical and experimental work is mainly because that the frictional interface in the numerical investigation is somehow over-simplified and is unable to realise the practical case that the real rough contact is made on asperities.

Two strategies are proposed to estimate the friction coefficient using the ultrasonic nonlinearity. The first strategy used the peak of the harmonic generation to estimate the cut-off stress where the contact is just unable to have 'stick-slip' motion under a certain shear stress introduced by ultrasound. The ratio of these stresses yields the friction coefficient. The second approach compares the numerical computation with experimental data for a range of friction coefficients. The most correlated value is the estimated friction coefficient. Coefficient of friction estimated ultrasonically is compared with the sliding test measurement and published data and reasonably good agreement is achieved, which suggests that the ultrasonic nonlinearity can be used to estimate the friction coefficient.

9 GENERAL DISCUSSION

This chapter presents discussions of the use of the ultrasonic method to estimate the friction coefficient. In addition, a pilot study for an alternative method to generate the contact nonlinearity. The use of oblique incident ultrasound is evaluated, and the usefulness of this alternative method is discussed as well.

9.1 Limitation of Experimental Approach

An ultrasonic technique to estimate the friction coefficient at a contact has been developed experimentally using the contact nonlinearity. There are some limitations with experimental approach.

In the experimental work, contact nonlinearity was coupled with the system inherent nonlinearity and it was difficult to isolate the true contact nonlinearity from the system inbuilt nonlinearity. Although methods were used to remove the system inbuilt nonlinearity, it only gave an approximate estimation of the true contact nonlinearity. Shear stress at a contact is critical in estimating friction coefficient and it is difficult to measure. A laser vibrometer was used to measure the displacement and the stress of an incident shear wave to calibration the ultrasound transmitter on a test specimen (Chapter 6). This was carried out under the assumption that the measured shear stress (from a solid-air interface) was equal to the true shear stress at a contact. With the current measurement configuration (Chapter 6 & 7), only low shear stress was achieved and the active normal stress range for the nonlinear 'stick-slip' motion was limited (approximately less than 5MPa). Contact nonlinearity

originating from the nonlinear ‘stick-slip’ motion at a contact was measured experimentally (Chapter 7). What happens microscopically, however, is still not clearly understood, especially very small asperity slips (in order of nanometres) occurring repeatedly. Possible signs of fretting were observed on the contacting surface of test specimen S1, in Figure 9.1, (the other end of the specimen where the ultrasonic transducers were placed) after the contact surface was exposed to numerous repeated ultrasonic oscillations and ‘stick-slip’ motions.

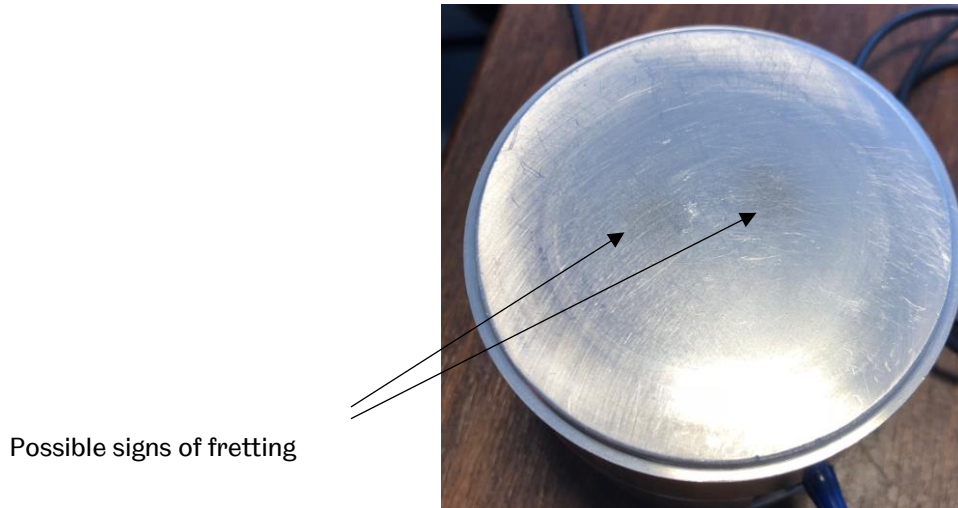


Figure 9.1 Possible signs of fretting on the contacting surface of test specimen S1.

9.2 Limitation of Numerical Study

9.2.1 Numerical Implementation

In the numerical study, a simple one-dimensional model was employed to study the harmonic generation from a rough interface when interacting with a high-power ultrasound. Comparison between the numerical and the experimental results (Chapter 8) showed that the simplified 1-D model was able to capture the key phenomenon (‘stick-slip’) and the nonlinearity generation on the ultrasound. With several assumptions, this over-simplified 1-D numerical model proved its usefulness in computing the nonlinearity from a rough contact (Blanloeuil et al., 2014c). Due to the assumptions made in the 1-D model, the numerical computation showed some differences between the experimental results, as discussed in Chapter 8.

The nonlinear interaction of a high-power shear polarised ultrasound with a frictional interface has mainly been investigated numerically and various numerical models have been implemented. From a simple 1-D numerical model (Blanloeuil et al., 2014c) to more advanced and complicated 2-D numerical study (Hirose 1994; Meziane et al., 2011), the numerical computation yields good agreement. The 1-D model used in this research work, although unable to compute the real propagation of ultrasound, is sufficient in revealing the nonlinearity originating at a contact.

9.2.2 Contact Mechanics

In the previous 1-D or 2-D numerical study, the contact interface is assumed to be a flat but frictional plane (Hirose, 1994; Meziane et al., 2011; Blanloeuil et al., 2014c). This assumption consequently results in the main difference between the numerical study and the experimental work, as discussed in Chapter 8. The real contact on the asperities is not taken into consideration in the numerical study in this research work.

The contact of rough surface has been studied for several decades and various models have been developed to explain the real contact at rough surfaces. Incorporating the contact mechanics with the linear ultrasound has been investigated at an interface (Kendall and Tabor, 1971; Królikowski and Szczepek, 1993; Dwyer-Joyce et al., 2001; Baltazar et al., 2002). The nonlinear interaction ('stick-slip') at a rough contact has also been investigated with micromechanical models (Pecorari, 2003). The Greenwood-Williamson approach was employed with a Hertzian model accounting for the contact under normal compression and Mindlin's work for the tangential oscillation under shear polarised ultrasound. A quasistatic spring model was also employed to relate the measured nonlinearity to the interfacial stiffness. The odd order harmonics were generated and the third harmonic showed a peak at low contact stresses. The contact model was also taken into account in a 2-D computational study (Delrue et al., 2018; Aleshin et al., 2018). Harmonic generation due to friction was also detected.

With the contact mechanics considered in the numerical model, the nonlinear interaction at the rough contact interface helps to achieve better understanding as the practical contact is properly modelled. An area for further study is the use of nonlinear ultrasound to study higher order interfacial stiffness.

9.3 Limitation of Prediction of Friction Coefficient

The numerical study used in this research work applies the classic Coulomb friction model. The effect of both static and kinetic friction coefficient on the ultrasonic nonlinearity generation was discussed in the numerical study in Chapter 5. In estimating the friction coefficient with ultrasound in Chapter 8, only the static friction coefficient was calculated and the kinetic friction coefficient was assumed equal to the static friction coefficient. This may lead to some errors in the estimation of friction coefficient.

In the experimental work, slipping takes places when the incident shear stress generated by ultrasound overcomes the static friction at the interface. During the slipping process, the contact interface is characterised by a kinetic friction coefficient rather than the static friction coefficient. The numerical computation employed to estimate friction coefficient used static friction coefficient and therefore the estimation presents an 'averaged' friction coefficient at the contact rather than the true static friction coefficient.

In the experimental work, the contact specimens remained macroscopically static. The amplitude of ultrasound incidence was of the order of nanometres. In this case, the rough surfaces slip several nanometres under the shear ultrasound oscillation. However, it is still negligible with respect to the globally static contact. Therefore, the friction coefficient estimated using ultrasound is reasonably treated as the static friction coefficient.

Other friction laws could be investigated in the numerical study to account for the non-constant friction coefficient during the 'stick-slip' process. The results may be helpful in the estimation of both static and kinetic friction coefficient using ultrasound.

9.4 Pilot Study of an Alternative Method

In previous chapters, ultrasonic nonlinearity generation at a rough interface using a normal incident high-power ultrasound has been investigated. 'Stick-slip' motion is activated at the interface and contact nonlinearity is generated. The nonlinearity is measurable and useful in estimating the friction coefficient of two contact specimens.

Recently, contact nonlinearity generation using oblique incidence has also been studied by numerical and computational methods (Hirose, 1994; Pecorari, 2003; Blanloeuil et al., 2013; Blanloeuil et al., 2014a; Blanloeuil et al., 2016). The effect of the incident angle and the incidence amplitude on the nonlinearity generation were investigated. Research results suggest that the oblique incidence approach is useful in understanding the contact states ('open' or 'close', 'stick' or 'slip').

Using oblique incidence provides more feasibility in practical applications (especially where the normal incidence is not applicable). In this section, a short pilot study has been performed to evaluate the usefulness of this approach.

9.4.1 Test Configuration and Preparation

In the experimental investigation, the test configuration and preparation discussed in Chapter 6 has been adopted here. Details are given as follows.

9.4.1.1 Test Rig

When the incidence ultrasound changes from 0 to a non-zero angle, at the contact interface, the incidence shear wave results in two components, as shown in Figure 9.2.

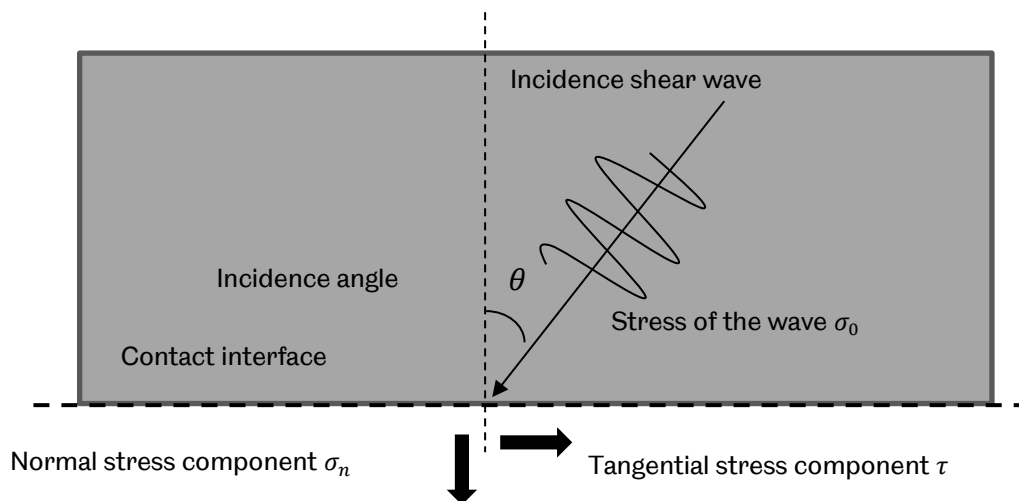


Figure 9.2 Oblique shear incident wave meeting at a contact interface. Normal and tangential stress components at the interface.

The normal stress component σ_n and the tangential stress component τ at the interface are calculated using Equations (9.1) and (9.2), respectively (Blanloeuil et al., 2013, Blanloeuil et al., 2014a). σ_u denotes the stress of the ultrasound within the host material.

$$\sigma_n = \sigma_u \sin 2\theta \quad (9.1)$$

$$\tau = \sigma_u \cos 2\theta \quad (9.2)$$

It is noticed that when the incidence angle is 0, only shear stress exists at the interface and the normal stress component is zero. When the angle is 45°, the tangential stress components vanishes while the normal stress reaches the maximum. At this angle, the incident ultrasound can only trigger clapping motion at the contact interface and permits no slipping (Blanloeuil et al., 2013; Blanloeuil et al., 2014a). For this work, an incidence angle of 25° was selected in the experiment to ensure that the slipping motion can take place at the contact under the ultrasonic oscillations.

An aluminium alloy wedge with two inclined angles at 25°, as shown in Figure 9.3, was used in the experimental study.

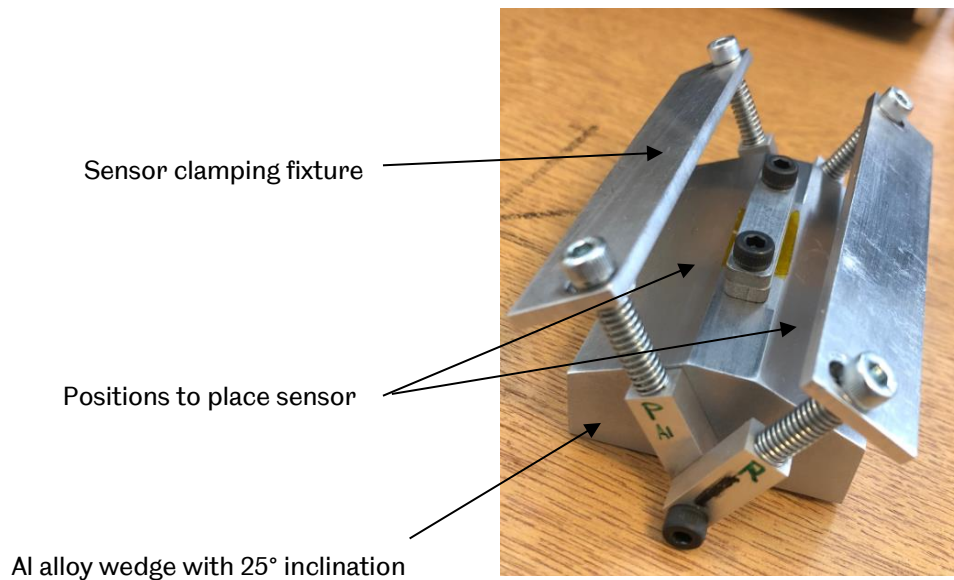


Figure 9.3 Al alloy wedge with 25° inclination in the experimental work.

9.4.1.2 Experimental Parameters

Knowing the shear stress at the contact interface is critical for the determination of friction coefficient, as shown in previous experiments with normal incidence. A laser vibrometer measurement was employed to measure the displacement at the contact face of the wedge. The displacement component normal to the contact face was measured. The stress was calculated using Equations (9.1) and (9.2). The laser vibrometer measurement and the stress components at the contact face are listed in Table 9.1.

Table 9.1 Laser vibrometer measurement with 25° wedge at varying input levels.

Input excitation	Displacement measured with laser vibrometer	Normal stress at contact face	Tangential stress at contact face
45V	8.57nm	0.468MPa	0.393MPa
90V	14.88nm	0.814MPa	0.683MPa
140V	24.67nm	1.35MPa	1.132MPa
280V	35.82nm	1.96MPa	1.644MPa

The displacement measured with the laser vibrometer increased with the amplification applied as well as the normal and tangential stress at the contact face. The normal stress component and the tangential stress component were similar in magnitude.

Due to the non-zero normal stress component, the externally applied normal stress needs to be sufficient so that the contact remains in the 'closed' state. In the experiment, the externally applied normal stress ranged from 0 to 12 MPa to ensure the contact was closed and 'stick-slip' motion was activated.

Two sensor configurations were employed in the experimental investigations, as shown in Figure 9.4. Configuration I (Figure 9.4 (a)) has been discussed in 9.4.1.1. and illustrated in Figure 9.2. With this configuration, the incident ultrasound results in the normal and tangential stress components. In the second configuration (Figure 9.4 (b)), the incident shear stress is in plane with the contact face and therefore there is no normal stress component.

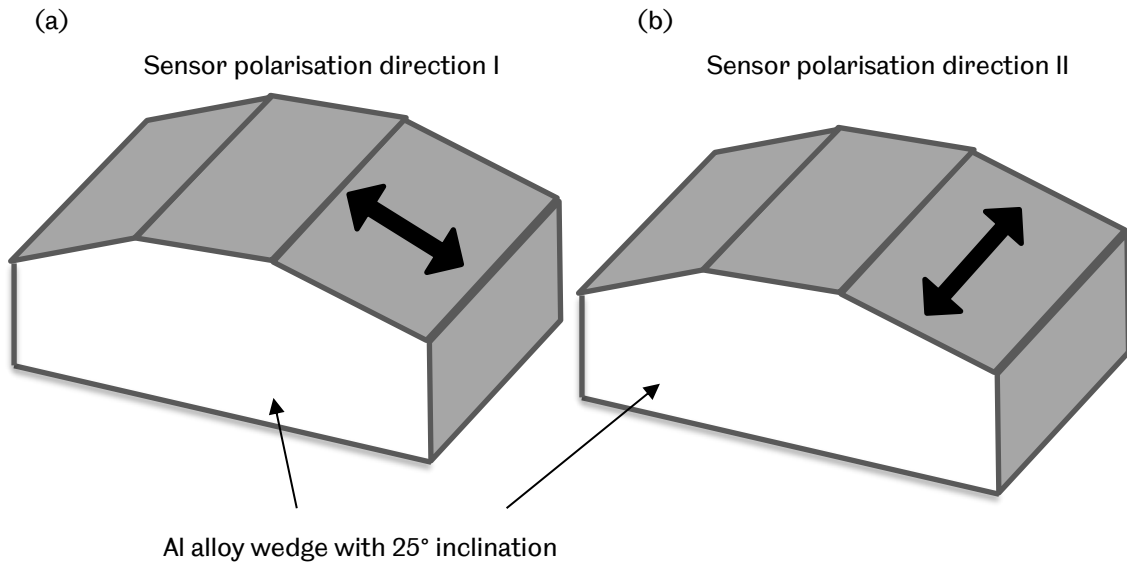


Figure 9.4 (a) Sensor configuration I. (b) Sensor configuration II.

9.4.2 Experimental Results

The pitch-catch reflection arrangement was applied in the experiment. The reflected signals were captured and analysed. The experimental results using oblique incident shear ultrasound are shown as follows.

9.4.2.1 Sensor Configuration I

The harmonic generation of the nonlinear interaction between an oblique incident shear ultrasound and a frictional interface is illustrated in Figure 9.5.

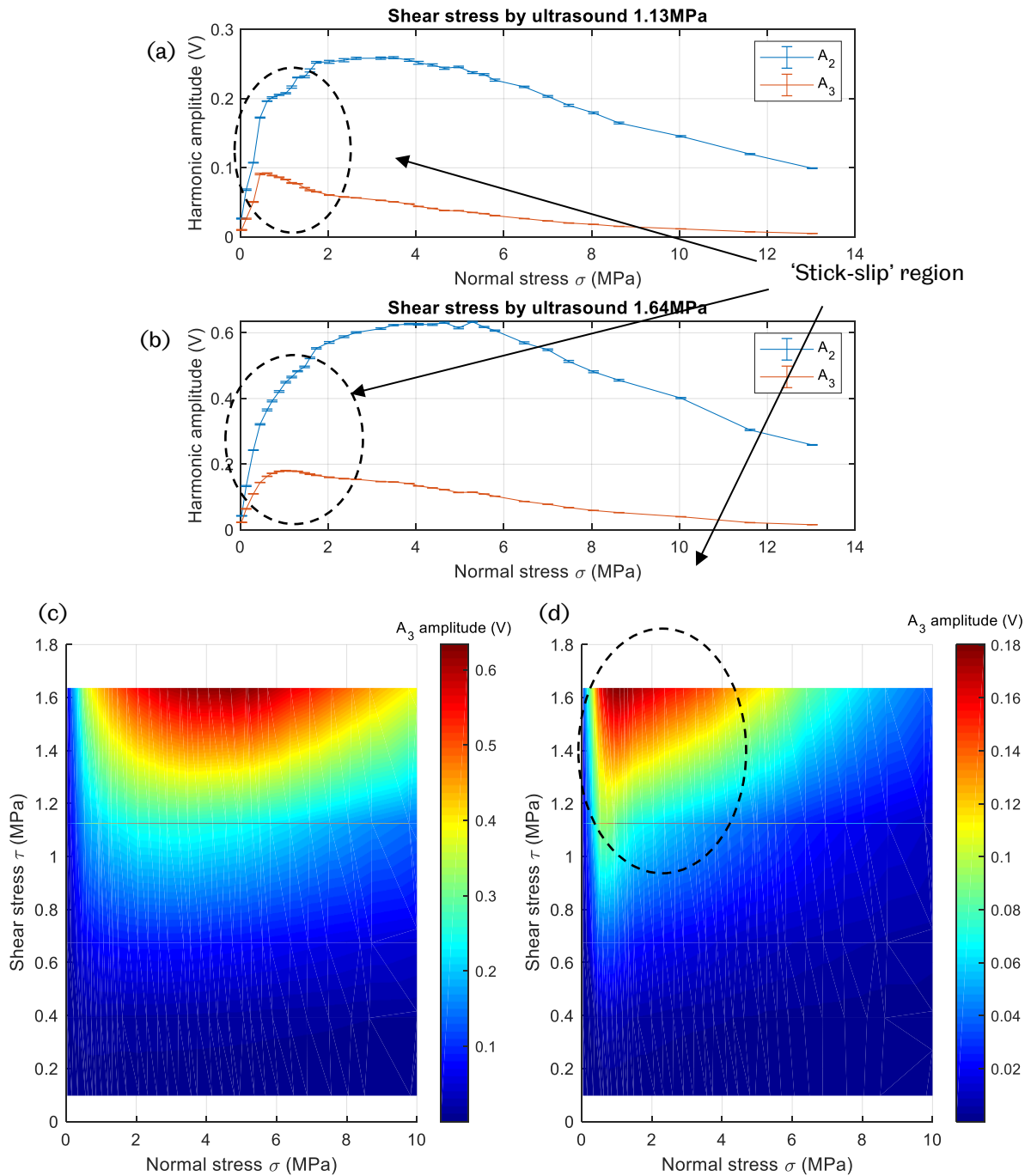


Figure 9.5 Harmonic generation at rough contact interface (Wedge-S4) using Configuration I. (a) Second and third harmonic generation subject to varying normal stress and excitation (a) 140V and (b) 280V (100 repetitions). (c) The second harmonic A_2 generation and (d) The third harmonic A_3 generation subject to varying normal stress and excitations (45 – 280V).

In Figure 9.5 (a), it is noticed that both the second harmonic A_2 and the third harmonic A_3 are dependent on the externally applied normal σ contact stress. The third harmonic, A_3 shows a 'rise-drop' trend over the normal stress, which

resembles the experimental results found in Chapter 7. The 'rise-drop' pattern indicates the activation of the 'stick-slip' motion at the contact.

It is worth noting that the second harmonic A_2 shows a greater value than that of the third harmonic A_3 . For a normal incident shear wave, only the third harmonic was generated after the nonlinear interaction ('stick-slip') at a rough interface (as discussed in Chapter 5 and Chapter 7). With an oblique incidence (Configuration I), the second harmonic, A_2 , however, was also generated. Nonlinearity in the form of the second harmonic A_2 has been found even if the contact remains closed and only pure 'slipping' occurs without any 'clapping' effect (Blanloeuil et al., 2013; Blanloeuil et al., 2014a).

The nonlinearity generation at a rough interface in the form of second harmonic A_2 and the third harmonic A_3 under all the test conditions are given in Figure 9.4 (b) and (c), respectively. The region in red (encircled by dashed line) indicates the active region of the nonlinearity generation from a rough interface.

9.4.2.2 Sensor Configuration II

The contact nonlinearity generation using the second configuration is illustrated in Figure 9.6.

In the second configuration, the sensor polarisation is in the plane of the contact face therefore only tangential stress actively functions at the contact interface. As illustrated in Figure 9.6 (a), only the third harmonic A_3 shows a dominant relationship over the applied contact stress, while the second harmonic A_2 varies slightly over stress. The 'rise-drop' trend of the third harmonic agrees with the findings in Chapter 7 where normal incidence ultrasound is applied. With this configuration, the contact remains closed and only 'stick-slip' motion is triggered, which is the origin of the measured nonlinearity.

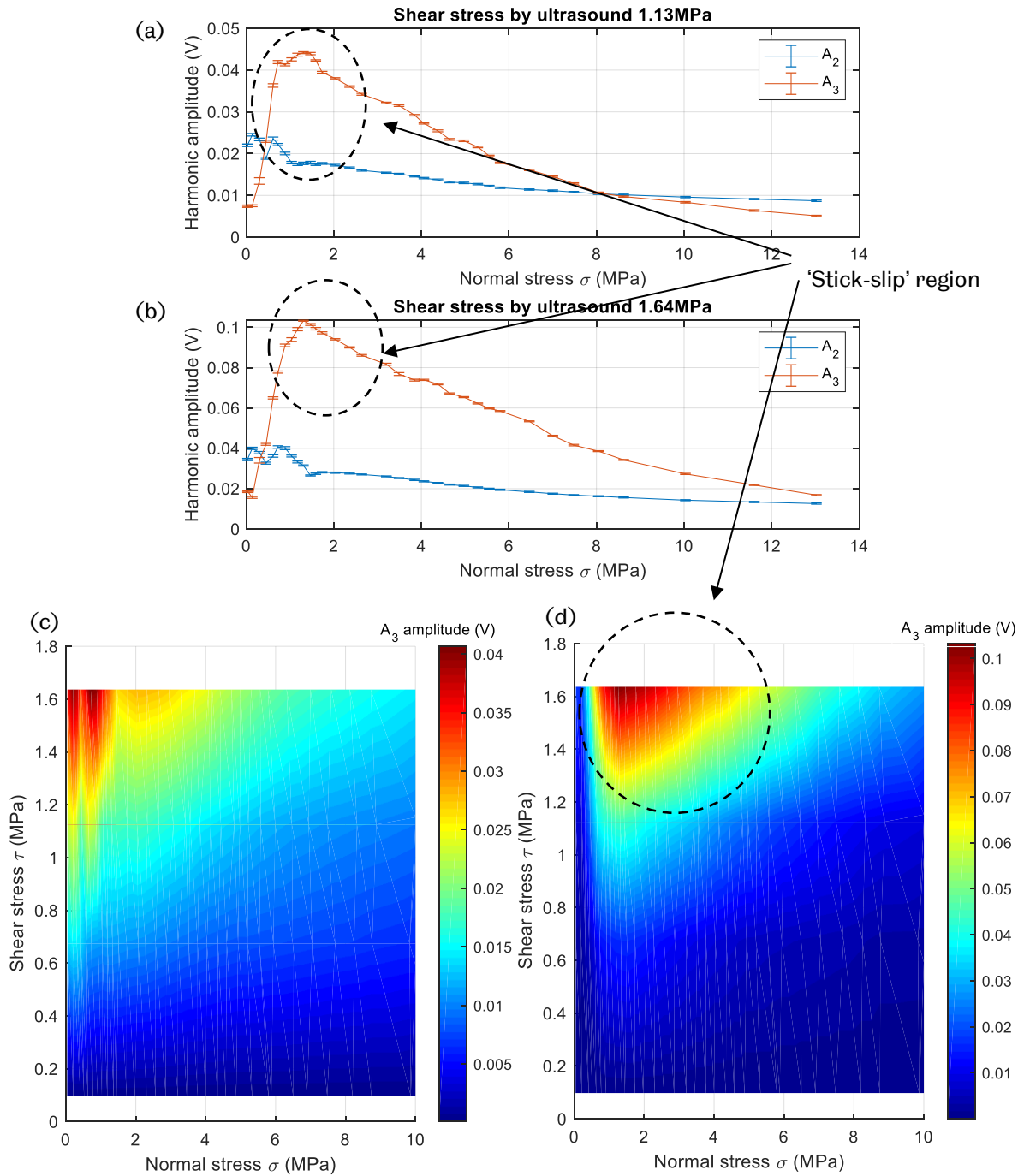


Figure 9.6 Harmonic generation at rough contact interface (Wedge-S4) using Configuration II. (a) Second and third harmonic generation subject to varying normal stress and excitation (a) 140V and (b) 280V, (100 repetitions). (c) The second harmonic A_2 generation and (d) The third harmonic A_3 generation subject to varying normal stress and excitations (45 – 280V).

For all the test conditions, the second and the third harmonic is shown in Figure 9.6 (b) and (c). As encircled in the dashed line, the red region indicates the most nonlinear interaction of a high-power ultrasound with a rough interface, which agrees with the experimental findings in Chapter 7.

Measurement of nonlinearity generation due to the interaction of a high-power ultrasound with a rough contact interface has been investigated experimentally using an oblique incident shear wave. Two sensor configurations were employed and both results show that the ultrasonic nonlinearity was generated at a frictional interface and the nonlinearity was measurable. In the first configuration, both second and third harmonics were detected and show strong relationship with the applied contact stress. When the sensor was placed in the second configuration, the third harmonic showed a 'rise-drop' trend over the normal stress which agrees reasonably with the normal incident experiment.

In both configurations, the ultrasonic nonlinearity from a frictional contact interface is detectable using oblique incidence. Experimental results demonstrate the usefulness of the method. It provides more viability of measuring the contact ultrasonic nonlinearity and is potentially an alternative tool in the estimation of friction coefficient.

With Configuration I, the contact stress at the interface is modulated by the normal stress component of the incident ultrasound. The contact nonlinearity originating at the interface in the form of second and third harmonic, contains more information about the rough interface. The presence of the normal stress component, however, can lead to the open state of a contact ('clapping' effect), which makes the measurement of harmonic generation due to 'stick-slip' motion more difficult. With Configuration II, the nonlinearity in the measured ultrasound mainly comes from the nonlinear 'stick-slip' motion. Before using the oblique incidence as an alternative tool to estimate the friction coefficient, further investigation is required to understand the role of the friction coefficient and the optimum incident angle of measurement.

9.5 From Lab measurement to Practical Application

9.5.1 Practical Estimation Friction Coefficient

The static friction coefficient was estimated using ultrasonic nonlinearity. The potential usefulness of this approach is significant. It provides a non-invasive approach to measure the friction coefficient at a rough contact interface. It also makes the in-situ measurement of friction coefficient feasible. Compared with the conventional methods of measuring the friction coefficient, no duplicated specimens are required such as those required in the pin-on-disc configuration.

Before this ultrasonic method can be applied to the practical friction coefficient measurement, several limitations are worth noting.

The ultrasonic method uses contact harmonic generation, i.e. the third order harmonic generation when a powerful ultrasound wave activates 'stick-slip' at the contact interface, to estimate the friction coefficient. In the current research work, the 'stick-slip' effect takes place only at a low-stress region, generally less than 5MPa subject to input voltage of 200–300V. Such stress is considerably low compared to the typical stresses in the practical engineering applications. For example, wheel-rail contact pressure is of 1500MPa (Marshall et al., 2006) and rolling bearings up to 2GPa (Quinn et al., 2002). Currently the ability to generate only low shear stress represents a serious limitation of the work. At the high contact stress, the activation of 'stick-slip' may be possible when the incident shear stress is sufficiently large, which is generally associated with large voltage input.

In the current work the ultrasonic probes are used as the transmitter. The damping material inside the probe reduces the amplitude of signal heavily. Undamped piezoelectric materials may also be useful in yielding higher signal amplitude compared to the damped transducers, which may be a possible approach to obtain higher incident shear stress. Other methods of generating incident shear waves may also be used instead of using a normal shear wave probe or piezo element. Mode conversion with longitudinal piezo elements can be used to generate the incident shear wave at boundaries. The larger amplitude from a longitudinal piezo element may yield larger shear stress after mode conversion.

In the current work, the applied ultrasound is at 1 MHz. The frequency does not play a significant role. Other frequencies may also be employed in this method. High-frequency transducers are available in a small size so the ultrasound wave can be targeted to a limited area. However, the incident amplitude from a high-frequency transducer does not permit high incidence shear stress. An even higher frequency transducer is also required for receiving the signal. When selecting a frequency, compromise needs to be made to ensure the optimum incident shear stress.

The materials of the contact specimens in the current research work were aluminium alloys. Other materials can be used in a similar way. If two dissimilar materials are employed, the numerical model needs to be modified to take account for the material difference before it is used to estimate the friction coefficient. Estimation of friction coefficient for a dissimilar contact pair is out of the scope the current research work.

In the current work, contact nonlinearity generation was only carried out for dry contacts and these were investigated by both numerical and experimental methods. Contact nonlinearity generation has not been studied for a lubricated contact. At a lubricated interface, contact is made on asperities as well as the lubricant. High-power shear ultrasound may behave differently and the contact nonlinearity generation then becomes complicated. This is an area that requires further work.

Further investigations on the optimum stress region, optimum shear wave generation method, optimum frequency and dissimilar materials can be carried out in the estimation of friction coefficient using ultrasound.

9.5.2 From Lab Measurement to Practical Application

In the current work, estimation of friction coefficient is carried out in a laboratory environment. It is noticed that the friction coefficient is estimated when a range of test data is available, i.e. a range of contact stress subject to a contact incident stress. The reason for this is that the ultrasonic method uses the peak of the harmonic generation and a range of the test data to produce such peak. The peak in the harmonic generation can be obtained in two ways, i.e. constant incident shear stress but varying contact stress, and constant contact stress but varying incident shear stress. Practically varying the incidence shear stress is more viable than varying the contact stress.

Several ways are available to transfer the current lab-based method to a practically useful tool to estimate the friction coefficient.

- Sweeping input power. The input power is programmable so that a range of the input power is swept, resulting in a range of incident shear stress. At constant contact stress, the sweeping input power enables the measurement of the peak of the harmonic.
- Multiple echoes. As previously discussed in Chapter 7, the subsequent echoes contain nonlinearity information. Due to the multiple interactions with the rough contact interface, the nonlinearity information is amplified. In such a way, with a lower power input, i.e. lowered incident shear stress, harmonic generation may still take place and can be used to estimation friction.
- Oblique incidence. As previously discussed in this chapter, harmonic generation also occurs under oblique incidence. At an optimum inclination angle, the incident shear stress activates the nonlinear interaction, i.e.

'slipping' motion. The resultant nonlinearity generation is useful in the estimation friction coefficient.

10 CONCLUSIONS

This thesis presents the work of developing an ultrasonic method to measure friction coefficient in-situ at an interface. Conclusions drawn from this study are summarised in this chapter, including the development of numerical model to investigate the nonlinear interaction between a shear ultrasound and a frictional interface, developing experimental technique to measure the contact nonlinearity and using the ultrasonic technique to measure the friction coefficient.

10.1 Modelling Nonlinearity Generation from a Frictional Interface

A simple one-dimensional numerical model has been developed to investigate the nonlinear interaction between a high-power shear polarised ultrasound and a frictional interface along with an analytical approach. When conventional low-power ultrasound meets an interface, the contact remains unchanged and no distortion is observed on the reflected and transmitted ultrasound. Whereas a high-power shear wave strikes at a frictional interface, ultrasonic oscillations change the contact state and activate 'stick-slip' motion at the interface. The nonlinear nature of the stick-slip motion distorts both the reflected and transmitted ultrasound and high odd order harmonics are generated.

With the one-dimensional finite difference model, nonlinearity generation at the frictional interface was studied. The numerical model was compared with the analytical method and good agreement between the analytical and numerical

solutions proved the validity and usefulness of the numerical model in investigating the nonlinearity generation from the interaction between a shear ultrasound and a frictional interface.

Parameters influencing the nonlinear interaction at the interface, i.e. 'stick-slip' motion, were investigated numerically. Activation 'stick-slip' motion and consequent nonlinearity generation at the interface was affected by the incident ultrasound amplitude, the normal contact stress and the friction coefficient at the interface. Contact nonlinearity was preferably generated at large incident amplitude, low contact stress and low friction coefficient. A dimensionless stress ξ was employed as the ratio of the frictional stress at the interface to the ultrasonic induced shear stress. Nonlinearity generation reached the maximum ($\xi = 0.5$) regardless of the incident ultrasound amplitude, contact stress and friction coefficient.

The numerical model employed in this work has been simplified, but nevertheless, the solution captures the physical phenomenon of the nonlinear interaction between a high-power shear ultrasound and a frictional interface. The numerical study provides guidance for the following experimental work.

10.2 Developing an Ultrasonic Method in Measuring Contact Nonlinearity

Measuring the contact nonlinearity at a rough interface using an ultrasonic method was investigated experimentally. Apparatus that meets the requirement has been selected in the experimental detection of the contact nonlinearity. A high frequency nonlinear ultrasonic technique was employed. Experimental variables were found to have a significant influence on the measurement of the contact nonlinearity. In practice, accurate and reliable measurement of the contact nonlinearity requires consistent test configuration, data acquisition and signal processing methods.

Experimental detection of contact nonlinearity was carried out using both pitch-catch transmission and pitch-catch reflection arrangement. Both arrangements were applicable in measuring the contact nonlinearity as the third harmonic were observed in both transmitted and reflected signals. Reflection arrangement was selected due to its practical benefits.

Practically measured ultrasonic nonlinearity consists of the system inherent nonlinearity (mainly from the test specimen and instruments) and the contact nonlinearity (only from the frictional interface). Methods have been developed to

separate the contact nonlinearity from the measured ultrasonic nonlinearity. Measurement results show that the nonlinear interaction, i.e. 'stick-slip' motion between a high-power shear wave and a rough interface can be experimentally measured. Nonlinearity generation increases with and then decreases with the contact stress. Larger incident amplitude introduces more nonlinearity being generated at the rough interface. In the subsequent echoes, nonlinearity is also observed.

10.3 Developing an Ultrasonic Method to Measure Friction Coefficient at an Interface

The contact nonlinearity measured experimentally were compared to the numerical computation solution. The difference between the numerical computation and experimental measurement was mainly because that the numerical model treats the contact between two rough surfaces as simplified flat smooth plane contact whereas practically contact of two rough surfaces are made on the asperities. Despite the difference, the agreement between the numerical and experimental nonlinearity generation allows the friction coefficient to be estimated.

Two strategies were developed to estimate the friction coefficient using ultrasonically measured contact nonlinearity. The first strategy used cut-off stress where the nonlinear 'stick-slip' stops occurring. The ratio of the incident shear stress and the cut-off stress gave the friction coefficient. The second strategy used the numerical model to compute the contact nonlinearity with the experimental test conditions and various friction coefficients. The friction coefficient that yielded the most correlated contact nonlinearity between the numerical and experimental solutions was the friction coefficient.

With the developed method, the ultrasonically measured friction coefficient agreed with the sliding test results (in total 54%) and published data. Despite limitations, the ultrasonic method using experimentally measured contact nonlinearity shows the usefulness in measure the friction coefficient in-situ in a contact interface.

10.4 Future Works

Further development and investigation directions are listed as follows.

- Improve the numerical model. In the current research work, the contact model representing what happens at a rough interface is not considered. Various contact models can be integrated with the numerical model to investigate the contact nonlinearity generation in a more realistic way. Advanced numerical techniques can be also applied.
- Extend the friction coefficient estimation application. The ultrasonic method estimating the friction coefficient in-situ is currently focused at similar-material contact pair. Friction coefficient estimation needs to be extended to dissimilar material pairs.
- Extend friction coefficient estimation in a high-stress contact. Practically, contacts are subject to high stress. To apply the ultrasonic method under this condition, further investigation is needed to increase the practically achievable shear stress.
- Extend the friction coefficient estimation in lubricated contact. Nonlinearity generation at a lubricated contact needs to study because the role of lubricant in the contact nonlinearity generation is unknown. Different mechanisms may be involved when high-power ultrasound interacts with liquid.
- Facilitate the practical implementation. Currently a high-power ultrasound is used to trigger the 'stick-slip' motion. The measurement is also carried out over a range of contact stress. Sweeping power method, multi-echoes method and oblique incidence method need to be investigated to evaluate the effectiveness and usefulness in practical implementations.
- Estimate friction coefficient in dry contacts. Friction coefficient estimation at a dry contact can be tried out and wheel-rail contact, machine tool joints and brakes are where dry contact occurs. Implementation of the ultrasonic method to estimate friction coefficient potentially provides real-time information at these dry contacts.
- Estimation friction coefficient in tribometers. The ultrasonic method can be implemented on a frictional test machine or tribometers. Friction measured simultaneously by tribometer and ultrasound can be investigated.

REFERENCES

- Achenbach, J.D. (1973) *Wave propagation in elastic solids*. Amsterdam, Elsevier.
- Aleshin, V., Delrue, D., Trifonov, A. Matar, O.M. and Van Den Abeele, K (2018) Two dimensional modeling of elastic wave propagation in solids containing cracks with rough surfaces and friction – Part I: theoretical background. *Ultrasonics*, 82, 11–18.
- Baik, J.M. and Thompson, R.B. (1984) Ultrasonic scattering from imperfect interfaces: a quasi-static model. *Journal of Nondestructive Evaluation*, 4, 177–196.
- Baltazar, A., Rokhlin, S.I. and Pecorari, C. (2002) On the relationship between ultrasonic and micromechanical properties of contacting rough surfaces. *Journal of the Mechanics and Physics of Solids*, 50, 1397–1416.
- Barnard, D.J., Dace, G.E., Rhebein, D.K. and Buck, O. (1997) Acoustic harmonic generation at diffusion bonds. *Journal of Nondestructive Evaluation*, 16, 77–89.
- Bengisu, M.T. and Akay, A. (1999) Stick–slip oscillations: dynamics of friction and surface roughness. *The Journal of the Acoustical Society of America*, 105, 194–205.
- Biwa, S., Nakajima, S. and Ohno, N. (2004) On the acoustic nonlinearity of solid-solid contact with pressure-dependent interface stiffness. *Journal of Applied Mechanics, Transactions ASME*, 71, 508–515.
- Biwa, S., Hiraiwa, S. and Matsumoto, E. (2006) Experimental and theoretical study of harmonic generation at contacting interface. *Ultrasonics*, 44, 1319–1322.
- Blanloeuil, P., Meziane, A. and Bacon, C. (2013) Nonlinear interaction of ultrasonic waves with a crack of different orientations. *AIP Conference Proceedings*, 1511, 99–106.
- Blanloeuil, P., Meziane, A. and Bacon, C. (2014a) Numerical study of nonlinear interaction between a crack and elastic waves under an oblique incidence. *Wave Motion*, 51, 425–437.

- Blanloeuil, P., Croxford, A.J. and Meziane, A. (2014b) Application of the noncollinear mixing method to an interface of contact. *AIP Conference Proceedings*, 1581, 623–630.
- Blanloeuil, P., Croxford, A.J. and Meziane, A. (2014c) Numerical and experimental study of the nonlinear interaction between a shear wave and a frictional interface. *The Journal of the Acoustical Society of America*, 135, 1709–1716.
- Blanloeuil, P., Meziane, A. and Bacon, C. (2015) 2D finite element modeling of the non-collinear mixing method for detection and characterization of closed cracks. *NDT and E International*, 76, 43–51.
- Blanloeuil, P., Meziane, A. and Norris. (2016) Analytical extension of finite element solution for computing the nonlinear far field of ultrasonic waves scattered by a closed crack. *Wave Motion*, 66, 132–146.
- Blanloeuil, P., Rose, L.R.F., Veidt, M and Wang, C.H. (2017) Time reversal invariance for a one-dimensional model of contact acoustic nonlinearity. *Journal of Sound and Vibration*, 394, 515–526.
- Blau, P.J. (2001) The significance and use of the friction coefficient. *Tribology International*, 34, 585–591.
- Bowden, F.P. and Tabor, D. (1964) *The friction and lubrication of solids*. Oxford, Clarendon Press.
- Brunskill, H.P. (2013) *The real-time characterisation of dry machine element contacts using ultrasonic reflectometry*. Ph.D thesis, University of Sheffield.
- Buck, O., Morris, W.L. and Richardson, J.M. (1978) Acoustic harmonic generation at unbonded interfaces and fatigue cracks. *Applied Physics Letters*, 33, 371–373.
- Bush, A.W., Gibson, R.D. and Thomas, T.R. (1975) The elastic contact of a rough surface. *Wear*, 35, 87–111.
- Cantrell, J.H. (2004) Substructural organization, dislocation plasticity and harmonic generation in cyclically stressed wavy slip metals. *Proceedings of the Royal Society A: Mathematical, Physical and Engineering Sciences*, 460, 757–780.

- Chaudhry, V. and Kailas, S.V. (2013) Elastic-plastic contact conditions for frictionally constrained bodies under cyclic tangential loading. *Journal of Tribology*, 136.
- Chen, J., Zhang, D., Mao, Y.W. and Cheng, J.C. (2006) Contact acoustic nonlinearity in a bonded solid-solid interface. *Ultrasonics*, 44, 1355–1358.
- Chen, W., Mills, R. and Dwyer-Joyce, R.S. (2015) Direct load monitoring of rolling bearing contacts using ultrasonic time of flight. *Proceedings of the Royal Society A: Mathematical, Physical and Engineering Science*, 471.
- Dahl, P. (1968) *A solid friction model*. Aerospace Corporation El Segundo, CA.
- Delrue, S., Aleshin, V., Truyaert, K., Matar, O.M., and Van Den Abeele, K. (2018) Two dimensional modeling of elastic wave propagation in solids containing cracks with rough surfaces and friction – Part II: numerical implementation. *Ultrasonics*, 82, 19–30.
- Dieterich, J.H. (1978) Time-dependent friction and the mechanics of stick-slip. *Pure and Applied Geophysics PAGEOPH*, 116, 790–806.
- Donskoy, D., Sutin, A. and Ekimov, A. (2001) Nonlinear acoustic interaction on contact surfaces and its use for nondestructive testing. *NDT & E International*, 34, 231–238.
- Drinkwater, B.W., Dwyer-Joyce, R.S. and Cawley, P. (1996) A study of the interaction between ultrasound and a partially contacting solid-solid interface. *Proceedings of the Royal Society A: Mathematical, Physical and Engineering Sciences*, 452, 2613–2628.
- Dunkin, J.E. and Kim, D.E. (1996) Measurement of static friction coefficient between flat surfaces. *Wear*, 193, 186–192.
- Dwyer-Joyce, R.S., Drinkwater, B.W. and Quinn, A.M. (2001) The use of ultrasound in the investigation of rough surface interfaces. *Journal of Tribology*, 123, 8.
- Dwyer-Joyce, R.S., Drinkwater, B.W. and Donohoe, C.J. (2003) The measurement of lubricant-film thickness using ultrasound. *Proceedings of the Royal Society A: Mathematical, Physical and Engineering Sciences*, 459, 957–976.

- Dwyer-Joyce, R.S., Harper, P. and Drinkwater, B.W. (2004) A method for the measurement of hydrodynamic oil films using ultrasonic reflection. *Tribology Letters*, 17, 337–348.
- Eriten, M., Polycarpou, A.A. and Bergman, L.A. (2010) Physics-based modeling for partial slip behavior of spherical contacts. *International Journal of Solids and Structures*, 47, 2554–2567.
- Etsion, I. (2010) Revisiting the Cattaneo–Mindlin concept of interfacial slip in tangentially loaded compliant bodies. *Journal of Tribology*, 132.
- Feeny, B., Guran, A., Hinrichs, N. and Popp, K. (1998) A historical review on dry friction and stick-slip phenomena. *Applied Mechanics Reviews*, 51, 321.
- Gonzalez-Valadez, M., Baltazar, A. and Dwyer-Joyce, R.S. (2010) Study of interfacial stiffness ratio of a rough surface in contact using a spring model. *Wear*, 268, 373–379.
- Greenwood, J.A. and Williamson, J.B.P. (1966) Contact of nominally flat surfaces. *Proceedings of the Royal Society of London. Series A, Mathematical and Physical Sciences*, 295, 300–319.
- Hirose, S. (1994) 2-D scattering by a crack with contact-boundary conditions. *Wave Motion*, 19, 37–49.
- Howard, T. (2016) *Development of a novel bearing concept for improved wind turbine gearbox reliability*. Ph.D. thesis, University of Sheffield.
- Hutchings, I.M. and Hutchings, I.M. (2017) *Tribology: friction and wear of engineering materials*. Kidlington, Butterworth-Heinemann.
- Jhang, K. (2009) Nonlinear ultrasonic techniques for non-destructive assessment of micro damage in material: a review. *Int. J. Precis. Eng. Manuf*, 10, 123–135.
- Jhang, K. and Kim, K. (1999) Evaluation of material degradation using nonlinear acoustic effect. *Ultrasonics*, 37, 39–44.
- Jiao, J.P., Liu, W.H. He, C.F., Wu, B. and Zhang, J. (2014) Nonlinear acoustic interaction of contact interfaces. *Experimental Mechanics*, 54, 63–68.

- Johnson, K.L. (1985) *Contact mechanics*, Cambridge, Cambridge University Press.
- Kawashima, K., Omote, R., Ito, T., Fujita, H. and Shima, T. (2002) Nonlinear acoustic response through minute surface cracks: FEM simulation and experimentation. *Ultrasonics*, 40, 611–615.
- Kendall, K. and Tabor, D. (1971) An ultrasonic study of the area of contact between stationary and sliding surfaces. *Proceedings of the Royal Society A: Mathematical, Physical and Engineering Sciences*, 323, 321–340.
- Kim, J.Y., Baltazar, A., Hu, J. W. and Rokhlin, S. I. (2006) Hysteretic linear and nonlinear acoustic responses from pressed interfaces. *International Journal of Solids and Structures*, 43, 6436–6452.
- Kinsler, L.E. Frey, A.R. Copperns, A.B. and Sanders, J.V. (2000) *Fundamentals of acoustics*. 4th ed. Chichester, John Wiley & Sons.
- Kligerman, Y. and Varenberg, M. (2014) Elimination of stick-slip motion in sliding of split or rough surface. *Tribology Letters*, 53, 395-399.
- Krautkramer, J. and Krautkramer, H. (1990) *Ultrasonic testing of materials*. 4th ed. New York, Springer.
- Królikowski, J. and Szczepek, J. (1991) Prediction method of contact parameters using ultrasonic. *Wear*, 148, 181–195.
- Królikowski, J. and Szczepek, J. (1992) Phase shift of the reflection coefficient of ultrasonic waves in the study of the contact interface. *Wear*, 157, 51–64.
- Królikowski, J. and Szczepek, J. (1993) Assessment of tangential and normal stiffness of contact between rough surfaces using ultrasonic method. *Wear*, 160, 253–258.
- Lavrentyev, A.I., Baltazar, A. and Rokhlin, S.I. (1998) Ultrasonic spectroscopy of two parallel imperfect interfaces. *Review of Progress in Quantitative Nondestructive Evaluation*, 17, 1379–1386.
- Liu, S., Croxford, A.J., Neild, S.A. and Zhou, Z. (2011) Effects of experimental variables on the nonlinear harmonic generation technique. *IEEE Transactions on Ultrasonics, Ferroelectrics, and Frequency Control*, 58, 1442–1451.

- Liu, S., Best, S., Neild, S.A., Croxford, A.J. and Zhou, Z. (2012) Measuring bulk material nonlinearity using harmonic generation. *NDT and E International*, 48, 46–53.
- Margetan, F.J., Thompson, R.B. and Gray, T.A. (1988) Interfacial spring model for ultrasonic interactions with imperfect interfaces: Theory of oblique incidence and application to diffusion-bonded butt joints. *Journal of Nondestructive Evaluation*, 7, 131–152.
- Marshall, M., Lewis, R., Dwyer-Joyce, R., Olofsson, U. and Bpirklund, S. (2006) Experimental characterization of wheel-rail contact patch evolution. *Journal of Tribology*, 128, 493-504.
- McCool, J. (1986) Comparison of model for the contact of rough surfaces. *Wear*, 107, 37–60.
- Mendelsohn, D.A. and Doong, J.M. (1989) Transient dynamic elastic frictional contact: A general 2D boundary element formulation with examples of SH motion. *Wave Motion*, 11, 1–21.
- Meziane, A, Norris, A.N. and Shuvalov, A.L. (2011) Nonlinear shear wave interaction at a frictional interface: Energy dissipation and generation of harmonics. *The Journal of the Acoustical Society of America*, 130, 1820.
- Nagy, P.B. (1992) Ultrasonic classification of imperfect interfaces. *Journal of Nondestructive Evaluation*, 11, 127–139.
- O'Neill, B., Maev, R.G. and Severin, F. (2001) Distortion of shear waves passing through a friction coupled interface. *Review of progress in Quantitative Nondestructive Evaluation*, 557, 1264–1267.
- Olsson, H., Åström, K. J., Gäfvert, C., Canudas De Wit, M., Lischinsky, P. and Åström, P. (1998) Friction models and friction compensation. *European Journal of Control*, 4, 176–195.
- Olympus NDT Inc. (2006) *Ultrasonic Transducers Technical Notes*. Waltham, MA, USA, Olympus NDT Inc.

- Pecorari, C. (2003) Nonlinear interaction of plane ultrasonic waves with an interface between rough surfaces in contact. *The Journal of the Acoustical Society of America*, 113, 3065–3072.
- Pecorari, C. and Poznić, M. (2005) Nonlinear acoustic scattering by a partially closed surface-breaking crack. *The Journal of the Acoustical Society of America*, 117, 592–600.
- Pecorari, C. (2015) Modeling non-collinear mixing by distributions of clapping microcracks. *Wave Motion*, 59, 69–80.
- Quinn, A.M., Drinkwater, B.W. and Dwyer-Joyce, R.S. (2002) The measurement of contact pressure in machine elements using ultrasound. *Ultrasonics*, 39(7), 495–502.
- Rabinowicz, E. (1951) The nature of the static and kinetic coefficients of friction. *Journal of Applied Physics*, 22, 1373–1379.
- Reddyhoff, T., Kasolang, S. Dwyer-Joyce, R.S. and Drinkwater, B.W. (2005) The phase shift of an ultrasonic pulse at an oil layer and determination of film thickness. *Proceedings of the Institution of Mechanical Engineers, Part J: Journal of Engineering Tribology*, 219, 387–400.
- Richardson, J.M. (1979) Harmonic generation at an unbonded interface— I. planar interface between semi-infinite elastic media. *International Journal of Engineering Science*, 17, 73-85.
- Ruan, J. and Bhushan, B. (1994) Atomic-scale friction measurements using friction force microscopy: Part I-general principles and new measurement techniques. *Journal of Tribology*, 116, 378–388.
- Rusli, M. and Okuma, M. (2007) Effect of surface topography on mode-coupling model of dry contact sliding systems. *Journal of Sound and Vibration*, 308, 721–734.
- Schirru, M., Sutton, M., Dwyer-Joyce, R., Smith, O. and Mills, R. (2015a) Development of a novel ultrasonic viscometer for real time and in - situ applications in engines. *SAE Technical Paper*. 2015-01-0679.

- Schirru, M., Mills, R., Dwyer-Joyce, R., Smith, O. and Sutton, M. (2015b) Viscosity Measurement in a Lubricant Film Using an Ultrasonically Resonating Matching Layer. *Tribology Letters*, 60, 1–11.
- Schoenberg, M. (1980) Elastic wave behavior across linear slip interfaces. *Journal of the Acoustical Society of America*, 68, 1516–1521.
- Shin, K. and Hammond, J.K. (1993) *Fundamentals of signal processing for sound and vibration engineers*. Chichester, John Wiley & Sons.
- Solodov, I.Y., Asainov, A.F. and Len, K.S. (1993) Non-linear SAW reflection: experimental evidence and NDE applications. *Ultrasonics*, 31, 91–96.
- Solodov, I.Y. (1998) Ultrasonics of non-linear contacts: propagation, reflection and NDE-applications. *Ultrasonics*, 36, 383–390.
- Tabor, D. (1981) Friction—the present state of our understanding. *Journal of Lubrication Technology*, 103, 169–179.
- Tattersall, H.G. (1973) The ultrasonic pulse-echo technique as applied to adhesion testing. *Journal of Physics D: Applied Physics*, 6, 819–832.
- Van Den Abeele, K. and Breazeale, M.A. (1996) Theoretical model to describe dispersive nonlinear properties of Lead Zirconate – Titanate Ceramics. *Journal of the Acoustical Society of America*, 99, 1430–1437.
- Wang, D., Xu, C. and Wan, Q. (2017) Modeling tangential contact of rough surfaces with elastic- and plastic-deformed asperities. *Journal of Tribology*, 139.
- Williams, J. (2005) *Engineering Tribology*. Cambridge, Cambridge University Press.
- Yan, D., Drinkwater, B.W. and Neild, S.A. (2009) Measurement of the ultrasonic nonlinearity of kissing bonds in adhesive joints. *NDT and E International*, 42, 459–466.
- Yuan, M., Lee, T., Kang, T., Zhang, J., Song, S.J. and Kim, H.J. (2015) Absolute measurement of ultrasonic non-linearity parameter at contact interface. *Nondestructive Testing and Evaluation*, 30, 356-372.

- Zhang, Z., Nagy, P.B. and Hassan, W. (2016) Analytical and numerical modeling of non-collinear shear wave mixing at an imperfect interface. *Ultrasonics*, 65, 165–176.
- Zhou, S. and Shui, Y. (1992) Nonlinear reflection of bulk acoustic waves at an interface. *Journal of Applied Physics*, 72, 5070–5080.

APPENDIX A

One-dimensional wave propagation finite difference MATLAB script

```
clear all
clc
%% material properties - Al
E=70E9; % young's modulus
nu=0.3; % poisson's ratio
rho=2700; % density
G=E/(2*(1+nu));
c=sqrt(G/rho);
Z=rho*c; % acoustic impedance
flw=1E6; % fundamental frequency 1MHz
plw=1/flw; % period of fundamental wave
sigma=1E6; % applied normal stress
mu=0.5; % coefficient of friction
lamda=c/flw; % wavelength
awvn=2*pi/lamda; % angular wavenumber
stresscoef=G*awvn;
%% numerical
L=3E-2; % length of specimen
T=24E-6; % total time
dx=2E-5; % space increment
dt=4.5E-9; % time increment
nx=round(L/dx); % number of space divisions, integer
nt=round(T/dt); % number of time divisions, integer

% stability check
CFL=c*dt/dx; % cfl condition
if CFL >= 1
    fprintf('CFL Stability is not met. Make sure CFL less than Unity')
else
    s=CFL;
    r=CFL^2; % coefficient
end

%% space discretisation and initial boundary condition
for k=1:nx+1
    x(k)=(k-1)*dx;
    u(k,1)=0;
    % du/dt=0 at t=0
end

%% time discretisation and boundary condition
f=zeros(nt+1,1); % initialise source term
js=round(5*plw/dt+1);

for j=1:nt+1
    t(j)=(j-1)*dt;
end
f(1:js)=50E-3*sin(2*pi*flw*t(1:js)); % modulated source, apply gaussian window
w=gausswin(js);
f(1:js)=f(1:js).*w;

%% implement explicit scheme
for j=1:nt
    if j==1
        % particle velocity v at i=nx+1,j=1
```

```

v(j)=0;
% assume sticking u(j+1)=u(j) at nx+1
u(nx+1,j+1)=u(nx+1,j);
% compute shear stress
tau(2:nx,j)=G*(u(3:nx+1,j)-u(1:nx-1,j))/(2*dx);
tau(nx+1,j)=G*(3*u(nx+1,j)-4*u(nx,j)+u(nx-1,j))/(2*dx);
tau(1,j)=G*(-3*u(1,j)+4*u(2,j)-u(3,j))/(2*dx);
% update left BC
u(1,j+1)=(1-3/2*s)*u(1,j)+2*s*u(2,j)-s/2*u(3,j)-2*f(j)*dt; % TBC+source
% check contact state, sticking or slipping
if abs(tau(nx+1,j)) >= mu*sigma % sliding
    % compute shear stress at boudary i=nx+1
    tau(nx+1,j)=sign(tau(nx+1,j))*mu*sigma;
    % update u(nx+1,j+1) for slipping
    u(nx+1,j+1)=((2*dx/G)*tau(nx+1,j)+4*u(nx,j)-u(nx-1,j))/3;
    % compute u for next time
    u(2:nx,j+1)=0.5*(r*u(3:nx+1,j)+(2-2*r)*u(2:nx,j)+r*u(1:nx-1,j));
    v(j+1)=(u(nx+1,j+1)-u(nx+1,j))/dt;
else
    % compute u for next time
    u(2:nx,j+1)=0.5*(r*u(3:nx+1,j)+(2-2*r)*u(2:nx,j)+r*u(1:nx-1,j));
    v(j+1)=(u(nx+1,j+1)-u(nx+1,j))/dt;
end
else
% assume sticking u(j+1)=u(j) at nx+1
u(nx+1,j+1)=u(nx+1,j);
% compute shear stress
tau(2:nx,j)=G*(u(3:nx+1,j)-u(1:nx-1,j))/(2*dx);
tau(nx+1,j)=G*(3*u(nx+1,j)-4*u(nx,j)+u(nx-1,j))/(2*dx);
tau(1,j)=G*(-3*u(1,j)+4*u(2,j)-u(3,j))/(2*dx);
% compute u for next time at i=1
u(1,j+1)=(1-3/2*s)*u(1,j)+2*s*u(2,j)-s/2*u(3,j)-2*f(j)*dt;
% check contact state, sticking or slipping
if abs(tau(nx+1,j)) >= mu*sigma % sliding
    % compute shear stress at boudary i=nx+1
    tau(nx+1,j)=sign(tau(nx+1,j))*mu*sigma; %!!! sign(v) or sign (u_dot)
    % update u(nx+1,j+1) for slipping
    u(nx+1,j+1)=((2*dx/G)*tau(nx+1,j)+4*u(nx,j)-u(nx-1,j))/3;
    % compute u for next time
    u(2:nx,j+1)=r*u(3:nx+1,j)+(2-2*r)*u(2:nx,j)+r*u(1:nx-1,j)-u(2:nx,j-
1);
    v(j+1)=(u(nx+1,j+1)-u(nx+1,j))/dt;
else % sticking
    u(2:nx,j+1)=r*u(3:nx+1,j)+(2-2*r)*u(2:nx,j)+r*u(1:nx-1,j)-u(2:nx,j-
1);
    v(j+1)=(u(nx+1,j+1)-u(nx+1,j))/dt;
end
end
end

% plot the graph after every 10th frame
if mod(j,10)==0
    subplot(2,1,1)
    plot(x,u(:,j))
    axis([0 L -1.2E-8 1.2E-8])
    title('displacement')
    ylabel('Amplitude (m)')
    xlabel('x (m)')
    subplot(2,1,2)
    plot(x,tau(:,j))
    axis([0 L -0.8E6 0.8E6])
    title('shear stress')
    ylabel('Amplitude (MPa)')
    xlabel('x (m)')
    pause(0.001)
end
end
end

```